Galaxy evolution across the Virgo cluster environment

by

Cameron Morgan

A thesis
presented to the University of Waterloo
in fulfillment of the
thesis requirement for the degree of
Doctor of Philosophy
in
Physics

Waterloo, Ontario, Canada, 2026

© Cameron Morgan 2026

Examining Committee Membership

The following served on the Examining Committee for this thesis. The decision of the Examining Committee is by majority vote.

External Examiner:	Karen Masters Professor, Dept. of Physics and Astronomy Haverford College
Supervisor:	Michael Balogh Professor, Dept. of Physics and Astronomy University of Waterloo
Committee Member:	Mike Hudson Professor, Dept. of Physics and Astronomy University of Waterloo
Committee Member:	Brian McNamara Professor, Dept. of Physics and Astronomy University of Waterloo
Internal-External Member:	Richard Kelly Professor, Dept. of Geography and Environmental Management University of Waterloo

Author's Declaration

This thesis consists of material all of which I authored or co-authored: see Statement of Contributions included in the thesis. This is a true copy of the thesis, including any required final revisions, as accepted by my examiners.

I understand that my thesis may be made electronically available to the public.

Statement of Contributions

This thesis is based on the following articles:

Chapter 2: **Morgan, C. R.**, Sazonova, E., Roberts, I. D., Balogh, M. L. et al. 2025. Deep galaxy stellar mass functions as a function of star formation rate in the Virgo cluster environment. *The Astrophysical Journal*, 987, 166, doi: 10.3847/1538-4357/addc6c

Chapter 3: **Morgan, C. R.**, Balogh, M. L., Boselli, A., Fossati, M. et al. 2024. A Virgo Environmental Survey Tracing Ionised Gas Emission (VESTIGE): XVI. The ubiquity of truncated star-forming discs across the Virgo cluster environment. *Astronomy & Astrophysics*, 691, A20, doi: 10.1051/0004-6361/202449225

Chapter 4: Based on work currently in preparation for publication.

Chapter 5: Based on work included in the CASTOR Phase 0 Technical Report (submitted to the Canadian Space Agency), and the GIRMOS GTO proposal, submitted to the Gemini Telescope leadership.

For each of these contributions, I am the lead researcher and author. I performed the majority of the computational analysis of the various datasets used and producing figures for the manuscripts. This work was carried out under the supervision of Michael Balogh, as well as Elizaveta Sazonova and Ian Roberts, who provided guidance and assisted with editing manuscripts.

The primary datasets used in these studies were that of VESTIGE (P.I. Alessandro Boselli), and NGVS (P.I. Laura Ferrarese). As such, data acquisition and reduction, as well as catalogues of parameters such as galaxy sizes and stellar masses used in these works were performed by the NGVS and VESTIGE teams, including Alessandro Boselli, Matteo Fossati, Laura Ferrarese, Patrick Côté, Stephen Gwyn, Jean-Charles Cuillandre, and Joel Roediger. Additional data was taken from GuViCS (P.I. Alessandro Boselli) and UVIT observations (P.Is. John Hutchings and Alessandro Boselli). Other data used was from publicly available datasets. Additional co-authors listed on the manuscript for Chapter 3 are members of the VESTIGE team who provided comments, as well as Cameron Lawlor-Forsyth, who provided guidance on some of the analysis.

Chapter 4 makes significant use of the CIGALE SED fitting code, with development led by Médéric Boquien, with contributions from the other authors listed in Boquien et al. (2019).

Chapter 5 discusses the CASTOR (P.I. Pat Côté) and GIRMOS (P.I. Suresh Sivanandam) projects, two proposed and Canadian-led instruments that will be transformational to galaxy science. The work discussed and plots shown are mainly based around my contribution to the CASTOR Galaxies Science Working Group and the GIRMOS GTO science team.

Abstract

In this thesis, I present three studies of the properties of galaxies in the Virgo cluster with the goal of providing new insights into how we can measure the effects of the cluster environment on these member galaxies. Throughout this work, I move from analyzing integrated quantities of galaxies toward studying galaxy star formation on a spatially-resolved scale.

First, I analyze deep stellar mass functions of galaxies in the Virgo cluster. I split these stellar mass functions according to star formation rate and region within the cluster. I find that the quenched fractions remain high across the cluster, including in the infall region, and especially at low stellar masses. Additionally, the shapes of the mass functions are mostly independent of position within the cluster. Using a simple model of infalling and backsplash galaxy populations, I show that the quenched fractions seen in the cluster outskirts require unrealistically high backsplash fractions, implying that galaxies are being pre-processed outside of the main cluster and are often already quenched upon first infall.

The second section of this thesis focuses on quantifying the edges of star-forming disks as a means to analyze truncation and outside-in quenching. I develop a novel method for measuring disk truncation that takes advantage of the depth and spatially-resolved nature of the VESTIGE Hα data. This method involves constructing radial sSFR profiles and identifying the turn-off point where star formation drops off. I compare this edge of the star-forming disk with a measure of the expected size based on normal star-forming galaxies, which gives a measure of the degree of truncation. Ultimately, I find that moderately-severely truncated disks are ubiquitous across the cluster environment, and show only mild correlations with parameters such as stellar mass, distance from the SFMS, and HI-deficiency. I invoke toy models of RPS and starvation to show the effects that each of these mechanisms has on disk truncation. While RPS can rapidly truncate the star-forming disk, it is only particularly effective toward the cluster centre. Starvation can slowly truncate disks much earlier by cutting off a galaxy's supply of fresh gas – as the gas density decreases, the outer part of the disk falls below the threshold necessary to sustain star formation first, causing a slow outside-in quenching. This again highlights the need for pre-processing to explain quenching in the Virgo environment, and indicates a "slow-then-rapid" quenching sequence.

Finally, I take advantage of the spatially-resolved and multi-wavelength data available for Virgo cluster galaxies to map signatures of quenching on more local scales. I do this by empirically calculating SFRs based on both Hα and FUV fluxes, thus giving me SFRs on both ~ 10 and ~ 100 Myr timescales. Comparing the two helps to identify regions where

rapid quenching is occurring. I perform spatially resolved SED fitting on a sample of Virgo galaxies using CIGALE which allows me to map out galaxy parameters. Combining the SED fitting results with emission line ratios from MaNGA, I derive corrections based on dust, NII contamination (in the Hα) and pAGB contribution to the FUV before converting the respective fluxes to SFRs. Taking the ratio of $SFR_{H\alpha}$ and SFR_{FUV} allows me to visually identify interesting features in these galaxies. I identify two key features: lopsidedness in the distribution of $SFR_{H\alpha}/SFR_{FUV}$, and outer disk truncation. I quantify these metrics, and find that while a few galaxies that have strong gas asymmetries and have been identified as RPS candidates have a high degree of lopsidedness, there are no strong correlations with other galaxy parameters. I discuss the possibility that these metrics are unique signatures of processes like RPS at certain stages, though drawing strong conclusions about their nature proves difficult.

I end off with future perspectives, based on my own work with the CASTOR and GIRMOS science teams, the broader context of new instrumentation and analysis tools, and my own goals for the coming years as I seek to continue work into the study of galaxy evolution. I look forward to pursuing studies with new data, exploring new redshift ranges and galaxy environments, and looking to continue developing novel techniques to help make inferences about galaxies in the broad context of understanding our Universe.

Acknowledgements

First off, I would like to thank my supervisor Dr. Michael Balogh. I am incredibly grateful to have had an advisor who I aligned with so well – your guidance and advice have been absolutely instrumental in my transformation into the researcher I am today. Your passion and dedication for science is unmatched, and despite your transition into exoplanet research, I hope that we will continue to find ways to work together in the future.

To my committee members, Dr. Mike Hudson, Dr. Brian McNamara, and Dr. Ghazal Geshnizjani: thank you for your support and advice over these last few years. You too have helped to place me in a position of readiness for the next steps in my career.

To all the members of the WCA, thank you for the contributions you each make to the research and social environment in the office. Particularly thanks for Carolyn for the amazing work you do in administering the WCA, and Will for your management.

To colleagues who have helped make this work possible, including Liza and Ian for your co-supervision and Cam for brainstorming sessions in our office, Roan for your mentorship and for encouraging us to see the importance in doing outreach.

A shout out to the members of collaborations of which I've been grateful to be a part: CASTOR, VESTIGE, NGVS, and GIRMOS. A special thank you to those of you who have always been willing to write recommendation letters.

A few of you have crossed the line from colleagues into friends. Liza, Roan, and MJ: we've introduced each other to new hobbies (ice fishing and climbing come to mind), and I've probably spent more time with you three in the past few years than almost anyone else. Thank you for being the backbone of Astrobeers, trivia, puzzle hunts, parties and celebrations and so much more. Truly it's hard to imagine what it'll be like without you once we each move onto our next positions, but I hope we will stay in touch and continue to cross paths in the future.

To Daniel and Karyn who have been with me since the start of our UW journeys, thank you for your friendship and the many many memories we've shared.

To my parents and my sister: I really can't thank you enough for how supportive you've been of me and my career path. It's impossible for me to express how much your support means.

And finally to Cait: by the time this is finalized after my defense, we'll be married. It's crazy to think how far we've come over these last nine years, and I'm so excited for what lies ahead for us. You've always been so supportive of me and my dreams, and it means everything to me. There are so many changes coming up this year, and I'm so happy to always have you by my side. Victoria here we come!

Land acknowledgement

During the four years I spent working on this thesis, I lived and worked on the traditional territory of the Neutral, Anishinaabeg and Haudenosaunee peoples. The University of Waterloo campus is located on the Haldimand Tract, the land granted to the Six Nations that includes six miles on each side of the Grand River. I acknowledge the privilege to work on these traditional lands. I also acknowledge that much of the data collected for this research was obtained from telescopes such as CFHT on the summit of Mauna Kea, a location with great cultural significance to the Native Hawaiian community.

Table of Contents

Examining Committee Membership ii

Author's Declaration iii

Statement of Contributions iv

Abstract vi

Acknowledgements viii

Land acknowledgement ix

List of Figures xv

List of Tables xviii

List of Abbreviations xix

1 Introduction 1

1.1 How galaxies came to map the Universe 1

1.2 A census of galaxies 4

1.2.1 Galaxy demographics 4

1.2.2 Galactic geography 7

1.3 The lives and deaths of galaxies . . . 8
1.3.1 Mass quenching . . . 9
1.3.2 Environmental quenching . . . 10
1.3.3 Morphological transformation . . . 15
1.4 Measuring galaxies and inferring their properties . . . 15
1.4.1 Spectral energy distribution fitting . . . 18
1.4.2 Measuring star formation rates . . . 20
1.5 This thesis . . . 22

2 Deep galaxy stellar mass functions as a function of star formation rate in the Virgo cluster environment 25
2.1 Introduction . . . 25
2.2 Data . . . 30
2.2.1 NGVS . . . 30
2.2.2 VESTIGE . . . 30
2.2.3 Cluster membership . . . 31
2.3 Methods . . . 32
2.3.1 Stellar masses . . . 32
2.3.2 Subcluster membership and mass scaling . . . 32
2.3.3 Star formation rates . . . 33
2.3.4 Stellar mass functions . . . 36
2.4 Results . . . 38
2.4.1 Full Virgo stellar mass functions . . . 39
2.4.2 Separating populations based on star formation rate . . . 40
2.4.3 The stellar mass function across the Virgo environment . . . 40
2.5 Discussion . . . 41
2.5.1 Cluster B and the Clouds . . . 41
2.5.2 The need for pre-processing . . . 43
2.5.3 Literature comparison . . . 48
2.6 Summary and conclusions . . . 53

3 A Virgo Environmental Survey Tracing Ionised Gas Emission (VESTIGE) XVI. The ubiquity of truncated star-forming discs across the Virgo cluster environment **56**

3.1 Introduction . . . 56

3.2 Observations and data reduction . . . 60

3.2.1 NGVS imaging . . . 61

3.2.2 VESTIGE imaging . . . 61

3.2.3 Galaxy identification . . . 63

3.2.4 Supplementary data . . . 64

3.3 Methods . . . 65

3.3.1 Extraction of radial profiles . . . 65

3.3.2 Quantifying the degree of truncation . . . 71

3.3.3 Final sample of galaxies . . . 76

3.4 Results . . . 77

3.4.1 Galaxy size as a function of stellar mass . . . 77

3.4.2 $R_{\rm sSFR}/R_{\rm norm}$ as a function of environmental indicators . . . 77

3.4.3 $R_{\rm sSFR}/R_{\rm norm}$ across the Virgo environment . . . 78

3.4.4 Modelling the radial profiles of galaxies . . . 81

3.4.5 Ram-pressure stripping . . . 82

3.4.6 Starvation . . . 86

3.4.7 Ram-pressure stripping and starvation in context . . . 88

3.5 Summary and conclusions . . . 91

4 Quenching signatures in Virgo cluster galaxies based on local variations in $\mathbf{SFR_{H\alpha}/SFR_{FUV}}$ **93**

4.1 Introduction . . . 93

4.2 Data . . . 96

4.2.1 NGVS . . . 96

4.2.2 VESTIGE . . . 96

4.2.3 Ancillary data . . . 98
4.3 Methods . . . 99
4.3.1 Resolution matching and noise considerations . . . 99
4.3.2 SED fitting . . . 99
4.3.3 SFR tracers . . . 100
4.3.4 SFR maps from Hα and FUV . . . 103
4.3.5 Morphological metrics . . . 106
4.4 Results . . . 108
4.4.1 Examples of visually interesting galaxies . . . 108
4.4.2 $A_{1,\mathrm{global}}$ and ∇ versus ram pressure stripping classifications . . . 114
4.4.3 $A_{1,\mathrm{global}}$ and ∇ versus other quenching indicators . . . 116
4.5 Discussion . . . 118
4.5.1 Effects of systematic uncertainties induced by flux corrections . . . 118
4.5.2 Timescales associated with local quenching . . . 123
4.6 Summary and conclusions . . . 124

5 A Look Ahead **127**
5.1 New Canadian-led instrumentation . . . 128
5.1.1 Cosmological Advanced Survey Telescope for Optical and UV Research (CASTOR) . . . 128
5.1.2 Gemini Infrared Multi-Object Spectrograph (GIRMOS) . . . 131
5.2 The cosmic web at cosmic noon . . . 133
5.2.1 The spectrum of galaxy environments . . . 133
5.3 Improving spatially-resolved galaxy studies . . . 134

6 Summary **137**
6.1 Summary of Chapter 2 . . . 138
6.2 Summary of Chapter 3 . . . 139
6.3 Summary of Chapter 4 . . . 140
6.4 Conclusions . . . 141

References **143**

APPENDICES **160**

A **161**

A.1 Data table 161

B **163**

B.1 Masking of contaminating sources 163

B.2 Correcting profiles for inclination effects 164

B.3 Examples of peculiar galaxies 165

B.3.1 Starburst galaxies with Hα filaments 165

B.3.2 Galaxies with unphysical $R_{\rm sSFR}$ 165

B.4 Updated VESTIGE footprint figure 167

B.5 Galaxy and quenching models 167

B.6 Additional radial profile plots 173

B.7 Additional postage stamps 174

C **177**

C.1 CIGALE parameters 177

C.2 MaNGA emission line analysis 177

C.3 Full data table and additional figures 177

List of Figures

1.1 Millennium-II simulation growth of structure. . . . 3
1.2 Galaxy bimodality in colour and star formation rate. . . . 6
1.3 Quenched fraction as a function of stellar mass. . . . 11
1.4 Environmental impacts on galaxies in the Virgo cluster. . . . 14
1.5 SED for a typical star-forming galaxy. . . . 19
1.6 Blackbody spectra of massive stars. . . . 21

2.1 Virgo cluster members binned by stellar mass. . . . 31
2.2 RA and DEC footprint of galaxies in the Virgo sample. . . . 34
2.3 SFMS of the VESTIGE sample. . . . 36
2.4 SMFs of the entire Virgo sample compared to the field from GAMA. . . . 38
2.5 SMFs and relative fractions of different populations (quiescent, low-SFR and SF) in Virgo. . . . 39
2.6 SMFs for the quiescent, low-SFR and SF populations in three radial bins centred on M87. . . . 42
2.7 Best fit parameters for the SMFs centred on M87. . . . 42
2.8 Quiescent, low-SFR and SF fractions for the bins centred on M87. . . . 43
2.9 SMFs for Cluster B and the Clouds. . . . 44
2.10 Best fit parameters for the SMFs in Cluster B and the Clouds. . . . 44
2.11 Quiescent, low-SFR and SF fractions for Cluster B and the Clouds. . . . 45
2.12 RA and DEC footprint of galaxies in the Virgo sample, highlighting the Infall population. . . . 47

2.13 Percentage of field+core quiescent samples that are inconsistent with the observed Infall quiescent population. 49
2.14 Schechter fits for our total Virgo SMF compared to three other cluster samples, as well as the GAMA field fit from Driver et al. (2022). 50
2.15 Quiescent fraction as a function of stellar mass. 51
2.16 Quiescent and low-SFR fractions as a function of clustercentric distance. . 53

3.1 Radial profiles for VCC 865 (NGC 4396). 66
3.2 Stellar mass comparison. 68
3.3 Continuum-subtracted Hα emission (*left*), r-band optical emission (*centre*), and sSFR profile (*right*) for VCC 865 (NGC 4396). 69
3.4 Size-stellar mass relations. 73
3.5 $R_{\rm sSFR}/R_{\rm norm}$ as a function of stellar mass. 75
3.6 $R_{\rm sSFR}/R_{\rm norm}$ against star formation indicators. 76
3.7 Right ascension and declination footprint of VESTIGE galaxies with measured values of $R_{\rm sSFR}/R_{\rm norm}$. 79
3.8 Box-and-whisker plot showing the median and first and third quartiles of the distributions of $R_{\rm sSFR}/R_{\rm norm}$ in different environment bins. 80
3.9 PPS diagram of VESTIGE galaxies with VESTIGE Hα detection fractions. 82
3.10 PPS diagram indicating regions where RPS is effective at gas removal. . . . 84
3.11 Evolution of total gas density over 8 Gyr for a galaxy undergoing simple starvation. 86
3.12 Evolution through time of $R_{\rm sSFR}$ for a galaxy undergoing starvation and RPS. 89

4.1 SFH and FUV contribution from old stars. 103
4.2 Diagnostic plots for three normal galaxies. 111
4.3 Diagnostic plots for three lopsided galaxies. 112
4.4 Diagnostic plots for three truncated galaxies. 113
4.5 $A_{1,\rm global}$ versus ∇/σ_{∇} for different gas stripping classifications. 115

4.6 Same as Figure 4.5, but with datapoints coloured according to stellar mass (top), HI-deficiency (middle), and distance from the Boselli et al. (2023a) SFMS (bottom). . . . 117
4.7 Same as Figure 4.5, but with datapoints coloured according to the strength of their star-forming disk break truncation as measured in Morgan et al. (2024). . . . 118
4.8 Line reddening derived from MAUVE. . . . 120
4.9 Emission line ratio diagnostics for five MAUVE galaxies. . . . 121
4.9 Emission line ratio diagnostics for five MAUVE galaxies. . . . 122

5.1 Size recovery of CASTOR simulated galaxies . . . 130
5.2 Size-mass relation of simulated CASTOR galaxies. . . . 131

B.1 Masking routine for VCC 483. . . . 164
B.2 Hα NB emission, r-band optical emission, and sSFR profile for VCC 1190. 166
B.3 Hα NB emission, r-band optical emission, and sSFR profile for VCC 465. . 166
B.5 Initial SFR (green), HI (red), H_2 (blue) and total gas (black) density profiles for a $10^{9.5}M_\odot$ galaxy. . . . 169
B.7 Same as Fig. 3.1 but for all galaxies shown in Fig. B.8. From top to bottom and left to right: VCC 304, VCC 2037, VCC 865 (NGC 4396), VCC 157 (NGC 4208), VCC 1605, VCC 565, VCC 1868 (NGC 4607) and VCC 596 (NGC 4321). . . . 173
B.8 Same as Fig. 3.3 for VCC 304, VCC 2037, VCC 865 (NGC 4396), and VCC 157 (NGC 4208). . . . 175

C.1 MaNGA NII/Hα ratios . . . 179
C.2 NII/Hα ratio as a function of stellar mass in MaNGA star-forming galaxies. 180
C.3 Same as Figure 4.8, but for VCC 92 (a) and VCC 483 (b). . . . 181
C.3 (Cont.) Same as Figure 4.8, but for VCC 630 (a) and VCC 1516 (b). . . . 182

List of Tables

2.1 Properties of Virgo cluster substructures (taken from Boselli et al. 2023b) . 29

2.2 Best fit parameters and uncertainties for the total Virgo SMF and the SMFs split according to Hα emission 37

3.1 Properties of Virgo cluster substructures (taken from Boselli et al. 2023b) . 62

4.1 Data used in `cigale` SED fits 97

4.2 SFH parameters used in `cigale` SED fitting 101

4.3 Normal galaxies: cases of galaxies with no visual lopsidedness or truncation. 109

4.4 Cases of galaxies with clear visual lopsidedness. 109

4.5 Cases of galaxies with clear visual truncation. 110

A.1 Best fit parameters and uncertainties for the fits to the quiescent, low-SFR and SF populations across the Virgo environment 162

B.1 PHOTUTILS parameters used in object masking routine 163

C.1 CIGALE SED fitting configuration parameters. 178

C.2 Relevant galaxy parameters for entire sample analyzed. 183

C.2 (Cont.) Relevant galaxy parameters for entire sample analyzed. 184

List of Abbreviations

ΛCDM Lambda–cold dark matter

2MASS Two-Micron All Sky Survey

AD Anderson-Darling

AGN Active galactic nucleus

ALMA Atacama Large Millimetre/submillimetre Array

AO Adaptive optics

BAGPIPES Bayesian Analysis of Galaxies for Physical Inference and Parameter ESti-mation

BCG Brightest cluster galaxy

BIC Bayesian Information Criterion

BPT Baldwin-Phillips-Telervich

CALIFA Calar Alto Legacy Integral Field Area Survey

CAS Concentration-asymmetry-smoothness

CASTOR Cosmological Advance Survey Telescope for Optical and UV Research

CFHT Canada-France-Hawaii Telescope

CGM Circumgalactic medium

CIGALE Code Investigating GALaxy Emission

COSMOS Cosmic Evolution Survey

DM Dark matter

E-ELT European Extremely Large Telescope

ELT Extremely-large telescope

ERIS Enhanced Resolution Imager and Spectrograph

FIR Far-infrared

FSPS Fast Stellar Population Synthesis

FUV Far-ultraviolet

FWHM Full-width at half-maximum

GALEX GALaxy Evolution eXplorer

GAMA Galaxy and Mass Assembly

GASP GAs Stripping Phenomena in galaxies with MUSE

GIRMOS Gemini Infrared Multi-Object Spectrograph

GTO Guaranteed time observations

GUViCS GALEX Ultraviolet Virgo Cluster Survey

HARMONI High Angular Resolution Monolithic Optical and Near-infrared Integral field spectrograph

HeViCS Herschel Virgo Cluster Survey

ICM Intracluster medium

IFU Integral-field-unit

IMF Initial mass function

IR Infrared

ISM Interstellar medium

JWST James Webb Space Telescope

KDE Kernel density estimation

KMOS K-band Multi-Object Spectrograph

LIER Low-ionization emission-line region

LSST Legacy Survey of Space and Time

LV Low-velocity

MaNGA Mapping Nearby Galaxies at Apache Point Observatory

MCMC Monte-Carlo Markov chain

MIR Mid-infrared

MLCR Mass-to-light versus colour relation

MOS Multi-object spectroscopy

MUSE Multi Unit Spectroscopic Explorer

NB Narrow-band

NFW Navarro-Frenk-White

NGC New General Catalogue

NGVS Next Generation Virgo Survey

NIR Near-infrared

NUV Near-ultraviolet

PPS Projected phase space

RPS Ram-pressure stripping

SB Surface brightness

SDSS Sloan Digital Sky Survey

SED Spectral energy distribution

SF Star-forming

SFH Star formation history

SFMS Star-forming main sequence

SFR Star formation rate

SKA Square-Kilometre Array

SMBH Supermassive black hole

SMF Stellar mass function

SNR Signal-to-noise ratio

SPS Stellar population synthesis

sSFR Specific star formation rate

SSP Simple stellar population

TMT Thirty Metre Telescope

UV Ultraviolet

UVIT Ultraviolet Imaging Telescope

VCC Virgo Cluster Catalogue

VESTIGE Virgo Environmental Survey Tracing Ionised Gas Emission

VLT Very-large telescope

Chapter 1

Introduction

"Essentially everything of astronomical interest is either part of a galaxy, or from a galaxy, or otherwise relevant to the origin or evolution of galaxies."

- Dr. Beatrice Tinsley in her 1980 paper, *Evolution of Stars and Gas in Galaxies*

From a physical perspective, galaxies are amalgamations of stars, gas, dust, and dark matter held together by gravity – the relative proportion of each ingredient varying with galaxy type and evolutionary history. From a cosmological perspective, galaxies are the tracers of the very structure of our Universe, congregating into large groups and clusters connected by filaments in the cosmic web. Galaxies are then, perhaps, the very *things* that are most inherently tied to our continued attempts to understand the Universe in which we live. Whether we look within galaxies at their individual ingredients or, at the other extreme, treat each galaxy simply as a point in three-dimensional space, studies involving galaxies are at the heart of astronomical, astrophysical, and cosmological research.

1.1 How galaxies came to map the Universe

Our current understanding of the Universe is that of an expanding spacetime made up almost entirely of two components. The dominant of the two is dubbed Λ, and began as a cosmological constant tacked onto the general relativity equations of Albert Einstein that was necessary to explain the static spacetime that he believed to be reality (Einstein, 1917). Later, after Edwin Hubble and Georges Lemaître provided evidence that our Universe is

expanding (Lemaître, 1927; Hubble, 1929), this constant was used to explain why and how the Universe could not only expand, but accelerate in its expansion (e.g. Riess et al., 1998). We now refer to Λ as "dark energy" – a mysterious property of the Universe that governs expansion and does not dilute in density the way that matter does (e.g. Perlmutter et al., 1999; Planck Collaboration et al., 2020).

Matter is the other key component of the Universe. Ordinary, luminous matter – the kind that we can see with telescopes – makes up only a small percentage of this, however. The most recent studies suggest that 69% of the Universe's energy budget is the aforementioned dark energy, while the other 31% is matter (and negligible amounts of radiation; Planck Collaboration et al. 2020). Of this 31%, only 5% is luminous matter, with the other 26% being "dark matter." Dark matter, as its name suggests, does not interact with light, though its presence is known due to its interaction with gravity. The first evidence for dark matter came nearly a century ago when Fritz Zwicky invoked it to explain the velocity dispersions of galaxies in the Coma cluster (Zwicky, 1933). These dispersions were far too high to be explained solely by the luminous matter seen. Since then, the evidence for dark matter has continued to accumulate, with other pioneers in the field such as Vera Rubin. Rubin observed flat rotation curves in nearby galaxies such as Andromeda, which again required some missing matter to explain the deviation from the declining surface brightness profiles of the luminous matter in these galaxies (Rubin & Ford, 1970).

These studies and various others led to the development of the "cold dark matter" theory in the 1980s (Peebles, 1982; Blumenthal et al., 1984). The "cold" here refers to the non-relativistic speeds expected from dark matter particles. The combination of dark energy with cold dark matter resulted in the current standard model of our Universe, known as ΛCDM. A key prediction of the ΛCDM model is hierarchical structure growth. In this model, the Universe was originally homogeneous and isotropic on large scales but, locally, small fluctuations led to over- and under-dense regions. As the Universe continued to expand and cool, these tiny density fluctuations became the seeds for structure growth, attracting more matter through gravity, against the expansion of the Universe. These seeds grew to a critical density and then collapsed under gravity into dark matter halos, as per the spherical collapse model (e.g. Gunn & Gott, 1972; Press & Schechter, 1974; Peebles, 1980). It is within these dark matter halos that gas could eventually cool to form stars, which ordered into galaxies. The continuation of hierarchical structure formation over time then led to the merging of halos to develop into more massive objects containing many galaxies – the galaxy clusters that we see in the Universe today. The Press-Schechter formalism (Press & Schechter, 1974), and extensions thereof (e.g. Sheth et al., 2001), predict the halo mass function – that is, the number of dark matter halos as a function of mass in a given

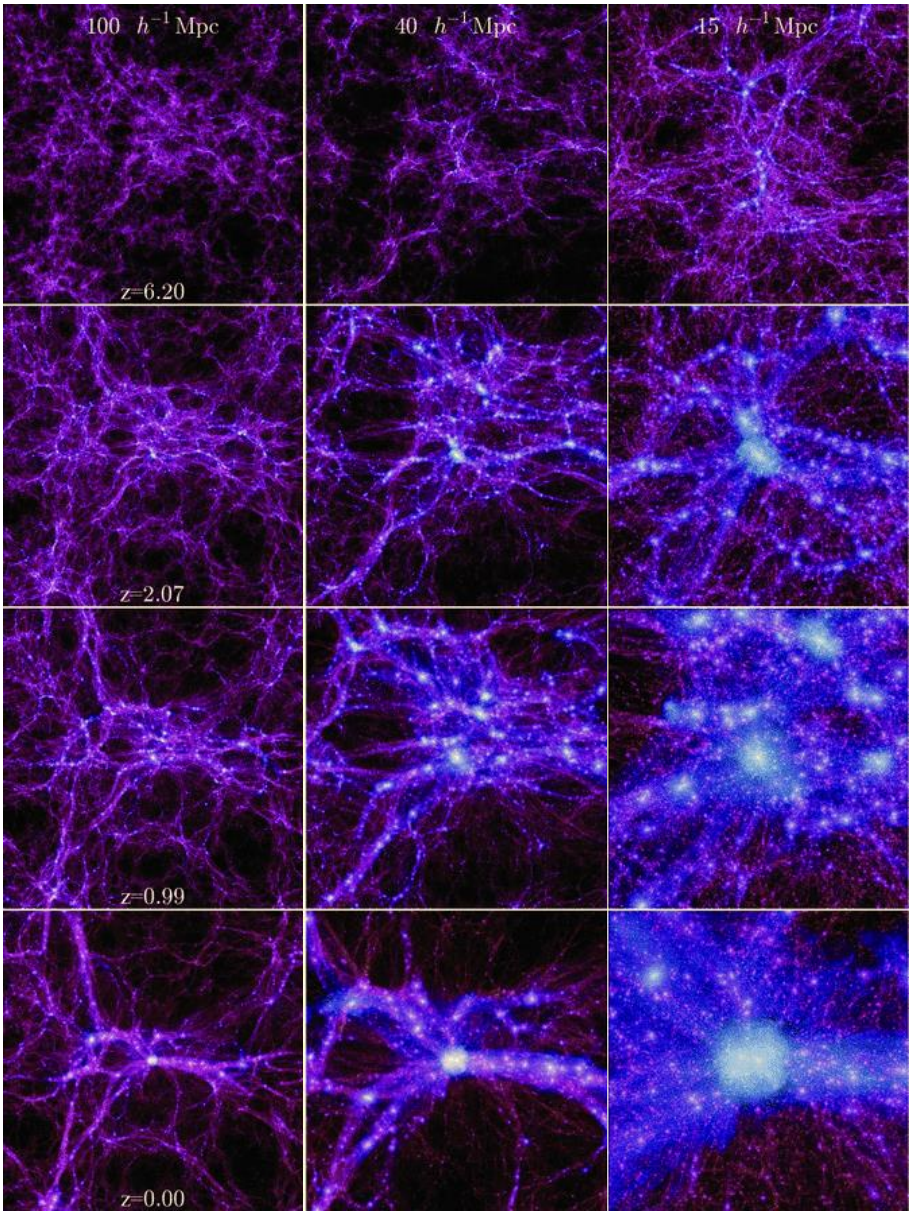


Figure 1.1: Images from the Millennium-II simulation (Boylan-Kolchin et al., 2009) showing the growth of structure in the Universe. From top to bottom, four different epochs are shown ($z = 6.20, 2.07, 0.99, 0$). From left to right, the same large halo is shown at the centre, but on three different scales (100, 40, 15 h^{-1} Mpc).

volume of the Universe. Simulation studies show the observed buildup of massive halos over time (e.g. Jenkins et al., 2001; Reed et al., 2003; Springel et al., 2005; Reed et al., 2007; Watson et al., 2013). Figure 1.1, from Boylan-Kolchin et al. (2009), shows snapshots from the Millennium-II simulation, focused on a massive halo that becomes a cluster at low-redshift. The stills show the growth of structure over time from top to bottom, and show the structure on three different scales from left to right. Observationally, abundances of galaxy groups and clusters in the local Universe are shown to be consistent with theoretical studies (e.g. Bahcall & Cen, 1993; Reiprich & Böhringer, 2002; Mandelbaum et al., 2006; Böhringer et al., 2017; Driver et al., 2022). Halo masses are determined observationally using various techniques such as galaxy dynamics (e.g. Driver et al., 2022), x-ray observations of hot gas in clusters (e.g. Reiprich & Böhringer, 2002; Bahcall & Cen, 1993; Böhringer et al., 2017), or via gravitational lensing (e.g. Mandelbaum et al., 2006).

Galaxies themselves, however, do not appear to form in a strictly hierarchical fashion in the way that dark matter halos do. Observations of the galaxy stellar mass function – the number of galaxies as a function of their stellar mass – over cosmic time show that massive galaxies formed the bulk of their stellar mass quickly and early-on (e.g. Fontana et al., 2004; Drory et al., 2005; Bundy et al., 2005; Faber et al., 2007; Ilbert et al., 2013; Muzzin et al., 2013; Weaver et al., 2023). The number density of low-mass galaxies, however, has continued to increase over time. Much of the stellar mass in the Universe was in place by $z \sim 2$, and the average star formation rate for a galaxy of a given stellar mass has decreased since the early Universe (e.g. Muzzin et al., 2013; Madau & Dickinson, 2014; Speagle et al., 2014; McLeod et al., 2021). These observations of "downsizing" show that the processes that govern galaxy formation and evolution are more complex than – and somewhat distinct from – the hierarchical growth of dark matter halos. Indeed, the ratio of the galaxy stellar mass function and the halo mass function is not flat – peak efficiency in galaxy formation occurs for intermediate mass galaxies, while high and low-mass galaxies seem to form less efficiently (e.g. Behroozi et al., 2019; Shuntov et al., 2022). The baryon cycle that allows gas to cool and form stars must contain various processes and mechanisms that affect the formation and evolution of galaxies.

1.2 A census of galaxies

1.2.1 Galaxy demographics

The first step in understanding galaxy evolution is being able to observe, measure, and understand populations of galaxies in terms of the variation in their properties. Galaxies

come in a range of shapes, sizes, and colours, and these observable physical properties are inherently tied to the galaxy's evolutionary history. Well-established is the bimodality of galaxy properties in the local Universe. This is perhaps most easily observed by taking a census of galaxy colours, where there exists a clear blue cloud and red sequence, with a relatively underdense transition population in between, often dubbed the "green-valley" (e.g. Strateva et al., 2001; Baldry et al., 2004; Bell et al., 2004; Martin et al., 2005; Brammer et al., 2009). Galaxy colours trace star formation rate (with influence from dust attenuation and metallicity): younger stars are hot and blue, while aging stellar populations peak in brightness toward the red-optical and infrared part of the electromagnetic spectrum. We show in Figure 1.2 the bimodality in galaxy colours from the Galaxy And Mass Assembly survey, where there are clear peaks in the number density of red and blue populations, with a valley in the middle. The bottom panel of the figure shows how this translates to star formation rate, with a clear star-forming main sequence and cloud of quenching and quenched galaxies.

The other key observable property of galaxies is their morphology. In the century since Hubble first classified galaxies along a tuning fork diagram (Hubble, 1926), highlighting the spectrum of galaxies from elliptical to spiral, we have continued to measure galaxy morphology in numerous ways. Parametrically, the surface brightness profiles of galaxies can be constrained by a Sérsic law (Sérsic, 1963), where the Sérsic index, n, indicates both how peaked the profile is in the centre of the galaxy, and how much of a tail exists toward the galaxy outskirts. Elliptical galaxies tend to have higher indices, $n \sim 4$, whereas spiral galaxies are dominated by exponential disks with $n \sim 1$. Of course these simple parametrizations of galaxy morphology do not pick up the local intricacies of real galaxies, and much work has been done in the last few decades to quantify the structural features of galaxies with ever-increasing resolution. Some of this work is done by human-eye classifications, including with the citizen-science projects of Galaxy Zoo (e.g. Lintott et al., 2011), while parametric and non-parametric measures of galaxy shapes, sizes, and features have become quite common as well, such as the concentration-asymmetry-smoothness (CAS; Conselice 2003) quantities. These types of measurements have proved powerful not only in classifying galaxies along the traditional sequence, but also in identifying unusual galaxies, such as those undergoing mergers (e.g. Lotz et al., 2004; Sazonova et al., 2021).

The bimodality of galaxies persists in both colour/star formation rate and morphology (e.g. Schawinski et al., 2014). Early-type galaxies are those that are elliptical in shape, are more centrally concentrated in their mass, tend to be red in colour with old stellar populations, and lack gas, dust, and ongoing star formation (are *quiescent*). Dynamically, they are usually found to be dispersion-supported, with stars on random orbits, though some rotation may still be present (e.g. Emsellem et al., 2007, 2011). Conversely, late-

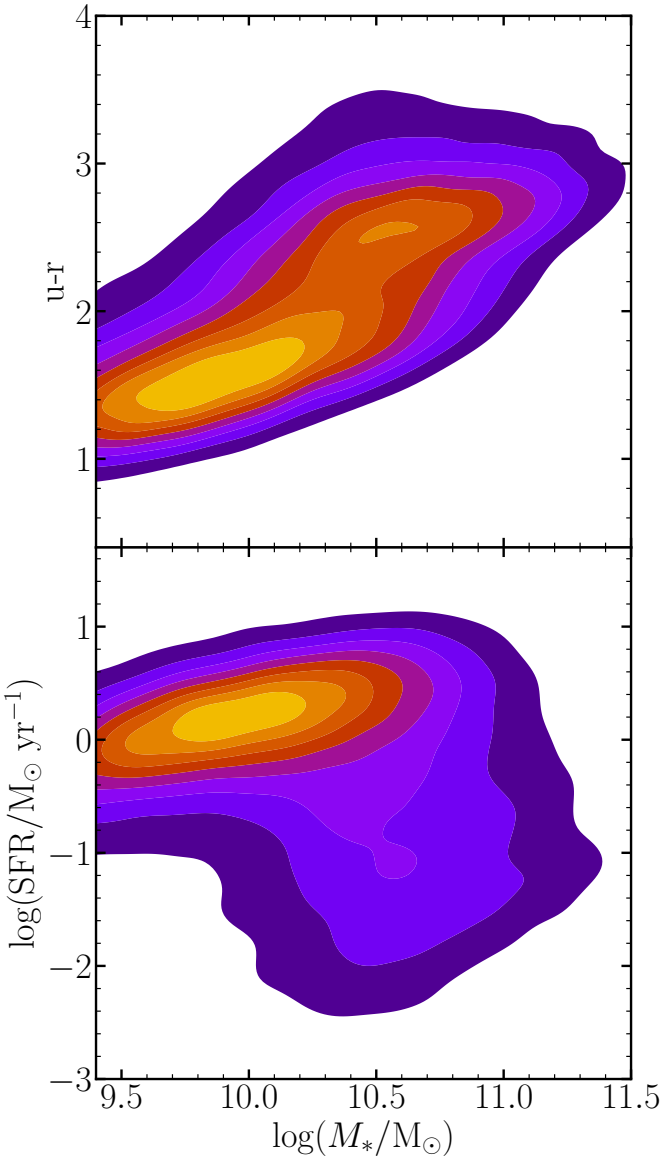


Figure 1.2: The galaxy bimodality as seen in the Galaxy And Mass Assembly (GAMA) survey. *Top:* density plot of extinction corrected $u-r$ colour as a function of stellar mass, showing peaks in red and blue populations. The dip in between the two populations is often referred to as the "green-valley." *Bottom:* density plot showing star formation rate as a function of stellar mass, showing the clear star-forming main sequence and cloud of quenching and quenched galaxies. Data taken from the GAMA DR4 database (Driver et al., 2009; Taylor et al., 2011; Driver et al., 2022)

type galaxies feature disks supported by ordered rotation of stars and gas. These galaxies tend to be blue in colour, with ongoing star formation and ample gas and dust. They are less centrally concentrated and contain features such as spiral arms and bars. Of course, some galaxies do not lie clearly in one group or the other. Through constraints on the stellar mass functions of both star-forming and quiescent galaxies across cosmic time, we see that most galaxies were star-forming at early times, with a strong buildup in the

quiescent population toward present day (e.g. Muzzin et al., 2013; McLeod et al., 2021). Concurrently, the star-forming stellar mass function evolves very little over this time. This observation indicates that galaxies must transition from star-forming to quiescent over their lifetimes, i.e. *quench* their star formation, becoming "red-and-dead" and undergoing morphological transformation.

1.2.2 Galactic geography

The hierarchical structure growth of the Universe has led to a cosmic web of structure at present day. Galaxies live in and amongst this cosmic web across a variety of environments. Being able to map the position of galaxies in this cosmic web is another key component toward our understanding of galaxy evolution.

Galaxy clusters

Galaxy clusters are the most massive virialized structures in the Universe – maybe. At least, they are the largest gravitationally-bound structures in the Universe. We often consider clusters as virialized, but clusters that are dynamically unrelaxed certainly cannot be virialized. The model of halo growth and spherical collapse for a uniform density halo that collapses into a virialized system shows that the approximate value for the virial radius corresponds to the radius inside which the mean density is equal to 200 times the critical density of the Universe (Gunn & Gott, 1972; Peebles, 1980)[1]. This value is dubbed R_{200} and it, and the associated mass M_{200}, are how we often define the size and mass of galaxy clusters (e.g. Navarro et al., 1996).

The total mass within R_{200} for clusters is typically $> 10^{14}$ $M_\odot$, with most of this mass made up of dark matter. $\sim 1\%$ of the mass lies in the galaxies themselves, despite the fact that massive clusters contain thousands of member galaxies. Clusters relax through repeated two-body interactions between member galaxies. The interaction between galaxies and the dark matter particles in the halo (dynamical friction) segregates the mass within clusters by causing more massive galaxies to fall towards the centre of the cluster potential. The accretion of material onto the central galaxy of the halo, along with the merging of galaxies near the centre form the brightest cluster galaxy (BCG; e.g. De Lucia & Blaizot, 2007). BCGs are some of the most massive galaxies found anywhere in the Universe, and

[1]It is worth noting that the results of the spherical collapse derivation actually lead to an overdensity of $18\pi^2 \approx 178$. Further results from early simulation studies helped to settle on the value of 200 (e.g. Davis et al., 1985).

have significant impact on further evolution of the cluster and its member galaxies (e.g. McNamara & Nulsen, 2007).

Permeating the space of galaxy clusters is the intracluster medium (ICM). The deep potential well of the cluster halo attracts gas from the cosmic web, which heats to high temperatures through gravitational heating, reaching $10^7 - 10^8$ K. As such, the ICM is observable in X-ray emission through thermal *Bremsstrahlung* radiation. In the cluster outskirts, the ICM cannot cool within the age of the Universe – in the denser cluster centre, cooling is prevented due to feedback associated with the BCG. Thus, the ICM remains hot, and traces the dark matter profile of the cluster. It has a significant impact on galaxies within the cluster, which will be discussed further in Section 1.3.2.

Galaxy groups, voids, sheets, and filaments

Galaxies rarely evolve in total gravitational isolation. Most galaxies in the local Universe are associated with a group-mass halo ($< 10^{14}$ $M_\odot$ and containing tens or hundreds of galaxies; e.g. Geller & Huchra, 1983; Tully, 1987; Eke et al., 2004). Outside the approximately-virialized regions of massive clusters and groups, the cosmic web is interconnected with massive thread-like filaments and planar sheets forming the boundaries to underdense cosmic voids. The high proportion of galaxies inhabiting these environments means that understanding their effects on galaxies is an important aspect of understanding galaxy evolution as a whole. Oftentimes, galaxies in small groups and filaments are grouped into "field" galaxies to distinguish them from those that inhabit massive clusters. This binary classification is valid to show differences in galaxy evolution as a function of environment, though local measures such as the distance of the Nth nearest neighbour or the galaxy overdensity are also frequently used (e.g. Dressler, 1980; Balogh et al., 2004; Baldry et al., 2006; Peng et al., 2010). However, as we move into the era of massive wide surveys reaching out to $z \sim 2$ (the so-called "cosmic noon,"), we are starting to be able to map the cosmic web in greater detail than ever before. This will allow an exploration of the effects of galaxy environment down to the particular position of a galaxy in the cosmic web, beyond simply whether or not it is part of a massive cluster halo.

1.3 The lives and deaths of galaxies

Nearly all aspects of galaxy evolution occur at rates far too slow to be observed in any human lifetime. The clearest exception are supernovae – on occasion, we witness the death of a star within the Milky Way or another nearby galaxy, signalling to us that changes do

occur within galaxies. In fact, considering the massive populations of stars within galaxies and the seeming eternity for which they live, stars being born and dying off is one of the key aspects of galaxy evolution. Galaxies then can be considered to "die" (or "quench") once they stop forming new stars. It is this picture of dying galaxies that is at the heart of much research into galaxy evolution: what is it that causes galaxies to die?

The seminal work by Peng et al. (2010) paints the picture that persists particularly in the local Universe. Galaxies quench because of internal processes (mass-driven quenching) and because of environmental processes. These processes are separable at low-redshift – that is to say, the likelihood of a galaxy undergoing a mass quenching process is dependent only on its stellar mass and not on its environment, and vice versa. This separability, however, does not appear to hold for high-redshift galaxies (e.g. Balogh et al., 2016; van der Burg et al., 2020). Alongside quenching is morphological transformation, with a leading question at present being whether morphological transformation leads to quenching, or quenching induces changes in morphology.

1.3.1 Mass quenching

In the local Universe, the quenched fraction of galaxies is strongly mass-dependent (e.g. Geha et al., 2012). High-mass galaxies ($M_* > 10^{10.5}$ $M_\odot$) are largely early-type, red galaxies, with little gas or ongoing star formation. Conversely, low-mass galaxies are more likely to be late-type, blue and actively star-forming. Recent studies, however, have pushed well into the dwarf galaxy regime, and shown that there may be an uptick in the quenched fraction at these low masses (e.g. Carlsten et al., 2026), though determining whether or not such a small galaxy has any active star formation is tricky due to the stochastic nature of star formation at these scales. The key internal mechanism quenching galaxies is *feedback*, processes from stars and active galactic nuclei (AGN) that prevent the cooling of gas into stars, both by heating the gas and stirring it up dynamically.

Stellar and supernova feedback

In order for a cloud of molecular gas to form stars, the gas must *cool* and *collapse*. However, the existence of massive stars provides a form of feedback that can prevent the cooling and collapse of molecular clouds. In this sense, star formation is a self-regulating process. Stellar winds and heating from powerful ultraviolet emission from massive stars, as well as energetic outflows from supernova explosions, transfer energy into the surrounding gas, heating and/or expelling it, and thereby preventing further star formation (e.g. Hopkins

et al., 2011, 2012). Given the shallow gravitational potential wells of dwarf galaxies, this form of feedback can be particularly effective at quenching star formation (e.g. Sawala et al., 2010). Low rates of supernovae can be enough to expel gas from the galactic disk, which may or may not eventually fall back onto the galaxy (Efstathiou, 2000).

AGN feedback

At the centre of most (and quite possibly, all) galaxies lies a supermassive black hole (SMBH; e.g. Magorrian et al., 1998). The accretion of material onto the SMBH produces an AGN, with powerful outflows that can have considerable effects of galaxy evolution. These outflows can be in the form of relativistic jets, radiation from the accreted material, and powerful winds. In radiative-mode AGN feedback, the rate of accretion is high, and large amounts of radiation are produced (e.g. Cano-Díaz et al., 2012). This is also known as quasar-mode feedback, and quasars are some of the brightest objects in the Universe. In mechanical-mode feedback, low accretion rates produce collimated, relativistic jets that can extend megaparsecs away from the galaxy (e.g. Fabian et al., 2003; McNamara & Nulsen, 2007). The transfer of energy and momentum from jets and radiation can serve to expel gas from the galaxy, or disrupt and heat it, preventing cooling and thereby reducing star formation (see Fabian, 2012 for a review). AGN feedback is invoked to explain galaxy quenching for massive galaxies, where AGN are more prevalent due to the deeper potential wells and larger SMBHs found in these galaxies (e.g. Kauffmann et al., 2003).

1.3.2 Environmental quenching

When discussing where a galaxy lives in the Universe, "environment" can be measured in various ways. Where massive halos associated with galaxy clusters and groups are found, galaxies can be determined as likely members of these halos based on two-dimensional position and radial velocity. Beyond simply membership, a galaxy's position within the phase space of the halo can be meaningful. A more broad approach is to use an Nth nearest neighbour distance to measure a local density of galaxies, $\Sigma_N = N/\pi d_N^2$. This value can be compared with a global average to measure an overdensity.

Dressler (1980) was one of the first studies to show that the fraction of early-type galaxies increases with local density. Since then, numerous studies have shown that galaxies in clusters, or dense environments in general, tend to be devoid of gas and lacking in star-formation, in line with their early-type morphologies (e.g. Giovanelli & Haynes, 1985; Balogh et al., 1997; Baldry et al., 2006; Cortese et al., 2011; Wetzel et al., 2012). Figure 1.3

shows the quenched fraction as a function of stellar mass in three different halo mass bins from the GAMA survey (Davies et al., 2019), as well as in a field sample. Clearly, the quenched fraction increases from low to high stellar mass, and is also elevated in more massive halos. We note that this figure only shows quenched fractions above 10^9 $M_\odot$. Below that mass, the quenched fraction of satellite galaxies especially has been shown to increase again (e.g. Baxter et al., 2021).

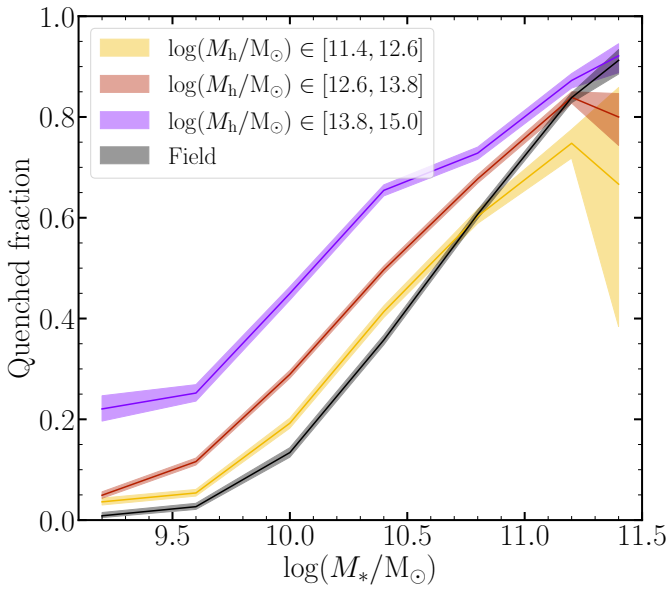


Figure 1.3: Quenched fraction as a function of stellar mass for three halo mass bins: $\log(M_h/M_\odot) \in [11.4, 12.6]$, $[12.6, 13.8]$, $[13.8, 15.0]$, as well as a field sample (isolated centrals). Data taken from the GAMA survey group catalogue (Robotham et al., 2011; Davies et al., 2019). Quenched versus star forming galaxies are separated using a cut on a SFR-M_* plot. Shaded regions show the 16$^{\text{th}}$ and 84$^{\text{th}}$ percentiles.

Gravitational interactions

Gravity is the force responsible for the large scale structure growth of the Universe that leads to the presence of galaxy groups and clusters. However, gravitational interactions between pairs of galaxies or between galaxies and their DM halos are a significant contributor to galaxy quenching and morphological transformation. Perhaps the most obvious and dramatic of these interactions are direct mergers of galaxies. When mergers happen, the interstellar medium (ISM) in the disks of the merging galaxies loses angular momentum and can fall toward the centre of the new-forming galaxy (e.g. Toomre & Toomre, 1972). This can cause a massive starburst – a rapid explosion of significant star formation – that can quickly consume the gas and leave the galaxy quenched (e.g. Mihos & Hernquist, 1996; Hopkins et al., 2006). It is thought that mergers can quickly take two late-type galaxies and leave a massive, early-type galaxy behind, as tidal disruptions of the disks lead to a

build-up of the galactic bulge. While stars are essentially collisionless (their small cross-sections relative to the distance between them makes direct collisions very unlikely), the gas itself is not, and collisions among the gas particles can shock heat the gas, preventing further star formation if it then cannot cool. These events are most common in major mergers, when the masses of the merging galaxies are similar ($\sim 1:3$). Minor mergers, on the other hand, where the mass ratio is on the order of $\sim 1:10$, play out more like the accretion of a satellite galaxy onto the more massive central galaxy (Lotz et al., 2011). While tidal interactions still occur, their effects on the central galaxy are likely much less pronounced. These types of tidal interactions between galaxies can occur even without direct merging. The left panel of Figure 1.4 shows NGC 4567 and NGC 4568, two galaxies that are about to merge in the Virgo cluster.

Repeated fly-bys of galactic neighbours (often dubbed "harassment"; e.g. Moore et al., 1996, 1998) can cause significant morphological change in galaxies in clusters. The large velocity dispersion of clusters makes direct mergers rare, but galaxies still constantly move within the gravitational influence of other galaxies, leading to cumulative tidal effects that, over time, can disrupt angular momentum and fuel central starbursts similar to mergers.

Ram-pressure stripping

As galaxies orbit through clusters, they pass through the hot ICM. The relative motion of the galaxy through the ICM causes a drag force between the ICM and ISM in the galactic disk known as ram-pressure stripping (RPS). This hydrodynamical interaction affects only the gas of the galaxy, so the stellar and dark matter components remain in motion, causing the gas to be stripped away (Gunn & Gott, 1972). The pressure experienced by the galaxy is directly related to the density of the ICM and the squared relatively velocity between the galaxy and the ICM:

$$P_{\rm ram} = \rho_{\rm ICM} v^2. \tag{1.1}$$

This means that, assuming a cluster density profile with a central peak or core, and a galaxy falling in on a near-radial orbit, peak ram-pressure is experienced at first pericentre, where the galaxy makes it closest approach to the cluster centre and is moving with maximum velocity.

The efficiency of RPS at removing gas from the galactic disk depends of course on the ability of the galaxy to hold onto its gas. The orientation of the galaxy relative to its direction of motion is a factor – galaxies falling in face-on have a larger cross-section for

the ICM wind to remove gas (Roediger & Brüggen, 2006). Most significant, though, is the depth of the gravitational potential well of the galaxy and its dark matter halo. To first order, stripping gas away from less massive galaxies is easier, but to be more precise, the actual distribution of matter in the halo must be considered. The restoring force per area of the galaxy is given by

$$f = \left[g_*(\mathrm{r}) + \mathrm{g_{HI}(r)} + \mathrm{g_{H_2}(r)} + \mathrm{g_{DM}(r)}\right]\ \Sigma_{\mathrm{HI}}(r), \tag{1.2}$$

where each $g(r)$ term is the gravitational acceleration from each component (stars, atomic gas, molecular gas, and DM, respectively), as a function of galactocentric radius. $\Sigma_{\mathrm{HI}}(r)$ is the surface mass density of the atomic gas being stripped. While some work shows that RPS can also strip molecular gas directly, this is likely less efficient since molecular clouds are dense and self-gravitating (e.g. Tonnesen & Bryan, 2009; Lee et al., 2017). Since, generally, the surface density of each component falls with distance from the galactic centre, it is much easier to remove gas from the outskirts of a galactic disk than near the centre. As such, RPS is considered an "outside-in" quenching process, where star formation ceases from the outer parts of the galaxy inward due to gas loss. When stripping is efficient, RPS can effectively quench galaxies on a single orbit of a cluster, or < 1 Gyr timescales. Galaxies with central bulges will hold onto gas in the centre more efficiently than galaxies with exponential profiles. In some cases, if the ram-pressure is not strong enough to completely remove the gas from the galaxy, the gas may fall back onto the galactic disk as the galaxy moves to a region of lower ICM density.

The early stages of RPS often produce dramatic tails of stripped gas. Star formation can continue occurring in these tails, making them visible in the optical where they become known as jellyfish galaxies (e.g. Smith et al., 2010; Poggianti et al., 2016). Studying these tails can be effective in helping to understand how RPS plays out, and can help to determine the fate of the stripped gas. However, observing the later stages of RPS can be difficult, as these gas tails may be stripped from the galaxy quickly, leaving a gas-deficient galaxy with little star formation. The right panel of Figure 1.4 shows NGC 4564, one of several galaxies known to be undergoing RPS in the Virgo cluster.

Starvation

Galaxies need a continuous supply of gas to maintain a rate of star formation over long timescales. Galaxy dark matter halos hold warm gas, which can be accreted and cooled onto the galactic disk. The halo in turn can have its gas replenished through accretion



Figure 1.4: *(left)* close pair galaxies NGC 4567 and 4568, about to begin their merger into a giant elliptical galaxy. *Image credit: International Gemini Observatory/NOIRLab/NSF/AURA. T.A. Rector (University of Alaska Anchorage/NSF NOIRLab), J. Miller (Gemini Observatory/NSF NOIRLab), M. Zamani (NSF NOIRLab) & D. de Martin (NSF NOIRLab). (right)* NGC 4564, a galaxy undergoing ram-pressure stripping in the Virgo cluster. *Image credit: KPNO/NOIRLab/NSF/AURA/Mitch and Michael Dye/Adam Block.*

along filaments from the cosmic web. If a galaxy's supply of fresh gas is cut off, its star formation will start to wane as it exhausts its existing gas supply (e.g. Larson et al., 1980).

When a galaxy falls into a massive group or cluster halo, this continual supply of gas accretion is disrupted. First of all, the existing hot gas halo may be removed through RPS – given that much of the gas exists far from the deep parts of the potential well, it will be easier for the interaction with the ICM to remove this gas than the cool gas in the disk. Once the halo gas is removed, either by accretion onto the galaxy or by RPS, the galaxy (sub)halo may no longer be able to accrete from the cosmic web, as it is no longer the dominant potential well as gas falls into the cluster. Direct observations constraining starvation may be difficult, as it is not typically associated with strong morphological indicators. The timescales expected for quenching through starvation alone are expected to be long (e.g. Balogh et al., 2000), so constraining the duration of quenching episodes can help to infer the existence of this mechanism.

1.3.3 Morphological transformation

Closely tied to galaxy quenching is morphological transformation. There is a clear correlation between galaxy star formation and morphological type (e.g. Kennicutt Jr.,, 1998a) – while late-type galaxies typically have ongoing star formation, early-type galaxies are typically quenched. This implies a connection between quenching and morphological transformation. However, it remains uncertain if one process typically precedes the other – i.e. does quenching drive morphological transformation, or do morphological changes contribute to quenching?

Likely the answer is complicated. Environmental processes such as RPS and starvation are sometimes used to explain observed populations of "red spiral" galaxies – galaxies that retain their late-type structure but have lost their ability to form stars (e.g. Kawata & Mulchaey, 2008). Given that RPS and starvation are hydrodynamical and only impact the gas in galaxies, it is feasible that they could quench galaxies without impacting the older stellar populations that form the basis of the galaxy's structure.

On the other hand, gravitational interactions can directly affect the structure of a galaxy. Since these interactions affect all components of the galaxy, they can have a direct impact on the orbit of stars, and change the angular momentum of the galaxy. This can lead to a build up of a central bulge feature. Perhaps the most dramatic example of this occurs during mergers – major mergers are one of the key processes believed to transform two late-type galaxies into a massive, early-type. While mergers do not actually result in the destruction of stars through collisions, they can induce rapid starbursts that quickly consume the remaining gas in galaxy, quickly leaving behind a "red-and-dead" galaxy.

Other structural features such as bars are thought to play a role in the dynamics of gas in the central regions of galaxies. Similar to gravitational processes, bars can funnel gas toward the centre, creating rings of star formation and central starbursts (e.g. Kormendy & Kennicutt, 2004; Géron et al., 2021).

1.4 Measuring galaxies and inferring their properties

Every observational study of galaxies comes down to measuring light. The information we can extract from that light comes down to three basic questions: *where* does the light come from?; *how much* light is there?; *what type* of light is it?

The first question pertains to the spatial resolution of our images, as well as the inherent size of the galaxy. Observing the night sky without a telescope reveals stars that look simply

like points of light, spread somewhat due to resolution limits in place by the atmosphere and our own eyes. When we point telescopes at stars, not much changes – stars are just too small and too far away to subtend a large enough angle on the sky. When we look at galaxies, however, the optics of powerful telescopes make it such that their light is spread across many pixels on the detector, allowing us to see resolved structural details and measure the sizes of these structures.

The second question considers how bright the galaxy is. This *observed* brightness (flux) is an inverse-squared function of distance. If we know the distance to the object, we can transform this into an absolute brightness, which is tied to how much luminous material (stars, gas, dust) is present in the galaxy. The surface brightness of a galaxy refers to the distribution of its flux over its apparent area. At low-redshift, this quantity is distance independent, since both apparent area and flux are inverse-squared functions of distance. When measuring the flux of a galaxy, the main contributions to statistical uncertainty come from the Poisson noise of the galaxy flux itself, as well as the noise in the sky background.

The third question helps to determine what we are looking at. A galaxy, yes, but which part? Different luminous components produce light along different regions of the electromagnetic spectrum – the bluest stars produce light peaking in the ultraviolet, while the reddest ones peak in the infrared. Dust absorbs ultraviolet light and re-emits it in the mid- and far-infrared. Gas, depending on its temperature, can emit anywhere from x-rays all the way down to radio waves.

Both photometric and spectroscopic observations are powerful in helping us interpret the light we see from galaxies, and each have advantages and disadvantages to the observer.

Photometry

Every photo ever taken of a galaxy could, technically, be a photometric datapoint for that galaxy. However, in practice, the number of digital data units needs to be calibrated back to a the number of photons that produced them, and we need to understand what photon energies our optics are sensitive to. Telescope image sensors (read: cameras) are built to be sensitive to a range of photon energies, so typically we lock onto smaller wavelength windows with telescope filters. The combined response of the filter and camera optics are well-defined such that we can easily determine the number of photons in the filter's wavelength range and measure how bright their combined light is.

Typical broadband filters cover ~ 100 nm of photon wavelengths. These filters are wide enough such that relatively short exposures can capture enough photons from the galaxy source to make high signal-to-noise (SNR) measurements, yet are still focused enough to

measure important quantities like galaxy colour, by comparing red and blue broadband filters. Moving down in scale gets to medium- and narrow-band filters. The narrower the filter, the longer the exposure needed to capture a certain number of photons. However, the trade off is more precise information about the *type* of light. For example, many narrow-band filters will span $\sim$ 10 nm, straddling an emission line for a given redshift range, allowing a measurement of the emission line flux without the need for spectroscopy, as discussed below.

Compared to spectroscopy, photometry is cheap and easy. Cutting-edge telescopes and cameras are expensive to build, and there is only so much dark sky time that must be shared. While limited in how much information they can provide in the spectral dimension, photometric measurements are powerful datasets that form the sole basis of many galaxy evolution studies. Especially combined with tools such as spectral energy distribution fitting, as discussed in Section 1.4.1, many measurements of galaxy properties can be inferred solely with photometry.

Spectroscopy

Spectroscopic observations bring a third dimension to astronomical observations, really getting into the details of *what type* of light is coming from the observed galaxy. While narrow-band filters can help focus in on individual emission lines, spectroscopy actually disperses the observed light into a spectrum, so with a single observation one gets flux as a function of wavelength, instead of just the integrated flux in some filter bandpass.

There are various types of spectroscopic instruments which, to first order, differ in how they record spatial and spectral information of an object. In slit spectroscopy, a slit is placed across an object (say, along the major axis of a galaxy disk), and the light that passes through the slit is dispersed, often with a grating. The result is a continuous spectra along the slit, dispersed orthogonally to the slit itself. While there is no overlap of spatial and spectral information, one is limited to information in just one spatial dimension. Oftentimes, slits can be placed over several different objects at once. Similarly, fibre spectroscopy is a technique where $\sim$ hundreds of fibres are set up to each collect light from a single target, feeding that light to a spectrograph. This is a powerful techniques for multi-object spectroscopy (MOS), though it does not retain spatial information about the targets.

Grism spectroscopy, on the other hand, combines a grating and a prism, often in a slitless setting, to obtain spectra over the whole image at once. The issue here is that the light will be dispersed along a spatial dimension, so while two-dimensional spatial

information in preserved, it will overlap with the spectral information. De-tangling the two is one of the major challenges of grism spectroscopy. However, when done successfully, it is a powerful technique for obtaining spatially-resolved spectra of many objects.

Integral-field unit (IFU) spectroscopy is able to retain all spatial and spectral information about a field by producing a three-dimensional datacube. Each resolved element (i.e. spaxel – **sp**atial or **sp**ectral pixel) is dispersed along the third dimension, giving a full spectrum for each spaxel. This is the most powerful technique for emission line measurements and dynamics of galaxies on a full spatially-resolved scale.

Regardless of the technique used, spectroscopic information is generally necessary to make measurements of several different emission lines, or to measure absorption lines that originate in stellar atmospheres and gas clouds. Beyond emission line fluxes, spectroscopy allows a direct measurement of redshift. When this can be done on spatial scales across a galaxy, one obtains information on the dynamics of the stars and gas, which cannot be obtained with photometry alone.

1.4.1 Spectral energy distribution fitting

Since all we can actually measure about galaxies is their light, we need to compare our photometric and spectroscopic data to models of the *things* that make up galaxies. A galaxy's spectral energy distribution (SED) is essentially its flux as a function of wavelength (or equivalently, frequency). To fit an SED, one typically wants to find a combination of simple stellar populations (SSPs) that reproduce the observed fluxes in different filters. An SSP is a population of stars with the same age, metallicity, and initial mass function (typically the same for all SSPs in a model), determined using stellar isochrones. A weighted combination of many SSPs then produces an overall stellar population with varying metallicity and age, where the weights represent the mass formed for each SSP. Then, other components can (and often should!) be added to the model such as dust (emission and attenuation models), nebular emission (especially if fitting emission lines), and AGN. The combination of SSPs and these other model components produces a model SED that can be convolved through the transmission curves of the filters used in the observations and produce model fluxes and/or a spectrum that can be compared with the observations. Figure 1.5 shows an SED for a typical star-forming galaxy, generated with the BAGPIPES SED fitting code (Carnall et al., 2018). The figure shows photometric datapoints from relevant telescopes along with their filter curves, and shows what the best-fit SED to those datapoints looks like.

Typically, there are two basic forms for producing a suite of models to compare with

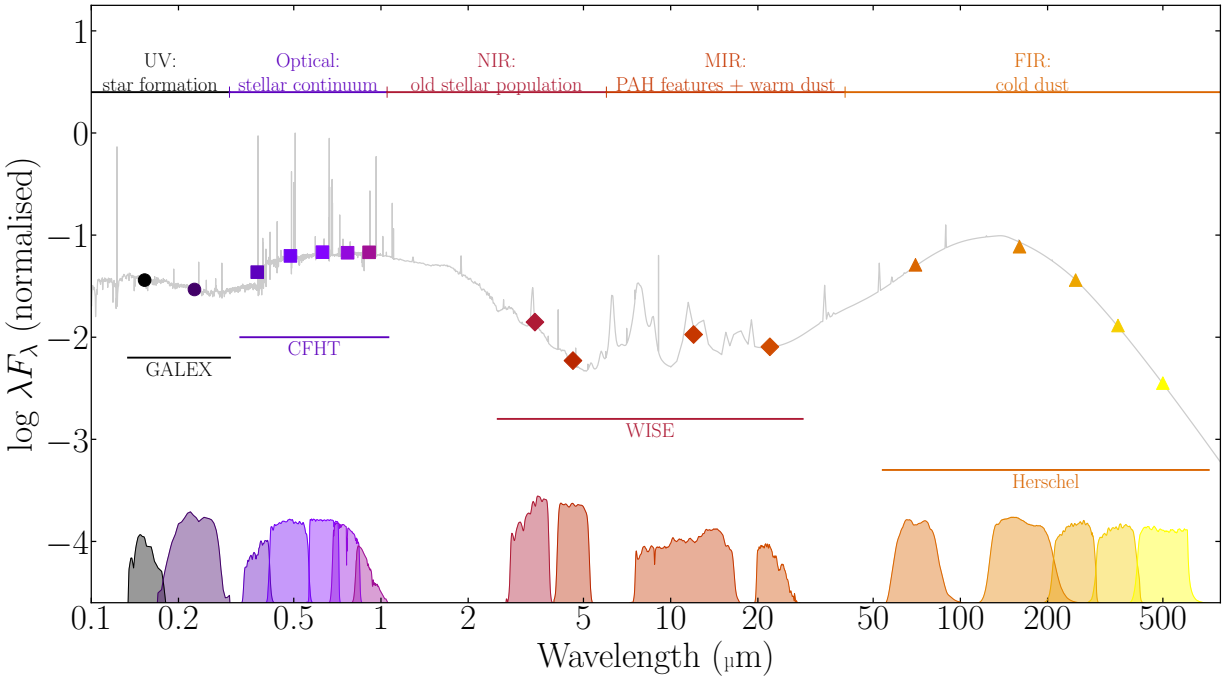


Figure 1.5: Spectral energy distribution of a typical star-forming galaxy (grey curve), generated with the BAGPIPES SED fitting code (Carnall et al., 2018). Coloured markers show photometric data points for filters used on GALEX, CFHT, WISE, and Herschel telescopes, with the filter transmission curves shown at the bottom (not to scale). The text at the top of the figure notes the various wavelength regimes and what they trace in a galaxy.

observed data. The most straightforward way is to compute a "pre-grid" of models. One can pick discrete prior values for each parameter in the model suite and produce an instance of the model for each unique combinations of prior values. Alternatively, if one sets a continuous distribution on the prior values, a set number of model instances can be computed, where the prior on each parameter is drawn from its respective distribution for each instance. In practise, this will generally be computationally less expensive, as the pre-grid can be computed and then used to fit many galaxies (or many pixels within a galaxy). Then in the fitting step, a chi-squared value is computed for each model given its fit to the observed data, and the best fit model can be determined. One can also compute a Bayesian posterior distribution for each parameter by weighting each parameter by its likelihood.

A more statistically-robust way to go about SED fitting is using a full Monte-Carlo

Markov Chain (MCMC) routine. The goal with MCMC is to effectively explore the parameter space by random sampling. In the SED sense, this means starting with a random set of model parameters (drawing from their prior distributions) measuring its likelihood, and then moving to a new, nearby point in the parameter space, and determining if its likelihood is better or worse. If it is better, the "chain" moves to that point – if it is worse, there is still a chance (based on the relative likelihood) that the chain will still move to that point. This is an important feature in MCMC routines to ensure the whole parameter space is well explored and the solution does not end up in a local likelihood minimum. As such, MCMC SED fitting routines do not make use of a pre-grid – they compute a new model with each new instance of parameters. This typically makes MCMC SED fitting much more computationally expensive than pre-grid fitting. However, the results are more statically sound.

1.4.2 Measuring star formation rates

In order to understand galaxy quenching, we first need to understand galaxy star formation. Like most changes that occur in galaxies, we cannot measure star formation in real time. Even the most efficient starbursts only have SFRs on the order of $100\,\mathrm{M_\odot\,yr^{-1}}$, while average star-forming galaxies like the Milky Way only produce a couple new stars each year on average. There are various ways to trace star formation observationally, a few of which detail here.

Hα emission

The most massive stars have emission that peaks below the Lyman limit at 912Å, meaning much of the radiation they produce is energetic enough to ionize hydrogen in their birth clouds. Recombination of these hydrogen ions produces emission lines in the Balmer (and Lyman, Paschen, etc.) series, most notably the $3 \rightarrow 2$ transition which produces the Hα emission line at 6563Å. Only O-type and massive B-type stars produce significant amounts of Lyman-continuum emission, meaning that Hα emission traces star formation rate on timescales associated with the main-sequence lifetimes of these massive stars, or ~ 10 Myr. This makes Hα emission one of the best tracers of very recent and ongoing star formation.

Because only the most massive stars ($\gtrsim 10\ \mathrm{M_\odot}$) produce significant Lyman-continuum emission, Hα as a SFR tracer is very sensitive to the shape of the initial mass function (IMF): for a Chabrier IMF, only ~ 10 stars with ($M_* > 10\ \mathrm{M_\odot}$) are produced for every

1000M$_\odot$ of stars produced. This means that for dwarf galaxies with low SFRs, or when looking at individual star-forming regions in larger galaxies, the SFR-Hα relation will suffer an added uncertainty due to stochasticity – a galaxies with $M_* < 10^7$ M$_\odot$ on the SFMS may only have a single O-type star producing the necessary Lyman-continuum emission.

Ionizing radiation can also be produced from sources not associated with star formation. Sources such as AGN and Low-Ionization Emission-line Regions (LIERs) can contribute significantly to ionization in the central regions of galaxies in particular. With spectroscopic data, star-forming regions can be distinguished from these other sources using emission line ratio diagnostics such as the Baldwin, Phillips & Telervich (BPT) diagram (Baldwin et al., 1981). However, with narrowband photometry, the NII lines that flank the Hα often cannot be separated out. This means they cannot be used to diagnose sources of ionizing radiation, and actually must be accounted for in the Hα line flux.

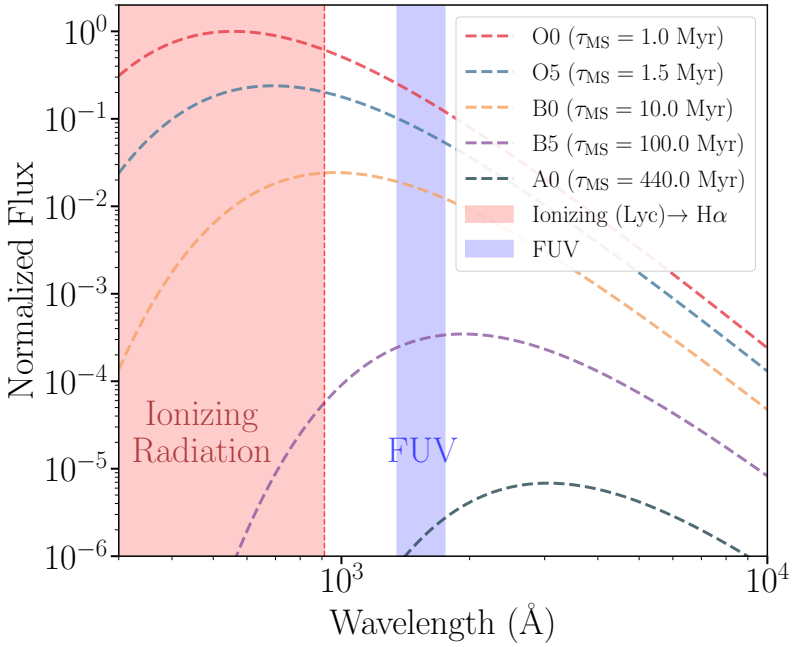


Figure 1.6: Blackbody spectra of massive stars that produce Lyman-continuum and/or significant FUV emission. Flux values are normalized such that the peak flux of the O0 star is at unity, and each of the other stars has its flux scaled appropriately, considering their blackbody temperatures and the typical size of the stars. We list the main sequence lifetimes associated with these stars.

Ultraviolet radiation

The most direct starlight tracer of star formation is ultraviolet (UV) radiation. O, B and some A type stars have peak emission in the ultraviolet, with O and B type stars peaking in or below typical far-UV (FUV) bands. These stars have main-sequence lifetimes of $\sim$ 100 Myr, making the UV a longer-timescale tracer than Hα, but still a good tracer of

recent star formation. UV, of course, is blocked by the Earth's atmosphere and thus cannot be observed from the ground (except for rest-frame UV in high-redshift observations). As such, UV requires space-based observing, making it more expensive to obtain than optical imaging. UV is also readily absorbed by interstellar dust in galaxies, meaning that it is best combined with infrared emission that traces this dust and can constrain its contribution. The UV is less sensitive to stochasticity than hydrogen emission line tracers, but can still have contamination from evolved stellar populations and other sources such as AGN. Figure 1.6 shows the blackbody spectra associated with massive stars from type O0 to A0. The figure shows how only the most massive stars have significant Lyman-continuum emission to ionize hydrogen and lead to Hα emission, and only stars with main sequence lifetimes of less than $\sim$ 100 Myr peak in the FUV.

Dust: UV is easily absorbed by dust, where it heats the dust, causing re-emission in mid- and far-infrared bands. Because of this, infrared emission itself can be used as a tracer of star formation. However, this requires a calibration between observed infrared emission and the UV emission that indirectly caused it, making it more uncertain than simply combining UV and infrared emission to measure star formation rates.

Direct gas tracers

Since stars form from clouds of molecular gas, which in turn is related to the atomic gas content, observing this gas directly can infer the star formation rate. The Kennicutt-Schmidt law describes the power law relation between gas surface density and SFR surface density (e.g. Schmidt, 1959; Kennicutt Jr.,, 1998b). Different calibrations exist depending on whether one is using molecular gas, atomic gas, or the total of the two. On resolved scales, studies such as Bigiel et al. (2008) have shown that there is a linear relationship between SFR density and molecular gas density specifically.

Detecting atomic and molecular gas directly typically requires radio observations. Atomic gas is traced typically through the 21cm emission coming from a spin flip in the hydrogen atom. Molecular hydrogen gas does not radiate on its own, but can be observed through tracers such as CO emission, which can observed through rotational emission lines in the sub-mm regime.

1.5 This thesis

The past 50 years have seen many studies working to untangle how galaxy evolution proceeds in galaxy clusters. Despite this, there remain many unanswered questions and details

on this subject. In this thesis, we use the Virgo cluster as an ideal laboratory to undertake high-resolution studies of star formation and quenching in a dynamically active local cluster. Studies such as these are necessary to untangle environmental quenching on local scales within galaxies, and inform studies at higher redshift that are becoming increasingly possible. The questions we look to answer are as follows:

1. How does the dynamically active environment of Virgo affect its populations of star forming and quenched galaxies?
2. Can we distinguish between quenching mechanisms in the Virgo cluster by measuring morphology of star formation?
3. What can SFR tracers tell us about the timescales associated with local quenching morphologies?

Chapter 2 looks at the stellar mass distribution of Virgo galaxies through deep stellar mass functions separated by star formation rate and position within the cluster. This allows us to constrain quenching of Virgo galaxies on a population level scale, and infer the effects of pre-processing beyond the cluster halo. We find that the shape of the quenched mass functions are invariant across the cluster, inconsistent with what is expected from infalling populations in the cluster outskirts. This is a strong case for pre-processing of galaxies in groups and filament before infall into the main halo of Virgo.

In Chapter 3 we use high-resolution and deep data to develop a new technique for measuring star-forming disk truncation in Virgo galaxies. This technique is physically-motivated, and remedies uncertainties with previous efforts. We find that truncated disk are ubiquitous across the Virgo environment, with varying strengths. The presence of truncated disks in regions where ram-pressure stripping is ineffective suggests that more subtle processes like starvation can contribute to disk truncation, which we describe with a simple toy model.

Chapter 4 takes a deep dive into mapping out local regions of rapid quenching in Virgo galaxies. By measuring SFRs from Hα and FUV tracers, we compare recent and ongoing star formation on sub-kpc scales. We identify galaxies with lopsided distributions of $\mathrm{SFR_{H\alpha}/SFR_{FUV}}$, and truncated outer disks with little $\mathrm{SFR_{H\alpha}}$. We discuss the possible nature of these signatures in the context of the literature on quenching mechanisms in Virgo cluster galaxies.

In Chapter 5 we take a look ahead. Astronomy has firmly entered the era of big data. Not only are we now pushing studies of galaxy evolution to the first galaxies in the

Universe with instruments such as the James Webb Space Telescope, instruments such as Euclid, the Vera C. Rubin Observatory, and the Nancy Grace Roman Space Telescope are allowing us to obtain surveys of millions of galaxies out to at least cosmic noon. With these massive photometric and spectroscopic datasets, we will push detailed studies of environmental galaxy evolution to the point where we can use a galaxy's precise position in the filamentary structure of the cosmic web as its environmental indicator, allowing us to map out the entire quenching sequence of galaxies in various environments from the formation of the first clusters to the present day. With these new datasets, we can build on the work presented here, using some of the novel techniques developed. We discuss the prospects of new instruments with a focus on theCosmological Advanced Survey Telescope for Optical and UV Research (CASTOR) and the Gemini Infrared Multi-Object Spectrograph (GIRMOS), and discuss how studies of galaxy environmental quenching will improve. We finally discuss improvements that can be made to spatially-resolved studies with improvements to SED fitting technology.

In Chapter 6 we sum up the three main studies presented in Chapters 2, 3, and 4, and conclude within the context of Chapter 5.

Chapter 2

Deep galaxy stellar mass functions as a function of star formation rate in the Virgo cluster environment

This chapter is based on the following article:
Morgan, C. R., Sazonova, E., Roberts, I. D., Balogh, M. L. et al. 2025. Deep galaxy stellar mass functions as a function of star formation rate in the Virgo cluster environment. *The Astrophysical Journal*, 987, 166, doi: 10.3847/1538-4357/addc6c

2.1 Introduction

Galaxy stellar mass functions (SMFs) are a critical tool to aid in understanding the formation and evolution of galaxy populations across different environments and over cosmic time. In the local universe, the shape of the total galaxy SMF has been well-established through large spectroscopic surveys including the Two Micro Sky Survey (2MASS; Skrutskie et al. 2006), the Sloan Digital Sky Survey (SDSS; York et al. 2000; Bell et al. 2003; Baldry et al. 2006), and the Galaxy And Mass Assembly survey (GAMA; Baldry et al. 2010, 2012). When split into blue and red galaxy populations, the red population dominates in the high-mass regime, whereas blue galaxies dominate at lower stellar masses.

Observations of SMFs as a function of redshift suggest that massive galaxies form their stellar mass early on, with lower mass galaxies assembling later, in contrast with the

theorized bottom-up growth of dark matter halos (e.g. Faber et al., 2007; Ilbert et al., 2013; Muzzin et al., 2013; Weaver et al., 2023). With most of the stellar mass in the universe in place by $z \sim 2$, these studies show that the SMF of star-forming (SF) galaxies alone evolves only weakly to the present day (e.g. Muzzin et al., 2013; McLeod et al., 2021). The stagnancy of the SF SMF coupled with the buildup of massive, quiescent galaxies over time implies galaxies must move from SF to quiescent - galaxies "quench" through the cessation of star formation.

Studies that have measured local SMFs have sought to compare SMFs across a range of local densities or halo masses. In comparing SMFs as a function of local density, Baldry et al. (2006) showed that the slope of the SMF shows little change with environment, whereas the characteristic mass increases with increasing density. Yang et al. (2009) compared conditional SMFs (the SMF conditional on the halo mass $\mathcal{M}_h$) in SDSS groups with 10^{12} $M_\odot < \mathcal{M}_h < 10^{15}$ $M_\odot$. They found increasing characteristic mass and steeper low-mass slopes with increasing halo mass. More recently, a similar analysis was performed by Vázquez-Mata et al. (2020) with the deeper GAMA survey. While the authors found the expected increase in characteristic mass with increasing halo mass, they found steeper low-mass slopes in the lowest halo mass bins, contrary to Yang et al. (2009).

While SMFs of galaxy clusters and proto-clusters have been studied at intermediate to high redshifts (e.g. van der Burg et al., 2020; Edward et al., 2024), SMFs in local ($D < 100$ Mpc) massive clusters specifically have been less well studied, in part due to the large angles subtended on the sky. On average, cluster galaxies are more deficient in cold gas (Giovanelli & Haynes, 1985; Cayatte et al., 1990; Gavazzi et al., 2005; Cortese et al., 2011; Boselli et al., 2014a; Alberts et al., 2022) and are less actively star-forming (Balogh et al., 1997, 1998; Lewis et al., 2002; Gómez et al., 2003; Kauffmann et al., 2004; Baldry et al., 2006; Weinmann et al., 2006; Wetzel et al., 2012; Gavazzi et al., 2013a; Boselli et al., 2023a) than their field counterparts. Balogh et al. (2001) analyzed the luminosity functions and corresponding SMFs of local field and cluster galaxies, finding that the cluster SMF has both a steeper low-mass slope and a larger characteristic mass. Analyzing the Shapley Supercluster, Merluzzi et al. (2010) found a low-mass slope shallower than that of Balogh et al. (2001), and closer to observed values in the field. Recently, Cuillandre et al. (2024) used early Euclid observations to measure the mass function of the Perseus cluster down to 10^7 $M_\odot$, finding a shallower low-mass slope, similar to field values. These studies all show that the characteristic mass of the SMF is dependent on environment, with denser environments showing higher characteristic masses.

Key observational works have indicated that galaxy quenching occurs primarily via one of two pathways: "mass quenching" and "environmental quenching", which have been shown to be separable in the local universe (Baldry et al., 2006; Peng et al., 2010). Mass

quenching processes are stellar mass-dependent, internal mechanisms including supernova feedback (e.g. Silk & Rees, 1998; Hopkins et al., 2006) and active galactic nuclei (AGN) feedback (e.g. Dekel & Silk, 1986; Ceverino & Klypin, 2009). These two processes are effective at quenching low and high-mass galaxies, respectively. "Environmental quenching", then, refers to mechanisms that induce galaxy quenching externally. This includes hydrodynamical interactions such as ram-pressure stripping (RPS; Gunn & Gott 1972; Boselli et al. 2022), where the interstellar medium of the galactic disk is stripped through interaction with the dense intracluster medium, rapidly removing star-forming material. Additionally, gravitational interactions can contribute to quenching in groups and clusters. Direct interactions such as mergers and tidal stripping can either strip material or induce starbursts by removing angular momentum from the gas in the disk, causing it to fall toward the centre (e.g. Moore et al., 1996, 1998). Finally, galaxies can undergo starvation if they are unable to accrete or cool fresh gas. RPS can remove hot gas from the halo, or the cluster environment can prevent gas from cooling onto galactic disks (e.g. Larson et al., 1980; Balogh et al., 2000).

The SMFs of the SF and quenched population as a function of environment and redshift can be used to trace the galaxy quenching process. For large surveys, this is often done with colour-magnitude or colour-colour cuts. Baldry et al. (2006) showed that, for SDSS galaxies, the increase in characteristic mass with increasing environmental density is due to the increase in massive, red galaxies in denser environments. Even where the shapes of the SMFs do not change considerably, the relative fraction of red galaxies increases with density across the stellar mass range. Interestingly, Yang et al. (2009) found that when SDSS galaxies were split into blue and red samples, the SMFs of the two populations both showed a dependence on halo mass. Galaxies can be split into SF and quenched populations more directly using direct tracers of star formation activity. Balogh et al. (2001) split their sample into emission line and non-emission line galaxies, and noted that the shape of the SMF of cluster non-emitters is similar to the total field population (dominated by emission-line galaxies), implying the cluster population may be built up by field emission line galaxies that ceased star formation after cluster infall.

What is missing from the literature is a comprehensive analysis of SMFs in the local Universe down to low stellar mass across local environments, with a robust star formation indicator. It is clear that the distribution of stellar mass depends on environment whether looking at the total SMF or the SMFs of SF and quiescent galaxies separately. However, it remains unclear how the populations in cluster infall regions differ from the cluster core, for example. Further, pre-processing of galaxies in smaller halos before infall into a massive cluster is likely an important yet poorly constrained step in the environmental evolution of galaxies (e.g. Fujita, 2004).

The Virgo cluster is an ideal environment to study the effects of environmental quenching at low-redshift. Virgo is a dynamically unrelaxed cluster. While it is dominated by a main cluster (Cluster A) centred around M87, a second smaller cluster (Cluster B, centred around M49; Mei et al. 2007) is merging into Cluster A from the south. Additionally, several smaller substructures have been identified, some of which appear to be infalling toward Virgo along filaments (Gavazzi et al., 1999; Mei et al., 2007; Cantiello et al., 2024). Thus, the Virgo environment contains galaxies in various stages of infall into the cluster, including populations in small structures that have not yet felt the influence of the main cluster.

At a distance of 16.5 Mpc (Mei et al., 2007), it is possible to image Virgo cluster galaxies at high physical resolution. The Next Generation Virgo Survey (NGVS; Ferrarese et al. 2012) has done just this in the optical with a deep survey of the Virgo environment complete to $M_* \sim 10^7$ $M_\odot$. More recently, the Virgo Environmental Survey Tracing Ionised Gas Emission (VESTIGE; Boselli et al. 2018a) followed up NGVS with a blind, narrowband Hα survey. The combination of these two surveys provide optical and star-formation maps at resolutions < 100 pc for galaxies in the Virgo environment spanning six decades in stellar mass. Numerous studies of the effects of the Virgo environment on galaxy evolution have been produced using this data (e.g. Ferrarese et al., 2016; Roediger et al., 2017; Lim et al., 2020; Fossati et al., 2018; Boselli et al., 2021, 2023a; Morgan et al., 2024).

In this work, we take advantage of the depth of NGVS and VESTIGE to probe the SMFs within the Virgo environment. With the comprehensive Hα data from VESTIGE, we can isolate galaxies into star-forming, transition and quiescent populations without relying on colour as a proxy for star-formation as often done in the literature. While SMFs have been used to understand galaxy populations in the field at low-redshift (e.g. Baldry et al., 2006, 2012), and clusters and protoclusters at intermediate and high redshifts (e.g. van der Burg et al., 2020; Edward et al., 2024), few studies have comprehensively analyzed low redshift cluster environments using this technique. Here we compare the SMFs of quiescent, transition and SF galaxies across the Virgo environment at a depth not before studied. With this effort, we look to understand the origin of the environmentally quenched population in Virgo as a function of stellar mass. This work represents the most comprehensive study of the stellar mass distribution throughout a local cluster, down to low stellar mass and using a robust star formation indicator.

Substructure	RA (deg)	DEC (deg)	Radius (deg)	Vel range (km s^{-1})	Distance (Mpc)	$\langle v \rangle$ (km s^{-1})	σ (km s^{-1})	Central galaxy
Cluster A	187.71	12.39	5.383	< 3000	16.5	955	799	M87
Cluster B	187.44	8.00	3.334	< 3000	16.5	1134	464	M49
Cluster C	190.85	11.45	0.7	< 3000	16.5	1073	545	M60
W Cloud	185.00	5.80	1.2	$1000 < v < 3000$	32	2176	416	NGC 4261
W′ Cloud	186.00	7.20	0.8	< 2000	23	1019	416	NGC 4365
M Cloud	183.00	13.40	1.5	$1500 < v < 3000$	32	2109	280	NGC 4168
LV Cloud	184.00	13.40	1.5	< 400	16.5	85	208	NGC 4216

Table 2.1: Properties of Virgo cluster substructures (taken from Boselli et al. 2023b)

2.2 Data

2.2.1 NGVS

The Next Generation Virgo Survey (NGVS; Ferrarese et al. 2012) includes optical imaging of the Virgo cluster environment out to 1.55 Mpc from M87, and 0.96 Mpc from M49. Using MegaCam on the Canada-France-Hawaii Telescope (CFHT), the survey covered 104 deg^2 in the u^*, g, i and z bands (with partial coverage in the r band). The long exposures of the survey allow for 5σ point-source depths of 26.3, 26.6, 25.8, and 24.8 mag in each of the four complete bands, respectively, with surface brightness depths of 29.3, 29.0, 27.4 and 26.0 mag arcsec^{-2}.

MegaCam on the CFHT consists of an array of 40 CCDs with pixel scale of 0.187″ pixel^{-1}. Seeing conditions during observations allowed for a resolution of $< 1''$ (full-width-half-maximum). NGVS images were processed using Elixir-LSB, a pipeline specifically developed for enhanced detection of low-surface brightness features in NGVS images. Photometric calibration and astrometric calibration follows procedures detailed in Gwyn (2008).

2.2.2 VESTIGE

The Virgo Environmental Survey Tracing Ionised Gas Emission (VESTIGE; Boselli et al. 2018a) is a blind, narrowband Hα followup to NGVS, covering the same 104 deg^2 of the Virgo cluster using the narrowband MP9603 filter on CFHT MegaCam (λ_c = 6591 Å; $\Delta\lambda$ = 106 Å) as well as the broadband r filter. The Hα Balmer line at 6563 Å and the two [NII] lines at 6548 Å and 6583 Å fall within the narrowband filter at the redshift range of Virgo ($-300 < v_{\rm hel} < 3000$ km s^{-1}). Long integrations (2h) in the narrowband achieved depths of $f(\mathrm{H}\alpha) \simeq 4 \times 10^{-17}$ erg s^{-1} cm^{-2} at 5σ for point sources and $\Sigma(\mathrm{H}\alpha) \simeq 2 \times 10^{-18}$ erg s^{-1} cm^{-2} arcsec^{-2} (1σ after smoothing the data to $\sim 3''$ resolution) for extended sources. r band exposures were 12 minutes, achieving a point source depth of 24.5 mag (5σ) and a SB limit of 25.8 mag arcsec^{-2} (1σ for scales comparable to the size of structures in target galaxies, $\sim$ 30 arcsec). Observations were taken under excellent seeing conditions (typical full-width-half-maximum of $0.76'' \pm 0.07''$). At the distance of Virgo, $1''$ is equal to 80 pc. The full observing strategy is discussed in detail in Boselli et al. (2018a).

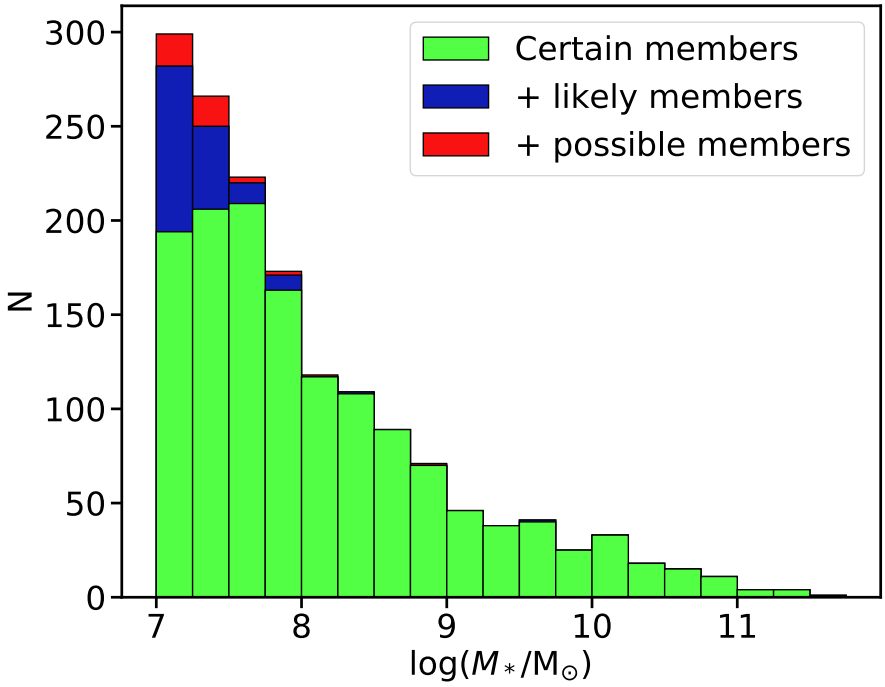


Figure 2.1: Virgo cluster members binned by stellar mass based on the three different groups of possible cluster members.

2.2.3 Cluster membership

To construct a robust catalogue of Virgo cluster members down to very faint luminosities and for which spectroscopic information was not available, the NGVS team developed a pipeline that included diagnostic plots based on photometric measurements, cuts on galaxy size, membership probability, and visual inspection. The result was a catalogue of galaxies with membership probability given a 0 (certain members), 1 (likely members) or 2 (possible members). The full strategy is discussed in detail in Ferrarese et al. (2020) where this process was applied to the initial catalogue for the core of the cluster. The catalogue used in this work extends to the rest of the NGVS sample. We show in Figure 2.1 a histogram of the number of galaxies assigned each of these membership probabilities as a function of stellar mass. Across most of the stellar mass range, the difference when "likely" and "possible" members are included is negligible, and there is only a small increase in

the number of galaxies at very low stellar masses if "possible members" are included. We choose to only include "certain" and "likely" members for this study. Including "likely" members ensures a complete sample, but one that may be impure at the lowest stellar masses. However, we perform the forthcoming analysis with and without including "likely" members and find no significant difference in any of the results.

2.3 Methods

2.3.1 Stellar masses

Stellar masses were derived as part of the NGVS project, as detailed in Roediger et al. (in prep). To summarize, spectral energy distribution (SED) fitting was performed on the u^*griz photometric data measured within one effective radius. All galaxies were assumed to be at the distance of the centre of Virgo, 16.5 Mpc. Flexible Stellar Population Synthesis simple stellar populations (Conroy et al., 2009) were used with a Chabrier initial mass function (Chabrier, 2003) and an exponentially-declining star-formation history. Mass-to-light ratios were then derived by fitting the observed SED to a grid of 50,000 synthetic models with a range of metallicities and ages. The final stellar mass catalogue is complete to 1.5×10^7 $M_\odot$, or $\mathcal{M}_{lim} = \log(M_{*,\mathrm{lim}}/M_\odot) \sim 7.2$, which we adopt as our mass limit.

2.3.2 Subcluster membership and mass scaling

The Virgo cluster is made of several different substructures, in addition to the main cluster, Cluster A, centred around M87 (Böhringer et al., 1994). The most prominent of these additional structures is Cluster B, centred on M49 (Gavazzi et al., 1999; Mei et al., 2007). Some works, based on the analysis of Gavazzi et al. (1999) have used a distance of 23 Mpc for Cluster B. However, we follow studies that have placed Cluster B at similar distance to Cluster A (e.g. Mei et al., 2007; Cantiello et al., 2024). In addition, Cluster C and the Low-Velocity (LV) Cloud are small structures identified within the footprint of and at the same distance as Cluster A. The W, W′ and M Clouds are smaller structures that have been determined to lie behind the Virgo cluster, falling toward the main cluster body along filaments (Mei et al., 2007; Cantiello et al., 2024). Following McLaughlin (1999), Ferrarese et al. (2012) determined R_{200} for Clusters A and B, calculating 1.55 Mpc and 0.96 Mpc, respectively. These values were used to establish the footprint for NGVS and VESTIGE, and are listed as the associated radii for these structures in Table 2.1. However,

more recent X-ray studies have suggested that the virialized region of the main cluster is smaller, $R_{200} = 0.974$ Mpc (Simionescu et al., 2017). In our analysis, we will use this value for R_{200} of Cluster A and discuss the impact of this choice in context.

Galaxies can be assigned to their most likely substructure based on 2D position and radial velocity information. However, our sample is only complete with radial velocities above $\sim 10^{8.5}$ $M_\odot$. As such, we assign galaxies to substructures based on 2D position only with the goal of keeping the Cluster A sample as pure as possible. Galaxies are preferentially assigned to the W, W′ and M Clouds if they fall within the footprint of these structures. Galaxies are assigned to Cluster B if they are located within the footprint of that structure and are > 1 Mpc ($\sim 1R_{200}$) from M87 at the centre of Cluster A. The remaining galaxies all lie within the footprint of Cluster A and may also be part of Cluster C and the LV Clouds. Since these structures are small, contain few galaxies and are located within Cluster A, we include these galaxies in Cluster A. The five populations discussed are shown in Figure 2.2 amongst the footprint of the NGVS survey. The radii used to define the boundaries of each substructures are listed in Table 2.1.

Our adopted distances for each structure are also shown in Tab. 2.1. Because the distance used in the calculation of the stellar masses was 16.5 Mpc for all galaxies, the stellar masses for galaxies in the W, W′ and M Clouds will be underestimated. To account for this, we scale the masses based on the distances to these structures. Since we initially made a stellar mass cut at $\mathcal{M}_{\rm low} = 7.2$, scaling the masses according to distance will move this lower limit to $\mathcal{M}'_{\rm lim} = 7.78$, since $\mathcal{M}'_{\rm lim} = \mathcal{M}_{\rm lim} + 2\log(d_{\rm max}/16.5)$, where $d_{\rm max} = 32$ Mpc is the distance to the furthest cloud and 16.5 Mpc is the distance to the main Virgo cluster.

2.3.3 Star formation rates

Integrated star-formation rates for all VESTIGE galaxies were derived in Boselli et al. (2023a), and we refer the reader to this work for a full description of the process and considerations made. In brief, SFRs were derived using the Calzetti et al. (2010) calibration converted to a Chabrier initial mass function (IMF). This produces the following relation:

$$\mathrm{SFR}\left[M_\odot\ \mathrm{yr}^{-1}\right] = 5.01 \times 10^{-42} L\left(\mathrm{H}\alpha\right)\left[\mathrm{erg\ s}^{-1}\right]. \tag{2.1}$$

As discussed in Boselli et al. (2023a), the sensitivity of VESTIGE probes Hα luminosities low enough to detect ionizing radiation produced by a single O or B-type star. At this extreme low range, effects such as stochasticity in the IMF can create large uncertainties

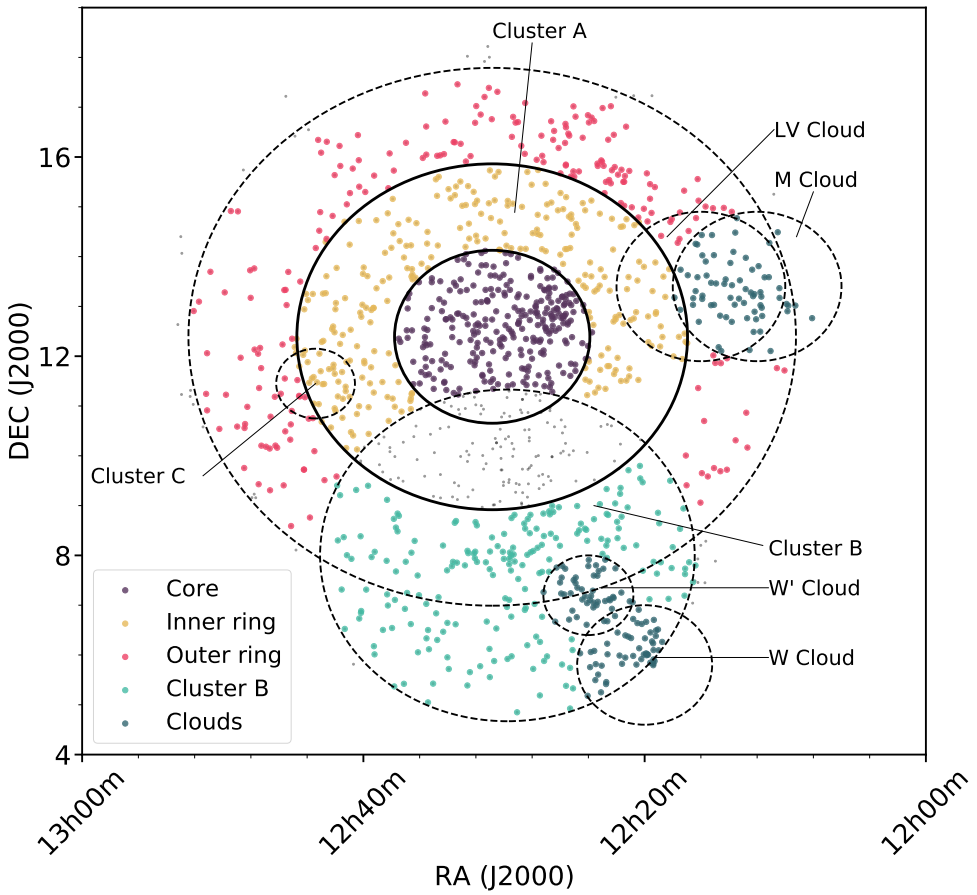


Figure 2.2: RA and DEC footprint of galaxies in the Virgo sample. Dashed circles outline the various substructures associated with the Virgo cluster. The solid black lines at 0.5 and 1 Mpc define boundaries for the three radial bins in which galaxies associated with Cluster A are grouped. Galaxies are coloured based on the bin they belong to, with smaller grey data points not belonging to any bin.

on the SFR. In this work, we only consider galaxies above 10^7 $M_\odot$, where we expect at least galaxies on the star-forming main sequence will have well-measured SFRs.

Boselli et al. (2023a) assigned galaxies to the various substructures of Virgo based on 2D position and radial velocity measurements. When calculating the SFRs, each galaxy was assumed to be at the distance corresponding to its assigned substructure. Since our substructure assignments do not completely overlap with those of Boselli et al. (2023a), we scale SFRs where necessary based on the distance assigned to a galaxy (and its substruc-

ture) as described in Section 2.3.2. This ensures the stellar mass and SFR for each galaxy are based on the same distance.

Using the measured SFRs, the VESTIGE SFMS was derived and analyzed in detail in Boselli et al. (2023a). The best fit to the sample of HI-normal galaxies is

$$\log(\mathrm{SFR}) = 0.92 \log(M_*) - 9.34, \tag{2.2}$$

with a scatter of ~ 0.4 dex. The SFMS is defined as a band spanning $\pm 1\sigma$ of the best fit line. We show this fit with our sample of galaxies plotted on Figure 2.3. 118 galaxies fall on the SFMS, with 8 galaxies located above the SFMS. For the purposes of this analysis, these galaxies with excess star formation are grouped into the SF sample. Thus, there are 126 galaxies in the final SF sample. Any galaxies with no detectable Hα emission are considered quiescent galaxies.

Massive early-type galaxies with AGN may have Hα emission that is not associated with star formation. Boselli et al. (2023a) checked for AGN contamination from nuclear spectra that is nearly complete for the VESTIGE sample (Cattorini et al., 2023), finding that the handful of galaxies that may have AGN based on BPT (Baldwin et al., 1981) or WHAN (Cid Fernandes et al., 2011) classifications all had clearly identifiable HII regions dominating their Hα emission when visually inspected. As such, we have not removed any galaxies or altered their measured SFRs due to AGN contamination.

A large sample of galaxies have measurable SFRs that are $> 1\sigma$ below the SFMS. We consider these galaxies to be low-SFR galaxies, and isolate them from our normal SF population for further analysis. A subset of low-SFR galaxies may represent a transition population between SF and quiescent galaxies. However, emission driven by low-luminosity AGN or LINERs cannot be completely ruled out. In the literature, the population is often defined using colour-colour cuts and may consist of transition galaxies and/or dust-obscured disks (e.g. Schawinski et al., 2014). However, we are able to directly measure the SFRs of galaxies and thus probe this transition population more directly. Recently, Boselli et al. (2023a) noted that these transition galaxies are mainly HI-deficient systems, and that their properties were consistent with RPS. However, work by Morgan et al. (2024, Chapter 3 of this thesis) suggested that the significant fraction of Virgo cluster galaxies in this transitionary phase could be indicative of slower quenching modes such as starvation, particularly for galaxies located beyond the cluster virial radius.

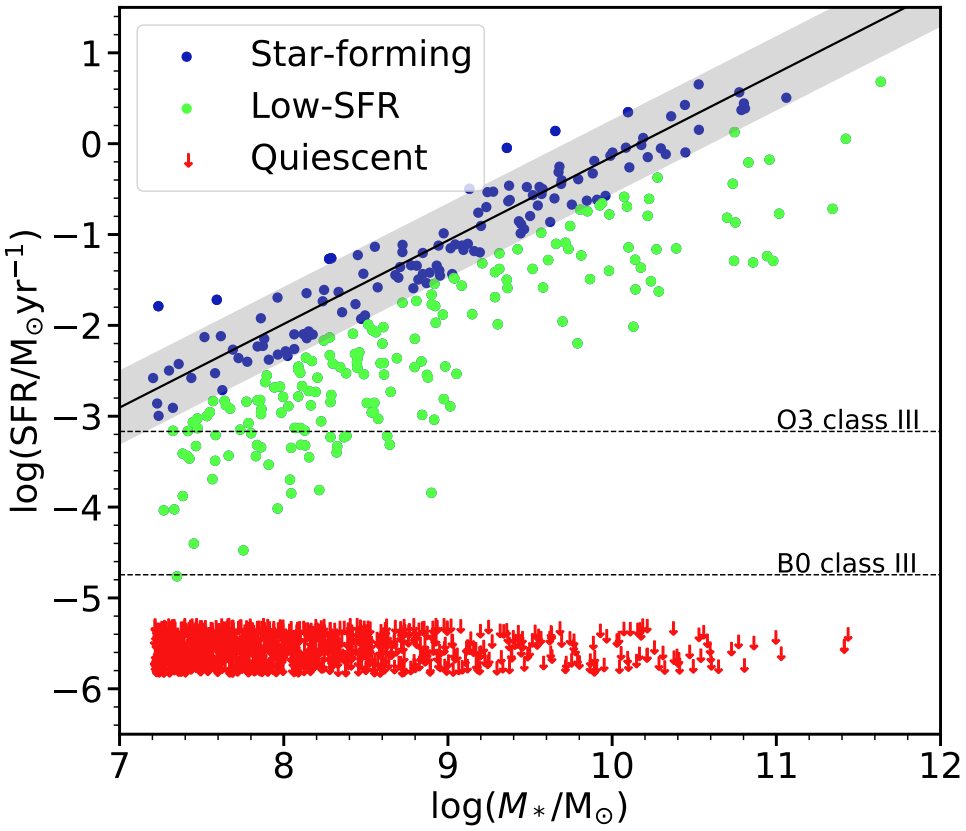


Figure 2.3: SFMS of the VESTIGE sample with the main sequence defined as in Boselli et al. 2023a. Galaxies within 1σ of the SMFS are considered SF galaxies (blue), while those detected in Hα but with SFRs that place them below the SFMS are shown as low-SFR galaxies (green). Galaxies undetected in Hα are quiescent galaxies (red), and placed at random low values of SFR for illustration only.

2.3.4 Stellar mass functions

We fit the distribution of logged stellar masses ($\mathcal{M} = \log(M_*/\mathrm{M}_\odot)$) using a Schechter function (Schechter, 1976), taking the form:

$$\phi(\mathcal{M}) = \ln(10)\phi^* \cdot \exp(-10^{(\mathcal{M}-\mathcal{M}^*)}) \cdot 10^{(\mathcal{M}-\mathcal{M}^*)(\alpha+1)}, \tag{2.3}$$

where $\mathcal{M}^* = \log_{10}(M^*/\mathrm{M}_\odot)$ is the characteristic mass, α is the low-mass slope of the

Environment	Sample	N	α	$\mathcal{M}^*$ ($\log(M_*/\mathrm{M}_\odot)$)	ϕ^* (cluster^{-1}dex^{-1})
All	Total	1308	$-1.35^{+0.02}_{-0.02}$	$11.33^{+0.17}_{-0.11}$	$18.25^{+3.54}_{-4.53}$
	non-Hα/Quiescent	997	$-1.44^{+0.02}_{-0.02}$	$11.35^{+0.31}_{-0.13}$	$6.88^{+1.68}_{-2.46}$
	Hα	269	$-1.15^{+0.03}_{-0.04}$	$11.13^{+0.16}_{-0.11}$	$19.47^{+4.07}_{-4.51}$
	Low-SFR	158	$-1.23^{+0.04}_{-0.05}$	$11.45^{+0.35}_{-0.16}$	$6.13^{+1.70}_{-2.47}$
	Star-forming	111	$-0.96^{+0.06}_{-0.07}$	$10.60^{+0.17}_{-0.12}$	$21.12^{+5.10}_{-5.65}$

Table 2.2: Best fit parameters and uncertainties for the total Virgo SMF and the SMFs split according to Hα emission

distribution, and ϕ^* is the normalization. We fit the Schechter function to the un-binned mass data using the parametric maximum-likelihood method (Sandage et al., 1979). To do so, we assign a probability to each mass in the sample in the manner presented in Oegerle et al. (1986) and Malumuth & Kriss (1986), where

$$p(\mathcal{M}_i) \equiv \frac{\phi(\mathcal{M}_i)}{\int_{\mathcal{M}_{\rm lim}}^{\infty} \phi(\mathcal{M}')\, d\mathcal{M}'}. \tag{2.4}$$

The log-likelihood is simply the sum of the logarithms of the individual probabilities. By maximizing the log-likelihood we estimate the posterior distribution of the parameters $\mathcal{M}^*$ and α using the Python package EMCEE (Foreman-Mackey et al., 2013). The normalization ϕ^* is not fit as a free parameter, but is calculated such that the integral of the fit Schechter function over the entire mass range of the sample is equal to the number of galaxies in the sample.

Several studies analyzing SMFs have shown that a double-Schechter fit can better represent the mass distribution of galaxy samples than a single-Schechter (e.g Baldry et al., 2008). The double-Schechter function used is simply a two-term function where each term has the same form as Eq. 2.3. The α and ϕ^* parameters for each term are fit, while the $\mathcal{M}^*$ parameter is fit but is the same in both terms. This functional form allows for cases such as a positive power law near the exponential cutoff, with an upturn (negative power law) to lower stellar masses. We performed double-Schechter fits on our total and quiescent populations where the binned data appeared visually to follow this shape. However, a Bayesian Information Criterion (BIC) test showed that the single-Schechter is statistically a better fit to the data, given the risk for overfitting with additional parameters. As such, we use exclusively single-Schechter fits in our analysis.

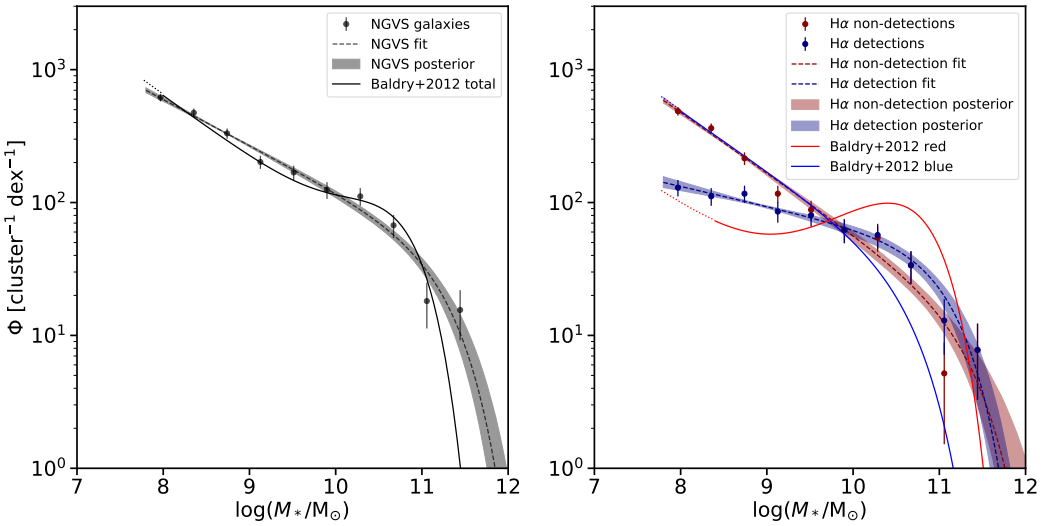


Figure 2.4: SMFs of the entire Virgo sample compared to the field from GAMA. *Left:* The total SMF of the Virgo sample is shown with the renormalized field SMF from GAMA (Baldry et al., 2012). *Right:* The SMFs of the Hα (blue) and non-Hα (red) selected populations in Virgo. The renormalized blue and red SMFs from the GAMA field are shown for comparison. The data points and errorbars (determined from Poisson statistics) show binned data for visualization. The single Schechter is fit to the unbinned data, with the best fit shown along with the 1σ uncertainties. The dotted extensions of the GAMA curves are extrapolations below the mass limits of the survey.

2.4 Results

We present SMFs for the total Virgo environment, as well as SMFs split into environmental bins. Further, we break up our sample based on SFR determined from VESTIGE Hα data. We have removed the brightest cluster galaxies of Clusters A and B (M87 and M49, respectively) from our sample, such that our SMFs are of satellite galaxies of the cluster. We have not removed the central galaxies from the smaller substructures listed in Table 2.1. We show the fit parameters for the SMFs of the full Virgo sample in Table 2.2. In Appendix A.1, Table A.1 displays the results from fits to individual environmental bins.

2.4.1 Full Virgo stellar mass functions

We fit the full Virgo SMF with a single Schechter fit as described in Section 2.3 for $\mathcal{M}'_{lim} > 7.78$. Because the total mass function includes galaxies in the W, W′, and M Clouds where we have scaled the masses, we only fit the total mass function to $\mathcal{M}'_{lim}$, since our sample of stellar masses will be incomplete below this mass. We show the results on the left panel of Figure 2.4, including the 1σ posterior distribution. For a comparison with a local field population, we show the fit from (Baldry et al., 2012) to field galaxies in the GAMA survey. While the GAMA survey completeness extends down to only $\mathcal{M} > 8$, we have renormalized the fit such that the integral of the field SMF is equal to the total number of galaxies within the mass range of the Virgo sample.

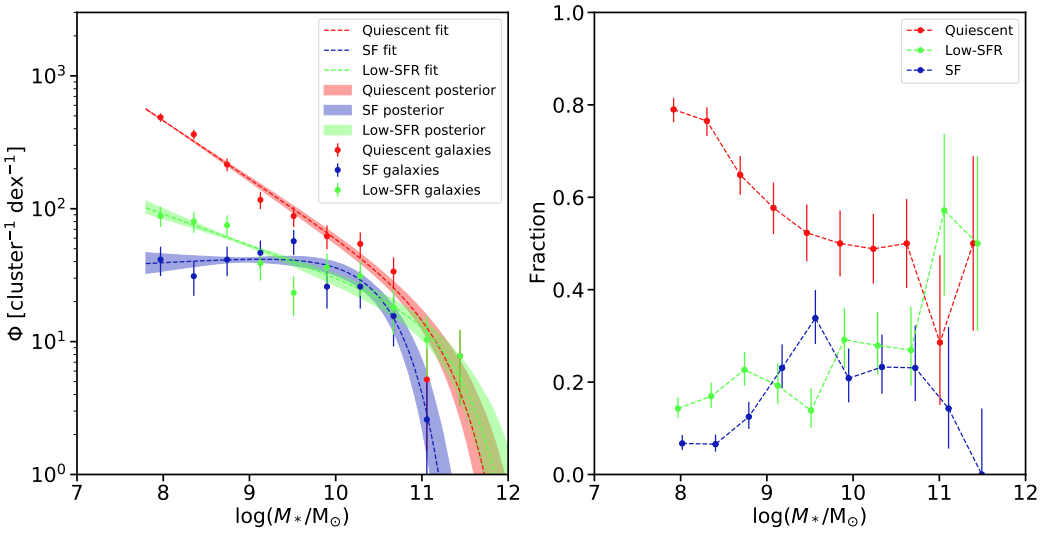


Figure 2.5: SMFs and relative fractions of different populations (quiescent, low-SFR and SF) in Virgo. *Left:* The SMF of quiescent (red), SF (blue) and low-SFR (green) populations in the Virgo sample. The data points and errorbars (determined from Poisson statistics) show binned data for visualization. The single Schechter is fit to the unbinned data, with the best fit shown along with the 1σ uncertainties. *Right:* The fraction of quenched (red), low-SFR (green), and SF (blue) galaxies in the Virgo sample as a function of stellar mass, with associated uncertainty ranges.

Since we will use the Hα data from the VESTIGE survey to separate Virgo galaxies into star-forming and quiescent populations, we separate galaxies into Hα detections and

non-detections on the right side of Figure 2.4. As we expect both VESTIGE and NGVS samples to be complete down to $\mathcal{M}'_{lim} > 7.78$, the H$\alpha$-selected SMF contains all cluster galaxies detected with VESTIGE above this limit. The non-Hα SMF, then, contains all NGVS Virgo detections without an Hα counterpart in VESTIGE. For comparison to the field, we plot the SMFs from Baldry et al. (2012) separated into blue and red populations. The red and blue populations were separated using a $u - r$ colour-magnitude cut, and the SMFs for the two populations fit simultaneously. We have renormalized the Baldry et al. (2012) curves such that the sum of the integrals under the blue and red curves is equal to the total number of galaxies in the Virgo sample, but the relative fractions of blue and red galaxies follow the GAMA field values. We note that Gunawardhana et al. (2015) presented the mass function of Hα-selected galaxies in the GAMA dataset. While this selection is a better match to ours, their Hα-selected SMF is in fact very similar to the Baldry et al. (2012) blue SMF. As such, we plot the blue and red populations for comparison here and discuss them later in the paper.

2.4.2 Separating populations based on star formation rate

On the left side of Figure 2.5 we show the SMFs of the quiescent, SF and low-SFR populations in Virgo. Each SMF was fit with a single Schechter function as described in Sect. 2.3 for $\mathcal{M}'_{lim} > 7.78$. On the right side we show the quiescent, SF and low-SFR fractions as a function of stellar mass. We use the binned stellar masses to calculate the relative fractions and uncertainties. Virgo is dominated by quiescent galaxies through most of the stellar mass range, and particularly at low masses. At high masses, there are few SF galaxies (the SF fraction peaks around $10^{9.5}$ $M_\odot$), but larger abundances of low-SFR galaxies. This is also evident on Fig. 2.3, where many of the most massive galaxies have some Hα emission but are well below the SFMS.

2.4.3 The stellar mass function across the Virgo environment

Because Virgo has a complicated structure, it is interesting to measure and compare the SMFs in different regions of the cluster with each other and with the field. First, we are interested in pure samples of galaxies associated with Cluster A. Using the Cluster A sample as defined in Section 2.3.2, we construct three bins based on distance to M87: 0 Mpc $\leq R <$ 0.5 Mpc, 0.5 Mpc $\leq R <$ 1.0 Mpc and 1.0 Mpc $\leq R <$ 1.5 Mpc (Core, Inner Ring, and Outer Ring, respectively). Adopting $R_{200} \sim 1$ Mpc (Simionescu et al., 2017) as the virial radius of Virgo, we can consider galaxies in the Outer Ring to be in the infall region of the main cluster.

We show in Figure 2.6 the SMF fits for quiescent, low-SFR and SF populations in the three Cluster A radial bins. Since we have constructed a pure sample of Cluster A galaxies located at 16.5 Mpc, we can safely fit these SMFs down to $\mathcal{M}_{lim} > 7.2$. In Figure 2.7 we show the best fit and 1σ contours for the two free Schechter parameters (α and $\mathcal{M}^* = \log(M^*/\mathrm{M}_\odot)$) for the three populations in each of these bins as well as the total Virgo population. The shapes of the mass functions differ only slightly and insignificantly across the three radial bins. In each case, the population is dominated by a steep power-law quiescent mass function and comparatively flat SF mass functions. The low-SFR SMF has a slope that is intermediate between the SF and quiescent populations, indicating that these galaxies are not simply a subset of one of the other populations. There are no significant environmental variations in the characteristic masses of each population.

In Figure 2.8 we show the fractions of quiescent, low-SFR and SF galaxies as a function of stellar mass in the three Cluster A radial bins. Across the Cluster A environment, the low-mass end is dominated by quiescent galaxies. As one moves toward the high-mass end, the quiescent fractions decrease, and the low-SFR and SF fractions increase. Quiescent and low-SFR galaxies tend to dominate the high-mass regime again beyond $\mathcal{M} > 11$, though low numbers of galaxies in this regime increase the uncertainties on these fractions. The SF fraction peaks in each environment at $\mathcal{M} \sim 10.5$. While the shapes of the SMFs do not change significantly across the environment, the relative contributions of the quiescent, SF and low-SFR populations do change, with slightly lower quiescent fractions (below $\mathcal{M} < 10.5$) in the Inner Ring and Outer Ring than the Core. The Hα-emitting population in the Outer Ring is dominated by SF galaxies, whereas in the Inner Ring, low-SFR galaxies dominate. With that said, the quiescent populations dominate across all environments in this mass range. We will further discuss the impact of the Virgo environment on the relative fraction of quiescent and low-SFR galaxies and compare to values seen in the field in Sect. 2.5.

2.5 Discussion

2.5.1 Cluster B and the Clouds

When separating galaxies into different environmental bins, we assigned galaxies to Cluster B if they fell within the Cluster B footprint, and > 1 Mpc from M87. Galaxies that overlap in the virialized region of Cluster A and Cluster B are quite likely to have been affected by the Cluster A environment. In addition, there is no significant overdensity of galaxies in this region compared to the Outer Ring to assume they belong to Cluster B. We show the

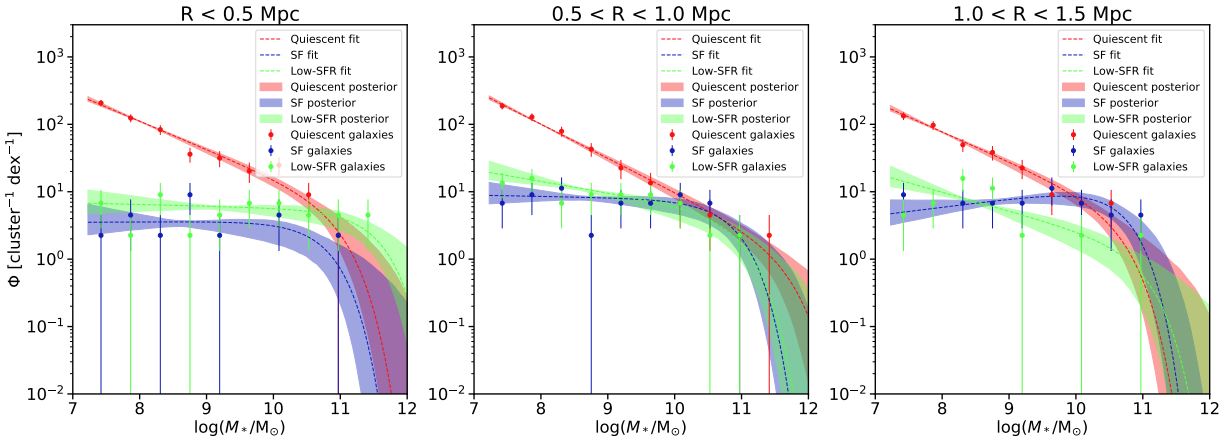


Figure 2.6: SMFs for the quiescent, low-SFR and SF populations in three radial bins centred on M87. Methodology and colours are the same as Figure 2.5.

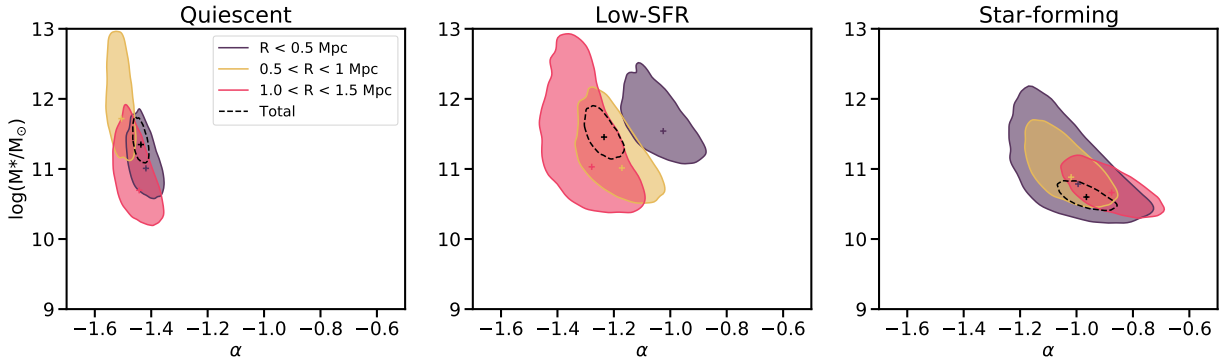


Figure 2.7: Best fit and 1σ contours for the fit values of α and $\mathcal{M}^* = \log(M^*/\mathrm{M}_\odot)$ for quiescent, low-SFR and SF SMFs, shown for the three radial bins of Cluster A and the total Virgo population. The black data point and contour represent the best fit and 1σ for the total SMF of all Virgo galaxies. Errorbars on the fractions display binomial confidence intervals.

quiescent, low-SFR and SF SMF fits to the Cluster B and Clouds regions in Figure 2.9, with the fit parameters in Figure 2.10. Since Cluster B is located at 16.5 Mpc, we fit the SMFs down to $\mathcal{M}_{lim} > 7.2$ in this region, while the Clouds SMFs can only be fit down to $\mathcal{M}'_{lim} > 7.78$ because of their greater distance. The SMFs of these two regions are again consistent with the total SMFs of the Virgo cluster within uncertainties. We note that the characteristic mass of the quiescent and low-SFR SMFs of the Clouds are higher than

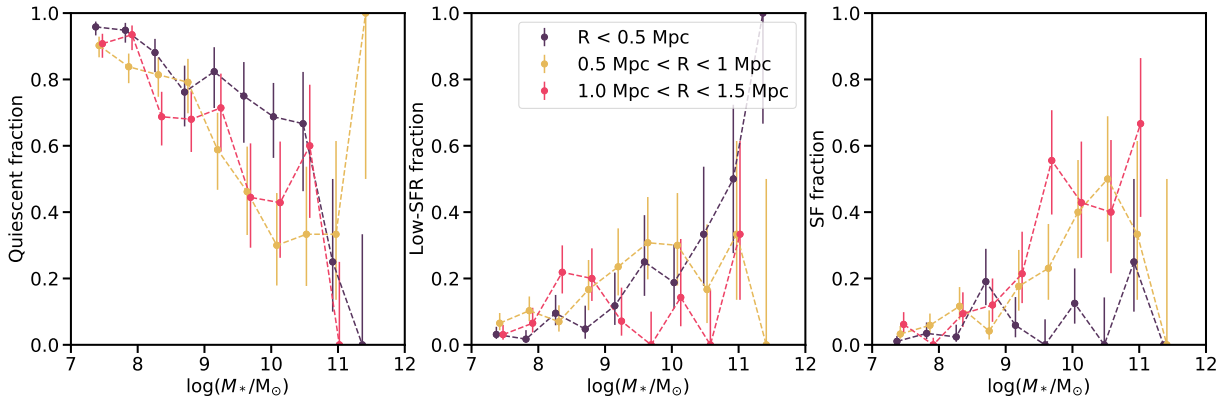


Figure 2.8: Quiescent, low-SFR and SF fractions as a function of stellar mass. Fractions are shown for the three radial bins of Cluster A based on the binned stellar masses shown in Figures 2.6 and 2.9.

other regions. We do not expect the Clouds region to be pure - some galaxies may actually be located at 16.5 Mpc and be part of Cluster A, B or the LV Cloud. If some galaxies have incorrectly had their masses scaled, this may be pushing the SMF to higher characteristic masses. We show the relative fractions of these regions in Figure 2.11. While we see a more moderate quiescent fraction and higher SF fraction in the Clouds, the quiescent fraction is still significant. However, it is difficult to determine whether this is due to contamination from Cluster A and B galaxies, or due to environmental effects in the Clouds themselves.

In Cluster B, our sample should be quite pure, with some possible contamination from Outer Ring galaxies from Cluster A. Nonetheless, this population is made up of galaxies beyond the virial radius of Cluster A. While we do see a lower quiescent fraction and higher SF fraction at intermediate masses in Cluster B, the low mass end is still dominated by quiescent galaxies and the high mass end by low-SFR galaxies. We will discuss these results further in Section 2.5.3 when comparing to other studies of field and cluster quenched fractions.

2.5.2 The need for pre-processing

In an attempt to explore the infall region of the cluster, we define a new Infall region that contains the Outer Ring as defined in the previous section, but also any Cluster B galaxies that fall from 1.0 Mpc $\leq R <$ 1.5 Mpc (we continue to exclude galaxies assigned to the W, W$'$ and M clouds since they are located far behind the cluster). The choice to include

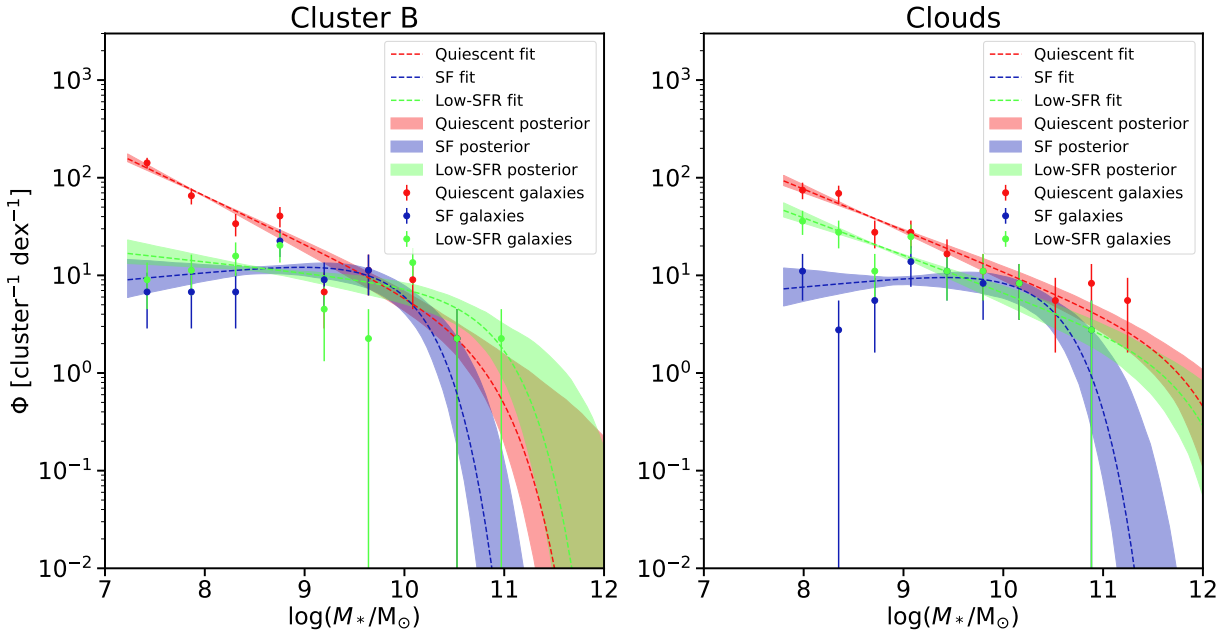


Figure 2.9: SMFs for the quiescent, SF and low-SFR populations in Cluster B and the Clouds. Methodology and colours are the same as Figures 2.5 and 2.6.

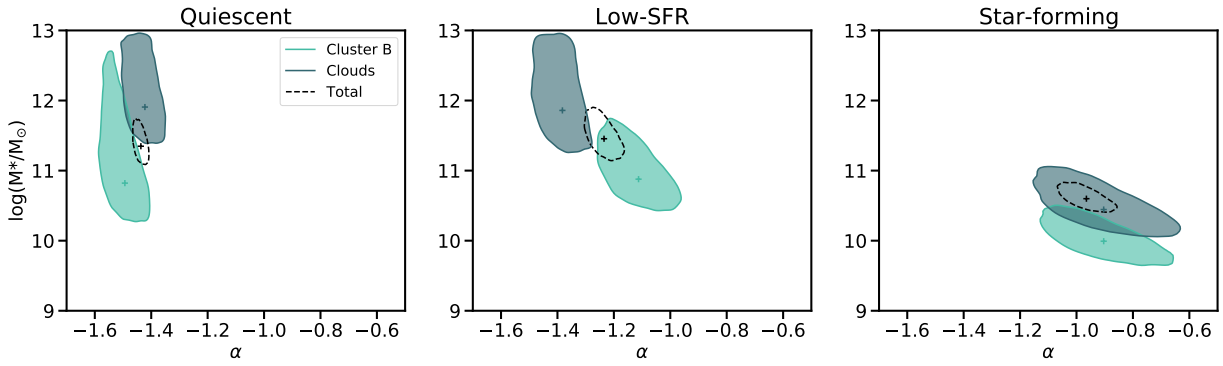


Figure 2.10: Same as Figure 2.7 but for the Cluster B and Clouds populations.

Cluster B galaxies stems from the fact that at $z = 0$, $\sim$ 40% of galaxies in clusters were satellites of group halos prior to cluster infall (e.g. McGee et al., 2009). Thus, a true infall population should include galaxies infalling as part of smaller halos. We show the galaxies being analyzed in Figure 2.12.

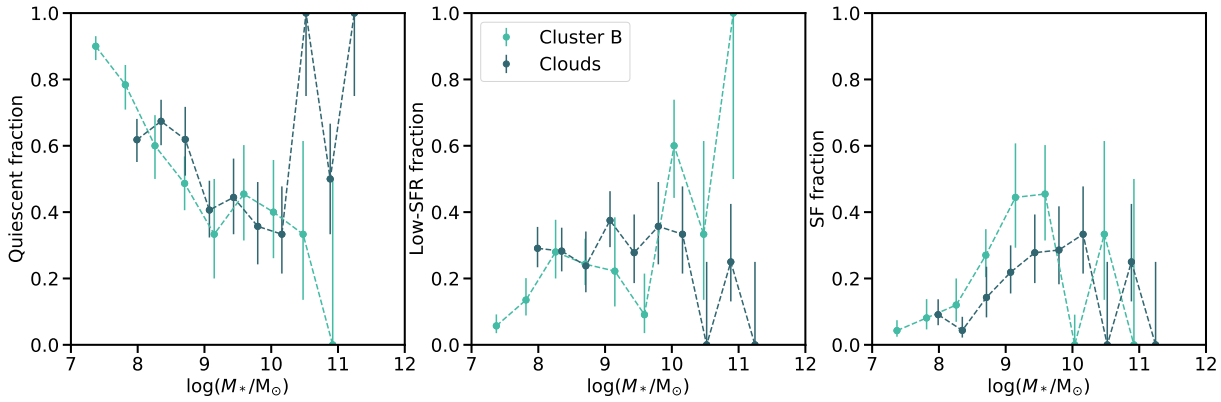


Figure 2.11: Same as Figure 2.8 but for the Cluster B and Clouds populations.

Fig. 2.4 shows that the SMF of quiescent Virgo galaxies is of a completely different shape from that of the field. This is true even of the Infall and Outer Ring populations, for which the SMF is statistically indistinguishable from the Core (Fig. 2.7)[1]. Therefore, environmental effects must dominate the galaxy population, even in the Infall regions of Virgo. One possibility is that this region is dominated by backsplash galaxies. The similarity between the Core and Infall region SMFs means that the contribution from field quiescent galaxies must be small and backsplash galaxies would have to account for a large majority of the infall population, which is not supported by simulations (e.g. Haggar et al., 2020). The other possibility is that galaxies are being environmentally pre-processed in smaller halos before their infall into Virgo, or are being processed by Virgo well beyond R_{200}. By quantifying the maximum contribution from field quiescent galaxies allowed given the statistical uncertainties on the data, we can attempt to rule out the backsplash-only scenario in favour of a scenario involving some degree of pre-processing.

We consider a simple model where the quiescent SMF in the Infall bin is comprised of a linear combination of the field quiescent mass function and the Core quiescent mass function. This assumes that the environmentally processed quiescent galaxy population has a universal SMF shape, which is the simplest assumption given the lack of environmental dependence observed in the sample. It follows that

$$\phi_{\mathrm{q,infall}} = A \times \phi_{\mathrm{q,core}} + B \times \phi_{\mathrm{q,field}}, \tag{2.5}$$

[1]We note that we do not show the SMF for the quiescent Infall population as it is essentially identical to that of the Outer Ring population shown in Fig. 2.6. For completeness, we run the following tests using both the Infall and Outer Ring populations and find no difference in the results.

where A and B are coefficients that determine the relative contributions of the core and field populations. $\phi_{\rm q,core}$ is the quiescent population in the core of Virgo shown in Fig. 2.6, while $\phi_{\rm q,field}$ represents the red population[2] shown in Fig. 2.4, taken from the GAMA survey (Baldry et al., 2012). The fraction of galaxies coming from the core and field populations respectively can be determined by

$$f_{\rm q,core} = \frac{A \int_{M_{\rm lo}} \phi_{\rm q,core}}{\int_{M_{\rm lo}} \phi_{\rm q,outer}} \tag{2.6}$$

and

$$f_{\rm q,field} = \frac{B \int_{M_{\rm lo}} \phi_{\rm q,field}}{\int_{M_{\rm lo}} \phi_{\rm q,outer}}, \tag{2.7}$$

where $M_{\rm lo} = 10^{7.2}$ M$_\odot$ is the lower completeness limit for galaxies in the NGVS sample as outlined in Sect. 2.2.1.

Since the quiescent SMFs in the Infall region and Core look similar, we expect a high fraction of Core galaxies. As such, we vary the Core fraction $f_{\rm q,core}$ between 0.5 and 1, with $f_{\rm q,field} = 1 - f_{\rm q,core}$. We then draw a sample of 247 galaxies (the number of observed quiescent galaxies in the Infall region), split between the Core and field populations based on $f_{\rm q,core}$ and $f_{\rm q,field}$, and run an Anderson-Darling (AD) test between this population and the real population of galaxies in the Infall region. For each value of $f_{\rm core}$, we repeat this test 1000 times to visualize the distribution of p-values from the AD tests. From the 1000 runs, we calculate the percentage of samples that can be ruled out as inconsistent with the observed population at the 2σ and 3σ levels (p-values of 0.05 and 0.003, respectively), as shown in Figure 2.13. The regions where the majority of our samples are consistent with the observed population are indicated as anything to the right of the blue and red dashed vertical lines. When using a 2σ AD confidence, the majority of drawn samples look like the observed population for $f_{\rm core} > 0.84$. This drops to $f_{\rm core} > 0.71$ if we use a 3σ confidence level for the AD tests. In both cases, the Core fraction limits show that the fraction of environmentally-impacted galaxies in the Infall region is much higher than the fraction of

[2]While the definition of red galaxies from GAMA is based on colour, we noted previously that the work of Gunawardhana et al. 2015 found nearly a nearly identical SMF for Hα-selected GAMA galaxies as the blue population in Baldry et al. 2012. This implies that a quiescent population in GAMA selected based on Hα non-detections would have a similar SMF to the red population, justifying the use of the GAMA red SMF here.

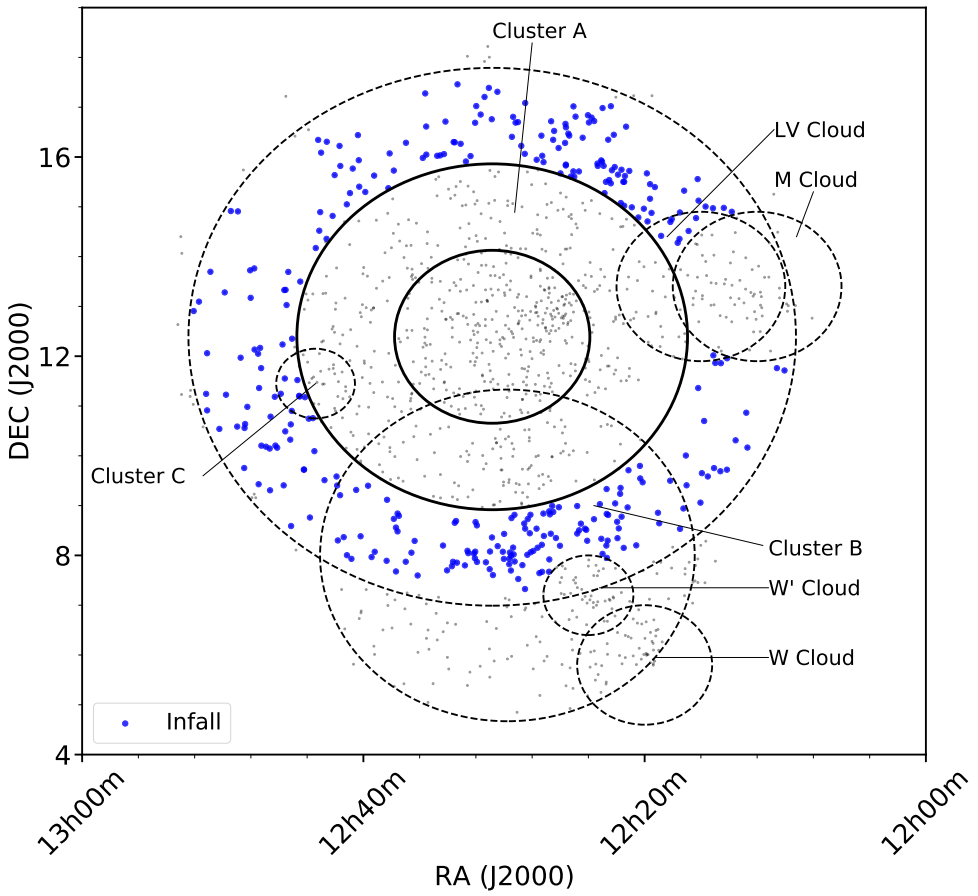


Figure 2.12: Same as Fig. 2.2 but highlighting just the Infall population.

backsplash galaxies at this radius found in simulations (Haggar et al., 2020), $52 \pm 19\%$, shown as the green shaded region in Figure 2.13.

Assuming that Virgo has a typical fraction of backsplash galaxies ($\sim 52\%$), this rules out the hypothesis that all environmentally-quiescent galaxies in the Infall region are backsplash. Thus, there must be some amount of pre-processing in at least ~ 20 per cent of the population, prior to the first crossing of R_{200} into the main Virgo cluster. There is significant cluster-to-cluster variation in the backsplash fractions determined from simulations. If Virgo has a backsplash fraction of $> 1\sigma$ above the median, the conclusions become less significant, as a majority of drawn samples cannot be ruled out as different from the Infall population at the 3σ level.

Thus, pre-processing likely plays an important role in shaping the quiescent mass func-

tions in the Virgo cluster. This inference is bolstered by the observed quiescent SMF in Cluster B and the Clouds. The Clouds are located behind the main cluster, meaning that if galaxies in this region are quiescent, they have either quenched secularly in the field, or quenched via environmental mechanisms in the much smaller group environments. Processes such as RPS are likely much less common in smaller groups, since small groups lack the intracluster medium density of massive clusters. However, some cases of RPS in group-sized halos have been identified (e.g. Catinella et al., 2013; Roberts et al., 2021a; Kolcu et al., 2022). Additionally, while direct stripping of cold gas is difficult, the loosely bound circumgalactic medium (CGM) could be stripped, driving starvation if the galaxy cannot accrete fresh gas. Given that dwarf galaxies will have smaller restoring forces with which to hold onto their gas, stripping of dwarf galaxies in group structures in more likely than stripping of massive spirals. Since most galaxies in the local universe are found in groups (e.g. Geller & Huchra, 1983; Robotham et al., 2011), pre-processing in these structures likely plays an important role in building up the quiescent population in Virgo. While this holds true for the Virgo cluster, results may be different for other local clusters, especially those are are dynamically inactive.

In addition, one cannot rule out the effects of the main cluster environment beyond the virial radius. The intracluster medium may extend far enough to strip gas from dwarf galaxies (e.g. Boselli et al., 2022), and starvation may begin well before the first crossing of R_{200} (e.g. Bahé et al., 2013; Morgan et al., 2024). It is also worth noting that various measurements of R_{200} exist for Virgo, with values as high as 1.7 Mpc (Kashibadze et al., 2020). The variation in R_{200} is due in part to the asymmetric structure of the cluster, where different studies have made different choices about how to treat the southern extension of Virgo (i.e. Cluster B). If the virial radius is in fact much larger than the value we have adopted here, the Infall region as described would actually be within the virial radius.

2.5.3 Literature comparison

Cluster and field Schechter fits

Ferrarese et al. (2016) determined the total SMF in the very core of Virgo (central 0.3 Mpc^2) to have a slope of $\alpha \sim -1.35$, though their fit did not effectively constrain the characteristic mass. Combining our quiescent, SF and low-SFR populations into a total Core population yields a SMF with $\alpha = -1.36$, consistent with the results of Ferrarese et al. (2016). Our Schechter fit for the total SMF of Virgo yields $\alpha = -1.35$ and $\mathcal{M}^* = 11.33$, which we compare with other cluster Schechter fits in Figure 2.14. The comparison studies include the Perseus cluster (Cuillandre et al., 2024), the Shapley Supercluster (Merluzzi et al.,

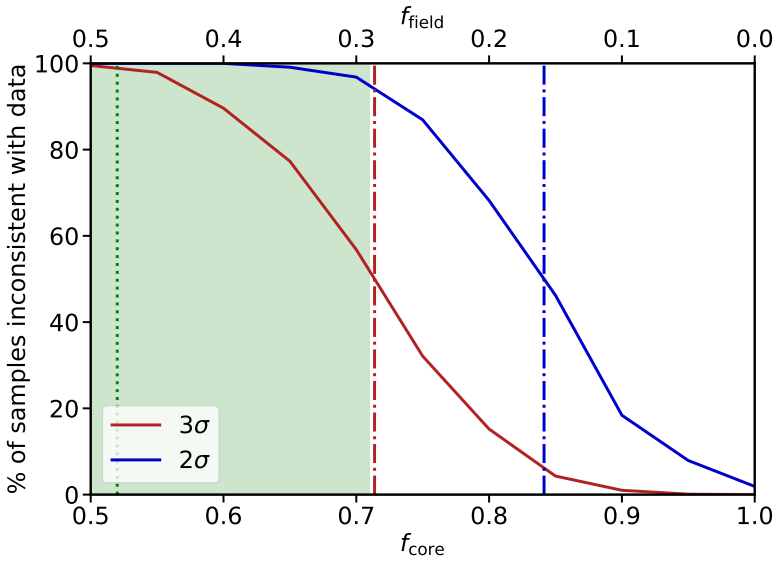


Figure 2.13: Percentage of field+core quiescent samples that are inconsistent with the observed quiescent population in the Infall region of Virgo, as a function of core fraction. Samples are determined to be inconsistent at a 2σ (blue curve) or 3σ (red curve) level based on an Anderson-Darling test comparing the samples with the observed Infall population. The dashed-dot lines show where $< 50\%$ of the samples are determined to be inconsistent with the data, meaning that the majority of samples drawn cannot be ruled out as being drawn from the same distribution as the data. The green dotted line shows the median backsplash fraction between 1 and $1.5R_{200}$ from Haggar et al. (2020) for unrelaxed clusters, while the shaded green area shows the 68% confidence interval . This test shows that the maximum field galaxy contribution to the Infall quiescent population is not enough to remedy the high backsplash fractions, implying the need for pre-processing beyond R_{200}.

2010) and SDSS halos with similar mass to Virgo ($10^{13.8} < M_h/\mathrm{M}_\odot < 10^{14.4}$; Yang et al. 2009). Our value for the low-mass slope α is consistent with the SDSS value and steeper than the Perseus and Shapley studies. Cuillandre et al. (2024) note that a fit to the low-mass end of their Perseus sample gives a slope of $\alpha = -1.35$, consistent with the slope in our Virgo sample. Steeper low-mass slopes are consistent with deep field samples where a double-Schechter fit was used, such as in Baldry et al. (2012), where a low-mass slope of $\alpha = -1.47$ is found.

While the slopes of the cluster and field samples are often consistent within their uncertainty, we find a steeper α than field values. In addition, the characteristic mass is always

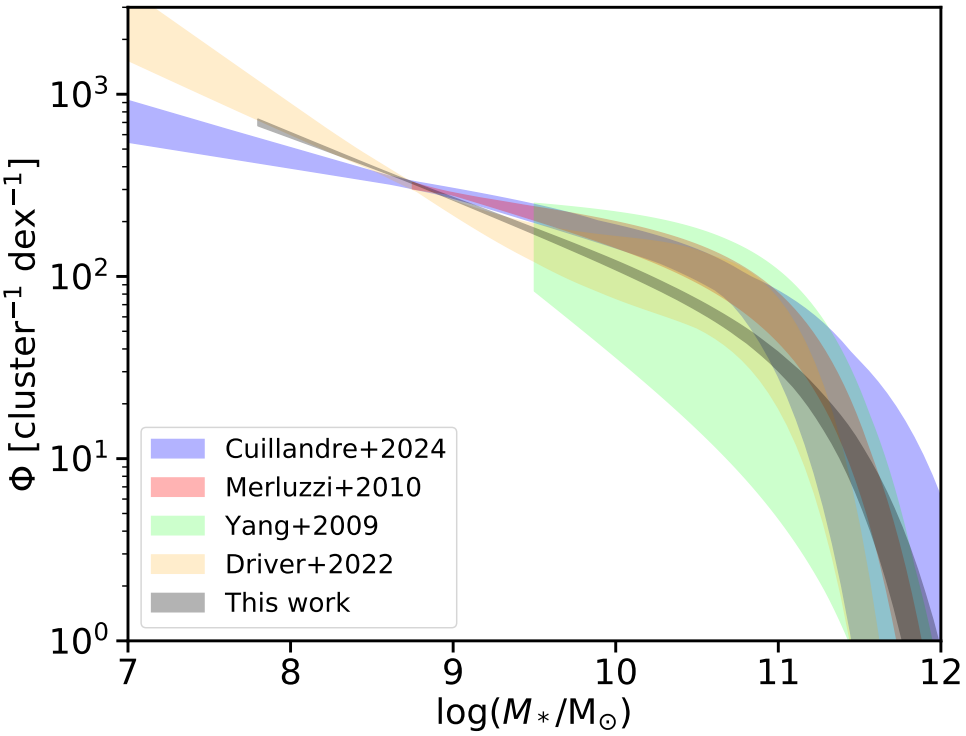


Figure 2.14: Schechter fits for our total Virgo SMF compared to three other cluster samples, as well as the GAMA field fit from Driver et al. (2022).

found to be higher in clusters than the field. While our characteristic mass is consistent with the cluster fits we compare to, typical field values are often smaller by 0.5-1 dex.

Quiescent and low-SFR fractions

While galaxies are often split into a bimodal population of star-forming and quiescent, either via a direct SFR tracer or by colour, we have isolated low-SFR galaxies from our sample to probe this transition population. We are able to isolate this sample by choosing galaxies with Hα emission from star formation that fall below the SFMS. As is seen in Fig. 2.5, the low-mass end of our sample is dominated by quiescent galaxies showing no evidence for ongoing star formation. The relative fraction of SF galaxies peaks near the middle of our stellar mass range, and the low-SFR fraction increases with increasing stellar mass.

To compare our quiescent fraction trends with other works, we first produce a sample of

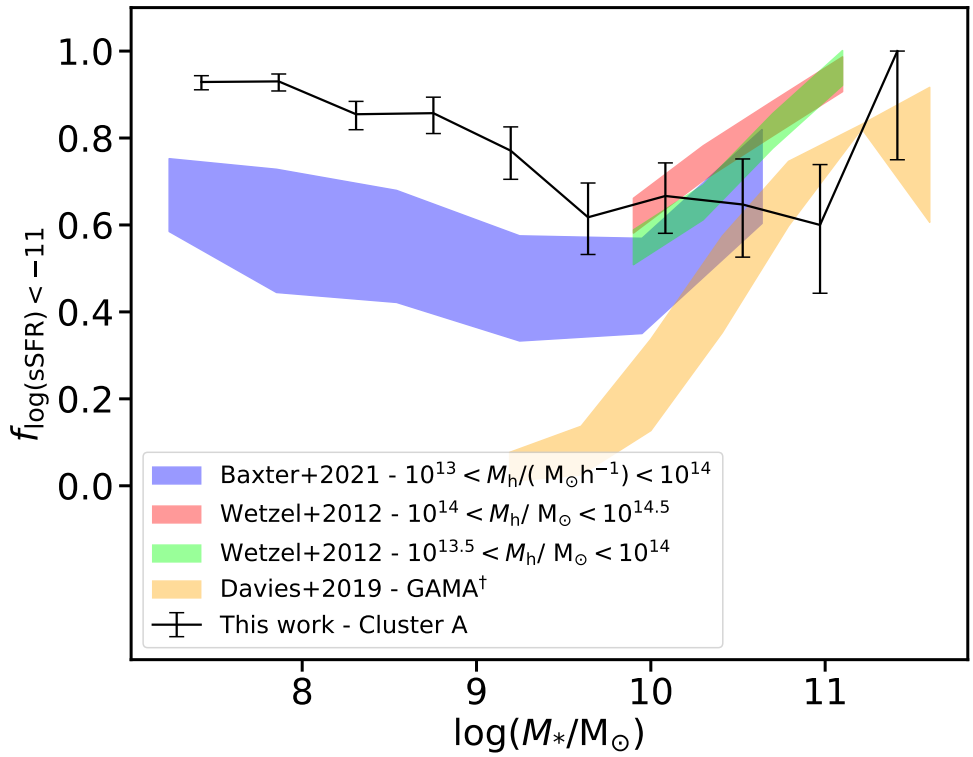


Figure 2.15: Quiescent fraction as a function of stellar mass. The black data with error bars are Virgo galaxies from Cluster A, with the quiescent sample chosen as galaxies with $\log(\mathrm{sSFR}) < -11$. The red and green shaded regions show 1σ uncertainty ranges for the quiescent fractions from Wetzel et al. (2012) for two halo mass bins: $10^{14} < M_h/\mathrm{M}_\odot < 10^{14.5}$ and $10^{13.5} < M_h/\mathrm{M}_\odot < 10^{14}$. The blue shaded region shows the satellite quiescent fractions for the halo mass range $10^{13} < M_h/(\mathrm{M}_\odot h^{-1}) < 10^{14}$ from Baxter et al. (2021). The purple region shows the range of quiescent ($\log(\mathrm{sSFR}) < -10.5$) fractions for the GAMA sample from Davies et al. (2019), where the width of the GAMA shaded region is shown to encompass both the satellite and central galaxy quiescent fractions. Wetzel et al. (2012) and Baxter et al. (2021) use $\log(\mathrm{sSFR}) < -11$ as their quiescent cut, while Davies et al. (2019) uses $\log(\mathrm{sSFR}) < -10.5$.

all galaxies belonging to Cluster A, the main cluster of Virgo (Core, Inner Ring and Outer Ring). We then re-determine a quiescent sample by taking all galaxies with $\log(\mathrm{sSFR}) < -11$ for proper comparison with other works that employ a sSFR cut (where $\mathrm{sSFR} = \mathrm{SFR}/\mathrm{M}_*$). We note that, because of the depth of our Hα data, this new quiescent sample will contain low-SFR galaxies at all stellar masses. We show the quiescent fraction of this

sample as a function of stellar mass in Figure 2.15. For comparison, we show the quiescent fractions from Wetzel et al. (2012) for two halo mass bins ($10^{13.5} < M_h/\mathrm{M}_\odot < 10^{14}$ and $10^{14} < M_h/\mathrm{M}_\odot < 10^{14.5}$; the virial mass of Cluster A is $\sim 10^{14}$ $\mathrm{M}_\odot$ based on Simionescu et al. 2017). In addition we show the satellite quiescent fractions from Baxter et al. (2021) for local massive groups with halo mass $10^{13} < M_h/(\mathrm{M}_\odot h^{-1}) < 10^{14}$. Finally, we show quiescent fractions from the GAMA survey (Davies et al., 2019), encompassing both satellite and central quenched fractions. At low stellar masses, we find our quiescent fraction is much higher than that of the field, where the field has dropped to nearly zero at $\sim 10^9$ $\mathrm{M}_\odot$. At stellar masses less than this, our galaxies are $> 80\%$ quiescent. Studies such as Geha et al. (2012) show that from $\sim 10^7$ $\mathrm{M}_\odot$ to $\sim 10^9$ $\mathrm{M}_\odot$, fully quiescent galaxies are essentially non-existent in isolated field samples. However, low mass galaxies in large, low-redshift groups display high quenched fractions as shown by the values from Baxter et al. 2021. This again may speak to the impact of pre-processing of low-mass galaxies prior to infall into massive clusters, as discussed in Section 2.5.2.

The interpretation made in Section 2.5.2 were motivated by the high fraction of quiescent galaxies seen in the Infall region of Virgo. We show on the left side of Figure 2.16 the quiescent fraction as a function of clustercentric radius compared to two relevant studies. The first is a study of clusters in the 2df Galaxy Redshift Survey (2dFGRS, Colless et al., 2001; Lewis et al., 2002), where a proxy for sSFR was used to separate SF and quiescent galaxies. The second is again the SDSS study of Wetzel et al. (2012), where we choose the halo mass bins $10^{13.2} < M_h/\mathrm{M}_\odot < 10^{14.1}$ and $10^{14.1} < M_h/\mathrm{M}_\odot < 10^{15}$. To make our stellar mass range comparable to these two studies, we restrict our sample only to galaxies with $M_* > 10^{9.7}$ $\mathrm{M}_\odot$ and choose only galaxies with $\log(\mathrm{sSFR}) < -11$. We find that for more massive galaxies, our quiescent fractions are consistent with these previous studies even beyond R_{200}. It is low-mass galaxies, then, that are driving the high quiescent fractions in the outer regions of the Virgo cluster.

On the right side of Fig. 2.16, we return to our original definition of quiescent and low-SFR galaxies and show the relative fractions of each in three bins of stellar mass as a function of clustercentric radius. For the two smaller stellar mass bins, we see less of a radial decline in quiescent fraction, indicating again that galaxies with lower stellar masses are likely quenching before first infall. Throughout the cluster we observe a typical low-SFR fraction of $\sim 10 - 20\%$, with values in certain radial bins as low as $\sim 0\%$ and as high as $\sim 50\%$. If this population is dominated by transition galaxies, then galaxies undergoing quenching can be found across the Virgo environment.

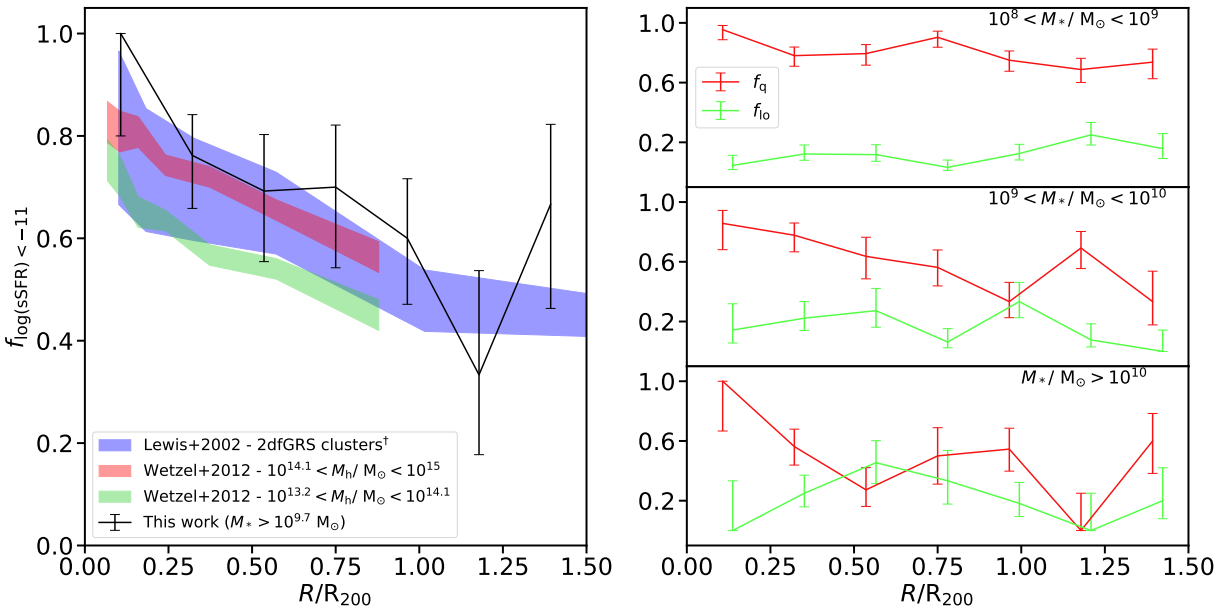


Figure 2.16: Quiescent and low-SFR fractions as a function of clustercentric distance. *Left:* The black data with error bars are for Virgo galaxies from Cluster A, with the quiescent sample chosen as galaxies with $\log(\mathrm{sSFR}) < -11$, and have limited the stellar mass range to be $M_* > 10^{9.7}$ $\mathrm{M}_\odot$ for consistency with comparison studies. The red and green shaded regions show 1σ uncertainty ranges for the quiescent fractions from Wetzel et al. (2012) for two halo mass bins: $10^{14.1} < M_h/\mathrm{M}_\odot < 10^{15}$ and $10^{13.2} < M_h/\mathrm{M}_\odot < 10^{14.1}$. The blue shaded region shows the quiescent fractions from the cluster sample of the 2dFGRS (Lewis et al., 2002). While the Wetzel et al. (2012) study uses $\log(\mathrm{sSFR}) < -11$ to isolate quiescent galaxies, the Lewis et al. (2002) study uses a proxy for sSFR based on Hα equivalent width and continuum luminosity. *Right:* Quiescent and low-SFR fractions based on our definitions from Section 2.4.2, for galaxies of Cluster A split into three different bins of stellar mass.

2.6 Summary and conclusions

Using a deep stellar mass catalogue of the Virgo cluster environment constructed with NGVS optical data, we have produced and analyzed SMFs across the Virgo environment. With deep Hα data from VESTIGE, we split our galaxies into quiescent, low-SFR and SF samples, and compared the shapes of the SMFs across the Virgo environment. In general, the Virgo cluster is dominated by a quiescent population with steep low-mass slope

while the SMFs of the low-SFR and SF populations are flatter. There are only marginal differences in the shapes of the SMFs across the Virgo environment. We summarize our key findings:

- The shape of the total SMF of Virgo is similar to other cluster studies. The low-mass slope is similar to the field, with a larger characteristic mass (Fig. 2.14). The shapes of the quiescent and SF SMFs in Virgo are significantly different from the field. The Virgo quiescent SMF has a nearly identical slope to the field SF SMF, consistent with the interpretation that the quiescent cluster population results from the quenching of SF field galaxies.

- The main body of Virgo, Cluster A, is dominated by low-mass quiescent galaxies ($f_q > 0.7$ for galaxies with $M_* < 10^9$ $M_\odot$), with a smaller number of more massive SF and low-SFR galaxies. This trend remains true in smaller substructures of Virgo such as the Clouds and Cluster B, though the relative fraction of quiescent galaxies is as low as ~ 0.4 in some mass bins (Figs. 2.6-2.11).

- The Infall region of the Virgo cluster is largely dominated by quiescent galaxies. If one assumes that this population is made up of backsplash galaxies and field galaxies on their first infall, the backsplash fractions necessary to reproduce the observed population are $> 70\%$, while simulation studies such as Haggar et al. (2020) have shown that typical backsplash fractions in this region for dynamically active clusters are $\sim 52\%$ (Fig. 2.13). This result suggests galaxies may be pre-processed outside of the Virgo cluster virial radius, either by the cluster or by group structures prior to cluster infall.

- For $M_* < 10^9$ $M_\odot$, the quiescent fractions ($\log(\mathrm{sSFR}) < -11$) as a function of stellar mass are $> 80\%$ in Cluster A This is in stark contrast to isolated field galaxies (0%), and is even higher than satellites of massive groups ($< 75\%$; Fig. 2.15). This again implies that low-mass galaxies are likely quenched partly or entirely before entering the cluster environment.

- For high-stellar mass galaxies, the quiescent fractions ($\log(\mathrm{sSFR}) < -11$) in Cluster A as a function of clustercentric distance are $\sim 60\%$, consistent with studies of other massive systems at low redshift such as Lewis et al. (2002) and Wetzel et al. (2012). At lower stellar masses, the quiescent fractions are $> 70\%$, at all clustercentric distances. In addition, there is a population of low-SFR galaxies at all stellar masses and all clustercentric radii, implying that across the cluster, there are galaxies that may be undergoing quenching of their star formation.

Although Virgo is a dynamically young cluster with a mass of only $\sim 10^{14}$ $M_{\odot}$, it is dominated by quiescent galaxies lacking star-formation, particularly at low stellar masses. This population is ubiquitous throughout the cluster and its various substructures, and is in stark contrast with the population of isolated, field galaxies. We infer that galaxy quenching is very efficient in dense environments at $z = 0$, and likely begins long before galaxies reach the virialized body of the main cluster.

Chapter 3

A Virgo Environmental Survey Tracing Ionised Gas Emission (VESTIGE) XVI. The ubiquity of truncated star-forming discs across the Virgo cluster environment

This chapter is based on the following article:
Morgan, C. R., Balogh, M. L., Boselli, A., Fossati, M. et al. 2024. A Virgo Environmental Survey Tracing Ionised Gas Emission (VESTIGE): XVI. The ubiquity of truncated star-forming discs across the Virgo cluster environment. *Astronomy & Astrophysics*, 691, A20, doi: 10.1051/0004-6361/202449225

3.1 Introduction

Galaxies in the local Universe exhibit a bimodality in terms of their colour and star formation rate (SFR). Star-forming (SF) galaxies are blue in colour and are dominated by a disc shape and features such as spiral arms where ongoing star formation occurs. Conversely, 'quiescent' galaxies are typically elliptical and red in colour, containing evolved stellar populations with little ongoing star formation. Measurements of the redshift evolution of the

stellar mass function (SMF) have shown that the population of quiescent galaxies has built up over time, indicating that galaxies transition or 'quench' from actively SF to quiescent (e.g. Faber et al., 2007). Galaxy quenching is known to be a function of mass, as the quiescent fraction is greater at the high end of the SMF in all environments and at all redshifts (Peng et al., 2010; Muzzin et al., 2013; Lin et al., 2014; Balogh et al., 2016).

Galaxies are also known to evolve as a function of their environment (Oemler, 1974; Dressler, 1980; Butcher & Oemler, 1984). Galaxies in clusters, particularly those at low redshift, exhibit lower rates of star formation (Balogh et al., 1997, 1998; Lewis et al., 2002; Gómez et al., 2003; Kauffmann et al., 2004; Baldry et al., 2006; Weinmann et al., 2006; Wetzel et al., 2012; Gavazzi et al., 2013c; Boselli et al., 2023a) and are more gas-deficient (Giovanelli & Haynes, 1985; Cayatte et al., 1990; Gavazzi et al., 2005; Cortese et al., 2011; Boselli et al., 2014a; Alberts et al., 2022) than galaxies in the field. The observed morphology of galaxies also varies by environment, with the fraction of quiescent elliptical galaxies increasing as a function of density (Dressler, 1980; Huchra et al., 1983; Goto et al., 2003). Measurements of this morphology-density relation (e.g. Dressler et al., 1997; Sazonova et al., 2020) and the SFR-density relation (e.g. Quadri et al., 2012; Cooke et al., 2016; Kawinwanichakij et al., 2017; Strazzullo et al., 2019; van der Burg et al., 2020) up to $z \sim 2$ indicate that the drivers of environmental quenching in clusters were in place at earlier epochs.

A variety of different environmentally driven mechanisms are known to quench galaxies in clusters (e.g. Boselli & Gavazzi, 2006, 2014). Galaxies can interact with each other through direct mergers, which can induce starbursts in the resulting system, alter the morphology of the merged galaxy, and drive active galactic nucleus (AGN) feedback (Barnes, 2004; Saitoh et al., 2009; Rich et al., 2011; Kelkar et al., 2020; Lotz et al., 2021). Close encounters can strip material to form tidal arms, and can cause gas to lose angular momentum and fall to the centre of the galaxy where a nuclear starburst is induced ('harassment'; Moore et al., 1996, 1998). Galaxies falling into clusters will also interact with the hot intra-cluster medium (ICM), during which ram-pressure stripping (RPS) serves to actively strip gas from the disc of the galaxy, removing the fuel necessary for sustained star formation (Gunn & Gott, 1972; Boselli et al., 2022). Additionally, infalling galaxies can undergo 'starvation' or 'strangulation' as the potential of the galactic dark matter halo becomes subdominant to the cluster potential, preventing the accretion of fresh gas (Larson et al., 1980). The existing hot gas contained within the subhalo of the galaxy may also be stripped off via ram-pressure and/or tidal forces (Balogh et al., 2000; McCarthy et al., 2008; Kawata & Mulchaey, 2008; Bekki, 2009), or prevented from cooling due to feedback. Starved galaxies passively quench as they exhaust their remaining cold gas supply.

Each quenching mechanism produces signatures that can be observed and measured to

find trends with mass and environment. For example, RPS can produce elaborate tails of stripped gas that extend beyond the optical disc (e.g. Gavazzi et al., 2001; Kenney et al., 2004; Chung et al., 2007). In some cases, star formation can occur in the stripped material, producing stars in the tails that can result in a 'jellyfish' appearance in the optical (e.g. Smith et al., 2010; Ebeling et al., 2014; Poggianti et al., 2016). Over time, RPS will lead to a truncated SF disc as all the gas is stripped from the outside in (see Boselli et al., 2022 for a comprehensive review on the effects of RPS).

In many cases, multiple mechanisms could be quenching galaxies at the same time, or in sequence (e.g. Cortese et al., 2021). Understanding the interplay of various mechanisms in the overall evolutionary picture is an area of ongoing research. For example, while the morphological signatures of RPS may be present in many galaxies, that does not necessarily imply that RPS has been solely responsible for reducing the gas content of the galaxy. A galaxy that has been pre-processed may become even more susceptible to RPS if its gas has been initially displaced by tidal interactions (e.g. Serra et al., 2023) or its gas content has been reduced by starvation.

Hα emission is a powerful tool with which to observe morphological signatures of environmental quenching mechanisms, since it traces star formation on 10 Myr timescales (e.g. Kennicutt Jr.,, 1998a). Early studies such as Moss & Whittle (1993, 2000) undertook Hα surveys of local rich clusters, observing concentrated Hα emission that suggested induced star formation due to tidal interactions, particularly for galaxies in denser environments. Gavazzi et al. (2006, 2013b) showed that Hα emission is correlated with HI gas content in galaxies, and that the specific star formation rate (sSFR) is correlated with Hubble type morphology. Koopmann & Kenney (2004) and Fossati et al. (2013) compared the sizes of SF discs measured in Hα with optical bands to show truncations in the Virgo cluster. More recently, integral field unit (IFU) spectroscopy has become a powerful tool for observing Hα emission on a spatially resolved scale across the planes of galaxies. The GASP survey (Gas Stripping Phenomena in galaxies with MUSE; Poggianti et al., 2017) is a programme that has targeted more than 100 nearby jellyfish galaxy candidates to study the kinematics and physical properties of the ionised gas being stripped from the galactic discs. With the advent of IFU spectroscopy and deep, high-resolution imaging with surveys like VESTIGE (the Virgo Environmental Survey Tracing Ionised Gas Emission; Boselli et al., 2018a), detailed Hα maps can now be observed for nearby galaxies, allowing star formation and quenching mechanisms to be studied on a spatially resolved scale.

The Virgo cluster is of particular interest to the study of environmentally driven quenching mechanisms due in part to its proximity. At a distance of 16.5 Mpc (Mei et al., 2007), Virgo is the closest massive galaxy cluster, and has been imaged on sub-kiloparsec scales with many recent surveys, including in the UV (GUViCS; Boselli et al., 2011), optical

(NGVS; Ferrarese et al., 2012), and Hα (VESTIGE; Boselli et al., 2018a). Indeed, RPS has been identified as a likely driver of environmental quenching in Virgo through many studies of individual objects and small samples of galaxies (Koopmann & Kenney, 2004; Koopmann et al., 2006; Cortese et al., 2012; Fossati et al., 2013; Chung et al., 2009; Boselli et al., 2016; Junais et al., 2022; see Boselli et al., 2022 for a review). These studies have identified tails of stripped gas and truncated discs associated with RPS. The majority of SF galaxies in Virgo are also known to be HI-deficient (Chamaraux et al., 1980; Giovanelli & Haynes, 1983; Gavazzi et al., 2005; Boselli et al., 2023a) with truncated gas discs (Cayatte et al., 1990, 1994; Chung et al., 2009; Boselli et al., 2014a; Zabel et al., 2022), indicating the presence of mechanisms to either remove gas or prevent a fresh supply of hot gas from cooling onto galactic discs.

Measuring the size of the SF disc (for example with UV, Hα, or 24 μm imaging) provides information on the radial extent of star formation, and can be compared to the disc size measured in optical bands to allow a measurement of disc truncation. This is a common method in the literature to determine the presence of an outside in quenching mechanism (e.g. Koopmann & Kenney, 2004; Cortese et al., 2012; Fossati et al., 2013; Finn et al., 2018). A popular measurement of the size of the galactic disc is the effective radius, or half-light radius.[1] The total light of the galaxy can be measured through extrapolation of the flux growth curve, or by using a low-surface brightness isophote. However, the effective radius is sensitive to the concentration of light in the galaxy; this value may be different between the SF and optical discs (e.g. Trujillo et al., 2020; Chamba et al., 2020). Taking the ratio of isophotal radii in SF and optical bands is another method to quantify truncation (e.g. Cortese et al., 2012), where the isophotal radii provide a more meaningful representation of the extent of the disc. In using a Sérsic fit to define the radial profile of a galaxy, the effective or isophotal radius are well-defined measures of size, but neither correspond to an actual edge of the disc.

Chamba et al., 2022 (hereafter C22) identified the edges of galaxies ($R_{\rm edge}$) based on visual identification of turn-off points in their stellar mass surface density and optical colour profiles. They showed that this visually identified edge corresponds to a critical stellar mass surface density that depends weakly on the integrated stellar mass of the galaxy. For massive disc galaxies ($M_* \gtrsim 10^9$ M$_\odot$), this turn-off corresponds with the edge of the SF disc, as is indicated by a sudden change in the slope of the UV surface brightness profiles. As such, the edge of the stellar disc should correspond with the edge of the SF disc for normal, SF galaxies. A follow-up work, Chamba et al., 2024 found that galaxies

[1]The measurement is often termed as the 'effective radius' when determined with a Sérsic fit to a galaxy (de Vaucouleurs, 1948; Sérsic, 1963), while 'half-light radii' typically is used when the total flux of the galaxy has been determined and used to find the radius that contains half the flux.

in the Fornax cluster have edges that occur at higher stellar mass surface density, giving rise to smaller measured disc sizes.

In addition to physical disc edges, various studies have observed other features that represent deviations from a single exponential fit to a surface brightness profile. Since the work of Freeman (1970), it has been shown that galaxy discs are often best fit by two exponential components, separated by a break, where the outer part of the disc may have a steeper (Type II) or shallower (Type III) slope than the inner part (e.g. Pohlen & Trujillo, 2006; Hunter & Elmegreen, 2006; Erwin et al., 2008; Herrmann et al., 2013, 2016; Watkins et al., 2019). These breaks are often identified in optical bands, though comparisons with SF bands (UV and Hα) show that in some cases, the breaks are more even more significant in these bands than in the optical (e.g. Herrmann et al., 2016), suggesting that these breaks may correspond to the edge of the SF disc.

In this work we look to quantify, in the Virgo cluster, the presence of galactic discs with a truncated SF component relative to the underlying optical disc. Boselli et al. (2020) identified truncated SF discs in a subset of VESTIGE galaxies through the decline in the number density of HII regions. Other previous studies of truncated SF discs in Virgo were limited to massive galaxies (e.g. Koopmann & Kenney, 2004; Boselli et al., 2022) or used size measurements such as the effective radius that do not explicitly trace the edge of the SF disc (e.g. Fossati et al., 2013). In our approach, we take advantage of the unique NGVS and VESTIGE data to analyse sSFR profiles and identify a physically meaningful edge to the SF disc. By comparing the edge of the SF disc to the expected disc size based on a comparable field sample, we can quantify how truncated the SF discs are in the Virgo cluster. With our cluster-wide sample that includes all SF galaxies within the cluster virial radius and a sample beyond, we look to provide insights into the different possible quenching pathways that may produce the observed distribution of truncated discs.

A description of the data used in this work is outlined in Section 3.2. In Section 3.3 we outline the methods used to measure SF disc edges. Section 3.4 presents the main results of this paper, which are discussed in context in Section 3.4.3. We summarise and conclude in Section 3.5. Where necessary, such as in the modelling of Section 3.4.3, we adopt a flat ΛCDM cosmology with $H_0 = 70$ km s^{-1} Mpc^{-1} and $\Omega_m = 0.3$.

3.2 Observations and data reduction

This study focusses on the Virgo cluster, the nearest massive cluster at a distance of 16.5 Mpc (Mei et al., 2007). The main cluster of Virgo (Cluster A) is a virialised system

comprised of mostly early-type quiescent galaxies (including dwarfs and massive ellipticals), while several smaller substructures merging into the cluster contain more SF systems (Binggeli et al., 1987; Gavazzi et al., 1999; Solanes et al., 2002; Boselli et al., 2014b). Early studies of the dynamics of Virgo derived a mass profile for the cluster with $R_{200} = 1.55$ Mpc (e.g. McLaughlin, 1999). However, recent work deriving the mass profile from X-ray observations have measured a Navarro-Frenk-White (NFW; Navarro et al. 1996) profile with $R_{200} = 0.974$ Mpc and $M_{200} = 1.05 \times 10^{14}$ $M_\odot$ (Simionescu et al., 2017). These latter values will be adopted throughout this work.

3.2.1 NGVS imaging

The Next Generation Virgo Survey (NGVS) is an optical survey of the entire Virgo cluster out to 1.55 Mpc (Ferrarese et al., 2012). Using MegaCam on the Canada-France-Hawaii Telescope (CFHT), NGVS imaged a 104 deg^2 footprint of the Virgo cluster in the u^*, g, i and z bands (and partially in the r band). In this work, we make use of the g-band images from NGVS to determine radial $g-r$ colour profiles for galaxies observed with the VESTIGE survey (with r-band imaging coming from VESTIGE). Total integration times of 3170 s were used to reach point source depths of 25.9 mag (10σ) and surface brightness (SB) depths of 29 mag arcsec^{-2} in the g-band.

CFHT MegaCam consists of an array of 40 CCDs with pixel scale of $0.187''$ pixel^{-1}, and observations were carried out under seeing conditions of $< 1''$ (FWHM). The NGVS images used in this work were processed using Elixir-LSB, a pipeline designed for NGVS that employs specific methods for detection of low surface brightness features (Ferrarese et al., 2012). Photometric calibration and astrometric correction of the data follows the MegaCam procedures detailed in Gwyn (2008).

3.2.2 VESTIGE imaging

In addition to g-band images from NGVS, this work makes use of images obtained for the VESTIGE survey. VESTIGE is a blind, narrow-band (NB) Hα survey covering 104 deg^2 of the Virgo cluster following closely the footprint defined by NGVS. Imaging was carried out with MegaCam on CFHT using the NB MP9603 filter ($\lambda_c = 6591$ Å; $\Delta\lambda = 106$ Å) as well as the broadband r filter. At the low redshift of Virgo ($-300 \leq v_{\rm hel} \leq 3000$ km s^{-1}), the NB filter contains the Hα Balmer line at $\lambda = 6563$ Å as well as the two [NII] lines at $\lambda = 6548, 6583$ Å. Integration times of 2 hours in the NB filter have been used to achieve depths of $f(\mathrm{H}\alpha) \simeq 4 \times 10^{-17}$ erg s^{-1} cm^{-2} at 5σ for point sources and $\Sigma(\mathrm{H}\alpha) \simeq$

Substructure	RA deg	DEC deg	Radius deg	Vel range km/s	Distance Mpc	$\langle v \rangle$ km s^{-1}	σ km s^{-1}	Central galaxy	# of galaxies
Cluster A	187.71	12.39	5.383	< 3000	16.5	955	799	M87	182
Cluster B	187.44	8.00	3.334	< 3000	23	1134	464	M49	115
Cluster C	190.85	11.45	0.7	< 3000	16.5	1073	545	M60	5
W Cloud	185.00	5.80	1.2	$1000 < v < 3000$	32	2176	416	NGC 4261	18
W′ Cloud	186.00	7.20	0.8	< 2000	23	1019	416	NGC 4365	17
M Cloud	183.00	13.40	1.5	$1500 < v < 3000$	32	2109	280	NGC 4168	25
LV Cloud	184.00	13.40	1.5	< 400	16.5	85	208	NGC 4216	22

Table 3.1: Properties of Virgo cluster substructures (taken from Boselli et al. 2023b)

2×10^{-18} erg s^{-1} cm^{-2} arcsec^{-2} (1σ after smoothing the data to $\sim 3''$ resolution) for extended sources. r-band exposures are 12 minutes, achieving a point source depth of 24.5 mag (5σ) and a SB limit of 25.8 mag arcsec^{-2} (1σ for scales comparable to the size of structures in target galaxies, $\sim$ 30 arcsec). At the time of writing, the survey is 76% complete, with observations having been taken in excellent seeing conditions (FWHM = $0.76'' \pm 0.07''$). At the distance of Virgo, $1''$ is equal to 80 pc. The full observing strategy is discussed in detail in Boselli et al. (2018a).

Stellar continuum subtraction of the NB images is described in Boselli et al. (2019) and is done using a combination of the r-band images and $g - r$ colours.

3.2.3 Galaxy identification

Hα emitting sources in VESTIGE images were identified as described in Boselli et al. (2023a). We summarise the method here:

1. Counterparts to galaxies in the Virgo Cluster Catalogue (VCC; Binggeli et al. 1985) with redshifts in the range of Virgo (307 objects).
2. Counterparts of the HI detections from the ALFALFA survey (Giovanelli et al., 2005) with redshifts in the range of Virgo (37 more objects).
3. Counterparts of galaxies identified as Virgo members based on the scaling relations determined using NGVS data in Ferrarese et al. (2012, 2020) and Lim et al. (2020) (31 more objects).
4. Four bright galaxies outside the VCC and NGVS footprints with extended Hα emission.
5. Five additional line emitter objects not previously identified, but whose extended emission suggests they are local bright compact dwarfs.

Thus, the total number of Virgo members with Hα emission in the VESTIGE survey is 384. spanning a stellar mass range $10^6 M_\odot < M_* < 10^{12} M_\odot$. The morphology distribution of the sample is 61% late-type spirals, 5% early-type/lenticular, 20% late-type dwarf (including blue-compact dwarfs), 9% early-type dwarf, and 5% with unclassified morphologies.

Galaxy membership in subcluster regions

The Virgo cluster is made up of several subclusters and clouds currently in the process of merging into Cluster A, which features M87 at its centre. We make use of the most recent information of the Virgo substructures as in Boselli et al. (2023b), which we summarise in Table 3.1. The distances to the substructures are based on measurements from Gavazzi et al. (1999) who employed Fundamental Plane and Tully-Fisher relations for redshift-independent distance determination. However, for consistency with Boselli et al. (2023b) and other works from the VESTIGE collaboration, we use a distance of 16.5 Mpc (Mei et al., 2007) for Clusters A and C and the Low-Velocity cloud instead of 17 Mpc which was used in previous studies (Gavazzi et al., 1999). Additionally, a sole galaxy (VCC 357) has a measured velocity of 3008 km s^{-1}, which places it outside the Virgo range of -300 km $s^{-1} \leq v_{\rm hel} \leq 3000$ km s^{-1}. However, we consider VCC 357 to be a Virgo member, following Boselli et al. (2023b).

The radii in Table 3.1 for Clusters A and B are R_{200} values derived in McLaughlin (1999) and Ferrarese et al. (2012); we consider these values upper limits on the virial radii and use them only to assign galaxies to their likely subclusters. Galaxies are assigned potential membership to substructures based on 2D position and radial velocity information following the argument of Boselli et al. (2014b) and in consistency with Boselli et al. (2023b). In overlapping regions, galaxies are assigned to the smaller substructure, except in the overlap between Clusters A and B where galaxies are assigned based on proximity to the centres of the subclusters.

3.2.4 Supplementary data

Stellar masses

Stellar masses were also derived in Boselli et al. (2023a), and we briefly highlight the process here. Spectral energy distributions (SEDs) were fit using the Code Investigating GALaxy Emission (CIGALE; Boquien et al. 2019). A delayed star formation history (SFH) with a recent burst or quench was used, along with Bruzual & Charlot (2003) stellar population synthesis (SPS) models and a Chabrier (2003) initial mass function (IMF). SEDs were fit to multi-frequency observations including (where available) GALEX far-UV and near-UV bands, NGVS u, g, r, i and z bands (or SDSS magnitudes where needed; Kim et al. 2014), WISE 22 μm and *Herschel* at 100, 160, 250, 350 and 500 μm. The resulting stellar masses have uncertainties < 0.15 dex, with a mean uncertainty of 0.07 dex. Results were compared

with SED fitting done on NGVS data using PROSPECTOR (Johnson et al., 2021), with excellent agreement found.

HI-deficiency

HI-deficiency is defined as the logarithmic difference between the observed mass of HI gas in a galaxy compared to the expected HI mass for isolated galaxies of similar size and morphology. The process for determining the HI-deficiency parameter is detailed in Boselli et al. (2023a). The calibration used is from a local sample of ~ 8000 galaxies from the work of Cattorini et al. (2023). Where available, deep observations from the GOLDMine database (Gavazzi et al., 2003) were used to determine HI mass, and otherwise ALFALFA (Haynes et al., 2018) data was used. The scatter in the calibration corresponds to ~ 0.26 dex, and galaxies with HI-deficiency ≥ 0.4 ($\sim 1.5\sigma$) are considered with high probability to be gas deficient, perturbed systems.

3.3 Methods

The pipeline used for measuring SF discs in VESTIGE galaxies is outlined in the following. Throughout this section, we use VCC 865 (NGC 4396) as a case study and refer back to Fig. 3.1 to exemplify each step of the pipeline. VCC 865 has a stellar mass of $10^{9.4}\mathrm{M}_{\odot}$. It has a SFR that places it on the SFMS, yet appears to be somewhat gas deficient, and is likely on first infall into the cluster based on its location in phase space. For these reasons, we use VCC 865 as an illustrative example of a galaxy that is most relevant to our analysis, as further discussed in Sects. 3.4 and 3.4.3.

3.3.1 Extraction of radial profiles

Our analysis relies on using radial sSFR profiles to determine the edge of the SF disc. The sSFR is determined using SFR and stellar mass surface density (Σ_{SFR} and Σ_{*}) profiles, which we obtained using g, r, and Hα surface brightness profiles.

Creating object masks

In order to properly extract SB profiles of our target galaxies, we needed to mask any contaminating stars or background galaxies. For each galaxy in VESTIGE, we cut a

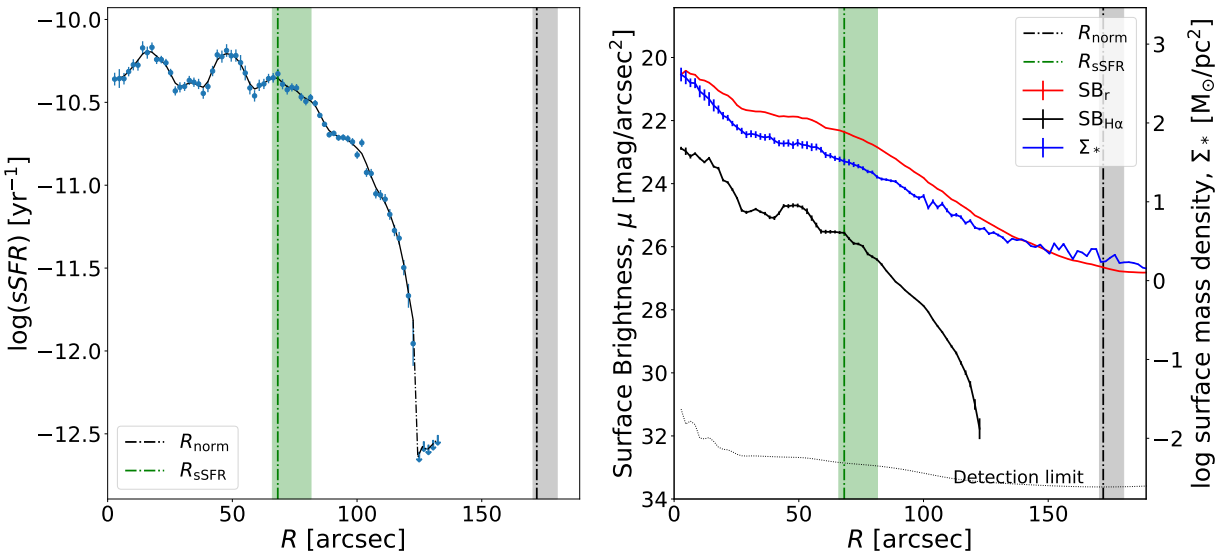


Figure 3.1: Radial profiles for VCC 865 (NGC 4396). *Left*: sSFR profile (blue data points) with a smoothed profile shown as a black curve. The next five upper limits (where no Hα is detected but stellar mass is) are shown as blue arrows, connected by a dot-dashed line. *Right*: Surface brightness profiles for Hα NB (black) and r-band emission (red), along with the Σ_* profile (blue). The dashed black profile shows the detection limit for the Hα profile. In both panels, the green vertical line shows the median SF disc edge, $R_{\rm sSFR}$, and the shaded green band the uncertainty range based on the 16$^{\rm th}$ and 84$^{\rm th}$ percentiles computed using a Monte Carlo simulation with 1000 iterations. The vertical black line shows the expected edge, $R_{\rm norm}$, of the galaxy and the shaded grey band uncertainty range based on the 16$^{\rm th}$ and 84$^{\rm th}$ percentiles of the Monte Carlo simulation.

postage stamp around the object with a size of $10\,r_{\rm e,i}$ on each axis, where $r_{\rm e,i}$ are i-band effective radii coming from Sérsic profile and growth curve fitting performed on NGVS images (in the few case where $r_{\rm e,i}$ is unavailable from NGVS, we use $r_{\rm e,i} = 60''$). We used the Python package PHOTUTILS (Bradley et al., 2021) to create object masks for our postage stamps. Since our galaxies span a wide range of sizes and luminosities and our data quality and depth pick up small structures and low-SB features, we found a single masking run would not suffice.

We chose to employ a 'hot, cool, cold' masking routine based on Galametz et al. (2013) and Sazonova et al. (2021). First, the images were passed through a 2D top-hat smoothing kernel with a size equal to $0.2R_{\rm e,i}$. For the 'hot' run, we used a very high detection threshold, small minimum area and a small amount of deblending to identify the brightest peaks in the image. The 'cool' run followed, where we used a low detection threshold, large area and strong deblending. Using these first two runs, we masked 'cool' regions that are far from the galaxy centre, and masked nearby 'cool' regions where a 'hot' peak was identified (this attempts to mask areas around saturated stars, for example), except for the central hot peak associated with the galaxy. Finally, we performed the 'cold' run, where we used the mask created in the previous step and performed one more detection run using a low threshold, no deblending and a minimum area of 20 pixels.

We found that this routine worked well based on a visual inspection of all masks. In certain cases where over- or under-deblending occurred, we re-ran the masking routine, altering certain parameters as necessary until a good mask was produced. We show a table of the PHOTUTILS parameters used in each run in Appendix B.1. For a more detailed explanation of the 'hot, cool, cold' masking technique, we refer the reader to Sazonova et al. (2021).

Radial surface brightness extraction

The next step in our analysis was to extract surface brightness profiles of VESTIGE galaxies in the g, r and Hα bands ($\mu_{\rm r}, \mu_{\rm g}$ and $\mu_{\rm H\alpha}$). We used the non-parametric surface brightness extraction pipeline AUTOPROF (Stone et al., 2021). AUTOPROF is based on the work of Jedrzejewski (1987) but with addition of machine learning regularisation techniques. The software provides a full pipeline for background fitting, centroid finding, masking and surface brightness extraction, and is proven to be proficient is extraction of low-surface brightness features. We used the deep g-band images in our initial AUTOPROF run, and set the object centre to be the same as the optical positions used in Boselli et al. (2023a), determined with NGVS (Ferrarese et al., 2012). We ran AUTOPROF with a fixed isoband width of 10 pixels (1.87″); full width of band) and sampled linearly in increments of 10

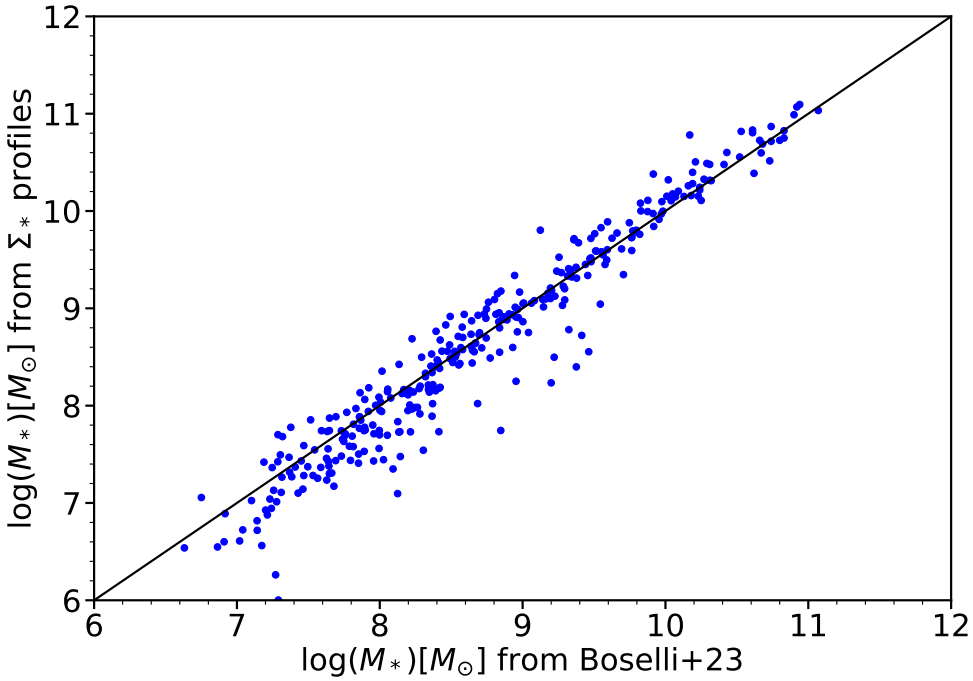


Figure 3.2: Recovered total stellar masses obtained by numerically integrating Σ_* profiles up to $R_{\rm norm}$ compared to stellar masses obtained by Boselli et al. (2023a) through SED fitting.

pixels, applying the masks created, as is described in Sect. 3.3.1. AUTOPROF varies the ellipticity and position angles of the isophotes with each radial step as the shape of the galaxy changes. Since the structure of SF galaxies is complex, especially with high-resolution data, varying the ellipticity and position angle in this way provides a more accurate measure of the galaxy shape in each radial bin. We then used the AUTOPROF forced photometry method to force the extracted g-band profile onto the r-band and Hα images in order to obtain the same radial sampling, ellipticities and position angles in all three bands.

In the right panel of Fig. 3.1 we show radial SB profiles for the r-band in red and the NB Hα in black. The dotted black line shows the Hα detection limit based on the noise in the image and the size of our sampled annuli. Uncertainties on surface brightness values are computed by AUTOPROF dividing the inter-percentile range (between the 16^{th} and 84^{th} percentiles) by $2\sqrt{N}$ where N is the number of pixels contributing to the SB measurement.

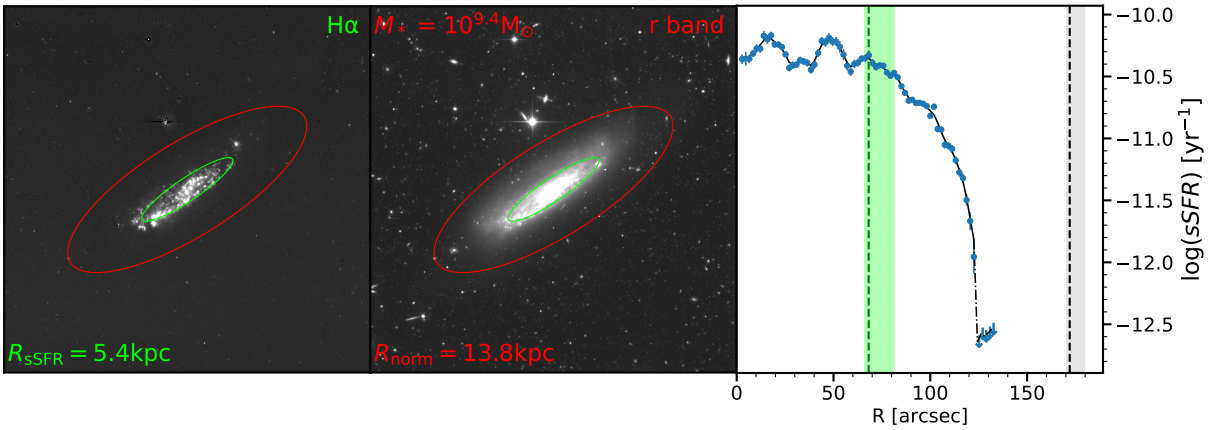


Figure 3.3: Continuum-subtracted Hα emission (*left*), r-band optical emission (*centre*), and sSFR profile (*right*) for VCC 865 (NGC 4396). In the left and centre postage stamps, the green ellipse outlines $R_{\rm sSFR}$ while the red ellipse outlines $R_{\rm norm}$. On the sSFR plots (*right*), we show $R_{\rm sSFR}$ and its associated uncertainty range as a green vertical line and band, and $R_{\rm norm}$ and its uncertainty range as a grey vertical line and band. Also included are the upper limits (down arrows) in the next five radial bins in which Hα is not detected (but stellar mass is); this represents the upper limit to the sSFR based on the Hα detection limits.

Stellar-mass surface density profiles

To obtain Σ_* profiles, we turned to the mass-to-light versus colour relations (MLCRs) calibrated in Roediger & Courteau (2015). These calibrations provide linear relations between colour and mass-to-light ratio $(M_*/L)_\lambda$ for a given waveband, λ, based on either Bruzual & Charlot (2003) or Conroy et al. (2009) (FSPS) stellar population synthesis (SPS) models. It follows that

$$\log\left(M_*/L\right)_\lambda = m_\lambda \times (\text{colour}) + b_\lambda. \tag{3.1}$$

We chose to use $\lambda = r$, $g-r$ colour and the Bruzual & Charlot (2003) SPS models with a Chabrier (2003) IMF, so $m_\lambda = 1.629$ and $b_\lambda = -0.792$ (see Table A1 of Roediger & Courteau 2015). After calculating $\log\left(M_*/L\right)_\mathrm{r}$ at each radial step from the g, and r-band SB profiles, we transformed our r-band SB profile into Σ_* using

$$\log\Sigma_* = \log\left(M_*/L\right)_\mathrm{r} + 0.4(m_{\mathrm{abs},\odot,\mathrm{r}} - \mu_\mathrm{r}) + 8.63, \tag{3.2}$$

where $m_{\mathrm{abs},\odot,\mathrm{r}} = 4.64$ (Willmer, 2018) and Σ_* has units of $\mathrm{M}_\odot/\mathrm{pc}^2$. The right panel of Fig. 3.1 shows the Σ_* profile for VCC 865 in blue, using the secondary y axis on the right.

While Eq. 3.2 provides a convenient measure of stellar mass, it does not account for variations in dust content amongst individual galaxies. Larger-than-average dust leads to an underestimated luminosity, biasing the mass low. This is partially mitigated by the fact that the larger dust content also reddens the light, and therefore increases the mass-to-light ratio inferred from observed colours. The net effect is that there is a small, systematic uncertainty in our stellar mass profiles. Based on radial dust attenuation profiles from the Calar Alto Legacy Integral Field Area (CALIFA: Sánchez et al. 2012; González Delgado et al. 2015) and Mapping Nearby Galaxies at Apache Point (MaNGA: e.g. Bundy et al. 2015; Goddard et al. 2017; Greener et al. 2020), we expect that, in the most extreme cases, the radial variation in a dust profile is ± 0.5 mag from the weighted average. Propagating this effect through Eqs. 3.1 and 3.2 shows that the attributed uncertainty on $\log\left(\Sigma_*\right)$ is $\lesssim 0.3$ dex.

As a consistency check of our Σ_* profiles, we numerically integrated the Σ_* profiles out to R_norm (as defined in 3.3.2) to obtain the total stellar mass for the galaxy, and compared the results to the stellar masses obtained from SED fitting by (Boselli et al., 2023a), finding good agreement, as is shown in Fig. 3.2. The mean difference in log-log space between our recovered stellar mass value and that measured in Boselli et al. (2023a) is 0.02 with a scatter of 0.21 after removing 3σ outliers. Our Σ_* profiles are corrected for inclination such that each profile describes a face-on galaxy, allowing consistent determination of galaxy edges based on critical Σ_* value. We describe the inclination correction in Appendix B.2.

Star formation rate profiles

To transform Hα SB profiles into SFR surface density ($\Sigma_{\rm SFR}$) profiles, we used the calibration of Calzetti et al. (2010) (which assumes solar metallicity and constant SFR) modified to include a Chabrier IMF (Chabrier, 2003), as in Boselli et al. (2023a). This model produces the relation

$$\mathrm{SFR}\,[\mathrm{M}_\odot\,\mathrm{yr}^{-1}] = 5.01 \times 10^{-42} L(\mathrm{H}\alpha)\,[\mathrm{erg\,s}^{-1}]. \tag{3.3}$$

Hα luminosities were determined based on the distance to the subcluster regions to which each galaxy belongs, based on the classifications in Section 3.2.3. We did not apply corrections for internal dust attenuation or [NII] contamination. Global corrections would not alter the shape of the radial profiles being studied, and deriving spatially resolved dust attenuation curves is beyond the scope of this work. As a check that dust corrections are not necessary for our results, we applied spatially resolved attenuation corrections ($A_{\rm H\alpha}$ as a function of radius) from CALIFA (Sánchez et al., 2012; González Delgado et al., 2015) and MaNGA (e.g. Bundy et al., 2015; Goddard et al., 2017; Greener et al., 2020) to a subset of our galaxies and re-ran our algorithm for finding $R_{\rm sSFR}$. We found no changes in our measured $R_{\rm sSFR}$, showing that typical dust gradients would have no effect on our measured values.

3.3.2 Quantifying the degree of truncation

We measured the edges of the SF discs of VESTIGE galaxies by identifying a turn-off point in their sSFR profiles, as is described in detail below (Sect. 3.3.2). In order to determine how truncated VESTIGE SF discs are relative to the field, we would ideally measure the edges of SF discs from an isolated field sample matched on colour and stellar mass. However, the VESTIGE sample does not extend beyond the Virgo cluster environment, and existing large Hα field samples have comparatively shallow depths. Instead, we compared our SF disc sizes to the expected sizes of discs based on the field sample of C22. At least for massive galaxies on the SFMS, C22 show that the optical edge corresponds to the edge of the SF disc, evidenced by breaks in the UV profile. We describe this process in more detail in Sect. 3.3.2.

Measuring the edge of the star-forming disc

We take inspiration from the methods of C22 who determined the edges of galactic discs by looking for breaks in surface brightness and optical colour profiles. Combining our

constructed SFR and stellar mass density profiles, we calculated specific star formation rate (sSFR) profiles determined by

$$\mathrm{sSFR}(r) = \frac{\mathrm{SFR}(r)}{\Sigma_*(r)}. \tag{3.4}$$

Uncertainties on the sSFR profiles were determined by compounding the uncertainties associate with the SFR and Σ_* profiles. Because the Σ_* profiles are so precisely defined, the uncertainties on the sSFR values are typically small relative to even local variations in the sSFR profile.

For disc galaxies on the SF main sequence (SFMS), sSFR profiles are shown to be flat for galaxies with $M_* < 10^{10.5}$ $\mathrm{M}_\odot$ (the majority of our sample), with central suppressions in massive SF galaxies (e.g. Belfiore et al. 2018). This makes it straightforward to identify a drastic change in the shape of the profile, which signifies a change in the SFR distribution relative to the underlying stellar mass distribution. This means that features such as inner disc breaks will not be captured unless they correspond to a SF disc edge, as desired.

We then defined R_{sSFR} as the last local maximum in the sSFR profile before it drops off, ignoring small peaks that may occur while the sSFR profile is dropping off. Because VESTIGE imaging has high-resolution, our profiles are sensitive to small structures across the galaxy. We chose to smooth our profiles with a 1D Gaussian filter with $\sigma = 1$ to reduce the risk that a peak due to small-scale structure is determined to be the turn-off point. In certain extreme cases, galaxies were found to have centralised star formation when visually inspected. This observation results in a very truncated disc according to our criteria, though the sSFR profile may not have any detectable local maxima. Thus, we added a condition in our algorithm to check if the sSFR profile falls by at least 1 dex over the range of radii for which sSFR values are measured. If this is the case, we identified the smallest radial value as the edge of the SF disc (R_{sSFR}= 2.805″).

In Fig. 3.1, R_{sSFR} is shown with its associated uncertainty range (Sect. 3.3.2) as a green band and dashed green line. In this example, R_{sSFR} clearly corresponds to a the location where a sharp decline in the sSFR profile begins. While there is still non-negligible star formation beyond this radius, the large change in slope represents a well-defined edge. We show the equivalent of Fig. 3.1 for eight total galaxies of varying stellar mass in Fig. B.7. In some galaxies (e.g. first example in Fig. B.7) the drop in sSFR is even more severe, with no detectable star formation beyond R_{sSFR}.

There exists in the literature many different methods for detecting features such as disc breaks that in some cases may correspond with the SF disc edges that we measure (e.g. Hunter & Elmegreen, 2006; Herrmann et al., 2013, 2016). While beyond the scope of

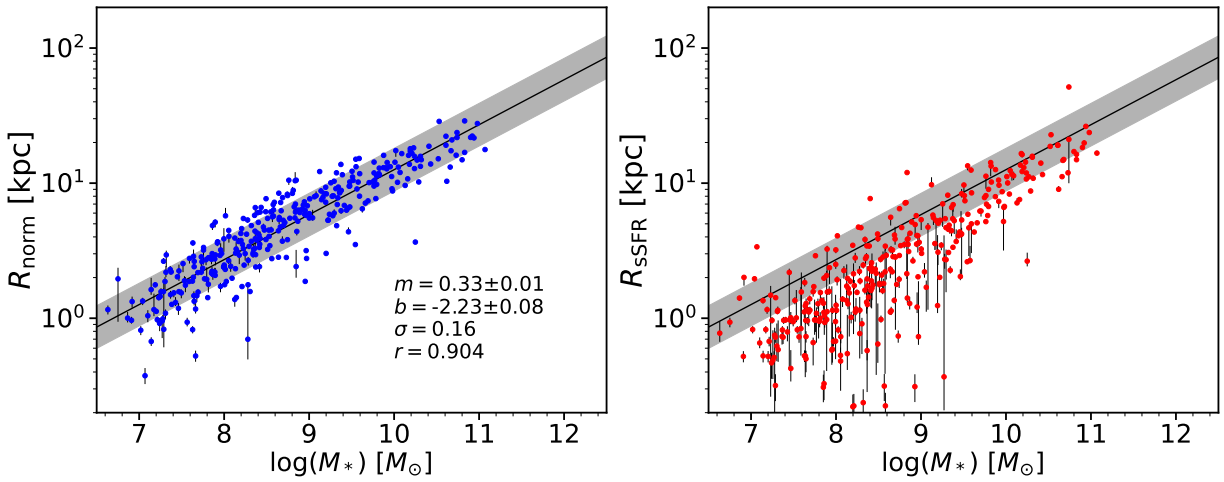


Figure 3.4: Size-stellar mass relations. *Left*: Size-stellar mass relation for galaxies with identified $R_{\rm norm}$. We fit a linear relation to the data and show that a slope of $m = 0.34 \pm 0.01$ is measured, consistent with C22. The shaded grey region shows the 1σ scatter in the linear relation. *Right*: Size-stellar mass relation using $R_{\rm sSFR}$, showing the linear fit to the $R_{\rm norm}$-mass relation.

this paper, a study comparing the features identified by these different methods and the physical interpretations of each would be an interesting future work.

Determining the expected edges of galaxies

We wished to define an 'expected' edge for isolated counterparts to our cluster galaxies. We wanted to define this edge in a way that is insensitive to properties of the Virgo galaxies, such as colour profiles, which may be affected by environment. Therefore, we defined $R_{\rm norm}$, the edge of the optical disc for an unperturbed galaxy of a given stellar mass, by first fitting a piecewise function to the $\Sigma_*(R_{\rm edge})$ versus M_* relation from C22 to find the critical Σ_* value for a galaxy of a given stellar mass. This function is

$$\Sigma_*(R_{\rm edge}) = \begin{cases} 0.6, & \log(M_*) < 9.6\ {\rm M}_\odot \\ 10^{(0.3\log(M_*)-3.1)}, & \log(M_*) \geq 9.6\ {\rm M}_\odot \end{cases}, \tag{3.5}$$

where Σ_* has units of $\rm M_\odot\ pc^{-2}$. Using inclination-corrected Σ_* profiles, we determined $R_{\rm norm}$ by finding the point at which the profile drops below the threshold Σ_* value. In

Fig. 3.1 we show $R_{\rm norm}$ as a black line with a grey band for its uncertainty. Figure 9 of Chamba et al. 2022 shows the ratio between $R_{\rm edge}$ to the effective radius as a function of stellar mass. The ratio is ~ 4 for all stellar masses but contains significant scatter, stemming from the tighter size-mass relation that is produced when using $R_{\rm edge}$.

Quantifying uncertainties

The measurement of $R_{\rm sSFR}$ is sensitive to the noise in the sSFR profile, the radial bin size, and the presence of small local maxima in the sSFR profile. Similarly, $R_{\rm norm}$ is sensitive to the noise in the Σ_* profile and the radial bin size. To quantify the uncertainties in these measurements, we performed a Monte Carlo simulation with 1000 iterations for each galaxy. During each iteration, we drew sSFR values for each radial bin from a Gaussian centred on the calculated values with a scale equal to the measured noise. We then ran the algorithm for finding the turn-off point, as is described in Sect. 3.3.2, and drew the final value for $R_{\rm sSFR}$ from a uniform distribution spanning the width of the radial bin. For each iteration, we also drew the Σ_* values in each radial bin from a Gaussian centred on the measured value and with a width equal to the noise. The Σ_* threshold value has an associated uncertainty from our piecewise fit to the C22 relation, so we also drew that value from a Gaussian distribution centred at the measured value with a width equal to the uncertainty. We then determined $R_{\rm norm}$, which we again drew from a uniform distribution equal to the width of the radial bin. With 1000 values for both $R_{\rm sSFR}$ and $R_{\rm norm}$, we had 1000 values for the ratio between the two and chose the accepted value to be the median and used the $16^{\rm th}$ and $84^{\rm th}$ percentile values as the upper and lower limits on the error.

Fig. 3.3 shows Hα and r-band imaging for VCC 865, with ellipses outlining $R_{\rm sSFR}$ and $R_{\rm norm}$. We show eight total galaxies spanning a range of stellar masses in Fig. B.8. The ellipticities and position angles used for these ellipses are the local values determined by AUTOPROF at those radial points. On the right-hand side of the postage stamps are the sSFR profiles for these galaxies, again highlighting $R_{\rm sSFR}$ and $R_{\rm norm}$. On the sSFR plots, we have included the upper limits of sSFR (based on Hα detection limits) for the next five radial bins in which Hα is not detected (but stellar mass is). This helps to highlight cases where, even in the absence of an obvious local peak to define $R_{\rm sSFR}$, an edge is still clearly present.

Figs. B.7 and B.8 display the variety of shapes that sSFR profiles exhibit due to local peaks of star formation or off-centre star formation, and show the success of our algorithm at detecting a physical $R_{\rm sSFR}$ in each of these cases. This success is validated by the green ellipses on the continuum-subtracted Hα images, which capture the Hα emission of the galaxies very well.

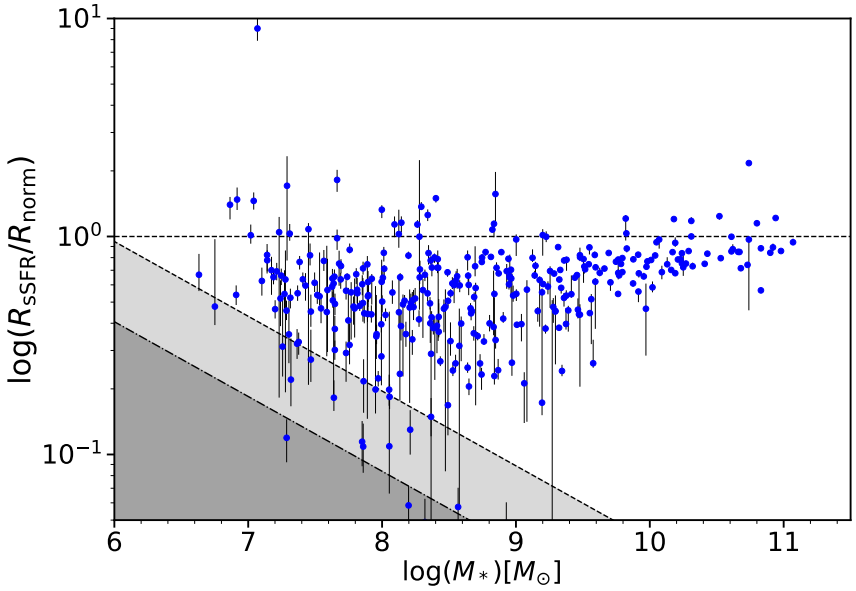


Figure 3.5: $R_{\rm sSFR}/R_{\rm norm}$ as a function of stellar mass. The two shaded grey regions show limits on the measurements of $R_{\rm sSFR}/R_{\rm norm}$. We have excluded any galaxies where the sSFR profile spans fewer than three data points, so the dashed black line has $R_{\rm sSFR} = 6.545''$. In principle, any sSFR profile with more than three data points could still have a truncation at the first data point, so the dash-dotted line has $R_{\rm sSFR} = 2.805''$. In both cases, $R_{\rm norm}$ is determined from the size mass relation in Fig. 3.4 at a distance of 16.5 Mpc.

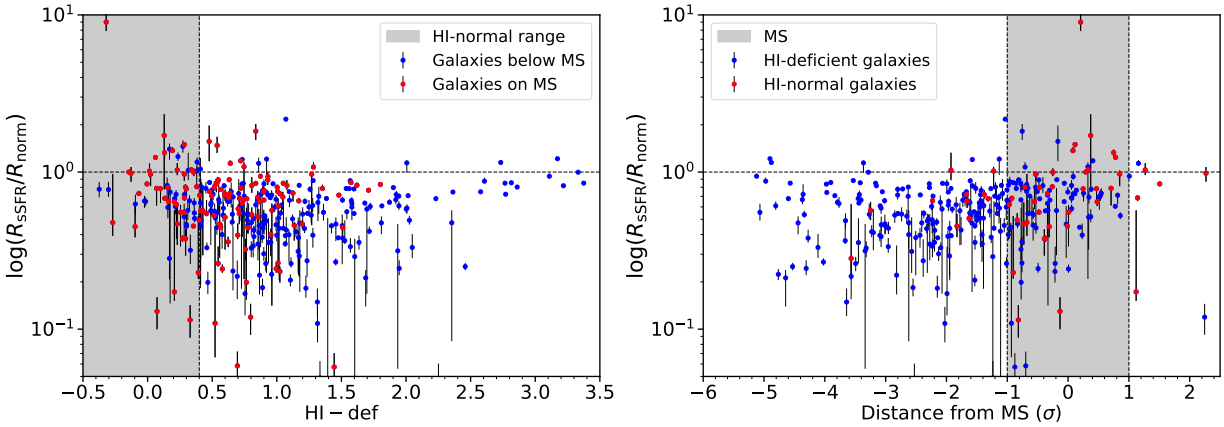


Figure 3.6: $R_{\rm sSFR}/R_{\rm norm}$ against star formation indicators. *Left*: $R_{\rm sSFR}/R_{\rm norm}$ as a function of HI-deficiency, with galaxies located on or above the SFMS shown in red and galaxies below the SFMS shown in blue. The range of HI-normal galaxies is shaded. *Right*: $R_{\rm sSFR}/R_{\rm norm}$ as a function of distance from the SFMS, with HI-normal galaxies shown in red and HI-deficient galaxies shown in blue. The SFMS is shown as a shaded region.

3.3.3 Final sample of galaxies

The full VESTIGE sample consists of 384 Virgo galaxies with Hα emission. We have removed a subset of galaxies from our sample based on the following criteria:

- Three massive elliptical galaxies with Hα emission (M84, M86, M87)
- Six additional faint galaxies for which the AUTOPROF routine did not produce good surface brightness profiles
- 22 additional galaxies with fewer than three data points in their measured sSFR profile
- 18 additional galaxies for which $R_{\rm sSFR}$ is clearly unphysical based on inspection of radial profiles (Appendix B.3)

In total, we have removed 49 galaxies, leaving us with a sample size of 335 down to $M_* \simeq 10^7 {\rm M}_\odot$.

3.4 Results

3.4.1 Galaxy size as a function of stellar mass

We first consider the size-stellar mass relation of our sample using $R_{\rm norm}$ and $R_{\rm sSFR}$ as our measurements of size, shown in Fig. 3.4. This puts our $R_{\rm norm}$ measurements in context with the results of C22. Fitting a linear relation to the log-log size-stellar mass relation, we find a slope of 0.33 ± 0.01 with a scatter of 0.16. This is similar to the fits of C22 who found slopes of 0.31 ± 0.01, 0.27 ± 0.02 and 0.32 ± 0.03 (with scatter of ~ 0.1) when fitting their whole sample, giant spirals and dwarf SF galaxies, respectively. We find that our $R_{\rm norm}$ measurements are systematically smaller than the C22 $R_{\rm edge}$ values by $\sim 10\%$. In contrast, Chamba et al. (2024) found that Fornax cluster galaxies are $\sim 50\%$ smaller than isolated galaxies, as $R_{\rm edge}$ (defined in the same way as C22) occurs at a higher stellar mass surface density. This is expected in the case where cluster galaxies have had their SF discs truncated. This justifies our use of the field-derived critical mass density for determining $R_{\rm norm}$.

The relationship between $R_{\rm sSFR}$ and stellar mass does not follow a clear linear relation and has much more scatter than the size-mass relation with $R_{\rm norm}$. This is expected in the case where galaxies with $R_{\rm sSFR} < R_{\rm norm}$ are undergoing quenching mechanisms that may be mass-dependent.

We plot $R_{\rm sSFR}/R_{\rm norm}$ against stellar mass in Fig. 3.5. Galaxies of all masses tend to have $R_{\rm sSFR}/R_{\rm norm} < 1$. There is a trend whereby galaxies with lower stellar masses have smaller values of $R_{\rm sSFR}/R_{\rm norm}$ on average, though there is much scatter. Shown in grey bands are the detection limits based on our methods. The first results from our removal of any galaxies whose sSFR profiles contained fewer than three data points ($R_{\rm sSFR}= 6.545''$). The second detection limit is at the radius for the first data point in the profiles, $R_{\rm sSFR}= 2.805''$, since any galaxy could have a measured edge at the first data point.

3.4.2 $R_{\rm sSFR}/R_{\rm norm}$ as a function of environmental indicators

In Fig. 3.6 we plot $R_{\rm sSFR}/R_{\rm norm}$ as a function of both HI-deficiency and distance from the SFMS (determined in Boselli et al., 2023a). On the HI-deficiency plot we indicate which galaxies are on/above the SFMS and which are below. Similarly on the SFMS plot we indicate which galaxies are HI-normal and which are HI-deficient. While most HI-normal galaxies are on the SFMS, the converse is not true: many galaxies on the SFMS are HI-deficient. We observe that most galaxies have $R_{\rm sSFR}/R_{\rm norm} < 1$ regardless of HI

content or SFR. Galaxies that are more HI-deficient or that are below the SFMS have more substantially truncated discs. Even for many galaxies on the SFMS, however, we find that $R_{\rm sSFR}/R_{\rm norm} < 1$. We interpret the ubiquity of truncated discs across the range of HI-deficiency and distance from the SFMS as evidence that nearly all Virgo galaxies are truncated relative to the field. For galaxies on the SFMS with normal gas content, the data points scatter around $R_{\rm sSFR}/R_{\rm norm} \sim 0.8$. While we expect that even the most normal galaxies in our sample may be somewhat affected by the Virgo environment, without a direct field comparison we cannot say for certain that galaxies with $0.8 < R_{\rm sSFR}/R_{\rm norm} < 1$ are truncated with respect to the field. Being mindful of this caveat, in further analysis we focus on galaxies with $R_{\rm sSFR}/R_{\rm norm} < 0.8$ We shall further discuss these results in context in Sect. 3.4.3.

A peculiar feature in Fig. 3.6 is the handful of galaxies that are extremely HI-deficient (HI-def > 2.5) and well below the SFMS with only mildly truncated discs. Upon inspection, some of these galaxies appear to be starbursts and feature low-SB ionised gas emission stemming from a central burst of star formation. Our measure of disc truncation is not able to pick these galaxies out, however they do not really have SF discs anymore at all. We show an example in Appendix B.3.

3.4.3 $R_{\rm sSFR}/R_{\rm norm}$ across the Virgo environment

The Virgo cluster is made up of a main cluster (Cluster A), along with another large structure (Cluster B) and several smaller substructures outlined in Table 3.1. Throughout our discussion of the main cluster structure, we adopt the NFW model of Simionescu et al. (2017) to describe the mass profile of the cluster. This fit infers $R_{200} = 0.974$ Mpc.

The footprint of the Virgo cluster with its substructures is shown in Fig. 3.7. Each galaxy is shown at its 2D position in the cluster region, with the data points sized according to the stellar mass of the galaxy and coloured according to the value of $R_{\rm sSFR}/R_{\rm norm}$ The radii of the circles depicting different substructures are those listed in Table 3.1. We use a discrete colour mapping on Fig. 3.7 to separate galaxies into three categories based on their values of $R_{\rm sSFR}/R_{\rm norm}$[2]. Blue data points have $R_{\rm sSFR}/R_{\rm norm} > 0.8$ and are considered at most mildly truncated. Since we have not used a control sample to directly determine the scatter in $R_{\rm sSFR}/R_{\rm norm}$ for normal SF galaxies, we do not focus on these mildly truncated galaxies in our analysis. Yellow data points ($0.3 < R_{\rm sSFR}/R_{\rm norm} \leq 0.8$) are considered moderately truncated and red points ($R_{\rm sSFR}/R_{\rm norm} \leq 0.3$) are considered

[2]Since the original publication of this work, we have created a new and improved version of this figure, which we show in Appendix B.4

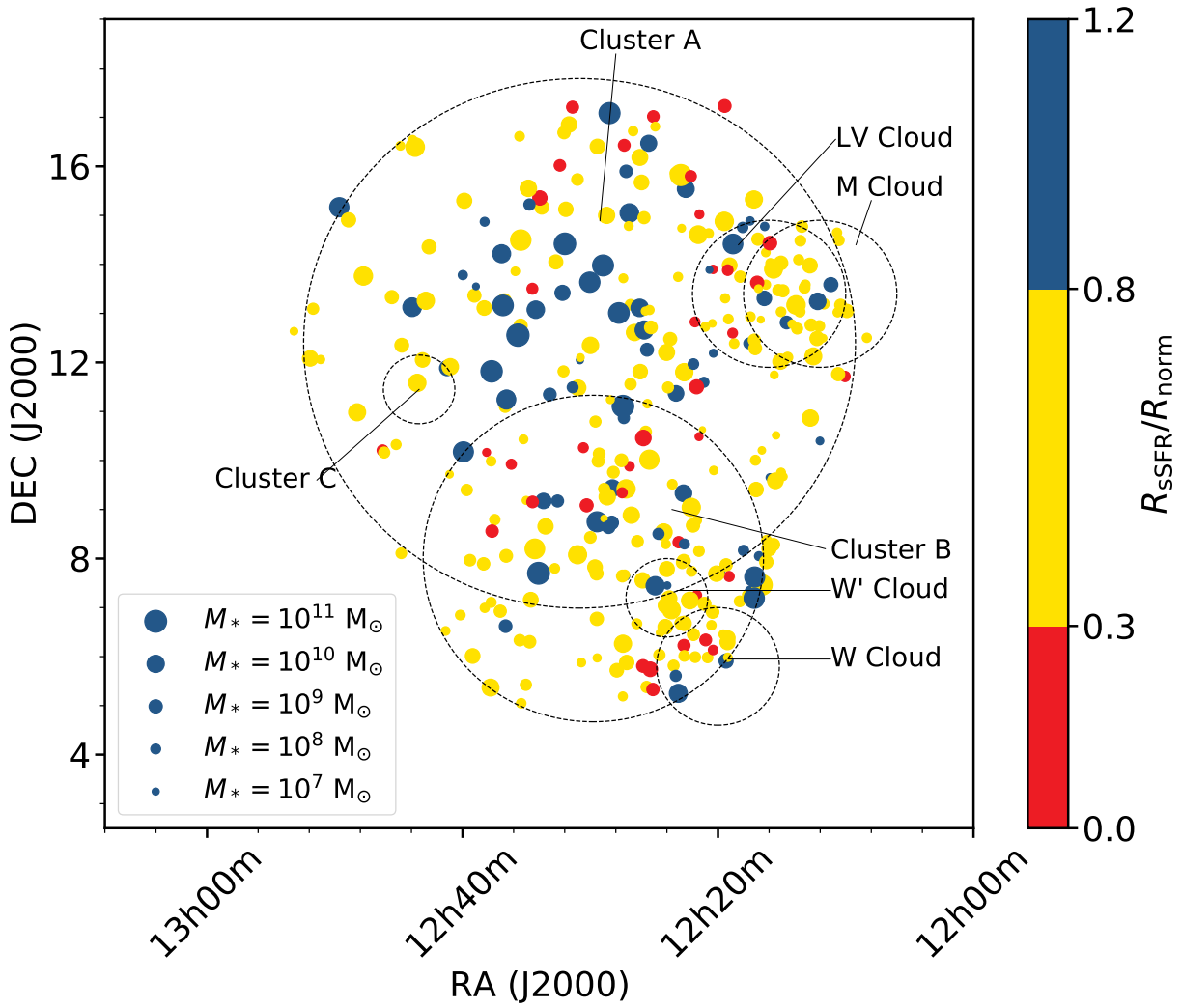


Figure 3.7: Right ascension and declination footprint of VESTIGE galaxies with measured values of $R_{\rm sSFR}/R_{\rm norm}$. Overplotted are the seven identified regions associated with the Virgo cluster: Clusters A, B and C, the W and W′ clouds, the M cloud and the Low-Velocity cloud, with the radii noted in Table 3.1. Data points are sized proportionally to the stellar mass of the galaxy, and coloured based on the value of $R_{\rm sSFR}/R_{\rm norm}$.

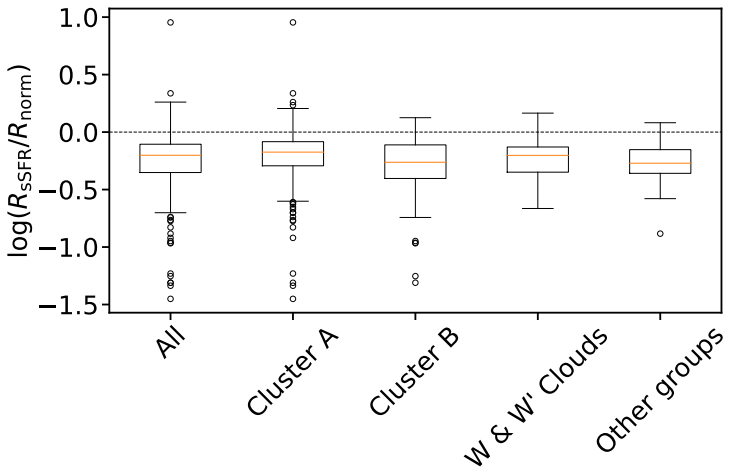


Figure 3.8: Box-and-whisker plot showing the median and first and third quartiles of the distributions of $R_{\rm sSFR}/R_{\rm norm}$ in the entire sample and four groupings of Virgo cluster substructures. 'Other groups' covers the M and low-velocity clouds as well as Cluster C.

extremely truncated. We can see from Fig. 3.7 that there are groupings of galaxies with at least moderately truncated discs in the M and Low-Velocity clouds, as well as in and around the W and W′ cloud regions. If these galaxies are truly a part of these substructures, this result indicates the possible importance of pre-processing in group structures beginning to perturb galaxies before they fall into the main cluster. We assign galaxies to their most likely substructure as outlined in Sect. 3.2.3. In Fig. 3.8 we show a box-and-whisker plot displaying the median and interquartile range of $R_{\rm sSFR}/R_{\rm norm}$ for five groupings of Virgo substructures: all regions, Cluster A alone, Cluster B alone, the W and W′ clouds together, and the M cloud, low-velocity cloud and Cluster C together. In each grouping, the median value of $R_{\rm sSFR}/R_{\rm norm}$ is less than unity, with the scatter varying across the groupings.

We also look at the distribution of galaxies in projected phase-space (PPS) in Fig. 3.9. To do so, we plot the radial velocities of galaxies (as collected in Boselli et al. 2023a) relative to the cluster against the 2D distance from the cluster centre (M87). While PPS diagrams often normalise the x axis by R_{200} and the y axis by the velocity dispersion (σ), we use physical (unnormalised) coordinates to ensure our interpretation of the results is not sensitive to the assumed value of R_{200} and σ. The data points are colour-coded according to $R_{\rm sSFR}/R_{\rm norm}$, as in Fig. 3.7. Evidence of truncations can be found throughout the cluster, including in the area beyond the virial radius of 0.974 Mpc. Interestingly, we do not find a strong trend between degree of truncation (based on the colours of the data points) and location in PPS. This contrasts sharply with the distribution of quenched

galaxies relative to star forming galaxies, illustrated as the background greyscale shading. This is created by comparing the 2D kernel density estimation (KDE) of the VESTIGE Hα sample distribution to that of the full NGVS sample, for the mass range $M_* > 10^8$ M$_\odot$ where NGVS is mostly redshift complete.

As was expected, the VESTIGE detection fractions are lower in regions of phase space near the centre of the cluster and with lower velocities, corresponding to ancient infall regions where galaxies have interacted with the cluster environment likely on multiple passes through the centre. If these ancient infallers have quenched, we would not expect detectable Hα emission and thus they are absent from the VESTIGE sample. On the contrary, the VESTIGE detection fractions are highest in the infall regions of the cluster, at higher relative velocities and far from the centre.

3.4.4 Modelling the radial profiles of galaxies

In this section we model the radial stellar and gaseous components of a normal SF galaxy (prior to any quenching) and explore how they change under two different simple quenching models. Starting with a chosen stellar mass, we use the scaling relations of Huang et al. (2012) to obtain an HI mass and integrated SFR for our galaxy. With the relations from Sect. 3.3, we obtain the critical Σ_* value and edge radius ($R_{\rm norm}$; $R_{\rm sSFR}$ at $t = 0$) of our galaxy. This allows us to determine the scale radius for an exponential Σ_* profile. For simplicity, we assume that the SFR profile will have the same scale radius, though in practice the scale radii for the two components could differ. Following the sub-kiloparsec Kennicutt-Schmidt law of Bigiel et al. (2008), the SFR profile of the model galaxy is proportional to the H_2 profile. The HI profile is flat at 8 M$_\odot$ pc^{-2}, which is a good approximation based on the observations of Bigiel et al. (2008).

Observations comparing gas density profiles and Hα profiles have identified that breaks in Hα profiles correspond to a critical gas density for star formation (e.g. Kennicutt Jr., 1989), which can signify the edge of the SF disc. Additionally, through our analysis we have used $R_{\rm norm}$ to define the expected edge of the SF disc for a normal, isolated galaxy. By incorporating the critical gas threshold for star formation, our SFR (and therefore H_2) profiles drop off abruptly at $R_{\rm norm}$, where $R_{\rm sSFR}$=$R_{\rm norm}$ at $t = 0$ and the threshold gas density is the value of the total gas density at $R_{\rm norm}$ at $t = 0$. The stellar mass surface density profile also has a break at $R_{\rm norm}$. However, unlike $R_{\rm sSFR}$, the location of this break will not change as we evolve the model.

In our simple model, the break at the gas density threshold is abrupt, with no star formation occurring beyond this radius; in reality, galaxy disc edges are less drastic due

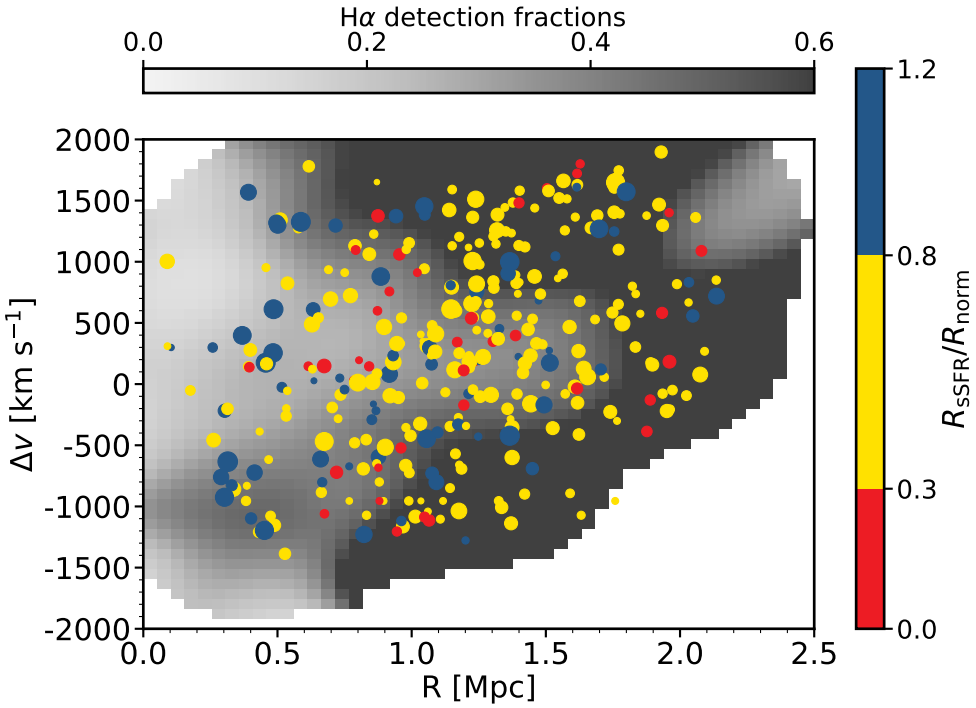


Figure 3.9: PPS diagram of VESTIGE galaxies with VESTIGE Hα detection fractions computed using the ratio of 2D Gaussian KDEs of the VESTIGE and NGVS distributions. Data points are sized proportionally to the stellar mass of the galaxy, and coloured based on the value of $R_{\rm sSFR}/R_{\rm norm}$. While the detection fractions show the expected structure, truncated discs exist across the cluster environment.

(for example) to localised peaks of dense gas fuelling small amounts of star formation in the outer disc. This simplification does not change our results as our goal is to explore how $R_{\rm sSFR}$ changes with time in different quenching scenarios. As gas is consumed and/or removed from the galaxy, the total gas density will decrease, causing the position of $R_{\rm sSFR}$ to change.

3.4.5 Ram-pressure stripping

The effects of RPS are known to be present in the Virgo cluster based on studies of individual or small samples of galaxies that display evidence of stripped HI gas through direct observations of the HI (e.g. Gavazzi et al. 2001; Kenney et al. 2004; Chung et al.

2007; Sorgho et al. 2017; Minchin et al. 2019; Boselli et al. 2023c) or observations of radio emission (e.g. Vollmer et al. 2004; Vollmer & Huchtmeier 2007; Vollmer et al. 2010, 2013; Crowl et al. 2005; Chyży et al. 2007; Kantharia et al. 2008) or ionised gas (e.g. Yoshida et al. 2002; Boselli et al. 2016, 2018b; Fossati et al. 2018; Boselli et al. 2021) in the stripped material. A multitude of simulation studies have shown that RPS can deplete the gas reservoir of a galaxy on timescales of < 1 Gyr (e.g. (Vollmer et al., 2001; Boselli et al., 2006; Steinhauser et al., 2016; Boselli et al., 2016; Fossati et al., 2018; Junais et al., 2022). However, substantial removal of SF gas may not occur until the galaxy approaches first pericentre as the combination of a dense ICM and high relative speeds are necessary to remove gas from a deep galactic potential well. Other high-resolution simulations have shown that while removal of the SF gas is rapid, removal of the entire gas reservoir may require timescales of > 1 Gyr (e.g. Tonnesen et al., 2007).

Additionally, the multi-phase nature of gas plays a role in the efficiency of stripping, with denser gas being harder to strip (e.g. Tonnesen & Bryan, 2009). Our simple model below neglects any direct stripping of the molecular gas and assumes that H_2 depletion occurs only through star formation. Once the HI gas is entirely removed after a stripping event, the H_2 gas cannot be replenished. In fact, stripping of molecular gas has been shown to occur in Virgo (Watts et al., 2023). Factoring this into our model would only serve to speed up the RPS timescales, which will not affect the interpretation of this model since the RPS timescales are much faster than starvation-only models.

To explore the range of effectiveness of RPS throughout the cluster, we invoke a simple model to determine where the combined ICM density and galaxy velocity becomes large enough to overcome the gravitational restoring force holding the gas in the galactic disc. Using a $M_* = 10^{9.5}$ $M_\odot$ model galaxy, we can calculate the restoring force from each component. While previous works have considered only the stellar disc component of the restoring force acting to hold the HI gas (e.g. Yoon et al. 2017; Boselli et al. 2022), we loosely follow Roberts et al. (2019) and consider the force from the stellar disc, dark matter halo, and the self-gravity of the gas itself.[3] Therefore, the restoring force is given as

$$f = \left[g_*(\mathrm{r}) + \mathrm{g_{HI}(r)} + \mathrm{g_{H_2}(r)} + \mathrm{g_{DM}(r)}\right]\ \Sigma_{\mathrm{HI}}(r), \tag{3.6}$$

where $g_*(\mathrm{r})$, $g_{\mathrm{HI}}(r)$, $g_{\mathrm{H_2}}(r)$ and $g_{\mathrm{DM}}(r)$ are the contributions to the gravitational acceleration from the different galactic components (stars, HI, H_2 and dark matter) and $\Sigma_{\mathrm{HI}}(r)$ is the surface density of HI gas. We leave further details of the model to Appendix B.5.

[3] Roberts et al. (2019) also factored in a bulge component of the stellar mass based on bulge-disc decomposition, but we model the stellar component of our galaxies as a disc only.

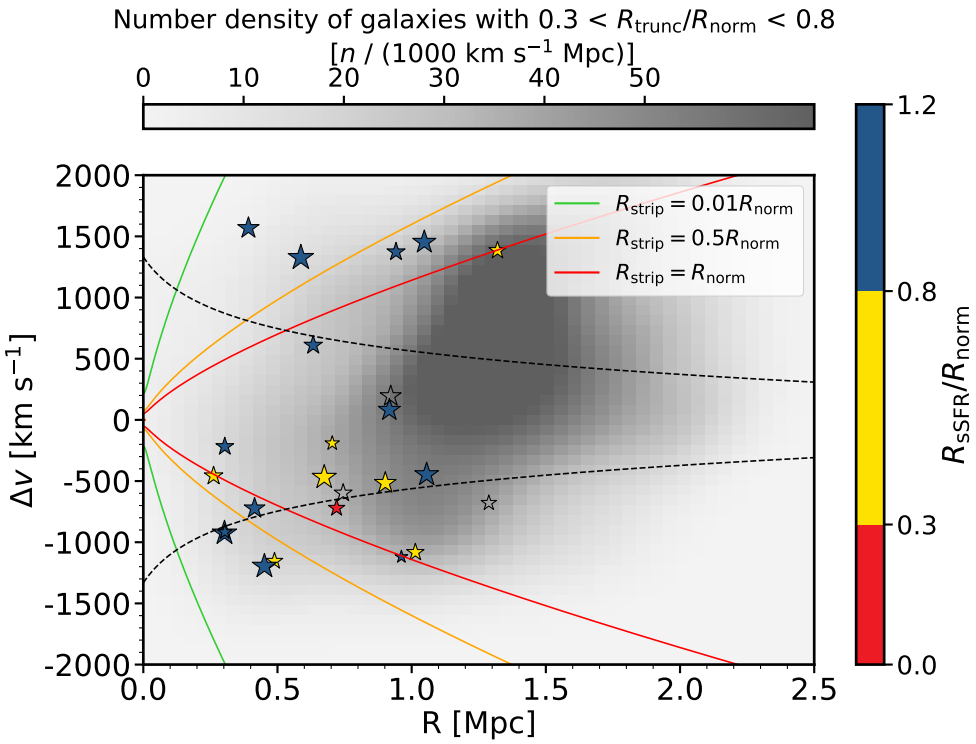


Figure 3.10: PPS diagram showing the region within the escape velocity of the cluster as the region between the two dashed black lines. The escape velocity is determined based on the NFW profile of Simionescu et al. (2017). The green, yellow, and red lines show the contours where a $M_* = 10^{9.5}$ $M_\odot$ galaxy could have its gas removed by RPS from 0.01, 0.5, and $1R_{norm}$, respectively, assuming isotropic orbits. Data points are sized proportionally to the stellar mass of the galaxy, and coloured based on the value of R_{sSFR}/R_{norm}. The background greyscale shows the phase-space number density of galaxies with $0.3 < R_{sSFR}/R_{norm} < 0.7$ determined using a 2D Gaussian KDE.

Ram-pressure is determined by $\rho_{\rm ICM}v^2$, where $\rho_{\rm ICM}$ is the density of the ICM and v is the relative velocity of the galaxy within the cluster. We can then calculate the strength of the ram-pressure at any point in phase space. We assume that a galaxy with some observed radial velocity, $v_{\rm r}$, has a three-dimensional velocity $v = \sqrt{3}v_{\rm r}$, since the ram-pressure depends on this three-dimensional velocity through the ICM. While this factor is statistically sound for a population of galaxies on isotropic orbits, the orbits of individual galaxies may vary. A more realistic analysis of the ram-pressure experienced by infalling Virgo galaxies was reviewed by Boselli et al. (2022), using a simulation to characterise accurate orbital parameters.

With this model, we can calculate whether the ram-pressure at a given 2D point in projected phase space is sufficient to overcome the restoring force of the galaxy at a given galactocentric radius. We show a second PPS diagram in Fig. 3.10, where the x- and y-axes are the same as in Fig. 3.9. The two dashed black curves on the plot indicate the escape velocity of the cluster based on the potential from the Simionescu et al. (2017) NFW profile. Also plotted are, for a $M_* = 10^{9.5}$ M$_\odot$ galaxy modelled as in section 3.4.4, the lines in phase space where the ram-pressure from the ICM can strip gas from the optical edge ($R_{\rm norm}$) of the galaxy (red), from $0.5R_{\rm norm}$ (amber) and from the centre ($0.01R_{\rm norm}$; green). The data points on Fig. 3.10 are galaxies previously identified to be undergoing RPS (Boselli et al. 2022 and references therein). These galaxies have a wide range of HI-deficiencies and are located across the cluster environment; however, the most perturbed galaxies are preferentially located closer to the cluster centre, and at high relative velocities, near the contours where we expect a significant fraction of gas to be stripped from galaxies on typical orbits. There are also several galaxies undergoing RPS that are located beyond the red contours, where our model predicts ram pressure is typically not effective. This is unsurprising, as the strength of RPS on individual objects depends on the shapes of orbits and the exact radial profiles of the galactic components, which can differ significantly from our statistical model assumptions.

The background greyscale of Fig. 3.10 shows the phase space number density of galaxies with moderate truncations ($0.3 < R_{\rm sSFR}/R_{\rm norm} < 0.8$), determined using a 2D Gaussian KDE. A dense region of truncated discs is located just outside the virial radius (between 1 and 1.5 Mpc) and with relative velocities between 0 and 1500 km s^{-1}. Statistically, many of these galaxies are likely to be on their first infall based on their location in phase space (Rhee et al., 2017). This region of phase space can also contain backsplash galaxies. However, if the galaxies in our sample had already passed through the densest region of the ICM in the cluster centre they likely would have been completely stripped due to RPS. In fact, we find the quenched fractions to be lower in these regions (Fig. 3.9), again supporting that many of these galaxies are likely on their first infall into the cluster. While RPS may

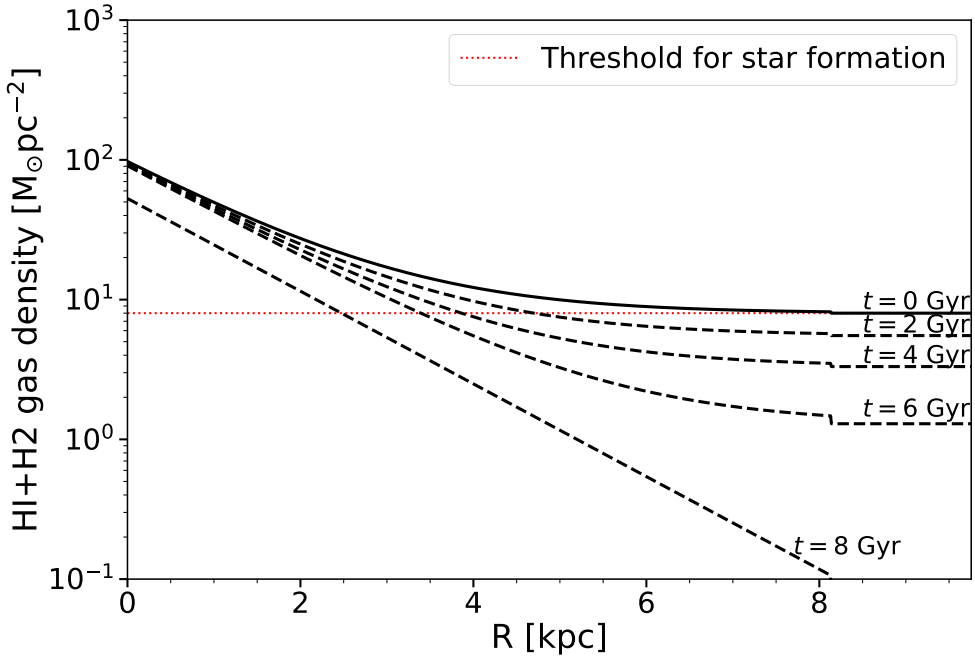


Figure 3.11: Evolution of total gas density ($\Sigma_{\rm HI} + \Sigma_{\rm H2}$) over 8 Gyr for a $M_* = 10^{9.5}$ $M_\odot$ galaxy undergoing simple starvation. The threshold gas density for star formation (explained in Appendix B.5)
is shown as a dashed red line. By the $t = 8$ Gyr curve, all HI gas has been consumed and as such the H_2 is not being replenished, causing the total gas density to decrease at all radii.

still be effective for some galaxies in this region of PPS, depending on their precise orbital geometries and restoring forces, the ubiquity of truncated discs in these regions suggests other effects may also be at play.

3.4.6 Starvation

In a simplified steady-state scenario, a galaxy forms stars from molecular gas that is replenished by atomic gas, which is in turn replenished by hot gas that has accreted from the cosmic web onto the galactic halo. If accretion of gas ceases (e.g. Larson et al., 1980) or halo gas is removed via stripping ('harassment': Moore et al. 1996, 1998) when the galaxy becomes a satellite of a more dominant system, the galaxy will eventually exhaust its reservoir of both atomic and molecular gas through star formation and become quenched. As

such, starvation is typically thought of as a process that uniformly lowers the gas density and suppresses star formation across the galactic disc, producing an anaemic, but not necessarily truncated, disc (e.g. Boselli et al. 2006). However, starvation models typically do not account for observations that suggest that there is a critical total gas density threshold required to fuel local star formation. We show below that a simple starvation model that factors in a gas density threshold for star formation will, in time, produce a galaxy with a truncated disc.

We demonstrate this with a simple toy model: At $t < 0$ (where $t = 0$ is the time at which starvation begins) a galaxy is in a 'steady state' of gas accretion where the radial gas density profiles of atomic and molecular gas remain constant over time due to accretion of hot halo gas; this in turn fuels a constant $\Sigma_{\rm SFR}$ profile. The radial profiles for the galactic components are determined as outlined in Sect. 3.4.4. We then allow our model to evolve from $t = 0$. At this point, we assume the galaxy is completely unable to accrete fresh gas, and thus the HI reservoir cannot be replenished as it converts into H_2. The model assumes that as long as there is HI in the galaxy then the H_2 profile (and thus the SFR profile) will remain constant[4]. At each timestep, stars form from the H_2 gas and the H_2 is replenished by the HI. Once the HI has been used up, subsequent star formation will deplete the remaining molecular gas, which will in turn reduce the SFR, moving the galaxy off of the main sequence.

In Fig. 3.11 we show the evolution of the total gas density profile in this model, for a $M_* = 10^{9.5}$ $M_\odot$ galaxy over 8 Gyr of starvation. Also plotted is the threshold gas density for star formation. Therefore, the points where the red line crosses each black curve are the points where the galaxy would be truncated at each timestep. In this model, while starvation takes a long time to move a galaxy off the SFMS and completely deplete its gas reservoir (as is shown in Appendix B.5), moderate truncation can still happen after just 1-2 Gyr. While this model is based on oversimplified assumptions about the gas distribution, consumption, and redistribution, as a toy model it effectively illustrates that any model of starvation that globally reduces the total gas density profile will also truncate the SF disc, if a critical gas threshold for star formation is included.

Quantitatively, these results will depend on the treatment of starvation in the model, and also on the stellar mass of the galaxy, but qualitatively the behaviour would remain the same. In future work a gas threshold for star formation should be incorporated into a more sophisticated model, like the chemo-spectophotometric model of Boselli et al. (2006). Such a model should then be tested in order to see if it can also re-produce observed colour

[4]This prescription is likely an oversimplification as HI-deficient galaxies have been shown to have reduced star formation efficiency; e.g. Villanueva et al. 2022; Brown et al. 2023.

and metallicity gradients in galaxies.

3.4.7 Ram-pressure stripping and starvation in context

In Fig. 3.12 we show a representation of the effects on $R_{\rm sSFR}$ and HI content of our starvation model compared to our RPS+starvation model for a galaxy falling radially into the cluster. Previous studies have indicated that starvation and removal of hot halo gas can be efficient as far out as $5R_{200}$ in clusters (e.g. Bahé et al. 2013). While we have not directly modelled the halo gas removal here, we assume for simplicity that starvation begins at $2R_{200}$, at which point the galaxy can no longer accrete fresh gas from the cosmic web. This choice of starting point is not meant to predict exactly where or how starvation begins for individual galaxies, but rather to show how starvation onset beyond R_{200} produces galaxies with truncated discs before ram-pressure is sufficient to strip gas directly from the galactic disc.

For a $M_* = 10^{9.5}$ M$_\odot$ galaxy in our model, it takes ~ 1.3 Gyr for the galaxy to fall radially from $2R_{200}$ to R_{200}, during which time the size of the SF disc shrinks significantly, by a factor of ~ 2. In the absence of any ram pressure stripping or other effects, the disc would continue to shrink gradually for several gigayears, as shown by the blue line. However, for this galaxy on a radial orbit our model predicts RPS begins at $t \sim 1.8$ Gyr, when the galaxy is at $\sim 0.5R_{200}$, and is the dominant quenching force until $t \sim 1.95$ Gyr. This rapid timescale (~ 150 Myr) for RPS is broadly consistent with the findings of other recent studies (e.g. Boselli et al. 2006, 2021; Fossati et al. 2018). At this point, when $R_{\rm trunc} = 3.1$ kpc, the H_2 gas becomes dominant in the gas profile, and shortly after the remaining HI gas from the galactic centre is removed by RPS. Once the galaxy is completely HI-deficient, the consumption of H_2 takes over and slowly truncates the disc further, moving it off the main sequence as the SFR decreases with decreasing H_2 content[5].

This shows that there is the potential for a galaxy to become completely stripped of HI by its first pericentre approach in the cluster. The removal of HI by RPS is most pronounced near the cluster centre, however, which makes our starvation model a natural choice to explain galaxies near and beyond R_{200} that appear to be on first infall with already-truncated discs.

Our toy model indicates that, while starvation has a long timescale to completely quench a galaxy, it may contribute to considerable disc truncation in only 1-2 Gyr. This means a galaxy can already have a truncated disc before RPS becomes dominant, especially if

[5]We have not considered the effects of RPS on the H_2 in our model; if RPS also removed H_2 then the quenching of the galaxy in this final stage would be even more rapid.

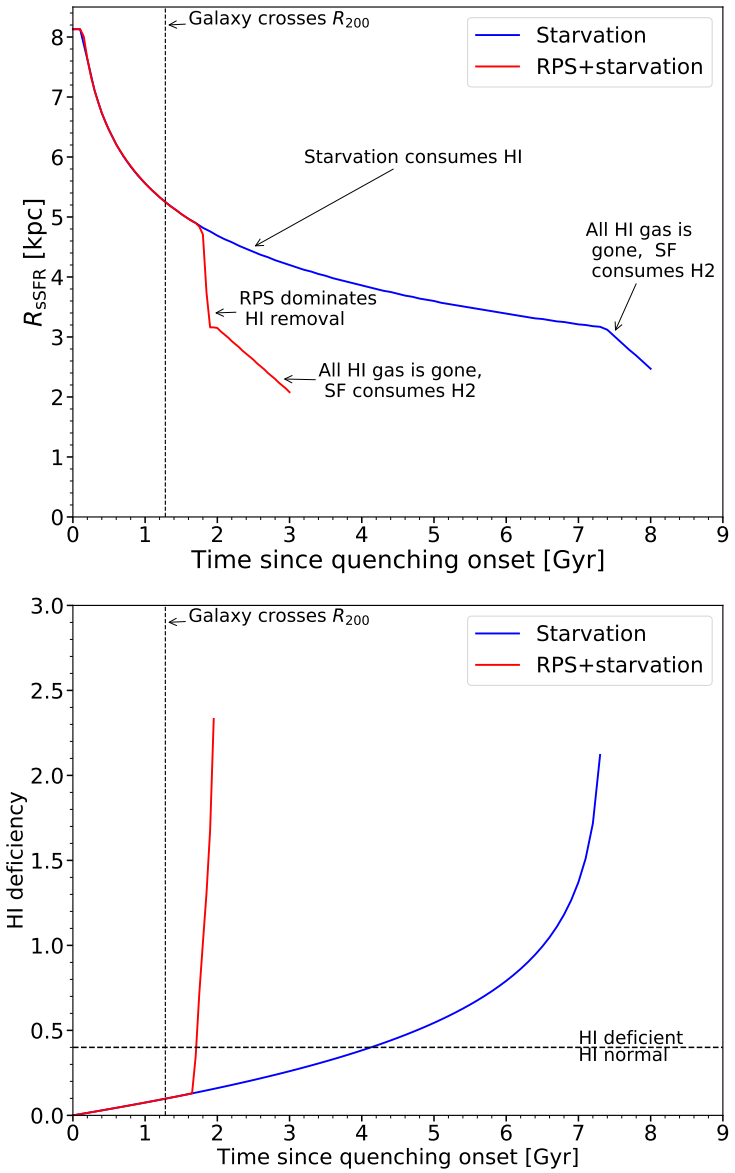


Figure 3.12: Evolution through time of $R_{\rm sSFR}$ (*top*) and HI-deficiency (*bottom*), for a $M_* = 10^{9.5}$ $M_\odot$ galaxy undergoing a simple starvation model (blue curves) and a galaxy falling into Virgo radially and experiencing RPS along with starvation (red curves). The horizontal dashed black line at HI-def=0.4 represents the point above which a galaxy is considered HI-deficient.

starvation begins early, when the galaxy is well beyond the virial radius. This implies a 'slow-then-rapid' quenching sequence, whereby galaxies begin slow quenching via starvation and, at a critical point during first infall, RPS becomes dominant and rapidly quenches the galaxy. These findings are consistent with those of Roberts et al. (2019), who found that the quenched fraction of galaxies in nearby clusters increases sharply at a threshold ICM density corresponding to the point where galaxies are susceptible to having the majority of their gas removed by RPS.

We argue that this slow-then-rapid quenching scenario is also consistent with the 'delayed-then-rapid' scenario of Wetzel et al. (2012). In our case, the early starvation quenching mode is the 'delayed' phase because it does not rapidly quench star formation in the galaxy. The global SFR and HI content of the galaxy do decrease during the time that starvation is dominant ($\sim$ 1.8 Gyr), but slowly enough that the integrated SFR drops by only $\sim$ 10% ($\sim$ 0.07 $M_\odot$ yr^{-1} for the modelled galaxy in Fig. 3.12). This means the galaxy would remain on the SFMS during the starvation phase, according to the main sequence fit defined in Boselli et al. (2023a).

We find this to be an attractive model to explain the dense region of moderately truncated discs beyond the virial radius of the main cluster as is seen in Fig. 3.10. The galaxies in this region have a range of HI-deficiencies and SFRs. The precise effects of starvation on the global gas content and SFR will depend on the details of the starvation mechanism and the time since starvation onset. Galaxies of different stellar masses will experience qualitatively the same effects, though the timescales may vary due to differences in gas content and SFR. While reproducing the parameters of individual galaxies is beyond the scope of this work, the peculiar trends seen in Fig. 3.6 can be qualitatively explained with this model. In Fig. 3.6, galaxies with moderate truncations can be seen with only mild HI-deficiencies and on the SFMS. Additionally, while SFMS galaxies are scattered across the range of HI-deficiencies, most HI-normal galaxies are on the SFMS. A slower process such as starvation truncating a disc, removing HI gas and then moving a galaxy off the main sequence successively over long timescales explains these trends since there is a high chance of observing a given galaxy in one of these three stages. Starvation before R_{200} could occur when a galaxy is a part of a smaller substructure, providing an explanation for the large number of truncated discs seen in the cloud structures of Virgo (Fig. 3.7). Other pre-processing mechanisms such as gravitational effects and even RPS (shown to be present in some groups and smaller clusters: Roberts et al. 2021b; Serra et al. 2023) could occur in these regions as well, and should be explored further with dedicated studies of pre-processing in Virgo substructures.

3.5 Summary and conclusions

We have used spatially resolved Hα imaging from VESTIGE, coupled with optical data from NGVS, to measure the edge of SF discs of galaxies across the entire footprint of the Virgo cluster, for $M_* > 10^7$ M$_\odot$. To quantify the expected sizes of discs for isolated counterparts ($R_{\rm norm}$), we have developed a methodology inspired by the physically motivated definition for the edge of a galactic disc outlined by Chamba et al. (2022). We have used AUTOPROF to measure surface brightness profiles in Hα, as well as the r and g bands, allowing us to construct Σ_* profiles and sSFR profiles. From our sSFR profiles, we have identified the turn-off point ($R_{\rm sSFR}$) based on the derivative of the profiles. We summarise our key results below:

- Disc truncations, where $R_{\rm sSFR}/R_{\rm norm} < 1$, appear ubiquitous across the Virgo cluster and as a function of stellar mass, HI-deficiency, and distance from the SFMS. However, we are cautious to assume that galaxies with minor disc truncations ($R_{\rm sSFR}/R_{\rm norm} > 0.8$) are truly truncated due to the lack of a control sample and the presence of SF, gas-normal galaxies with minor truncations (Sect. 3.3.2).

- We find that moderate disc truncations are more common at lower stellar mass, greater HI-deficiency, and for galaxies that have fallen off the SFMS. However, these trends are not strong and contain considerable scatter (Figs. 3.5, 3.6). Chamba et al. 2024 measured the edges of galaxies using a method analogous to Chamba et al. 2022 and found that galaxies in the Fornax cluster are systematically smaller than field counterparts, with a similar trend in stellar mass to our findings.

- Disc truncations occur to varying degrees across the entire cluster footprint, including in areas outside of the main cluster where galaxies may be infalling in groups (Fig. 3.7). The ubiquity of truncated discs across the cluster environment was also noted for the Fornax cluster by Chamba et al. 2024. We note as well that our sample consists only of galaxies with detectable Hα emission, most of which are therefore SF systems. This means that galaxies that are entirely quenched and would therefore have no measurable $R_{\rm sSFR}$ are not shown in our results. A comparison with galaxy densities from NGVS shows that the quenched fraction does indeed increases close to the cluster centre, so the truncated discs we measure are not representative of all galaxies in these regions (Fig. 3.9). This is consistent with results from Boselli et al. (2014b).

- The high number of galaxies with moderately truncated discs in regions with low quenched fractions and low ICM density implies additional drivers giving a head-start to quenching before RPS becomes the dominant gas removal mechanism.

- Galaxies on first infall may experience starvation before RPS, whether only in the main cluster or in smaller structures prior to cluster infall. We have shown that a starvation model can produce disc truncations when including a threshold gas density for star formation. Starvation beginning early, followed by a dominant RPS phase suggests a slow-then-rapid quenching sequence, consistent with the findings of Roberts et al. (2019). The nature of this quenching sequence is also broadly consistent with the delayed-then-rapid mechanism described in Wetzel et al. (2012), since the early starvation phase only mildly affects the integrated SFR of the galaxy before the RPS phase rapidly quenches it. Our results show that galaxies in the W and W′ Cloud regions have truncated discs, and a further study of group pre-processing prior to infall into the main Virgo cluster is critical to understanding the full evolutionary sequence of galaxies in these dense environments.

Chapter 4

Quenching signatures in Virgo cluster galaxies based on local variations in $\mathbf{SFR}_{\mathrm{H}\alpha}/\mathbf{SFR}_{\mathrm{FUV}}$

4.1 Introduction

The evolution of galaxies is inherently tied to the formation of stars from cold gas. By extension, processes that regulate gas content and cooling govern how star formation progresses or quenches. Measuring galaxy gas content, star formation rate (SFR), and stellar mass help to infer the evolution that has led a galaxy to its observable state. Deriving and constraining galaxy star formation histories (SFR across time; SFH), then, is one of the most critical tools for understanding galaxy evolution.

SFHs are one ingredient in spectral energy distribution (SED) fitting. SED fitting involves fitting models of stellar populations to observed photometric and spectroscopic data to constrain galaxy properties such as stellar mass, dust attenuation, metallicity and star formation rate. As a time series of stellar population models are fit over the expected history of the galaxy, a SFH is produced. Most SED fitting codes will assume a model for the SFH and fit the parameters of that model. For example, a delayed exponential ("delayed-τ") model fits the galaxy age and the decay timescale. One can also fit non-parametric, binned SFHs, where each time bin is chosen to correspond to various star formation rate tracers, with a continuity parameter between bins. Both of these options are available in popular SED codes such as PROSPECTOR (Johnson et al., 2021) and BAGPIPES (Carnall et al., 2018).

At a basic level, constraining the recent SFH of a galaxy helps to identify a galaxy undergoing a burst of star formation, or, conversely, a galaxy which is quenching or recently quenched. Different science questions can then be explored from this measurement. For example, dwarf galaxies are seen in simulations to have bursty star formation histories governed by strong feedback mechanisms (e.g. Hopkins et al., 2014; Sparre et al., 2017). Observational studies have then sought to determine the actual burstiness of local dwarfs compared to theory (e.g. Weisz et al., 2012; Guo et al., 2016; Emami et al., 2019). More recently, several studies have shown that galaxies in the early Universe observed with HST and JWST have bursty SFHs (e.g. Mehta et al., 2023; Asada et al., 2024; Gelli et al., 2025; Perry et al., 2025).

The quenching of galaxies is often split into two regimes: mass quenching and environmental quenching. In the local Universe, the two pathways have been shown to be separable (e.g. Peng et al., 2010). Mass quenching refers to quenching mechanisms tied to a galaxy's stellar mass. For example, the presence of strong active-galactic nuclei feedback is thought to drive quenching in massive galaxies through feedback that stirs up gas and prevents cooling (e.g. McNamara & Nulsen, 2007; Cano-Díaz et al., 2012; Fabian, 2012). Conversely, dwarf galaxies are more substantially effected by feedback from supernova explosions (e.g. Sawala et al., 2010; Hopkins et al., 2011, 2012). On the other hand, environmental quenching mechanisms are governed by the halo mass and local environment in which a galaxy resides. Processes such as ram-pressure stripping (RPS; e.g. Gunn & Gott, 1972; Boselli et al., 2022) can rapidly shutdown star formation through removal of the interstellar medium by interaction with the hot intracluster medium permeating galaxy clusters. A galaxy falling into a massive halo may lose its ability to accrete gas from the cosmic web, cutting off the supply of star-forming fuel and leaving the galaxy to fade in a process known as starvation (Larson et al., 1980). Gravitation interactions are also important, whether direct mergers or frequent fly-bys which can funnel gas into a central starburst, or otherwise strip material in tidal interactions (e.g. Toomre & Toomre, 1972; Moore et al., 1996, 1998).

Galaxy morphology is inherently tied to quenching – red, quiescent galaxies typically exhibit early-type morphologies, while star-forming systems often feature disks and spiral arms (e.g. Strateva et al., 2001; Kauffmann et al., 2003). In some sense, morphological quenching can be thought of as a third pathway to quiescence, as studies have suggested that the build-up of a galactic bulge and the presence of structural features such as bars may drive quenching internally (e.g. Kormendy & Kennicutt, 2004; Martig et al., 2009; Fang et al., 2013; Géron et al., 2021). On the other hand, certain quenching mechanisms will produce identifiable morphological signatures, such as the tails of stripped gas that can be seen in strong RPS galaxies. When star formation progresses in these tails, the tails

become optically-visible and are known as jellyfish galaxies - one of the most dramatic morphologies seen in the local Universe (e.g. Poggianti et al., 2017). The presence of truncated star-forming disks is a morphological feature often associated with outside-in quenching progressing in clusters by RPS, or starvation (e.g. Morgan et al., 2024).

Comparing the scaling relations of samples of galaxies in dense environments to those in the field highlights the interplay between quenching and morphological transformation. The morphology-density relation shows that galaxies in dense environments are more likely to be early-type ellipticals in the local Universe (e.g. Dressler, 1980; Huchra et al., 1983; Goto et al., 2003), and out to $z \sim 2$ (e.g. Dressler et al., 1997; Sazonova et al., 2020). Cluster galaxies are also known to be deficient in gas (e.g. Giovanelli & Haynes, 1985; Cayatte et al., 1990; Gavazzi et al., 2005; Cortese et al., 2011; Boselli et al., 2014a; Alberts et al., 2022) and exhibit lower rates of star formation (e.g. Balogh et al., 1997, 1998; Lewis et al., 2002; Gómez et al., 2003; Kauffmann et al., 2004; Baldry et al., 2006; Weinmann et al., 2006; Wetzel et al., 2012; Gavazzi et al., 2013a; Boselli et al., 2023a) than those in the field.

To further our understanding of galaxy quenching, we must move away from global scaling relations and continue to push our efforts into studying galaxies on highly resolved scales. This has been possible for some time at low-z, and is now becoming possible for galaxies in the early Universe with the James Webb Space Telescope. To build up our understanding of galaxy evolution across cosmic time, we can use highly-resolved studies of local galaxies to help shape the observations we undertake at high-redshift.

The Virgo cluster is an excellent local environment to studies galaxy evolution on resolved scales. At 16.5 Mpc, it is one of the closest massive clusters, meaning obtaining highly-resolved photometry is easily with modern instrumentation and data processing techniques. The Next Generation Virgo Survey (NGVS; Ferrarese et al. 2012) imaged the entire cluster region in optical bands using CFHT MegaCam with deep imaging, complete for galaxies down to $M_* \sim 10^7$ $M_\odot$. The Virgo Environmental Survey Tracing Ionised Gas Emission (VESTIGE; Boselli et al. 2018a) followed up NGVS in the Hα narrowband with a deep survey to detect emission from ionized gas. Various studies of the effects of the Virgo environment on galaxy evolution have been produced using this highly-resolved data (e.g. Ferrarese et al., 2016; Roediger et al., 2017; Lim et al., 2020; Fossati et al., 2018; Boselli et al., 2021, 2023a; Morgan et al., 2024).

While it is thought that RPS is a dominant quenching mechanism in Virgo (e.g. Boselli et al., 2016), the effects of other mechanisms such as tidal effects and starvation have also been noted (e.g. Koopmann & Kenney, 2004; Brown et al., 2023; Morgan et al., 2024). Virgo is dynamically unrelaxed – it is made up of two merging cluster structures and several

other infalling groups. The filamentary structure around the cluster contains groups of galaxies likely falling toward the main cluster, and has been shown to be involved in the pre-processing of galaxies before cluster infall (e.g. Finn et al., 2025). As such, the Virgo region contains galaxies across various stages of infall, meaning that the entire sequence of a galaxy's journey into a massive cluster can be explored with a statistical sample of galaxies around this one cluster.

4.2 Data

4.2.1 NGVS

The Next Generation Virgo Survey (NGVS; Ferrarese et al. 2012) includes optical imaging of the Virgo cluster environment out to 1.55 Mpc from M87, and 0.96 Mpc from M49. Using MegaCam on the Canada-France-Hawaii Telescope (CFHT), the survey covered 104 deg^2 in the u^*, g, i and z bands (with partial coverage in the r band). The long exposures of the survey allow for 5σ point-source depths of 26.3, 26.6, 25.8, and 24.8 mag in each of the four complete bands, respectively, with surface brightness depths of 29.3, 29.0, 27.4 and 26.0 mag arcsec^{-2}.

MegaCam on the CFHT consists of an array of 40 CCDs with pixel scale of $0.187''$ pixel^{-1}. Seeing conditions during observations allowed for a resolution of $< 1''$ (full-width-half-maximum). NGVS images were processed using Elixir-LSB, a pipeline specifically developed for enhanced detection of low-surface brightness features in NGVS images. Photometric calibration and astrometric calibration follows procedures detailed in Gwyn (2008).

4.2.2 VESTIGE

The Virgo Environmental Survey Tracing Ionised Gas Emission (VESTIGE; Boselli et al. 2018a) is an untargeted, narrowband Hα followup to NGVS, covering the same 104 deg^2 of the Virgo cluster using the narrowband MP9603 filter on CFHT MegaCam ($\lambda_c = 6591$ Å; $\Delta\lambda = 106$ Å) as well as the broadband r filter. The Hα Balmer line at 6563 Å and the two [NII] lines at 6548 Å and 6583 Å fall within the narrowband filter at the redshift range of Virgo ($-300 < v_{\rm hel} < 3000$ km s^{-1}). Long integrations (2h) in the narrowband achieved depths of $f(\mathrm{H}\alpha) \simeq 4 \times 10^{-17}$ erg s^{-1} cm^{-2} at 5σ for point sources and $\Sigma(\mathrm{H}\alpha) \simeq 2 \times 10^{-18}$ erg s^{-1} cm^{-2} arcsec^{-2} (1σ after smoothing the data to $\sim 3''$ resolution) for extended sources. r band exposures were 12 minutes, achieving a point source depth of

Instrument	Band	Survey	PSF $''$	Pixel scale $''$ pixel^{-1}	SB depth at nominal res.	Calibration uncert. %
GALEX	FUV	various	4.2	1.5	$\sim$ 28.6 mag arcsec^{-2}[a]	4.6
	NUV	various	5.3	1.5	$\sim$ 28.6 mag arcsec^{-2}[a]	2.8
CFHT MegaCam	u	NGVS	< 1	0.187	29.3 mag arcsec^{-2}	0.6
	g	NGVS	< 1	0.187	29.0 mag arcsec^{-2}	0.6
	r	VESTIGE	< 1	0.187	25.8 mag arcsec^{-2}	0.6
	Hα NB	VESTIGE	< 1	0.187	2×10^{-18} erg s^{-1} cm^{-2} arcsec^{-2}[b]	0.6
	i	NGVS	< 1	0.187	27.4 mag arcsec^{-2}	0.6
	z	NGVS	< 1	0.187	26.0 mag arcsec^{-2}	0.6
WISE	3.4μm	All-Sky	6.1	1.375	0.12 kJy sr^{-1}[c]	2.4
	4.6μm	All-Sky	6.4	1.375	2.4 kJy sr^{-1}[c]	2.8
	12μm	All-Sky	6.5	1.375	1.4 kJy sr^{-1}[c]	4.5
	22μm	All-Sky	12	1.375	5.6 kJy sr^{-1}[c]	5.7
Herschel PACS	100μm	HeViCS	6.77	3.2	8.6 MJy sr^{-1}	5
	160μm	HeViCS	11.92	6.4	4.9 MJy sr^{-1}	5
Herschel SPIRE	250μm	HeViCS	17.9	6	1.3 MJy sr^{-1}	5

[a] GALEX data comes from various observations with different exposure times. Values quoted here are based on a 5000s exposure (Morrissey et al., 2007).
[b] After smoothing to 3$''$ (Boselli et al., 2018a).
[c] Assuming a $5' \times 5'$ beam (Wright et al., 2010).

Table 4.1: Data used in `cigale` SED fits

24.5 mag (5σ) and a SB limit of 25.8 mag arcsec^{-2} (1σ for scales comparable to the size of structures in target galaxies, ~ 30 arcsec). Observations were taken under excellent seeing conditions (typical full-width-half-maximum of $0.76'' \pm 0.07''$). At the distance of Virgo, $1''$ is equal to 80 pc. The full observing strategy is discussed in detail in Boselli et al. (2018a).

4.2.3 Ancillary data

Ultraviolet: GALEX and UVIT

The GALEX Ultraviolet Virgo Cluster Survey (GUViCS) was an amalgamation of existing and new, deep GALEX observations of galaxies in the Virgo cluster region. Most of these observations have integration times of $t_{\rm int} > 1500$ s in the GALEX near-UV (NUV; $\lambda_{\rm eff} = 2316$Å, $\Delta\lambda = 1060$Å) and far-UV (FUV; $\lambda_{\rm eff} = 1539$Å, $\Delta\lambda = 442$Å) bands, exceeding the depth of the Medium Deep Imaging Survey. While complete in coverage in the NUV band, the survey only covers about one-third of the cluster with deep FUV imaging. For some galaxies, shallower GALEX imaging from the Medium Deep Imaging Survey or the All-Sky Imaging Survey are used. GALEX imaging has a nominal point-spread function (PSF) of $\sim 5''$, with pixel size of 1.5 arcsec/pixel or 120 pc at the distance of Virgo.

In addition to GALEX imaging, Astrosat/UVIT imaging is available for many of the galaxies studied here. These observations come from a mix of archival observations, as well as two recent proposals (A08_003; PI. J. Hutchings and A10_070; PI. A. Boselli). The deepest images are 12000s in the BaF2 filter ($\lambda_{\rm eff} = 1541$Å, $\Delta\lambda = 380$Å), very similar to the GALEX FUV filter. UVIT has $\sim 1 - 1.2''$ resolution with a pixel size of 0.417 arcsec/pixel, providing a closer spatial match to the resolution of the MegaCam data.

Mid-infrared

The mid-infrared (MIR) is a crucial tracer of heated dust and polycyclic aromatic hydrocarbon emission (PAHs) in galaxies. We use all-sky data from WISE (Wright et al., 2010), which covers the MIR at 3.4, 4.6, 12 and 22 μm, at angular resolutions of 6.1, 6.4, 6.5 and $12.0''$ in each of the four bands.

Far-infrared

We use far-infrared (FIR) data to trace the dust continuum peak. This data comes from the Herschel Virgo Cluster Survey (HeViCS; Davies et al. 2010), and includes 100 and

160 μm emission from Herschel PACS and 250, 350 and 500 μm emission from Herschel SPIRE. Since resolution decreases quickly as a function of wavelength in the FIR, and the dust emission peak is almost always < 250 μm, we exclude the 350 and 500 μm bands here. The three bands we include have resolutions of 6.77, 11.92, and 17.9″, respectively.

4.3 Methods

4.3.1 Resolution matching and noise considerations

Without a model that can account for differences in resolution of multiband photometric data and account for correlations between pixels, we must resolution-match our data to perform spatially-resolved SED fits. This means that the spatial resolution we can achieve for maps of derived galaxy parameters will be limited by the lowest resolution data – in this case that is the 250μm FIR data from *Herschel* SPIRE, which has a resolution of $\sim 17.9''$ and a pixel size of $6''$ pixel^{-1}. We make use of the convolution kernels provided by Aniano et al. (2011)[1] in order to convolve all of our photometric science images and noise maps to SPIRE 250μm resolution, using the `astropy.convolution` module. We then downsample the pixel scale to $6''$ pixel^{-1}.

This downsampling considerably reduces the resolution of the optical data from NGVS and VESTIGE. It also considerably increases the signal-to-noise on these already-deep datasets. While downsampling introduces pixel-to-pixel correlations that should be accounted for in the new noise values, the signal-to-noise values of the optical images would still be unrealistically high and the range of S/N values across our multi-band data would remain too high to achieve a high-likelihood fit to all the data. In most cases, the downsampled datasets will now be limited by the uncertainty in their photometric calibrations (listed in Tab. 4.1), and as such we set our noise values to be the sum in quadrature of the convolved noisemap and the calibration uncertainty.

4.3.2 SED fitting

Once all our photometry is matched to the same resolution and we have realistic noise values, we are able to perform spatially-resolved SED fitting. We choose to use `cigale` (Boquien et al., 2019) for its modularity and for the fact that it is relatively computationally inexpensive for running pixel-based fits on a large sample of galaxies. `cigale` computes a

[1] https://www.astro.princeton.edu/~draine/Kernels.html

pre-grid of models based on discretized priors for various modules – for us, this includes parameters for SFH, metallicity, dust attenuation, and dust emission. We employ a custom SFH module in `cigale` where the functional form of the SFH is a delayed-exponential with two recent bursting or quenching episodes. This is based off the `sfhdelayedbq` module that is standard in `cigale` that fits a delayed-exponential with a single recent bursting or quenching episode. We choose to add a second recent burst in order to allow both the Hα and UV to constrain an independent burst. We fix the value for $t_{\rm bq,1}$ at 10 Myr and $t_{\rm bq,2}$ at 400 Myr. The SFR during these bursts are constant, where SFR($t_{\rm bq,2}$) is the SFR from $t_{\rm bq,2}$ to $t_{\rm bq,1}$ and SFR($t_{\rm bq,1}$) is the SFR from $t_{\rm bq,1}$ to $t = 0$. We show in Table 4.2 the possible values for our SFH parameters, and provide the full list of `cigale` parameters in Table C.1 in Appendix C.

4.3.3 SFR tracers

Instead of using the SFH itself to measure recent star formation, we use the FUV from GALEX and UVIT and the Hα from VESTIGE as direct tracers. This reduces the reliance on the shape of the parametric SFH, and allows us to empirically measure the SFRs from these two tracers. Hα emission stems from the ionization of hydrogen gas in the regions around hot, young stars (primarily O-type with some contribution from B-type). As such, Hα traces star formation on the order of 10 Myr, comparable to the lifetimes of these stars. The FUV, on the other hand, is traced by slightly cooler stars that have peak emission around 100-150 nm. Thus FUV traces star formation on the order of 100 Myr – the main sequence lifetimes of these stars. As such, comparing the SFRs derived by Hα and FUV provides a measure of burstiness or rapid quenching in the recent SFH of the galaxy, adding a temporal component to morphological signatures of quenching. Doing so however, requires careful corrections to both the FUV and Hα flux to ensure contamination from sources not associated with young stellar emission are removed.

Dust attenuation

We use a modified Calzetti dust attenuation model (Calzetti et al., 2000) in our SED fits. The modification is that the Calzetti model is replaced with the model of Leitherer et al. (2002) for $\lambda < 1500$ Å. In `cigale`, this is implemented mainly by fitting a range of prior values for the colour excess in the line flux, E$(B-V)_l$. We fix the ratio between E$(B-V)_l$ and the colour excess in the stellar flux, E$(B-V)_s$ at 0.44. We note that while the attenuation to the continuum is based on the modified Calzetti curve, the extinction for emission lines is calculated based on a Milky Way emission curve (Cardelli et al., 1989).

Parameter	Symbol	Possible values
e-folding time of main stellar population	τ	500, 750, 1000, 1250, 1500, 1750, 2000, 2250, 2500, 3000 Myr
Age of main stellar population	$t_{\rm age}$	4000, 5000, 6000, 7500, 10000, 13000 Myr
Age of most recent burst	$t_{\rm bq,1}$	10 Myr
Ratio of SFR before bursts and during most recent burst	$r_{\rm SFR,1}$	0.0, 0.05, 0.1, 0.15, 0.2, 0.25, 0.3, 0.35, 0.4, 0.45, 0.5, 0.6, 0.75, 0.9, 1.0, 1.2, 1.5
Age of earlier burst	$t_{\rm bq,2}$	400 Myr
Ratio of SFR before bursts and during earlier burst	$r_{\rm SFR,2}$	0.0, 0.05, 0.1, 0.15, 0.2, 0.25, 0.3, 0.35, 0.4, 0.45, 0.5, 0.6, 0.75, 0.9, 1.0, 1.2, 1.5

Table 4.2: SFH parameters used in `cigale` SED fitting

From the best fit colour excess, we can then determine the attenuation parameter, $A_{\rm FUV}$, for the FUV flux by:

$$\begin{aligned} A_{\rm FUV} &= k(1550\,\text{Å})\,\mathrm{E}(B-V)_s \\ &= 10.19\,\mathrm{E}(B-V)_s \\ &= 4.48\,\mathrm{E}(B-V)_l. \end{aligned} \tag{4.1}$$

The Hα extinction parameter, then, can be determined as:

$$\begin{aligned} A_{\rm H\alpha} &= k(6563\,\text{Å})\,\mathrm{E}(B-V)_l \\ &= 2.53\,\mathrm{E}(B-V)_l. \end{aligned} \tag{4.2}$$

NII contamination in Hα narrowband emission

The MP9603 filter on MegaCam covers Hα+NII emission from galaxies at the distance of the Virgo cluster. The data reduction process includes continuum subtraction, leaving just the emission line flux. However, in order to extract just the Hα emission that we expect to trace recent star formation, the contamination from NII emission must be accounted for. Because we are mapping out star formation from Hα emission on a resolved scale, we want to check for variation in the NII/Hα ratio on spatial scales. To do this, we use the MaNGA dataset (Bundy et al., 2015). MaNGA provides integral-field unit spectroscopy for $\sim 10,000$ galaxies in the local Universe. Since we are focused on NII contamination in SF regions, we focus on SF spaxels in SF galaxies from MaNGA. To do so, we remove MaNGA galaxies with more than 50% non-SF spaxels based on BPT line diagnostics (Baldwin et al., 1981). We then look only at the gradients in NII/Hα ratio for the SF spaxels in these remaining SF galaxies, in four bins of stellar mass spanning $9 < \log(M_*/\mathrm{M}_\odot) < 12$. We find that there is no significant radial gradient in the NII/Hα ratios, though there is a dependence of the global value on stellar mass. We take this mass dependent global value and use it to correct our Hα fluxes before computing SFRs. Figure C.1 in Appendix C shows the resolved analysis of the NII/ha ratios in MaNGA star-forming galaxies, while Figure C.2 shows the global dependence of NII/Hα on integrated galaxy stellar mass.

FUV contamination from evolved stellar populations

To ensure that our SFR derived from FUV flux is tracing recent star formation on $\sim$ 100 Myr timescales, we must correct for any FUV flux that can be attributed to other

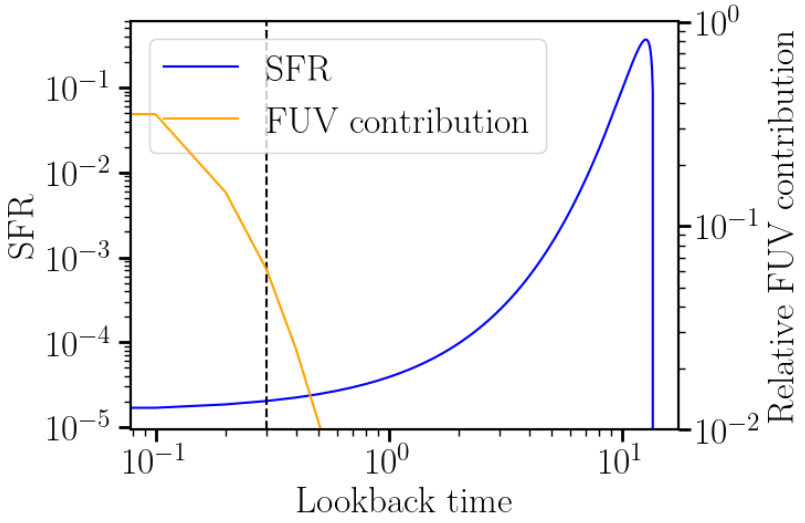


Figure 4.1: SFR (blue) and relative contribution to FUV flux from old stars (yellow) as a function of lookback time for a delayed-τ SFH for a typical star-forming galaxy. Note that SFR values are not given in physical units.

types of stars, including UV upturn populations from old stars, horizontal branch, and post-asymptotic giant branch stars. We modified the `cigale` code to output additional parameters and their uncertainties. Relevant here is the FUV flux from old and young stars, respectively, as well as the fraction of total FUV flux from old stars, which we choose to be any stars older than 400 Myr. This cut captures FUV flux from any of the old and post-main sequence populations mentioned above, which arise from the Bruzual & Charlot 2003 stellar population models, which in turn make use of the Padova 1994 tracks (Bertelli et al., 1994). We have `cigale` calculate this by splitting the SFH at 400 Myr, and integrating the spectra of the old and young stellar populations separately through the GALEX filter. Figure 4.1 shows an example of a delayed-τ SFH and the relative contribution to the FUV flux from the stellar populations at a given age.

4.3.4 SFR maps from Hα and FUV

We first create $\mathrm{SFR}_{\mathrm{H}\alpha}$ and $\mathrm{SFR}_{\mathrm{FUV}}$ maps at GALEX resolution ($\sim$ 120 pc) using the maps of Hα and FUV fluxes corrected with the corrections described above. To do this, we must upscale the resolution of our dust and old star FUV fraction maps, since they were produced at lower resolution during the SED fitting step. However, we expect any correlations

introduced between neighbouring pixels are small compared to the systematic uncertainties we include, as discussed below. We then take the ratio $\zeta = \log(\mathrm{SFR}_{\mathrm{H}\alpha}/\mathrm{SFR}_{\mathrm{FUV}})/\sigma$, normalized by the uncertainty in the ratio such that this becomes a significance map. The propagation of uncertainties is discussed further in Section 4.3.4. We further produce diagnostic plots where we bin our data in various ways to increase the signal-to-noise of the flux data and thus measure statistically significant values of ζ ($|\zeta| > 1$). We discus here the plots we create and how we compound our uncertainties. Consistent with previous VESTIGE papers, we use the Hα-to-SFR calibration from Calzetti et al. (2010), modified to include a Chabrier IMF:

$$\mathrm{SFR}_{\mathrm{H}\alpha}\,[\mathrm{M}_\odot\,\mathrm{yr}^{-1}] = 5.01 \times 10^{-42} L(\mathrm{H}\alpha)\,[\mathrm{erg\,s}^{-1}]. \tag{4.3}$$

For the FUV-to-SFR conversion, we follow the GALEX FUV calibrations of Salim et al. (2007):

$$\mathrm{SFR}_{\mathrm{FUV}}\,[\mathrm{M}_\odot\,\mathrm{yr}^{-1}] = 1.08 \times 10^{-28} L(\mathrm{FUV})\,[\mathrm{erg\,s}^{-1}\,\mathrm{Hz}^{-1}]. \tag{4.4}$$

Diagnostic plots

We bin our data to help visualize spatial variations in ζ. Our initial 2D maps at GALEX resolution are produced using GALEX FUV data, supplemented with UVIT where available. In many cases, the GALEX data is not particularly deep for a resolved analysis. We make a signal-to-noise cut of 3 on a per-pixel basis, which often removes all but the brightest star forming regions. However, we want to be able to measure ζ in low-surface-brightness regions as well, such as in the outer disks of galaxies where truncations may be occurring. As such, we apply a Voronoi binning technique to bin pixels to reach a common signal-to-noise (5) in each bin – as such, we expect small Voronoi bins near the centres and bright star-forming regions of galaxies and larger bins in the outskirts of the disk.

In addition, we create radial profiles of ζ. Radial profiles are computed using the optical ellipticities and position angles from the AUTOPROF runs of Morgan et al. (2024, Chapter 3 of this thesis). We run the profiles out to $6R_e$ of each galaxy, where R_e is the effective radius determined from surface brightness profile fits in NGVS (Ferrarese et al., 2026), and with an annuli width and spacing of $0.25R_e$ or $12''$, whichever is larger. This is well beyond the point where we can reliably measure SFRs for most of these galaxies, and we adopt 1×10^{-4} $\mathrm{M}_\odot\,\mathrm{yr}^{-1}\,\mathrm{kpc}^{-2}$ as the limit within which we can measure radial SFR. This number is based on the additional uncertainty associated with stochastic star formation,

which is expected to be of concern below $\sim 1 \times 10^{-3}$ $M_\odot\,yr^{-1}$. However, since we average over a large area in the radial annuli, particularly in the low-SB regime where the typical SFRs will be lower, we adopt a more liberal limit of 1×10^{-4} $M_\odot\,yr^{-1}\,kpc^{-2}$.

Propagation of uncertainties

Our goal is to identify local regions within Virgo galaxies with significant differences in their SFR as traced by both Hα and FUV. As such, it is vital to properly account for both statistical and systematic uncertainties for each diagnostic plot. For the GALEX-resolution maps, statistical uncertainties on the fluxes come from associated uncertainty images, combined with calibration uncertainty values. Uncertainties on the SED fit parameters are also computed by `cigale` in a Bayesian manner by taking a likelihood-weighted standard deviation across the pre-grid values. The dust attenuation values for both Hα and FUV are based on the same fit parameter, $E(B-V)_l$, and the NII/Hα correction computed from MaNGA has both an uncertainty associated with the pixel-to-pixel scatter in the galaxies as well as a galaxy-to-galaxy scatter.

For the pixel scale SFR maps, we run a Monte Carlo simulation by drawing 1000 samples of the Hα and FUV fluxes, $E(B-V)_l$, and the FUV old star fraction $f_{\rm old,FUV}$ within their respective uncertainty ranges. We then calculate 1000 values of $SFR_{H\alpha}$, SFR_{FUV}, and ζ. We then apply a systematic uncertainty to $SFR_{H\alpha}$ and ζ based on the scatter in NII/Hα, and a 30% uncertainty to $SFR_{H\alpha}$, SFR_{FUV}, and ζ to account for systematics in the SFR calibrations. We note that, if the systematics for the Hα and FUV SFR calibrations were exactly the same, the associated uncertainty would effectively cancel out for ζ. On the other hand, if the systematics are completely unique to each calibrations, two factors of the calibrations uncertainty should be applied to ζ. We choose a middle ground and apply a single factor of the 30% calibration uncertainty to ζ – while some systematics such as the choice of IMF are the same, the calibrations are from different studies using different methods.

When we bin the pixel-based maps – whether radially, azimuthally, or in Voronoi bins – the statistical uncertainties, particularly those on the fluxes themselves, are diluted. However, the fully systematic uncertainties (such as the those on NII/Hα and the SFR calibrations) not only remain, but now dominate. Additionally, we include a systematic uncertainty on the $E(B-V)_l$ and $f_{\rm old,FUV}$ values, since we expect any offsets are consistent between nearby pixels. We use the mean pixel-based uncertainty for these parameters within the bin to account for this.

4.3.5 Morphological metrics

There are two primary features that we want to identify quantitatively: truncation and lopsidedness. As such, we employ morphological metrics that can pick out these features.

Lopsidedness

Lopsidedness refers to an asymmetry in the galaxy disk, and particularly one with a coherent phase as a function of radius. The concept was first used as a quantification of HI disks (e.g. Baldwin et al., 1980; Richter & Sancisi, 1994). The use of Fourier-mode lopsidedness was extended to optical disks with studies such as Rix & Zaritsky (1995), Zaritsky & Rix (1997), and Rudnick & Rix (1998). Galaxies undergoing RPS, for example, may display lopsidedness in their SFR maps due to the stripping of gas along the trailing edge, and the possible compression of the ISM along their leading edge. This was shown in a study of simulations of galaxies with undergoing RPS-induced unwinding by Machado et al. (2025). Similarly, this feature would be present in our ζ significance maps. Non-axisymmetric features such as this are well-quantified using a Fourier decomposition of the significance map. Specifically, the first Fourier mode amplitude quantifies the lopsidedness of an image. We calculate this mode in radial annuli on our significance maps. Then, a series of high amplitudes and coherent phases across the radial annuli signifies a galaxy that has a clear lopsidedness in its ζ distribution. The value of ζ for a Voronoi bin in a given radial annulus, with mean radius $r = R$, can be expressed as the following Fourier transform:

$$\zeta(r = R, \varphi) = \sum_{m=-\infty}^{\infty} c_m(R) e^{-im\varphi}, \tag{4.5}$$

with φ being the azimuthal angle of the Voronoi bin, and m, $c_m(R)$ representing the wavenumber and complex Fourier coefficient, respectively. $A_0(R) = |c_0(R)|$ is the amplitude of the zeroth Fourier mode, which would represent the mean ζ value for the annulus at $r = R$. We subtract off $c_0(R)$ as a significantly non-zero mean value will skew the value of the $m = 1$ Fourier amplitude and the significance test that follows. Generally, a complex Fourier coefficient in one spatial dimension is calculated as:

$$c_m = \frac{1}{2\pi} \int_{-\pi}^{\pi} e^{imx} f(x) \mathrm{d}x, \tag{4.6}$$

for a continuous function, $f(x)$, evaluated over some domain x. However, since we have discrete spatial bins with a range of areas over the domain of φ in each radial annuli, we

discretize the calculation of the $m = 1$ Fourier coefficient, and weight the ζ value in each spatial bin by its area. As such:

$$c_1(R) = \frac{\sum_j N_j \ [\zeta(\varphi_j) - c_0(R)] \ e^{+i\varphi_j}}{\sum_j N_j}, \tag{4.7}$$

where we sum over j Voronoi bins, with N_j representing the area of the bin, $\zeta(\varphi_j)$ the significance value in that bin, and φ_j the azimuthal angle to the bin centre. Then simply, $A_1(R) = |c_1(R)|$ and $\varphi_1(R) = \arg(c_1(R))$. Typically, A_1 would be normalized by A_0, essentially the mean over the binned values. However, since ζ straddles zero, we use the mean of the absolute values of ζ_j to normalize instead ($\tilde{A}_1(R) = A_1(R)/|\zeta(R)|$). We also quantify uncertainties in our $A_1(R)$ measurement by re-sampling the values of $\zeta(\varphi_j)$ in the Voronoi bins to within their 1σ uncertainties 1000 times, and taking the median as the value of $A_1(R)$, with the 16^{th} and 84^{th} percentiles as the upper and lower uncertainties.

By measuring $\tilde{A}_1(R)$ and $\varphi_1(R)$ as a function of radius, we can determine the degree of lopsidedness and the phase direction along with it occurs. The galaxies with the strongest signal will have high amplitudes and coherent phases across several radial annuli. To quantify this, we can take a complex, weighted mean across the radial bins:

$$c_{1,\mathrm{global}} = \frac{\sum_r \tilde{A}_1(r) e^{i\varphi_1(r)} N_r}{\sum_r N_r}, \tag{4.8}$$

where N_r is the total area of the Voronoi bins in a given radial annulus. Then simply, $A_{1,\mathrm{global}} = |c_{1,\mathrm{global}}|$ and $\varphi_{1,\mathrm{global}} = \arg(c_{1,\mathrm{global}})$. The galaxies with the highest values of $A_{1,\mathrm{global}}$ are those with the strongest combination of high amplitudes and phase coherence.

Truncation

We quantify radial truncations by looking at the ratio of $\mathrm{SFR}_{\mathrm{H}\alpha}$ to $\mathrm{SFR}_{\mathrm{FUV}}$ across radial bins. In cases where a galaxy is experiencing a rapid outside-in quenching episode, its star-forming disk as traced by Hα should by more truncated than the disk traced by FUV, since the Hα traces star formation on shorter timescales. As such, the ratio of $\mathrm{SFR}_{\mathrm{H}\alpha}/\mathrm{SFR}_{\mathrm{FUV}}$ should have a negative radial gradient in these galaxies. We measure these radial gradients out to the radius where either of the SFR tracers falls below $1 \times 10^{-4}\,\mathrm{M}_\odot\,\mathrm{yr}^{-1}\,\mathrm{kpc}^{-2}$, our adopted lower limit for measurable star formation. We also exclude the central $0.5R_e$ since we have now accounted for the fact that central Hα emission in galaxies may be due to sources other than star formation (we discuss this more in Section 4.5.1). We note that this

measure of truncation is a different signature than that of Morgan et al. (2024, Chapter 3 of this thesis), though we will compare the two metrics and discuss them in context in Section 4.5.

Based on visual classification, we can group our galaxies into those that look normal and those with disturbed morphologies. We identify galaxies with clear visual lopsidedness, and galaxies with clear truncations. We then can explore how well the quantifications of these features correlate with what we identify visually. Of course, galaxies display a spectrum of these signatures – some galaxies have strong truncations while others may be weak, and some will display a significant lopsidedness compared to others. Our main goal here is to measure these signatures on our sample of galaxies, and compare with other indicators of morphology. We can then discuss how these signatures align with models of quenching mechanisms that are known to occur in the Virgo cluster.

4.4 Results

4.4.1 Examples of visually interesting galaxies

To show how the quantitative measures of lopsidedness and truncation correspond to the visual identification of these features, we visually inspected each galaxy in our sample and picked out three of the best visually normal candidates, as well as three with clear lopsidedness and three with clear truncations.

Visually normal galaxies

Most galaxies in the Virgo cluster are disturbed in some way (e.g. Boselli et al., 2023a; Morgan et al., 2024). However, we show here three galaxies without significant visual lopsidedness or truncation. We are careful to note that, just because these galaxies do not have significant lopsidedness or truncation does not mean that they have not been affected by the Virgo environment in some way, just that any quenching mechanisms they have experience or are experiencing are not detectable in these quantification of local variation in $\mathrm{SFR}_{\mathrm{H}\alpha}/\mathrm{SFR}_{\mathrm{FUV}}$. The most normal galaxies we find on visual inspection are NGC4321 (VCC596), NGC4208 (VCC157), and NGC4380 (VCC792). We highlight some key parameters of these galaxies, including their lopsidedness ($A_{1,\mathrm{global}}$) and their truncation (the slope, ∇ of the radial $\mathrm{SFR}_{\mathrm{H}\alpha}/\mathrm{SFR}_{\mathrm{FUV}}$ ratio) in Table 4.3. We also show their diagnostic plots in Figure 4.2, which shows the Voronoi binned significance (ζ) maps, the radial profiles of $\mathrm{SFR}_{\mathrm{H}\alpha}$ and $\mathrm{SFR}_{\mathrm{FUV}}$, respectively, and the ratio of these two values that is used to

NGC name	VCC name	$\log(M_*/\mathrm{M}_\odot)$	HI-def	σ from SFMS	$A_{1,\mathrm{global}}$	$\nabla(\mathrm{dex}/R_e)$
NGC4321	VCC596	10.83	0.41	-0.38σ	$0.16^{+0.01}_{-0.01}$	0.19 ± 0.13
NGC4208	VCC157	10.13	0.90	0.00σ	$0.12^{+0.03}_{-0.03}$	0.10 ± 0.09
NGC4380	VCC792	10.41	1.01	-1.68σ	$0.10^{+0.03}_{-0.03}$	0.08 ± 0.09

Table 4.3: Normal galaxies: cases of galaxies with no visual lopsidedness or truncation.

NGC name	VCC name	$\log(M_*/\mathrm{M}_\odot)$	HI-def	σ from SFMS	$A_{1,\mathrm{global}}$	$\nabla(\mathrm{dex}/R_e)$
NGC4351	VCC692	9.71	1.04	-1.97σ	$0.46^{+0.03}_{-0.04}$	0.00 ± 0.13
NGC4522	VCC1516	9.59	0.93	-0.48σ	$1.25^{+0.03}_{-0.03}$	-0.01 ± 0.05
NGC4402	VCC873	10.05	0.87	1.01σ	$1.32^{+0.06}_{-0.07}$	0.50 ± 0.18

Table 4.4: Cases of galaxies with clear visual lopsidedness.

measure the slope, ∇. The galaxy with the highest value of $A_{1,\mathrm{global}}$ is NGC4321 with 0.22, which is a median value amongst the sample. None of these galaxies have the negative slope, ∇ that we expect to be characteristic of truncated galaxies.

Lopsided galaxies

One of the key features that becomes readily apparent when looking at the ζ significance maps is a blue-to-red gradient, signifying a lopsidedness in the $\mathrm{SFR}_{\mathrm{H}\alpha}/\mathrm{SFR}_{\mathrm{FUV}}$ ratio. This can be seen in the ζ maps of the three galaxies shown in Figure 4.3: NGC4351 (VCC692), NGC4522 (VCC1516), and NGC4402 (VCC873). It is clear the arrow showing the global phase points along the visual direction of the gradient. We list their values of $A_{1,\mathrm{global}}$ amongst other parameters in Table 4.4. While each of these galaxies does have a slightly negative slope, ∇, none of them are particularly significant ($< 2\sigma$ from being flat).

Truncated galaxies

Finally here we show three galaxies with clear truncations: NGC4193 (VCC97), NGC4343 (VCC656), and NGC4535 (VCC1555). Each of these galaxies has a clear blue outer ring in their ζ maps shown in Figure 4.4, and has a slope, ∇ that is negative to at least 2σ significance. Each of these galaxies shows moderate lopsidedness. We list their parameters in Table 4.5.

NGC name	VCC name	$\log(M_*/\mathrm{M}_\odot)$	HI-def	σ from SFMS	$A_{1,\mathrm{global}}$	$\nabla(\mathrm{dex}/R_e)$
NGC4193	VCC97	10.27	0.48	-0.51σ	$0.30^{+0.05}_{-0.05}$	-0.16 ± 0.07
NGC4343	VCC656	10.16	0.75	-1.21σ	$0.25^{+0.06}_{-0.06}$	-0.33 ± 0.05
NGC4535	VCC1555	10.53	0.16	-0.47σ	$0.10^{+0.04}_{-0.04}$	-0.36 ± 0.13

Table 4.5: Cases of galaxies with clear visual truncation.

Table C.2 in Appendix C lists all 47 galaxies in our sample, along with their relevant parameters including lopsidedness and truncation, measured using both GALEX and UVIT FUV data, where available.

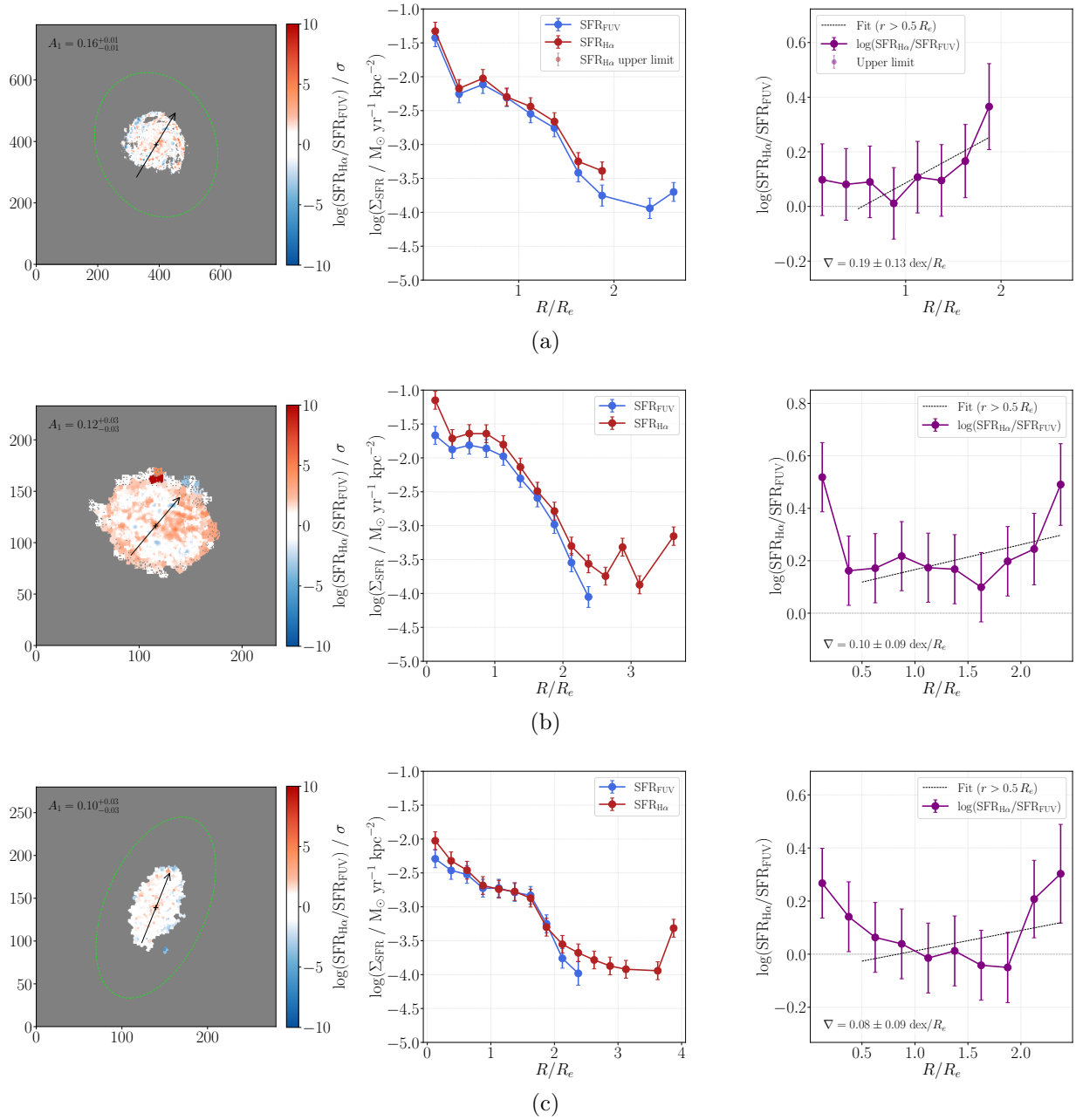


Figure 4.2: Diagnostic plots for three normal galaxies: VCC596 (NGC4321; top), VCC157 (NGC4208; middle), and VCC792 (NGC4380; bottom). The subplots show the Voronoi binned ζ image on the left, with the $A_{1,\mathrm{global}}$ value printed and the global phase shown with a black arrow (left); the SFR radial profiles as traced by both Hα and FUV (centre); and the log ratio of $\mathrm{SFR_{H\alpha}/SFR_{FUV}}$, with the best fit slope and uncertainty (right).

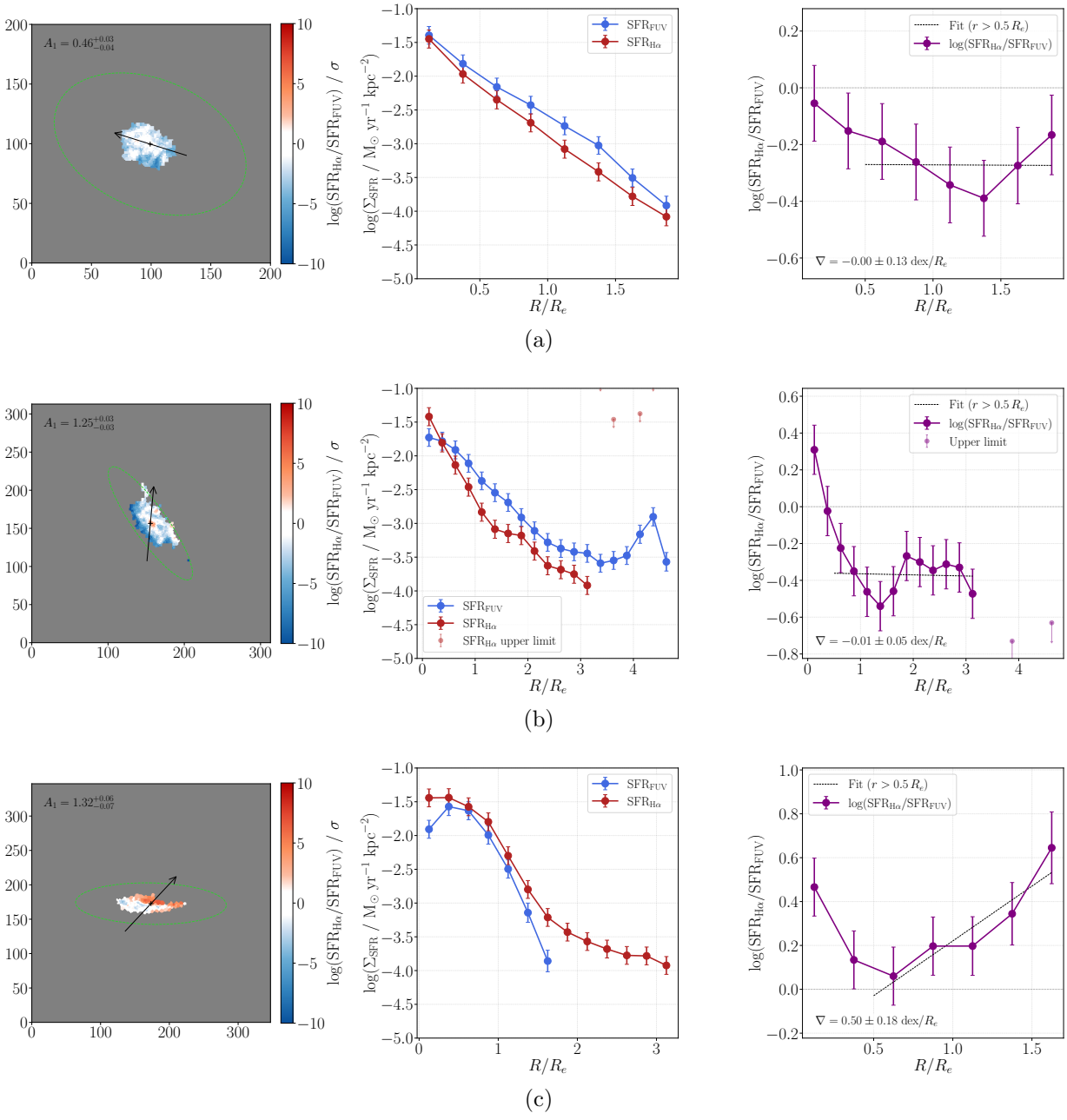
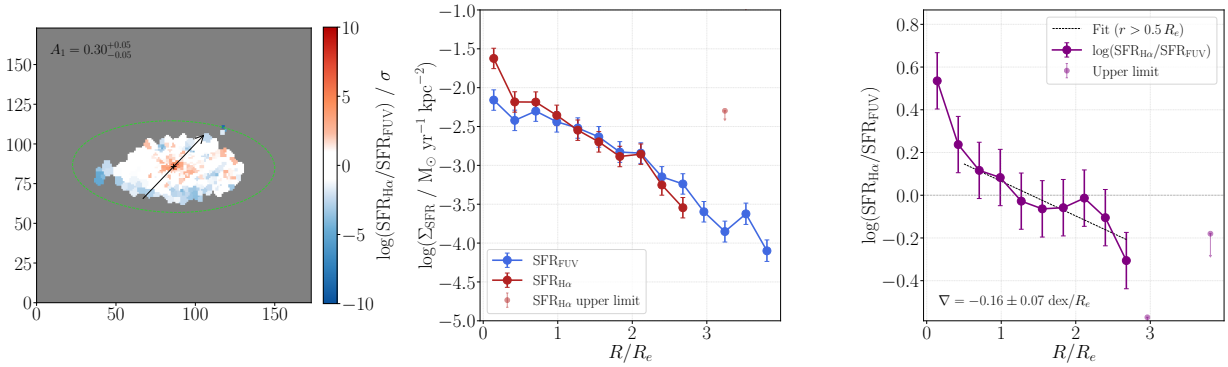
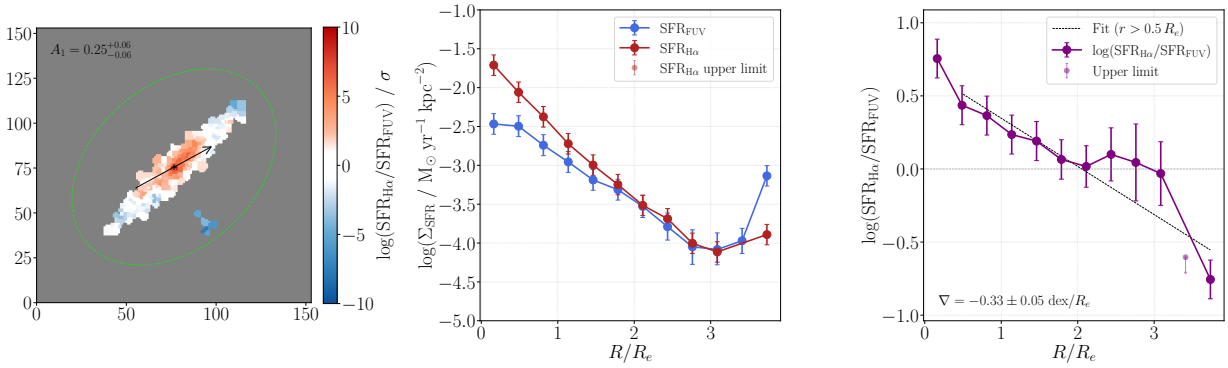


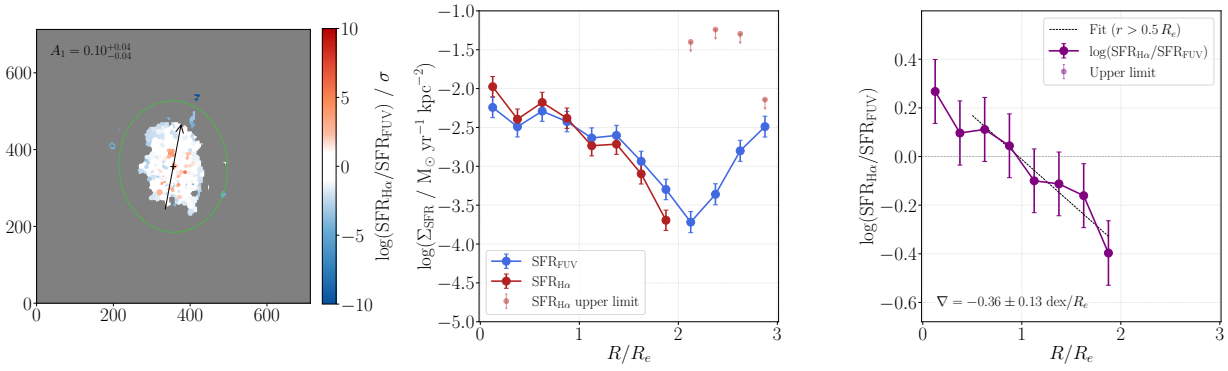
Figure 4.3: Diagnostic plots for three lopsided galaxies: VCC692 (NGC4351; top), VCC1516 (NGC4522; middle), and VCC873 (NGC4402; bottom). Subplots are the same as in Figure 4.2.



(a)



(b)



(c)

Figure 4.4: Diagnostic plots for three truncated galaxies: VCC97 (NGC4193; top), VCC656 (NGC4343; middle), and VCC1555 (NGC4535; bottom). Subplots are the same as in Figure 4.2.

4.4.2 $A_{1,\mathrm{global}}$ and ∇ versus ram pressure stripping classifications

The metrics we show here to describe lopsidedness and truncation based on the comparison of the Hα and FUV star formation rates may highlight specific quenching mechanisms that may be occurring such as RPS or starvation, or may capture a specific time in the quenching sequence of galaxies in the Virgo cluster. Many studies have looked at individual galaxies, or small numbers of galaxies in the Virgo cluster, using various means to determine if they are undergoing RPS. These various efforts have led to a list of ram-pressure candidates in Virgo, as listed in the Appendix of Boselli et al. (2022).

Additionally, we make a comparison to the classifications of Yoon et al. (2017). This study makes use of HI gas maps from the VIVA survey (VLA Imaging survey of Virgo galaxies in Atomic gas; Chung et al. 2009), and classifies galaxies based on truncations of the gas disk, gas deficiency, and asymmetries. The authors ultimately show that galaxies that appear to be undergoing active gas stripping tend to be on first infall into or just past first pericentre of the cluster, while those that show truncated disks tend to be further along their infall journey. The classes they employ are summarized as follows:

- Class 0: normal gas content, no truncations or asymmetries
- Class 1: fairly normal gas content, mild asymmetries
- Class 2: strongly asymmetric gas disk
- Class 3: symmetric, but severely truncated disk
- Class 4: symmetric, mildly truncated but low gas content

We show in Figure 4.5 our two key metrics, $A_{1,\mathrm{global}}$ versus the truncation slope (reported as ∇/σ_{∇} to show significance), with datapoints coloured according to their VIVA classification from Yoon et al. (2017) on the left, as well as based on whether they have been classified as undergoing RPS or not on the right. There are no strong trends with these other classifications, which is not entirely surprising. First, neither the VIVA work nor the Boselli et al. (2022) review necessarily provide a comprehensive list of galaxies undergoing RPS. Visually identifying RPS generally requires features such as asymmetries in the gas disk that may only be observable in the early stages of RPS. Secondly, our metrics are not exclusively meant to capture ram-pressure stripping, and we will discuss further interpretations for the morphologies we report in the comparison of $\mathrm{SFR}_{\mathrm{H}\alpha}$ and $\mathrm{SFR}_{\mathrm{FUV}}$. However, we do note that the galaxies with the largest values of $A_{1,\mathrm{global}}$ tend

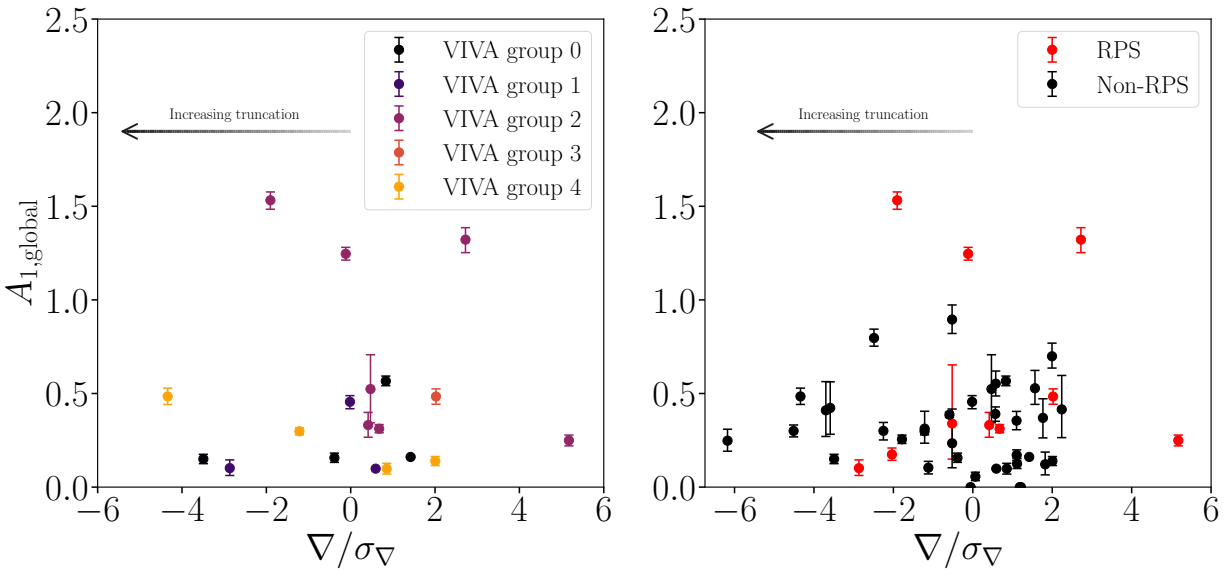


Figure 4.5: $A_{1,\mathrm{global}}$ versus ∇/σ_∇ for different gas stripping classifications. (left) Datapoints are coloured according to their class from VIVA (Yoon et al., 2017). (right) Datapoints are coloured based on whether they are listed as an RPS candidate in the review paper Boselli et al. (2022).

to belong to Class 2 which is the VIVA group with the highest HI asymmetries. However, the reverse is not true: not all galaxies in that group have high $A_{1,\mathrm{global}}$. This suggests that our measure of lopsidedness does not always correlate with asymmetry in the cold gas. It is also worth noting that since our $A_{1,\mathrm{global}}$ metric is run on the ζ significance maps, a wide range of $A_{1,\mathrm{global}}$ values is expected depending on the strength of the asymmetry, whether the lopsidedness is the entire disk or just local regions, and the strength of the phase coherence. Additionally, some of the galaxies that have been previously identified as RPS candidates are those with very large values of lopsidedness. However, not all RPS candidates have high lopsidedness values, suggesting that lopsidedness may only be an indicator of a certain stage of ram-pressure stripping.

4.4.3 $A_{1,\mathrm{global}}$ and ∇ versus other quenching indicators

It is interesting to see if our lopsidedness and truncation metrics correspond with other, global, measurements that may give indications of a the quenching state of a galaxy. Galaxy quenching is a function of stellar mass, with the quenched fractions in the Virgo cluster varying across the range of masses (Morgan et al., 2025, Chapter 2 of this thesis). In addition, we look at HI-deficiency and distance from the SFMS. These are two quenching indicators used in previous VESTIGE works, including Morgan et al. (2024, Chapter 3 of this thesis). The HI-deficiency compares the atomic gas content of a galaxy to normal galaxies of comparable stellar mass. A galaxy with an offset of > 0.4 dex from the normal relation is considered deficient. The distance from the SFMS is based on the main sequence derived for VESTIGE galaxies in Boselli et al. (2023a), and thus is derived solely from Hα-based SFRs. We show plots of $A_{1,\mathrm{global}}$ versus ∇/σ_{∇} in Figure 4.6, with the datapoints in each panel coloured based on stellar mass (top), HI-deficiency (middle), and distance from the SFMS (bottom). While there are no clear strong trends, it appears that galaxies with the most significant truncation measurements (∇/σ_{∇}) are on or near the SFMS, and have typically normal gas content, or are only mildly deficient. This suggests that this truncation metric can identify galaxies in the early stages of quenching, but is less effective when quenching has significantly proceeded.

We also compare with the results of Morgan et al. (2024) (Chapter 3 of this thesis). In that work, star-forming disk truncation was measured based on radial sSFR profiles constructed using VESTIGE Hα data. The radius of truncation (R_{sSFR}) was determined by finding a drop-off from the otherwise typically flat sSFR profiles. This was compared with a measure of the "expected" edge of the star-forming disk, based on previous studies of field galaxies (e.g. Chamba et al., 2022). The ratio of these two radii gave a measure of the strength of these truncations. While there were not strong trends with gas-deficiency or distance from the SFMS, moderately truncated disks were found to be ubiquitous across the Virgo cluster. We show in Figure 4.7 again our lopsidedness and truncation parameters, with datapoints coloured according to the truncation strength from Morgan et al. (2024). While there does not appear to be a correlation, even between the two different measures of truncation, it should be noted that these are actually significantly different measurements that could be tracing very different things. The results from Morgan et al. (2024) are interpreted as starvation kickstarting quenching early-on, slowly truncating the star-forming disk from the outside-in on much slower timescales than RPS. The truncation measurement from this work, however, gives information about how much *faster* the Hα disk is truncating compared to the FUV. If the Hα disk is substantially shrunk ($\nabla/\sigma_{\nabla} << -1$), this quenching has likely occurred within the past $\sim$ 100 Myr – the timescale difference

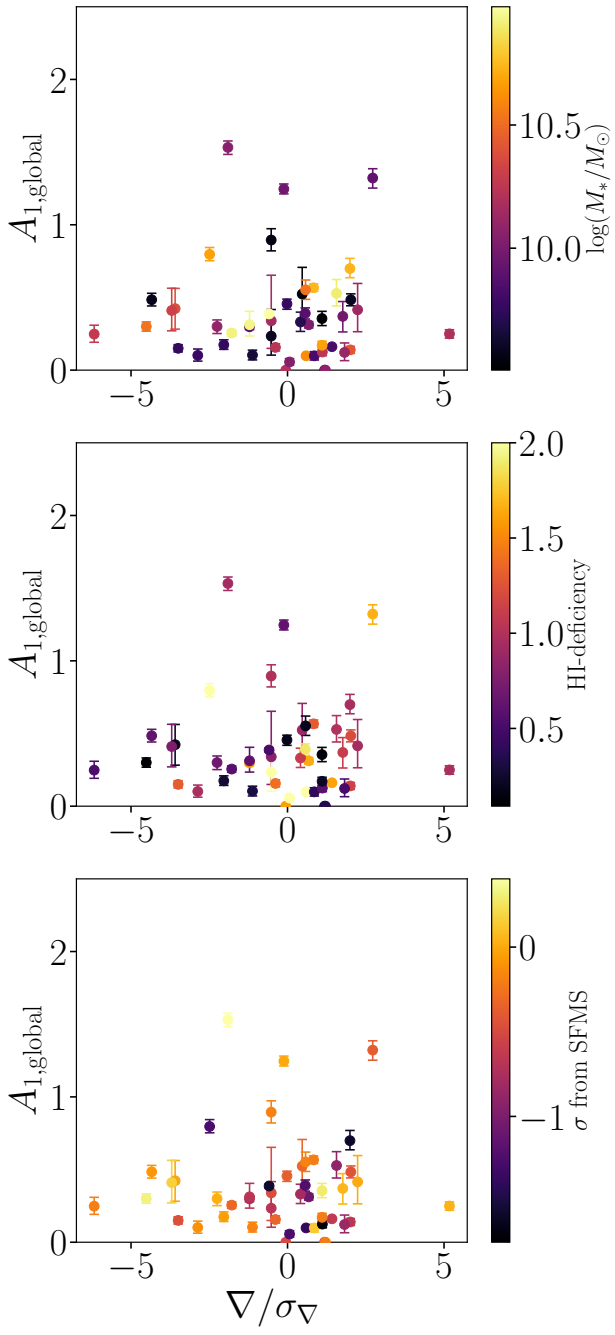


Figure 4.6: Same as Figure 4.5, but with datapoints coloured according to stellar mass (top), HI-deficiency (middle), and distance from the Boselli et al. (2023a) SFMS (bottom).

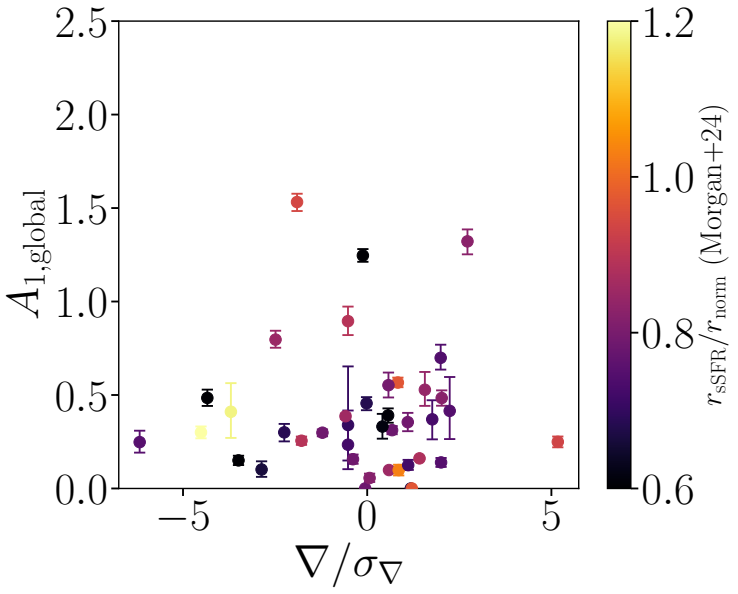


Figure 4.7: Same as Figure 4.5, but with datapoints coloured according to the strength of their star-forming disk break truncation as measured in Morgan et al. (2024).

between Hα and FUV as star formation tracers. This is more indicative of rapid quenching processes such as RPS, and we will discuss this further in Section 4.5.

4.5 Discussion

4.5.1 Effects of systematic uncertainties induced by flux corrections

In order to properly convert Hα and FUV fluxes into SFRs, we make corrections for dust attenuation (both), NII contamination (Hα) and pAGB star contamination (FUV). These corrections are necessary, but each induce their own statistical and systematic uncertainties. Here we discuss how some of these effects can be mitigated with IFU measurements from MAUVE. The Multiphase Astrophysics to Unveil the Virgo Environment (MAUVE; Catinella et al. 2025) project is a coordinated effort to combine IFU spectroscopy from VLA-MUSE and ALMA molecular gas observations to map out stellar populations and gas distributions across a sample of Virgo cluster galaxies. This effort is of course ex-

tremely complementary to existing Virgo cluster projects such as VESTIGE (Boselli et al., 2018a) and VERTICO (Brown et al., 2021).

Brown et al. (2026) showed early results from MAUVE-MUSE, highlighting resolved ionization and kinematic signatures of 12 galaxies. Five of these galaxies overlap with our sample. For these five galaxies, we then have resolved maps of emission lines beyond Hα. In our photometric analysis, we are unable to constrain the NII/Hα ratio directly for our galaxies, relying instead on similar galaxies from MaNGA. However, there is significant scatter in the median ratio from galaxy to galaxy, even at fixed stellar mass. Additionally, when we fit a dust attenuation model in `cigale`, we have little information that can be used to constrain the line reddening directly. Even though `cigale` technically fits $\mathrm{E}(B-V)_{\mathrm{lines}}$ as the main dust attenuation parameter, all of the information the model received from our photometry comes from the continuum, particularly the energy balance between the UV and the IR. In our main SED fits, we fix the ratio between $\mathrm{E}(B-V)_{\mathrm{lines}}$ and $\mathrm{E}(B-V)_{\mathrm{stars}}$ at 0.44. We tested varying this ratio, and even allowing this ratio to be a fit parameter, and found that $\mathrm{E}(B-V)_{\mathrm{stars}}$ did not change, but $\mathrm{E}(B-V)_{\mathrm{lines}}$ did, proving that all the constraining power in the dust attenuation model is in the continuum. However, with IFU data providing emission lines measurements, the Balmer decrement can be measured, adding significant constraint on $\mathrm{E}(B-V)_{\mathrm{lines}}$ and therefore improving the uncertainty on $A_{\mathrm{H}\alpha}$. We convolve and rebin the MAUVE IFU data to our GALEX pixel scale, and then calculate $\mathrm{E}(B-V)_{\mathrm{lines}}$ according to:

$$\mathrm{E}(B-V)_{\mathrm{lines}} = \frac{2.5}{k(H\beta)-k(H\alpha)} \log\left(\frac{F(H\alpha)/F(H\beta)}{2.86}\right), \tag{4.9}$$

where $k(H\beta)$ and $k(H\alpha)$ are the extinction coefficients for the Hα and $H\beta$ lines, respectively, based on the Cardelli et al. (1989) Milky Way extinction curve, and 2.86 is the theoretical, intrinsic Balmer decrement. We show in Figure 4.8 the map of $\mathrm{E}(B-V)_{\mathrm{lines}}$ and the ratio of $\mathrm{E}(B-V)_{\mathrm{lines}}/\ \mathrm{E}(B-V)_{\mathrm{stars}}$ on the right, where in both cases $\mathrm{E}(B-V)_{\mathrm{lines}}$ is calculated from the MAUVE IFU data and $\mathrm{E}(B-V)_{\mathrm{stars}}$ is calculated from the `cigale` SED fits. For each of the five MAUVE galaxies we run, we find that the median values of the ratio $\mathrm{E}(B-V)_{\mathrm{lines}}/\ \mathrm{E}(B-V)_{\mathrm{stars}}$ is similar to the value of 0.44 adopted in our SED fits. However, some galaxies do have localized regions of higher or lower ratios. In this work, we do not re-run our SFR analysis with these additional dust maps, given that relative to the other uncertainties already associated with dust in our analysis, the results are not likely to change significantly. We leave this analysis for a future project with a larger sample of MAUVE IFU galaxies, though we show the reddening maps (the analogues to Figure 4.8) for the four additional MAUVE galaxies in our sample in Figure C.3 in Appendix C.

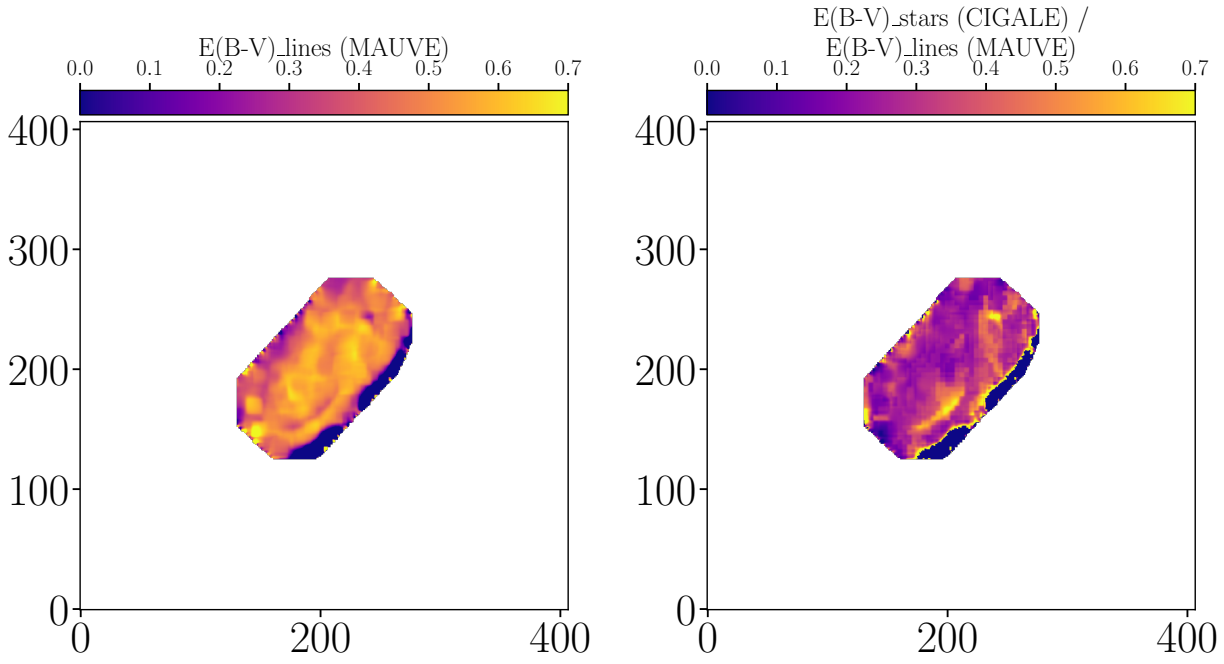


Figure 4.8: (*left*) Line reddening, $\mathrm{E}(B-V)_{\mathrm{lines}}$, determined from the Balmer decrement from MAUVE IFU emission lines. (*right*) Ratio of $\mathrm{E}(B-V)_{\mathrm{lines}}$/ $\mathrm{E}(B-V)_{\mathrm{stars}}$, using IFU data for the line reddening and the SED fits for the stellar continuum attenuation.

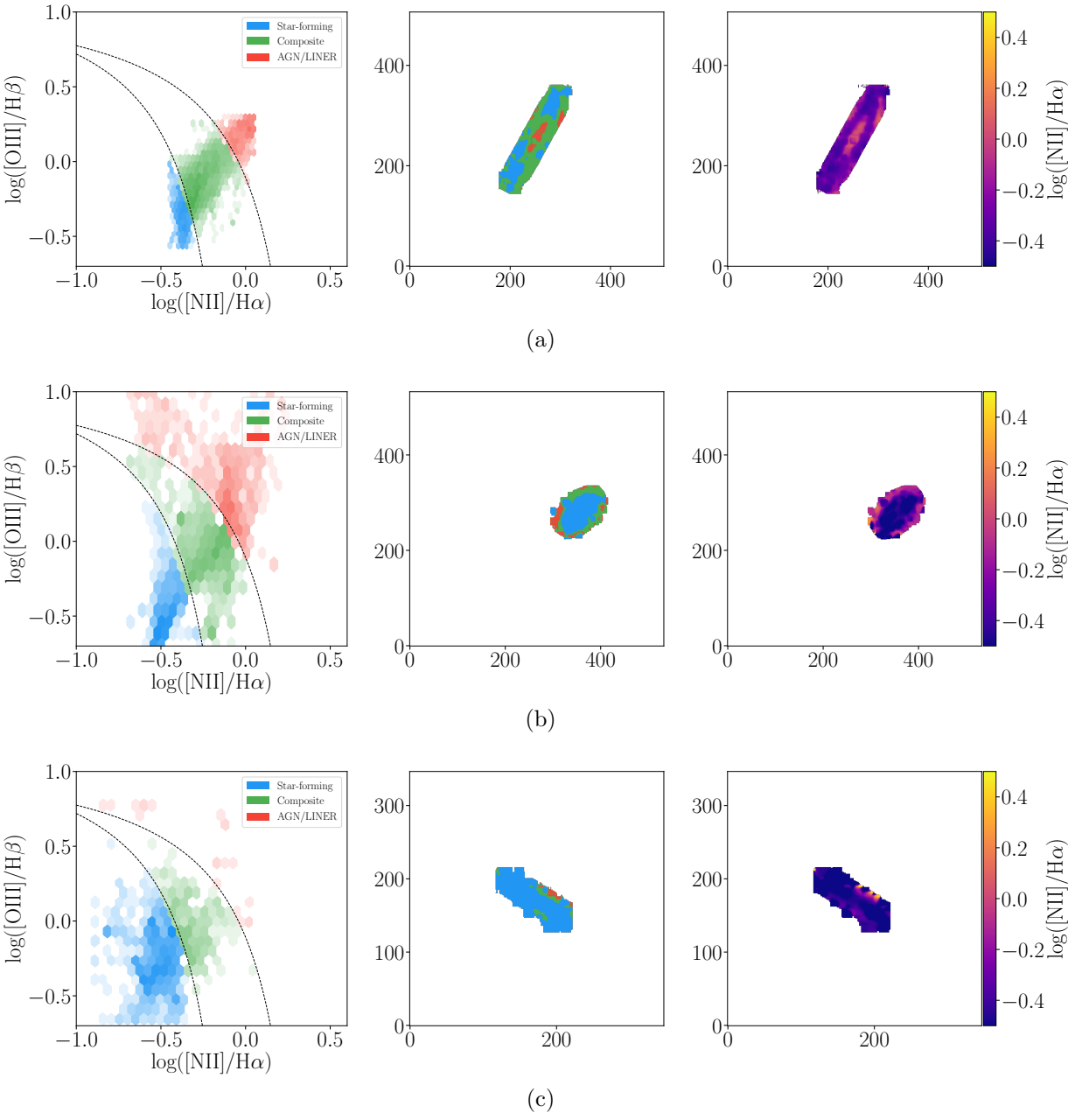
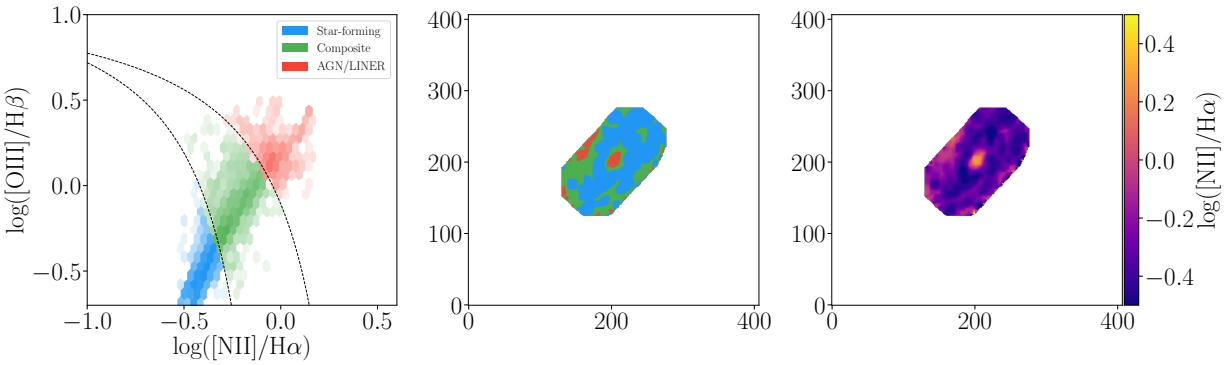
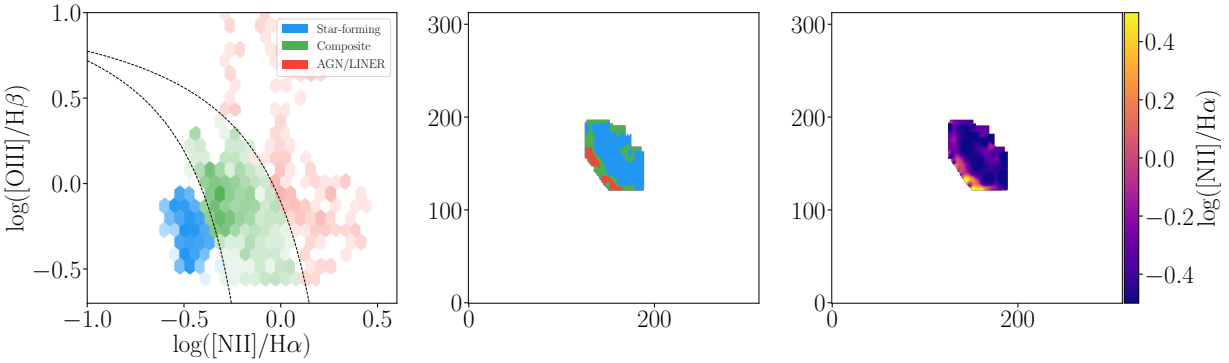


Figure 4.9: Emission line ratio diagnostics for VCC 92 (a), VCC 483 (b), and VCC 630 (c).



(d)



(e)

Figure 4.9: Emission line ratio diagnostics for VCC 92 (a), VCC 483 (b), VCC 630 (c), VCC 1401 (d), and VCC 1516 (e). (*left*) BPT diagram for individual spaxels, showing density in the star-forming, composite, and AGN/LINER regions. The dashed lines show the curves presented in Kewley et al. (2006) and Kauffmann et al. (2003). (*centre*) Spatial map of the galaxy IFU data, with spaxels coloured according to their location on the BPT diagram. (*right*) NII/ha ratio map from MAUVE IFU data.

Perhaps more significantly, the IFU data allows us to constrain the NII/Hα ratio directly on the galaxy. This will essentially remove the systematic uncertainty we include due to the galaxy-to-galaxy variation of the median NII/Hα ratio in the MaNGA data. We can also explore for these five galaxies the spatial variation in this line ratio, and use resolved BPT diagnostics to determine if there are regions of the galaxy where the line emission is not dominated by star formation. If this is the case, then we have doubly overestimated the $\mathrm{SFR}_{\mathrm{H}\alpha}$ in these regions – first, due to the higher NII/Hα that arise due to other sources of ionization, and then additionally from the fact that some fraction of the remaining Hα emission will not actually be due to star formation at all.

We show in Figure 4.9 the resolved emission line ratios on a BPT diagram (left). In the centre subplots we then show which spaxels are located in the star-forming, composite, and AGN/LINER regions of the BPT diagram. Finally we show the maps of the NII/Hα ratios on the right most subplots. Of the five galaxies, each is dominated by star-forming spaxels with significant regions of composite emission (except for VCC 92 where the composite spaxels cover a similar area to the SF spaxels). Some galaxies have small regions with LINER-type emission, particularly in the centres of VCC 92 and VCC 1401, and along the merging edge of VCC 483.

We run a test where we include the resolved NII/Hα ratio map from MAUVE in our analysis for VCC 92, which is chosen because of the five MAUVE galaxies, it has the most spatial variation in the emission line ratios. However, we do not find a significant change in the results, even with the lower uncertainty on the NII/Hα ratio. It is worth noting, however, that regions in the galaxy that have composite or AGN/LINER emission may have some of their Hα emission not attributed solely to star formation. In this case, our $\mathrm{SFR}_{\mathrm{H}\alpha}$ may be somewhat overestimated, which could explain the substantial red regions seen in some ζ maps. However, a comprehensive IFU survey is needed to analyze the spatial variation of emission line ratios in Virgo galaxies at a statistical level. This could potentially be probed using MAUVE in the future once the IFU data for the full sample of galaxies is obtained.

4.5.2 Timescales associated with local quenching

We discuss the morphological features we find in our ζ maps within the context of quenching timescales. Galaxies undergoing RPS are expected to quench fast – the timescales associated with this quenching mechanism are often on the order of several hundred Myr, comparable to the time a galaxy takes to infall from R_{200} to first pericentre. Assuming that gas stripping is efficient, this should leave visible signatures in the ratio of $\mathrm{SFR}_{\mathrm{H}\alpha}/\mathrm{SFR}_{\mathrm{FUV}}$.

Our measure of ∇/σ_∇ provides a measure of this – a negative gradient in the ratio of $SFR_{H\alpha}/SFR_{FUV}$ shows that star formation is ceding from the outside-in on timescales on the order of 100 Myr. This is evident by the remaining FUV-driven star formation (100 Myr timescales) and the relative absence of ongoing star formation traced by the Hα.

The toy models used in Morgan et al. (2024, Chapter 3 of this thesis) show how RPS and starvation can both shrink the SF disk of a galaxy. However, these processes occur on different timescales. In that work, starvation was invoked to explain the moderately truncated disks found in the infall regions of the cluster. By modelling an exponential SFR profile, along with HI and H_2 gas profiles from works such as Bigiel et al. (2008), it was shown that RPS could rapidly truncate the disk within the time it takes a galaxy to reach first pericentre, while starvation would take much longer, slowly truncating the disk before RPS took hold. It is unlikely, then, that the truncations we measure based on the $SFR_{H\alpha}/SFR_{FUV}$ ratio in this work are due to a slow process such as starvation. A significant negative gradient in the $SFR_{H\alpha}/SFR_{FUV}$ implies a process that is acting on much quicker timescales. Interestingly, we do not find significant trends with other indicators of quenching mechanisms, or with location within the cluster. This alludes to the complex environment of the Virgo cluster, which makes it difficult to understand the population of galaxies within the cluster as a whole without being able to probe the infall histories of individual members.

A high degree of lopsidedness could be another signature of RPS that may not be always correlated with other signatures. A galaxy undergoing RPS may have reduced star formation along its trailing edge with a potential for an induced burst along the leading edge. This would appear as a strong, coherent lopsidedness in the galaxy's ζ significance map. However, since this metric does not always seem to correlate strongly with other indicators of gas stripping, it is difficult to conclude whether lopsidedness is a pure signal of RPS.

4.6 Summary and conclusions

In this study, we have analyzed resolved maps of SFR in Virgo cluster galaxies, using Hα and FUV as tracers of ongoing and recent star formation. To empirically calculate SFR from these tracers, it is necessary to make corrections to the fluxes due to dust attenuation and contamination. This necessitates performing spatially-resolved SED fitting, using the abundance of multi-wavelength photometry available to constrain galaxy parameters. From these fits, we can determine the dust attenuation to apply to our fluxes, as well as the contribution of FUV flux coming from evolved stellar populations. Using star-forming

galaxies from MaNGA, we are able to determine the typical NII contamination in narrow-band Hα photometry. After making these corrections, we derive $\mathrm{SFR}_{\mathrm{H}\alpha}$ and $\mathrm{SFR}_{\mathrm{FUV}}$ maps. We compare the two on 2D Voronoi binned maps, creating an image of the significance of the logged ratio between the two SFRs, ζ. We also look at 1D radial trends in this ratio.

We note two interesting features in our sample galaxies, and derive metrics to measure them. The first is lopsidedness, which is quantified by measuring the amplitude and phase of the first Fourier mode in radial bins. The global value $A_{1,\mathrm{global}}$ is highest for galaxies with large amplitude values across several bins, with coherent phase. The second metric is a disk shrinking or truncation where the outer part of the galactic disk has significantly more SFR as measured by FUV than by Hα. This is quantified by measuring the slope of the $\mathrm{SFR}_{\mathrm{H}\alpha}/\mathrm{SFR}_{\mathrm{FUV}}$ ratio of the galaxy from the centre toward the outskirts – the more negative a slope, the faster and more significant the disk shrinking.

Our results are summarized as follows:

- Nearly half of the galaxies in our sample exhibit significant lopsidedness ($A_{1,\mathrm{global}} > 0.3$), a significant truncation ($\nabla/\sigma_{\nabla} < -2$), or both.
- When comparing with galaxies grouped by HI disk truncation or asymmetry, the most lopsided galaxies in our sample are in the most asymmetric HI class. However, the reverse is not necessarily true.
- The galaxies with the largest lopsidedness values have been identified as RPS candidates by previous studies. However, not all previous RPS candidates have high lopsidedness. This may indicate that the lopsidedness metric is sensitive to a certain stage of RPS, or could be associated with other mechanisms as well.
- Otherwise, there are no strong trends in lopsidedness or truncation with other quenching indicators, such as HI-deficiency, distance from the (Hα) star-forming main sequence, or truncation ratio from Morgan et al. (2024, Chapter 3 of this thesis). However, the most truncated galaxies do appear to be in the early stages of quenching, suggesting that these metrics may be less effective once quenching has proceeded for some time.
- We explored the use of IFU data available from the MAUVE survey available for five of our galaxies to improve the constraints on emission line reddening and the NII/Hα ratio, but found that our results did not change significantly. However, some galaxies have a significant fraction of pixels that lie in the composite region of the BPT diagram, meaning their $\mathrm{SFR}_{\mathrm{H}\alpha}$ may be overestimated. Future studies

with datasets such as MAUVE, with large IFU coverage for Virgo galaxies will allow detailed studies of sources of emission lines.

- Both truncation and lopsidedness in the ratio of $SFR_{H\alpha}/SFR_{FUV}$ could be physical signatures of processes such as RPS that are rapidly quenching galaxies from the outside-in, suppressing star formation along the trailing edge and inducing it on the leading edge. However, further work will need to be done to test these metrics against other signatures, and model how other quenching mechanisms may affect this ratio.

Chapter 5

A Look Ahead

Astrophysics has firmly entered into the era of "big data". With the recent launch of Euclid, recent first light of Rubin, and the prospects of Roman coupled with future radio arrays such as SKA, we are seeing the possibility for massive studies of galaxy evolution out to, and even beyond, cosmic noon. Previously, it was only with the Hubble Space Telescope (HST) and, more recently, the James Webb Space Telescope (JWST), that we could probe galaxies in the early Universe. However, these studies were limited to small samples due to the small field-of-view of these telescopes. Still, studies with HST set the baseline for high-redshift galaxy evolution, with JWST still pushing the frontier to the very earliest epochs of the Universe.

With JWST, we have been able to observe the very first galaxies in the Universe. A surprising discovery what that some of these early galaxies are much more massive than predicted by cosmological models (e.g. Castellano et al., 2022; Labbé et al., 2023; Naidu et al., 2026). This prompted follow-up studies, both observational and theoretical, that have argued in favour (e.g. Boylan-Kolchin, 2023) or against (e.g. Xiao et al., 2024) the idea that these early galaxies could be misaligned with ΛCDM. In addition, JWST has allowed the discovery of objects such as "little red dots" – compact red objects that do not fit into our existing understanding of galaxy types (e.g. Matthee et al., 2024; Kocevski et al., 2025). Follow-up has predicted these objects could actually be "black-hole stars" where a central massive black hole is actively accreted from a massive star inside which it is contained (e.g. Naidu et al., 2025; de Graaff et al., 2025). In the next decade, we will see first light from at least one of the planned extremely-large telescopes, which will employ next-generation adaptive optics to supersede JWST resolution from the ground.

Other new instruments and surveys will also allow us to map galaxies and the cosmic

web in more detail than ever before (e.g. Euclid Collaboration et al., 2025a,b,c). We have covered thousands of square degrees previously with surveys such as SDSS, but not with anywhere near the depth that Euclid, the Roman space telescope, and the Rubin observatory will probe. Even in wide surveys, millions of galaxies will be detected and measured beyond cosmic noon. And beyond that, the selected deep field surveys will push much, much deeper. The second key improvement is spatial resolution. Given that Euclid and Roman are both space based, the spatial resolution of galaxies at high redshift will be unprecedented – sub-kpc scales beyond $z = 2$.

Finally, with the advent of the Square Kilometre Array (SKA), we will gain an unprecedented look at radio wavelengths that trace neutral hydrogen (e.g. Wang et al., 2026). Being able to look at the gas within galaxies is an important complement to studies of stellar populations and star formation. Alongside SKA, the Atacama Large Millimetre Array (ALMA) will continue to be a powerful instrument for observing tracers of cold molecular gas – the direct fuel that feed star formation in galaxies.

The combination of all these instruments and surveys will push the study of galaxy evolution into a new era of massive datasets of galaxies at high-redshift, allowing both a detailed look at galaxies and their stellar and gaseous components, but also huge statistical samples to aid in effort to understand population scale evolution. In the following sections, I focus on a few proposed instruments for which I have played a role in the scientific development. Following that, I discuss a few broad areas of galaxy evolution that will benefit from these datasets, and the methodology that will be necessary to take full advantage of these data.

5.1 New Canadian-led instrumentation

5.1.1 Cosmological Advanced Survey Telescope for Optical and UV Research (CASTOR)

CASTOR is a proposed, Canadian led, UV-optical survey telescope. With the advent of instruments like Euclid and Roman, a gap is left in imaging rest-frame UV wavelengths out to cosmic noon. CASTOR would be entirely complementary to these instruments and fill this wavelength gap. CASTOR will have comparable resolution to the Hubble Space Telescope, but will have similar survey capabilities to GALEX, meaning Hubble-level depth and resolution but with 100x faster survey speed. In addition to wide and deep field photometry, CASTOR will have UV grism and MOS capabilities. The goals of

CASTOR extend to various subfields of astronomical research, but we focus primarily here on the survey capabilities for galaxy research.

The CASTOR Wide Survey will image the same 2227 deg^2 as the Roman High Latitude Survey, providing the blue-optical and UV photometry to complement Roman's IR bands. Even in this survey, a g-band depth of ~ 25.56 mag will allow measurements of UV-traced star formation and UV upturn populations in galaxies out to cosmic noon, the era of peak cosmic star formation. Perhaps more vital for galaxy evolution research, though, will be the CASTOR Deep and Ultra-deep Surveys, with 5 and 50h integration times, respectively. The Deep Survey will cover 83 deg^2, overlapping with Euclid and LSST deep fields, and will image approximately 40 million galaxies down to the dwarf regime, out approaching cosmic noon, reaching a UV depth of 28.31 mag. A 1 deg^2 Ultradeep Survey will push this even further, allowing pixel-based star formation measurements and SED fitting out to cosmic noon and beyond, reaching a UV depth of 29.61 mag.

I explored how well galaxies will be able to have their UV morphologies measured with the CASTOR Deep and Ultradeep Surveys. This is a crucial aspect of being able to measure the distribution of star formation in high-redshift galaxies, and constrain quenching mechanisms. To do so, galaxies were selected from the COSMOS field, where CASTOR fluxes were estimated and Sérsic parameters and redshifts had been measured. We simulated these galaxies using the CASTOR optics and filter curves and adding the necessary noise. We then used STATMORPH to measure the morphological parameters and evaluated the recovery. We show the results of this study in Figures 5.1 and 5.2. The former figure shows the size-magnitude relation for the galaxies tested. Each panel has the datapoints colour-coded by a different indicator of the success of the fit recovery: the error in the recovered size, the standard deviation of ten realizations in the fit where we vary the random noise, and the signal-to-noise per pixel. We mark the manually chosen region where the best fits occur. This region excludes galaxies that have an effective radius of less than approximately two pixels, and regions where the surface brightness of galaxies is very low, either due to very extended galaxies and/or galaxies with lower integrated fluxes. Overall, with the CASTOR Deep Survey, we expect to be able to measure Sérsic parameters of 2.5 million galaxies, based on the coverage, and the number density of galaxies that fall into the "good fit" range on these plots. Figure 5.2 sums up the results by showing the physical size-mass relation of galaxies in three redshift bins out to $z = 2.5$. The contours show the number density from the full sample of COSMOS galaxies, with the greyscale then showing the fraction of these galaxies that return a good fit in our tests.

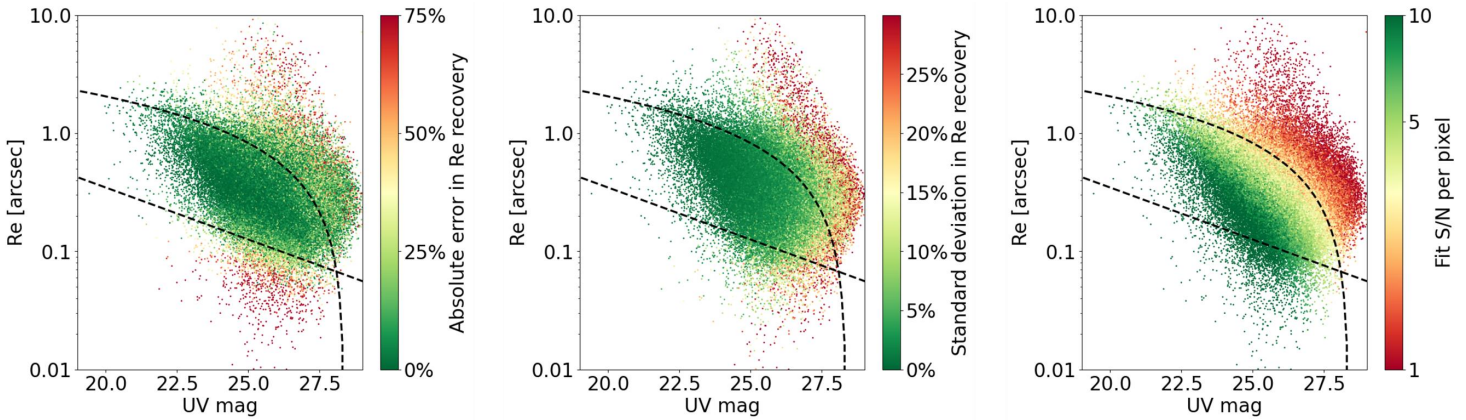


Figure 5.1: The size-magnitude relation of galaxies from the COSMOS catalogue simulated with CASTOR optics. In each panel, the colour of the datapoints show a different measure of the success of the recovery of the size parameter: *Left:* the error in the recovered size; *centre:* the standard deviation of ten realizations with the random noise varied; *right:* the average signal-to-noise per pixel of the galaxy. In each panel, the dashed curves represent a visually-chosen region encompassing good effective radius recovery based on the three uncertainty metrics.

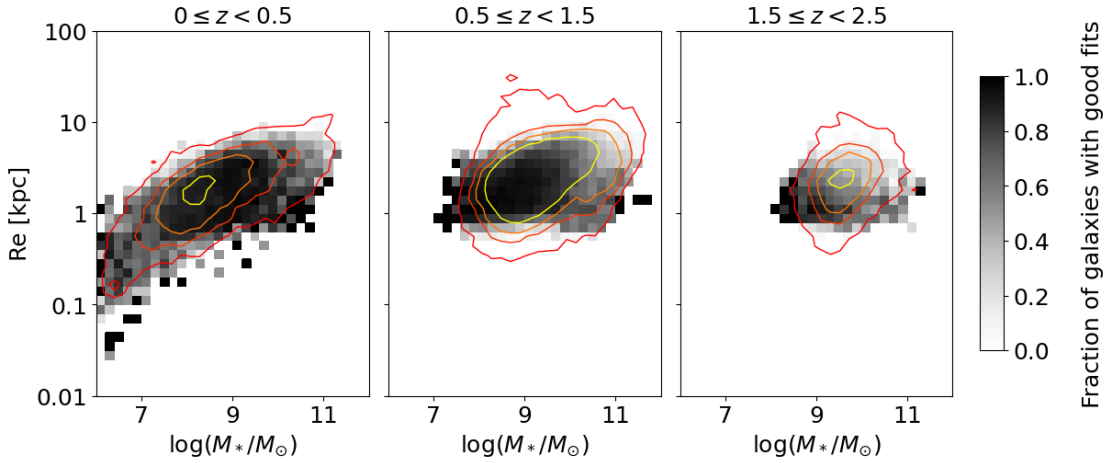


Figure 5.2: Size-mass relations of COSMOS galaxies simulated with CASTOR optics in the UV filter. The greyscale data shows the fraction of galaxies within the given bin for which good Sérsic fits were recovered. The overplotted contours represent the total (good and poor fits) number density of galaxies in each bin, with contour levels at 10, 50, 100 and 200 galaxies per bin. The sizes of the bins are 0.2 dex in stellar mass and 0.1 dex for effective radii.

5.1.2 Gemini Infrared Multi-Object Spectrograph (GIRMOS)

Integral field unit (IFU) spectroscopy is arguably the most powerful form of spectroscopy. It produces a three dimensional data cube, with two spatial dimensions like photometry, and spectra for each pixel in the third dimension. When entire galaxies can be imaged in the field of view of an IFU instrument, spatially-resolved information about emission lines can be achieved, and detailed kinematics can be modelled.

IFU instruments and surveys such as MaNGA (Bundy et al., 2015) and MUSE have been groundbreaking for the spatially-resolved spectroscopy they provided for thousands of low-redshift galaxies. We are also seeing instruments with high-redshift capabilities, such as KMOS and ERIS on VLT. Each of these instruments has its own strength – KMOS is a multi-object instrument, meaning it has strong survey capabilities. ERIS, on the other hand, is a single-object instrument but has new and improved adaptive optics capabilities to improve the spatial resolution of its observations. Both of these instruments have had successful GTO programs that are setting the stage for high-redshift IFU surveys. JWST

also has NIR and MIR IFU instruments – however, ground based adapative optics on large telescopes can actually achieve better resolution than JWST here. JWST instruments are powerful in their wavelength coverage, pushing into the MIR.

GIRMOS is designed to be the best-of-both-worlds ground based IFU, combining the strengths of KMOS and ERIS. GIRMOS will have multiplexing capabilities, with four arms that can independently measure four fields. GIRMOS will employ multi-object adaptive optics as well, with a novel and innovative system that combines a closed loop ground layer correction over the entire field with independent, high-altitude corrections performed for each of the GIRMOS arms independently.

The GIRMOS science team put together a comprehensive GTO proposal that exemplified the capabilities of GIRMOS for galaxy evolution science and beyond. This included a proposal that I led to probe galaxy quenching and the origins of the green-valley at cosmic noon. We showed how with GIRMOS, we could map out star formation in galaxies across various environments and in relation to the SFMS. By extracting the rest-frame Hα emission line, we could construct radial profiles of SFR and sSFR, which have been shown to be able to diagnose signatures of various quenching mechanisms, as discussed in Chapter 3 of this thesis, as well as studies such as Belfiore et al. (2017, 2018), Nelson et al. (2021), and Lawlor-Forsyth et al. (2026).

Of course the benefits of GIRMOS data are not in just Hα fluxes, but in gas kinematics and a suite of emission lines. We showed that outflows would be detectable for a sample of cosmic noon galaxies, and we could determine their prevalence, as well as the prevalence of turbulence and its correlation with star formation. With deep enough observations to measure other emission lines, BPT diagnostics could be performed on resolved, or at least Voronoi binned scales for these galaxies, providing novel insight into the prevalence of LIER emission at cosmic noon, and helping to determine if it is a driver of green-valley galaxies as has been shown at low-redshift (Belfiore et al., 2017, 2018).

GIRMOS ultimately will be a transformational instrument, providing the next generation of AO-fed IFU capabilities. Beyond the science that will be done with GIRMOS itself, it will set the stage for what will be possible as we move from 8m-class telescopes to 30m class telescopes. These instruments, such as HARMONI on E-ELT, will benefit from the innovation of GIRMOS.

5.2 The cosmic web at cosmic noon

In the past few years, we have seen the push to map the structure of the cosmic web on detailed scales and out to high redshift. Instruments such as the Dark Energy Spectroscopic Instrument (DESI; DESI Collaboration et al. 2016, 2022) were designed for the sole purpose of measuring the positions of redshifts of as many galaxies as possible. This effort has enabled the creation of the most detailed maps of the structure of our Universe out to $z \sim 1.6$. Beyond constraining the nature of dark energy, these maps are also crucial for characterizing the environments in which galaxies live. New instruments will use this baseline to build these maps out to beyond cosmic noon, adding additional high-resolution photometry and slitless spectroscopy. Another advantage instruments such as Euclid will bring to the table is their weak lensing methodology to trace dark matter directly instead of just the luminous portion of galaxies (Laureijs et al., 2011).

5.2.1 The spectrum of galaxy environments

The traditional approach to studying galaxy evolution across environment is a cluster versus field approach. It is relatively easy to identify galaxy clusters, using various means such as spectroscopic samples (e.g. Diaferio & Geller, 1997) or the cluster red sequence (e.g. Gladders & Yee, 2000), and then to define a field sample as galaxies isolated from these clusters . However, the true environment of a galaxy is less binary and better defined along a spectrum. Sometimes, the local density around a galaxy is used to infer how isolated (or not) the local environment is. The majority of galaxies in the low-redshift Universe live in groups, and thus are not truly evolving in isolation (e.g. Eke et al., 2004). These loosely-defined groups are a key part of the cosmic web structure, containing filaments and sheets connecting the massive halos of galaxy clusters.

Especially at low-redshift, we have started to explore galaxy evolution in these environments in more detail. Complimentary to the Virgo cluster studies presented in this thesis, the Virgo Filaments Survey is studying the environment out to $\sim 12R_{200}$ around the Virgo cluster. They are finding evidence for pre-processing of galaxies in filaments and groups connected to the cluster, adding direct evidence to the inferences we made in this work that suggest pre-processing outside the cluster to be a vital step in the environmental quenching sequence of galaxies in the Virgo cluster region. Broad studies uses surveys such as SDSS and GAMA have identified filamentary structures and shown that galaxies located within and near to filaments have lower star formation rates and are more likely to be early-type (e.g. Kuutma et al., 2017; Kraljic et al., 2018). At $z \sim 1$, work in

the COSMOS field (e.g. Darvish et al., 2014, 2017; Laigle et al., 2018) have found both suppression and enhancements to star formation in the cosmic web structure, implying the need for larger scale surveys.

Cluster and group environments have been probed at $z \sim 1$. As part of the Galaxy Environment Evolution Collaboration 2 (GEEC2) project, Balogh et al. (2014) identified 11 groups via faint X-ray emission. The Gemini Cluster Astrophysics Spectroscopic Survey (GCLASS; Muzzin et al. 2012) and the Gemini Observations of Galaxies in Rich Early Environments survey (GOGREEN; Balogh et al. 2017, 2021) studied large, early clusters identified via the cluster red sequence method and their Sunyaev-Zeldovich signature. An overarching result from studies stemming from these surveys is that the separability of mass and environment quenching seen in the local Universe does not hold at higher redshift – the quenched fraction excess in clusters compared to the field at this redshift is strongly mass dependent (e.g. Balogh et al., 2016; van der Burg et al., 2020). With surveys such as those performed with Euclid, the cosmic web around cluster and protocluster environments will be mapped out beyond cosmic noon, the time when the first clusters were forming. This will be critical for large-scale characterization of local galaxy environments across a broad redshift range. Various studies can then be undertaken to observe how galaxies evolve based on their local environment from the time of protoclusters to the present day. This will include deep studies in fields such as the Euclid Deep Field-North (EDF-N), where deep grism spectroscopy will make it possible to trace emission lines such as Hα on spatially resolved scales. Coupled with surveys such as the Deep Euclid u-band Survey (P.I. M. Sawicki), which will trace the rest-frame UV in this field out to cosmic noon, detailed studies of star formation burstiness can be undertaken for large samples of galaxies, building on the work we have presented here, and connecting higher redshift observations with those of local environments.

5.3 Improving spatially-resolved galaxy studies

The work presented in this thesis made use of multi-wavelength, spatially-resolved photometry. Access to this type of data is essential to constrain physical properties of galaxies on resolved scales. However, multi-wavelength data is rarely homogeneous in depth and resolution. Typically, datasets from different surveys with different instruments with different capabilities are put together. While this is essential, one often finds themselves limited by their worst dataset. Even in the case of the Virgo cluster studies we have undertaken, where much of the data were obtained from specific Virgo cluster surveys, there are still substantial differences in the quality of the data across the wavelength range. We find

ourselves limited in resolution by our FIR data from Herschel, since the diffraction limit of an optical system depends on wavelength.

In spatially-resolved SED fitting studies, such as that presented in Chapter 4, photometric data is often then convolved and binned to the lowest resolution data, and the resolved SED fits are done on that scale. This means that all fit parameters are only constrained on these poor scales. While we then upscale these parameter maps to the scale of our UV data, there is still an uncertainty associated with this upscaling. Ultimately this means information from the highly-resolved data is being wasted. Each pixel is also fitted individually. That is to say, fitting 1000 pixels in one galaxy is the same as fitting integrated light for 1000 galaxies – correlations between pixels are not accounted for.

This is a limit to spatially-resolved SED fitting capabilities that can be improved upon. With high-resolution, space based survey instruments such as Euclid and Roman coming online, we must move away from treating galaxies solely as integrated quantities, and therefore the analysis tools we use must be upgraded in tandem. There are various SED fitting tools that have been developed to have specific advantages, as we highlighted in Section 1.4.1. The methodologies from any of these fitters can be used to build a two-dimensional SED fitting tool. At its core, a spatially-resolved SED fitting tool should generate model parameter maps at the highest necessary resolution and forward model flux maps *at this model resolution*. Then, convolve and rebin to the native resolution of each instrument for which there is observed flux maps, and compare *at the instrumental resolution*. Additionally, a resolved SED fitting tool should account for correlations between neighbouring pixels, and propagate covariances along with per-pixel uncertainties. Gaussian process priors are one tool that can used to constrain the smoothness of certain parameter maps over a given scale. Additionally, one could add two-dimensional models such as Sérsic profiles to help with this. Finally, constraints on integrated quantities could be built in as well.

One of the obvious difficulties with this hierarchical resolved SED fitting is how computationally expensive it could be. Instead of fitting individual pixels at the lowest resolution scale of the data, maps would be created at the highest resolution scales. In our example, this would be the difference between fitting at the $6''$ pixel scale of the 250μm SPIRE data and fitting at the $0.187''$ pixel scale of the CFHT data – a $\sim$ 1000x increase in the number of pixels. This way of fitting can also not be straightforwardly parallelized, since each pixel is correlated. Using a pre-grid style of fitting instead of a full MCMC routine would significantly speed up fitting, but the precision of the results will be limited by the coarseness of the pregrid. An emulator used in combination with an MCMC routine is a good middle ground to help with interpolation and speed up the fitting process – however, the emulator must be retrained for each model (i.e. each combination of parameter models).

Spatially-resolved SED fitting is becoming essential as we see instruments such as Euclid provide highly-resolved optical-infrared data for distant galaxies. The trade-off is that the Euclid VIS band is very wide, and provides little spectroscopic constraints. Ground-based instruments such as Rubin/LSST, however, will provide more spectroscopic information at the expense of resolution. Of course the obvious synergy is to combine these datasets in such a way that each instrument provides different types of information. This is where hierarchical-Bayesian modelling as described above comes in. We are starting to see work by some of the teams who have built popular SED fitters (e.g. PROPSECTOR, BAGPIPES) to build hierarchical-Bayesian SED fitters that take advantage of their respective SED fitting strategies (e.g. Leung et al., 2026), while general strategies that take advantage of various SED fitting techniques are being developed (e.g. Sazonova, Morgan, Balogh et al. in prep).

The study of galaxy evolution is an incremental process. Advances in technology allow us to build increasingly powerful telescopes and cameras, which in turn allow us to obtain deeper and higher-resolution data. As we do so, we build on foundational studies that started to probe the interesting questions of the field, providing new insight into our understanding of how galaxies evolve and shape the very nature of our Universe. With the onset of instruments such as Euclid, the Roman space telescope, the Rubin observatory, and extremely large telescopes, we are entering into the era of massive datasets. An important focus now must be updating our analysis methods and tools to take advantage of this unprecedented data, so that we can continue to make new discoveries that will then further influence the next generation of instruments and surveys.

Chapter 6

Summary

This thesis comprises multiple studies that use the Virgo cluster environment as a laboratory to study how galaxies evolve in local clusters. While this topic has been of focus for several decades, we make use of deep and high-resolution datasets and novel techniques to build upon previous work and draw conclusions that will have implications for future studies, not only in the local Universe but at high-redshift as well. We start in Chapter 1 by introducing galaxy evolution in context of the wealth of literature that exists touching on various aspects of this topic.

While we use a range of multi-wavelength data in these studies, the focus is with optical data obtained obtained as part of the NGVS survey, coupled with NB Hα photometry obtained from VESTIGE. Both of these surveys were undertaken with MegaCam on CFHT. These datasets extend beyond the virial radius of the Virgo cluster, including infalling groups, making comprehensive studies of the cluster environment possible. The data are deep enough to measure integrated quantities of galaxies down to $M_* \sim 10^7$ M$_\odot$, and have resolution of $< 1''$, corresponding to 80 pc at the distance of the Virgo cluster. The depth and resolution of this data make it possible to study galaxies in the Virgo cluster on a resolved scale rarely possible on large samples of galaxies.

In the three studies presented in this thesis, we look to take advantage of the depth and resolution of these data, combined with novel analysis techniques, to make new inferences about the quenching of star formation in the Virgo cluster. We begin in Chapter 2 by constructing deep stellar mass functions of galaxies in Virgo, separated into different regions of the cluster and according to star formation rate. We then use radial sSFR profiles to quantify the truncation of star forming disks in Chapter 3. Finally, in Chapter 4, we perform spatially-resolved SED fitting on Virgo galaxies, and use the resulting parameter

maps to construct maps of star formation on different timescales, identifying regions of rapid quenching and quantifying their morphologies.

6.1 Summary of Chapter 2

Galaxy stellar mass functions (SMFs) are a well-used tool to quantify the distribution of stellar mass in the field (e.g. Skrutskie et al., 2006; Baldry et al., 2008, 2012), and in higher-redshift groups and clusters (e.g. van der Burg et al., 2020; Edward et al., 2024). However, detailed SMF studies of low-redshift clusters are rare owing in part to the rarity of dedicated spectroscopic studies that cover the entire cluster environment. Even where low-redshift studies do exist, such as with SDSS (e.g. Yang et al., 2009), no study has been able to analyze a single massive cluster and split the SMFs according to local environment and star formation rate while maintaining significant galaxy counts to make statistically-sound conclusions.

For these reasons, we undertook a deep, comprehensive study of the SMFs in the Virgo cluster. Using NGVS completeness limits and accounting for varying distances to different substructures, we were able to construct complete SMFs down to $\log(M_*/\mathrm{M}_\odot) = 7.78$. Stellar masses were computed with SED fitting of the NGVS optical data. We combine NGVS with VESTIGE to separate galaxies that have Hα detections. Given the depth of VESTIGE, any galaxy above our mass limit with star formation would be detectable, though at very low masses, Hα-measured SFRs suffer from stochasticity. We split our sample into galaxies on the SFMS, galaxies that are completely quenched, and galaxies in the transition population. We use an MCMC routine to fit Schechter functions to the unbinned data.

We find that the shape of the total mass function is similar to that of the field, based on results from the GAMA survey (Baldry et al., 2012). When we split into star-forming and quiescent mass functions, though, we see that the majority of low-mass cluster galaxies are quiescent, as expected. There is a significant transition (low-SFR) population as well, especially toward the high-mass end where many galaxies appear to have residual star formation. We note, however, that we do not attempt to exclude galaxies that may have Hα emission from other sources, which is likely the case for galaxies such as M87.

We split the Virgo environment up into five regions to look for variance in the SMFs across the cluster. This includes a region representing the core of the main cluster, a ring between the core and R_{200}, and a region outside of R_{200}. We also establish a region representing Cluster B, and another for infalling group and cloud structures. We find

that the shapes of the SMFs are nearly invariant across the different regions. What does change, however, are the relative fractions of SF, low-SFR, and quiescent galaxies. Even though the ring outside the virial radius does have a lower overall quiescent fraction than the core of the cluster, the quenched fractions are still very high compared to the field. We surmise that there are two basic explanations for these quenched galaxies: the first is that they are backsplash galaxies that have already passes through first pericentre; the second is that they are quenched prior to first infall. We set up a simple model that sets the quiescent SMF in the outer region to be a combination of the field quiescent SMF and the core (backsplash) SMF. We find that the best fit to this model has a backsplash fraction approaching 100%, which is far too high to be realistic according to simulations (Haggar et al., 2020). As such, galaxies on first infall must not look entirely like an isolated field population, but must be quenched before crossing R_{200}, either by the cluster halo, smaller group halos, or along filaments. This conclusion is well in line with galaxy pre-processing.

6.2 Summary of Chapter 3

The notion of a truncated star-forming disk is a representation of outside-in quenching, where a quenching mechanism is shutting down star formation in the outer parts of the galactic disk first. Oftentimes, this is associated with ram-pressure stripping in galaxy clusters, since the gas near the edge of the disk is more loosely bound and thus is easier to strip from a galaxy. Truncated disks are often quantified by comparing the effective radius in a band that traces recent star formation (such as UV) and a band that traces the older stellar populations, such as red-optical or IR. However, these comparisons make an inherent assumption that the shape of the surface brightness profile is the same in the two bands. Sometimes, isophotal radii are used to circumvent this issue, but these are not physically motivated.

We quantify disk truncation in Virgo cluster galaxies by actually measuring the edge of the star-forming disk and comparing with the intrinsic size of normal star-forming galaxies. To do this, we first construct sSFR profiles using the VESTIGE Hα as a measure of star formation rate, and the NGVS optical data to measure stellar mass surface density. sSFR are relatively flat for normal star-forming galaxies, making it easy to systematically identify a turn-off in the profile due to a rapid change in slope. Chamba et al. (2022) measured these edges for normal star-forming galaxies, and correlated them with a threshold mass density. We use this relation to determine the "expected" sizes of Virgo galaxies if they were not being quenched.

Ultimately, we find that most galaxies in Virgo have some degree of truncation, though

we are a bit cautious to interpret mildly truncated disks. However, the degree of truncation appears to have little to do with stellar mass, location on the SFMS, gas deficiency, or location in the cluster – truncated disks are ubiquitous. This includes regions beyond the virial radius where, based on the ICM density and typical galaxy velocities, we do not expect RPS to be significant. We introduce a toy model that shows how galaxy starvation can lead to moderate truncations over long timescales. The basis is that sustained star formation requires a local threshold in gas density. If a galaxy has its gas supply cut off and it begins to exhaust its remaining fuel, the low-density outer parts of the disk will fade first, leading to a truncation. This is an attractive explanation for early quenching that may begin beyond R_{200}, and/or in small substructures. This is again consistent with pre-processing, and a slow-then-rapid (Wetzel et al., 2012; Roberts et al., 2019) quenching sequence.

6.3 Summary of Chapter 4

Bursts and rapid quenching of star formation can be traced by measuring SFRs on different timescales. One common method is to compare the Hα and FUV fluxes, given that they trace SFR on $\sim$ 10 and $\sim$ 100 Myr timescales, respectively. Galaxies undergoing rapid quenching may have signatures in their Hα to FUV ratio, as environmental processes such as RPS are expected to act quick to quench star formation in cluster galaxies.

Instead of simply taking the ratio of Hα and FUV fluxes, we sought to actually empirically measure the SFRs based on these two tracers and compare them spatially across galaxies. To do so, careful corrections had to be made. The most obvious of these is dust attenuation which affects the Hα but even more significantly so the FUV. Hα narrowband photometry is contaminated by NII emission, and FUV flux has a contribution from evolved, pAGB stars. To deal with dust attenuation and old-star FUV flux, we perform spatially resolved SED fits using multiwavelength photometry available from the FUV to the FIR. We additionally employ MaNGA star-forming galaxies to derive the median NII/Hα ratios as a function of stellar mass. From here, we can construct diagnostic plots showing ζ, the ratio of $\mathrm{SFR}_{\mathrm{H}\alpha}/\mathrm{SFR}_{\mathrm{FUV}}$ normalized by the uncertainty, which gives an indication of how much more significant one SFR is over the other. We construct these plots on 2D Voronoi binned maps, as well as in radial bins.

Upon visual inspection, two clear signatures stand out amongst the galaxies in our sample. The first is a lopsidedness in the 2D ζ maps, where one side of the galaxy is more dominated by $\mathrm{SFR}_{\mathrm{H}\alpha}$ and the other side by $\mathrm{SFR}_{\mathrm{FUV}}$. We quantify this by measuring the first Fourier mode in radial annuli. Combining the amplitudes and phases into

a global measure, galaxies with the highest value of $A_{1,\mathrm{global}}$ have several bins with high amplitude which are coherent in phase. The galaxies with the highest lopsidedness value, we find, have asymmetric HI disks based on Yoon et al. (2017), and have been previously identified as RPS candidates. However, the reverse does not appear to be always true – some galaxies with asymmetric cold gas disks and previous RPS identification have modest values of lopsidedness. The second metric is the slope in the ratio of $\mathrm{SFR}_{\mathrm{H}\alpha}/\mathrm{SFR}_{\mathrm{FUV}}$. A significantly negative slope shows that the outer disk of the galaxy has little/no ongoing star formation, yet has had star formation in the past ~ 100 Myr. Both of these metrics could be interpreted as signatures of RPS. The lopsidedness suggests gas stripping and suppressed star formation along the trailing edge, and induced star formation along the leading edge of the galaxy. Truncations suggested an outside in suppression of star formation on rapid timescales. However, we do not find any significant trends with other indicators of environmental quenching that would allow us to draw strong conclusions about whether these metrics are pure indicators of a single quenching mechanism. It is likely that multiple quenching mechanisms may contribute to these signatures, which may be present or absent depending on the time through the quenching episode.

We also discuss the future of studies such as this with IFU data. With a small sample of five galaxies recently observed with the MAUVE survey, we discuss how resolved spectroscopy can help to further constrain extinction of emission lines, and explore line ratios on resolved scales, allowing one to carefully treat regions of star formation and regions of composite or AGN/LINER emission.

6.4 Conclusions

This thesis presents three studies analyzing quenching in the Virgo cluster, using novel techniques and analysis to build on the wealth of information and previous studies of Virgo galaxies. We move roughly from integrated to resolved, beginning with a study of the stellar mass functions across the cluster, moving to a 1D radial analysis of the edges of star-forming disks, and finally moving to a study that seeks to map out star formation quenching signatures on spatial scales.

One key overarching conclusion results from this work: the Virgo cluster is a complex environment, and untangling the effects of various quenching mechanisms on galaxies with varied infall and evolutionary histories is difficult. Our work points to a "slow-then-rapid" quenching sequence in the Virgo environment, whereby processes such as starvation kick-start quenching early, before the more dramatic effects of RPS take hold as galaxies fall

closer to the cluster centre. This also highlights the importance of understanding the environment beyond the cluster virial radius – Virgo has a network of filaments and infalling groups that clearly play a role in the environmental evolution of galaxies in the vicinity of the cluster. Future work must combine efforts to understand quenching in the cluster, with studies such as VESTIGE and MAUVE, with work to understand the effects of the environment outside the cluster, with studies such as the Virgo Filaments Survey (VFS).

Our final study has begun to show the power of resolved photometric and spectroscopic data in helping to constrain these environmental processes. In the same way we must move beyond the bimodal cluster-field separation, we must move away from treating galaxies solely as integrated quantities – there is a wealth of information to be found on sub-kpc or even sub-100pc scales, which we have just started to scratch the surface of.

With that in mind, Chapter 5 takes a look ahead to new instruments, new surveys, new tools, and new perspectives. Beyond local well-studied environments like Virgo, we are now becoming able to map the cosmic web in detail out to high redshift, and use the revolutionary data from new telescopes to study galaxies across these environments and redshifts in detail. At the same time we must continue to upgrade our tools – we highlight in particular the need for spatially-resolved SED fitting done in a hierarchical way that mitigates the loss of information due to PSF-matching, and accounts for correlations between pixels. The future of galaxy evolution promises new and exciting insights and results that are sure to challenge existing models, push boundaries, and revolutionize our understanding of the Universe.

References

Alberts S., Adams J., Gregg B., Pope A., Williams C. C., Eisenhardt P. R. M., 2022, ApJ, 927, 235

Aniano G., Draine B. T., Gordon K. D., Sandstrom K., 2011, PASP, 123, 1218

Asada Y., et al., 2024, MNRAS, 527, 11372

Bahcall N. A., Cen R., 1993, ApJ, 407, L49

Bahé Y. M., McCarthy I. G., Balogh M. L., Font A. S., 2013, MNRAS, 430, 3017

Baldry I. K., Glazebrook K., Brinkmann J., Ivezić Ž., Lupton R. H., Nichol R. C., Szalay A. S., 2004, ApJ, 600, 681

Baldry I. K., Balogh M. L., Bower R. G., Glazebrook K., Nichol R. C., Bamford S. P., Budavari T., 2006, MNRAS, 373, 469

Baldry I. K., Glazebrook K., Driver S. P., 2008, MNRAS, 388, 945

Baldry I. K., et al., 2010, MNRAS, 404, 86

Baldry I. K., et al., 2012, MNRAS, 421, 621

Baldwin J. E., Lynden-Bell D., Sancisi R., 1980, MNRAS, 193, 313

Baldwin J. A., Phillips M. M., Terlevich R., 1981, PASP, 93, 5

Balogh M. L., Morris S. L., Yee H. K. C., Carlberg R. G., Ellingson E., 1997, ApJ, 488, L75

Balogh M. L., Schade D., Morris S. L., Yee H. K. C., Carlberg R. G., Ellingson E., 1998, ApJ, 504, L75

Balogh M. L., Navarro J. F., Morris S. L., 2000, ApJ, 540, 113

Balogh M. L., Christlein D., Zabludoff A. I., Zaritsky D., 2001, ApJ, 557, 117

Balogh M. L., Baldry I. K., Nichol R., Miller C., Bower R., Glazebrook K., 2004, ApJ, 615, L101

Balogh M. L., et al., 2014, MNRAS, 443, 2679

Balogh M. L., et al., 2016, MNRAS, 456, 4364

Balogh M. L., et al., 2017, MNRAS, 470, 4168

Balogh M. L., et al., 2021, MNRAS, 500, 358

Barnes J. E., 2004, MNRAS, 350, 798

Baxter D. C., Cooper M. C., Fillingham S. P., 2021, MNRAS, 503, 1636

Behroozi P., Wechsler R. H., Hearin A. P., Conroy C., 2019, MNRAS, 488, 3143

Bekki K., 2009, MNRAS, 399, 2221

Belfiore F., et al., 2017, MNRAS, 466, 2570

Belfiore F., et al., 2018, MNRAS, 477, 3014

Bell E. F., McIntosh D. H., Katz N., Weinberg M. D., 2003, ApJS, 149, 289

Bell E. F., et al., 2004, ApJ, 608, 752

Bertelli G., Bressan A., Chiosi C., Fagotto F., Nasi E., 1994, A&AS, 106, 275

Bigiel F., Leroy A., Walter F., Brinks E., de Blok W. J. G., Madore B., Thornley M. D., 2008, AJ, 136, 2846

Binggeli B., Sandage A., Tammann G. A., 1985, AJ, 90, 1681

Binggeli B., Tammann G. A., Sandage A., 1987, AJ, 94, 251

Blumenthal G. R., Faber S. M., Primack J. R., Rees M. J., 1984, Nature, 311, 517

Böhringer H., Briel U. G., Schwarz R. A., Voges W., Hartner G., Trümper J., 1994, Nature, 368, 828

Böhringer H., Chon G., Fukugita M., 2017, A&A, 608, A65

Boquien M., Burgarella D., Roehlly Y., Buat V., Ciesla L., Corre D., Inoue A. K., Salas H., 2019, A&A, 622, A103

Boselli A., Gavazzi G., 2006, PASP, 118, 517

Boselli A., Gavazzi G., 2014, A&ARv, 22, 74

Boselli A., Boissier S., Cortese L., Gil de Paz A., Seibert M., Madore B. F., Buat V., Martin D. C., 2006, ApJ, 651, 811

Boselli A., et al., 2011, A&A, 528, A107

Boselli A., Cortese L., Boquien M., Boissier S., Catinella B., Gavazzi G., Lagos C., Saintonge A., 2014a, A&A, 564, A67

Boselli A., et al., 2014b, A&A, 570, A69

Boselli A., et al., 2016, A&A, 587, A68

Boselli A., et al., 2018a, A&A, 614, A56

Boselli A., et al., 2018b, A&A, 620, A164

Boselli A., et al., 2019, A&A, 623, A52

Boselli A., et al., 2020, A&A, 634, L1

Boselli A., et al., 2021, A&A, 646, A139

Boselli A., Fossati M., Sun M., 2022, A&ARv, 30, 3

Boselli A., et al., 2023a, A&A, 669, A73

Boselli A., et al., 2023b, A&A, 675, A123

Boselli A., et al., 2023c, A&A, 676, A92

Boylan-Kolchin M., 2023, Nature Astronomy, 7, 731

Boylan-Kolchin M., Springel V., White S. D. M., Jenkins A., Lemson G., 2009, MNRAS, 398, 1150

Bradley L., et al., 2021, astropy/photutils: 1.0.2, Zenodo, doi:10.5281/zenodo.4453725, doi:10.5281/zenodo.4453725, https://doi.org/10.5281/zenodo.4453725

Brammer G. B., et al., 2009, ApJ, 706, L173

Brown T., et al., 2021, ApJS, 257, 21

Brown T., et al., 2023, arXiv e-prints, p. arXiv:2308.10943

Brown T., et al., 2026, arXiv e-prints, p. arXiv:2604.20056

Bruzual G., Charlot S., 2003, MNRAS, 344, 1000

Bundy K., Ellis R. S., Conselice C. J., 2005, ApJ, 625, 621

Bundy K., et al., 2015, ApJ, 798, 7

Butcher H., Oemler A. J., 1984, ApJ, 285, 426

Calzetti D., Armus L., Bohlin R. C., Kinney A. L., Koornneef J., Storchi-Bergmann T., 2000, ApJ, 533, 682

Calzetti D., et al., 2010, ApJ, 714, 1256

Cano-Díaz M., Maiolino R., Marconi A., Netzer H., Shemmer O., Cresci G., 2012, A&A, 537, L8

Cantiello M., et al., 2024, ApJ, 966, 145

Cardelli J. A., Clayton G. C., Mathis J. S., 1989, ApJ, 345, 245

Carlsten S., Li J., Greene J., Drlica-Wagner A., Danieli S., 2026, arXiv e-prints, p. arXiv:2602.16778

Carnall A. C., McLure R. J., Dunlop J. S., Davé R., 2018, MNRAS, 480, 4379

Castellano M., et al., 2022, ApJ, 938, L15

Catinella B., et al., 2013, MNRAS, 436, 34

Catinella B., et al., 2025, The Messenger, 195, 15

Cattorini F., Gavazzi G., Boselli A., Fossati M., 2023, A&A, 671, A118

Cayatte V., van Gorkom J. H., Balkowski C., Kotanyi C., 1990, AJ, 100, 604

Cayatte V., Kotanyi C., Balkowski C., van Gorkom J. H., 1994, AJ, 107, 1003

Ceverino D., Klypin A., 2009, ApJ, 695, 292

Chabrier G., 2003, PASP, 115, 763

Chamaraux P., Balkowski C., Gerard E., 1980, A&A, 83, 38

Chamba N., Trujillo I., Knapen J. H., 2020, A&A, 633, L3

Chamba N., Trujillo I., Knapen J. H., 2022, A&A, 667, A87

Chamba N., Hayes M. J., LSST Dark Energy Science Collaboration 2024, A&A, 689, A28

Chung A., van Gorkom J. H., Kenney J. D. P., Vollmer B., 2007, ApJ, 659, L115

Chung A., van Gorkom J. H., Kenney J. D. P., Crowl H., Vollmer B., 2009, AJ, 138, 1741

Chyży K. T., Ehle M., Beck R., 2007, A&A, 474, 415

Cid Fernandes R., Stasińska G., Mateus A., Vale Asari N., 2011, MNRAS, 413, 1687

Colless M., et al., 2001, MNRAS, 328, 1039

Conroy C., Gunn J. E., White M., 2009, ApJ, 699, 486

Conselice C. J., 2003, ApJS, 147, 1

Cooke E. A., et al., 2016, ApJ, 816, 83

Cortese L., Catinella B., Boissier S., Boselli A., Heinis S., 2011, MNRAS, 415, 1797

Cortese L., et al., 2012, A&A, 544, A101

Cortese L., Catinella B., Smith R., 2021, Publ. Astron. Soc. Australia, 38, e035

Crowl H. H., Kenney J. D. P., van Gorkom J. H., Vollmer B., 2005, AJ, 130, 65

Cuillandre J. C., et al., 2024, arXiv e-prints, p. arXiv:2405.13501

DESI Collaboration et al., 2016, arXiv e-prints, p. arXiv:1611.00036

DESI Collaboration et al., 2022, AJ, 164, 207

Darvish B., Sobral D., Mobasher B., Scoville N. Z., Best P., Sales L. V., Smail I., 2014, ApJ, 796, 51

Darvish B., Mobasher B., Martin D. C., Sobral D., Scoville N., Stroe A., Hemmati S., Kartaltepe J., 2017, ApJ, 837, 16

Davies J. I., et al., 2010, A&A, 518, L48

Davies L. J. M., et al., 2019, MNRAS, 483, 5444

Davis M., Efstathiou G., Frenk C. S., White S. D. M., 1985, ApJ, 292, 371

De Lucia G., Blaizot J., 2007, MNRAS, 375, 2

Dekel A., Silk J., 1986, ApJ, 303, 39

Diaferio A., Geller M. J., 1997, ApJ, 481, 633

Diemer B., Kravtsov A. V., 2015, ApJ, 799, 108

Dressler A., 1980, ApJ, 236, 351

Dressler A., et al., 1997, ApJ, 490, 577

Driver S. P., et al., 2009, Astronomy and Geophysics, 50, 5.12

Driver S. P., et al., 2022, MNRAS, 513, 439

Drory N., Salvato M., Gabasch A., Bender R., Hopp U., Feulner G., Pannella M., 2005, ApJ, 619, L131

Ebeling H., Stephenson L. N., Edge A. C., 2014, ApJ, 781, L40

Edward A. H., et al., 2024, MNRAS, 527, 8598

Efstathiou G., 2000, MNRAS, 317, 697

Einstein A., 1917, Sitzungsberichte der Königlich Preussischen Akademie der Wissenschaften, pp 142–152

Eke V. R., et al., 2004, MNRAS, 348, 866

Emami N., Siana B., Weisz D. R., Johnson B. D., Ma X., El-Badry K., 2019, ApJ, 881, 71

Emsellem E., et al., 2007, MNRAS, 379, 401

Emsellem E., et al., 2011, MNRAS, 414, 888

Erwin P., Pohlen M., Beckman J. E., 2008, AJ, 135, 20

Euclid Collaboration et al., 2025a, A&A, 697, A1

Euclid Collaboration et al., 2025b, A&A, 700, A78

Euclid Collaboration et al., 2025c, A&A, 702, A73

Faber S. M., et al., 2007, ApJ, 665, 265

Fabian A. C., 2012, ARA&A, 50, 455

Fabian A. C., Sanders J. S., Allen S. W., Crawford C. S., Iwasawa K., Johnstone R. M., Schmidt R. W., Taylor G. B., 2003, MNRAS, 344, L43

Fang J. J., Faber S. M., Koo D. C., Dekel A., 2013, ApJ, 776, 63

Ferrarese L., et al., 2012, ApJS, 200, 4

Ferrarese L., et al., 2016, ApJ, 824, 10

Ferrarese L., et al., 2020, ApJ, 890, 128

Ferrarese L., et al., 2026, arXiv e-prints, p. arXiv:2607.18414

Finn R. A., et al., 2018, ApJ, 862, 149

Finn R. A., et al., 2025, ApJ, 985, 81

Fontana A., et al., 2004, A&A, 424, 23

Foreman-Mackey D., Hogg D. W., Lang D., Goodman J., 2013, PASP, 125, 306

Fossati M., et al., 2013, A&A, 553, A91

Fossati M., et al., 2018, A&A, 614, A57

Freeman K. C., 1970, ApJ, 160, 811

Fujita Y., 2004, PASJ, 56, 29

Galametz A., et al., 2013, ApJS, 206, 10

Gavazzi G., Boselli A., Scodeggio M., Pierini D., Belsole E., 1999, MNRAS, 304, 595

Gavazzi G., Boselli A., Mayer L., Iglesias-Paramo J., Vílchez J. M., Carrasco L., 2001, ApJ, 563, L23

Gavazzi G., Boselli A., Donati A., Franzetti P., Scodeggio M., 2003, A&A, 400, 451

Gavazzi G., Boselli A., van Driel W., O'Neil K., 2005, A&A, 429, 439

Gavazzi G., Boselli A., Cortese L., Arosio I., Gallazzi A., Pedotti P., Carrasco L., 2006, A&A, 446, 839

Gavazzi G., Fumagalli M., Fossati M., Galardo V., Grossetti F., Boselli A., Giovanelli R., Haynes M. P., 2013a, A&A, 553, A89

Gavazzi G., Fumagalli M., Fossati M., Galardo V., Grossetti F., Boselli A., Giovanelli R., Haynes M. P., 2013b, A&A, 553, A89

Gavazzi G., et al., 2013c, A&A, 553, A90

Geha M., Blanton M. R., Yan R., Tinker J. L., 2012, ApJ, 757, 85

Geller M. J., Huchra J. P., 1983, ApJS, 52, 61

Gelli V., Pallottini A., Salvadori S., Ferrara A., Mason C., Carniani S., Ginolfi M., 2025, ApJ, 985, 126

Géron T., Smethurst R. J., Lintott C., Kruk S., Masters K. L., Simmons B., Stark D. V., 2021, MNRAS, 507, 4389

Giovanelli R., Haynes M. P., 1983, AJ, 88, 881

Giovanelli R., Haynes M. P., 1985, ApJ, 292, 404

Giovanelli R., et al., 2005, AJ, 130, 2598

Girelli G., Pozzetti L., Bolzonella M., Giocoli C., Marulli F., Baldi M., 2020, A&A, 634, A135

Gladders M. D., Yee H. K. C., 2000, AJ, 120, 2148

Goddard D., et al., 2017, MNRAS, 465, 688

Gómez P. L., et al., 2003, ApJ, 584, 210

González Delgado R. M., et al., 2015, A&A, 581, A103

Goto T., Yamauchi C., Fujita Y., Okamura S., Sekiguchi M., Smail I., Bernardi M., Gomez P. L., 2003, MNRAS, 346, 601

Greener M. J., et al., 2020, MNRAS, 495, 2305

Gunawardhana M. L. P., et al., 2015, MNRAS, 447, 875

Gunn J. E., Gott J. Richard I., 1972, ApJ, 176, 1

Guo Y., et al., 2016, ApJ, 833, 37

Gwyn S. D. J., 2008, PASP, 120, 212

Haggar R., Gray M. E., Pearce F. R., Knebe A., Cui W., Mostoghiu R., Yepes G., 2020, MNRAS, 492, 6074

Haynes M. P., et al., 2018, ApJ, 861, 49

Hernquist L., 1990, ApJ, 356, 359

Herrmann K. A., Hunter D. A., Elmegreen B. G., 2013, AJ, 146, 104

Herrmann K. A., Hunter D. A., Elmegreen B. G., 2016, AJ, 151, 145

Hopkins P. F., Hernquist L., Cox T. J., Di Matteo T., Robertson B., Springel V., 2006, ApJS, 163, 1

Hopkins P. F., Quataert E., Murray N., 2011, MNRAS, 417, 950

Hopkins P. F., Quataert E., Murray N., 2012, MNRAS, 421, 3522

Hopkins P. F., Kereš D., Oñorbe J., Faucher-Giguère C.-A., Quataert E., Murray N., Bullock J. S., 2014, MNRAS, 445, 581

Huang S., Haynes M. P., Giovanelli R., Brinchmann J., 2012, ApJ, 756, 113

Hubble E., 1926, Contributions from the Mount Wilson Observatory / Carnegie Institution of Washington, 324, 1

Hubble E., 1929, Proceedings of the National Academy of Science, 15, 168

Huchra J., Davis M., Latham D., Tonry J., 1983, ApJS, 52, 89

Hunter D. A., Elmegreen B. G., 2006, ApJS, 162, 49

Ilbert O., et al., 2013, A&A, 556, A55

Jedrzejewski R. I., 1987, MNRAS, 226, 747

Jenkins A., Frenk C. S., White S. D. M., Colberg J. M., Cole S., Evrard A. E., Couchman H. M. P., Yoshida N., 2001, MNRAS, 321, 372

Johnson B. D., Leja J., Conroy C., Speagle J. S., 2021, ApJS, 254, 22

Junais et al., 2022, A&A, 667, A76

Kantharia N. G., Rao A. P., Sirothia S. K., 2008, MNRAS, 383, 173

Kashibadze O. G., Karachentsev I. D., Karachentseva V. E., 2020, A&A, 635, A135

Kauffmann G., et al., 2003, MNRAS, 346, 1055

Kauffmann G., White S. D. M., Heckman T. M., Ménard B., Brinchmann J., Charlot S., Tremonti C., Brinkmann J., 2004, MNRAS, 353, 713

Kawata D., Mulchaey J. S., 2008, ApJ, 672, L103

Kawinwanichakij L., et al., 2017, ApJ, 847, 134

Kelkar K., et al., 2020, MNRAS, 496, 442

Kenney J. D. P., van Gorkom J. H., Vollmer B., 2004, AJ, 127, 3361

Kennicutt Jr., R. C., 1989, ApJ, 344, 685

Kennicutt Jr., R. C., 1998a, ARA&A, 36, 189

Kennicutt Jr., R. C., 1998b, ApJ, 498, 541

Kewley L. J., Groves B., Kauffmann G., Heckman T., 2006, MNRAS, 372, 961

Kim S., et al., 2014, ApJS, 215, 22

Kocevski D. D., et al., 2025, ApJ, 986, 126

Kolcu T., Crossett J. P., Bellhouse C., McGee S., 2022, MNRAS, 515, 5877

Koopmann R. A., Kenney J. D. P., 2004, ApJ, 613, 866

Koopmann R. A., Haynes M. P., Catinella B., 2006, AJ, 131, 716

Kormendy J., Kennicutt Jr. R. C., 2004, ARA&A, 42, 603

Kraljic K., et al., 2018, MNRAS, 474, 547

Kuutma T., Tamm A., Tempel E., 2017, A&A, 600, L6

Labbé I., et al., 2023, Nature, 616, 266

Laigle C., et al., 2018, MNRAS, 474, 5437

Larson R. B., Tinsley B. M., Caldwell C. N., 1980, ApJ, 237, 692

Laureijs R., et al., 2011, arXiv e-prints, p. arXiv:1110.3193

Lawlor-Forsyth C., Balogh M. L., Sazonova E., Morgan C. R., McGee S. L., Rudnick G. H., 2026, ApJ, 1000, 61

Lee B., et al., 2017, MNRAS, 466, 1382

Leitherer C., Li I.-H., Calzetti D., Heckman T. M., 2002, ApJS, 140, 303

Lemaître G., 1927, Annales de la Société Scientifique de Bruxelles, 47, 49

Leung H.-H., et al., 2026, arXiv e-prints, p. arXiv:2602.13114

Lewis I., et al., 2002, MNRAS, 334, 673

Lim S., et al., 2020, ApJ, 899, 69

Lin L., et al., 2014, ApJ, 782, 33

Lintott C., et al., 2011, MNRAS, 410, 166

Lotz J. M., Primack J., Madau P., 2004, AJ, 128, 163

Lotz J. M., Jonsson P., Cox T. J., Croton D., Primack J. R., Somerville R. S., Stewart K., 2011, ApJ, 742, 103

Lotz M., Dolag K., Remus R.-S., Burkert A., 2021, MNRAS, 506, 4516

Machado R. E. G., Grinberg C. F. O., Mello-Terencio E. A., 2025, Galaxies, 13, 76

Madau P., Dickinson M., 2014, ARA&A, 52, 415

Magorrian J., et al., 1998, AJ, 115, 2285

Malumuth E. M., Kriss G. A., 1986, ApJ, 308, 10

Mandelbaum R., Seljak U., Cool R. J., Blanton M., Hirata C. M., Brinkmann J., 2006, MNRAS, 372, 758

Martig M., Bournaud F., Teyssier R., Dekel A., 2009, ApJ, 707, 250

Martin D. C., et al., 2005, ApJ, 619, L1

Matthee J., et al., 2024, ApJ, 963, 129

McCarthy I. G., Frenk C. S., Font A. S., Lacey C. G., Bower R. G., Mitchell N. L., Balogh M. L., Theuns T., 2008, MNRAS, 383, 593

McGee S. L., Balogh M. L., Bower R. G., Font A. S., McCarthy I. G., 2009, MNRAS, 400, 937

McLaughlin D. E., 1999, ApJ, 512, L9

McLeod D. J., McLure R. J., Dunlop J. S., Cullen F., Carnall A. C., Duncan K., 2021, MNRAS, 503, 4413

McNamara B. R., Nulsen P. E. J., 2007, ARA&A, 45, 117

Mehta V., et al., 2023, ApJ, 952, 133

Mei S., et al., 2007, ApJ, 655, 144

Merluzzi P., Mercurio A., Haines C. P., Smith R. J., Busarello G., Lucey J. R., 2010, MNRAS, 402, 753

Mihos J. C., Hernquist L., 1996, ApJ, 464, 641

Minchin R. F., Taylor R., Köppen J., Davies J. I., van Driel W., Keenan O., 2019, AJ, 158, 121

Moore B., Katz N., Lake G., Dressler A., Oemler A., 1996, Nature, 379, 613

Moore B., Lake G., Katz N., 1998, ApJ, 495, 139

Morgan C. R., et al., 2024, A&A, 691, A20

Morgan C. R., et al., 2025, ApJ, 987, 166

Morrissey P., et al., 2007, ApJS, 173, 682

Moss C., Whittle M., 1993, ApJ, 407, L17

Moss C., Whittle M., 2000, MNRAS, 317, 667

Muzzin A., et al., 2012, ApJ, 746, 188

Muzzin A., et al., 2013, ApJ, 777, 18

Naidu R. P., et al., 2025, arXiv e-prints, p. arXiv:2503.16596

Naidu R. P., et al., 2026, The Open Journal of Astrophysics, 9, 56033

Navarro J. F., Frenk C. S., White S. D. M., 1996, ApJ, 462, 563

Nelson E. J., et al., 2021, MNRAS, 508, 219

Oegerle W. R., Hoessel J. G., Ernst R. M., 1986, AJ, 91, 697

Oemler Augustus J., 1974, ApJ, 194, 1

Peebles P. J. E., 1980, The large-scale structure of the universe. Princeton University Press.

Peebles P. J. E., 1982, ApJ, 263, L1

Peng Y.-j., et al., 2010, ApJ, 721, 193

Perlmutter S., et al., 1999, ApJ, 517, 565

Perry M. N., et al., 2025, ApJ, 994, 14

Planck Collaboration et al., 2020, A&A, 641, A6

Poggianti B. M., et al., 2016, AJ, 151, 78

Poggianti B. M., et al., 2017, ApJ, 844, 48

Pohlen M., Trujillo I., 2006, A&A, 454, 759

Press W. H., Schechter P., 1974, ApJ, 187, 425

Quadri R. F., Williams R. J., Franx M., Hildebrandt H., 2012, ApJ, 744, 88

Reed D., Gardner J., Quinn T., Stadel J., Fardal M., Lake G., Governato F., 2003, MNRAS, 346, 565

Reed D. S., Bower R., Frenk C. S., Jenkins A., Theuns T., 2007, MNRAS, 374, 2

Reiprich T. H., Böhringer H., 2002, ApJ, 567, 716

Rhee J., Smith R., Choi H., Yi S. K., Jaffé Y., Candlish G., Sánchez-Jánssen R., 2017, ApJ, 843, 128

Rich J. A., Kewley L. J., Dopita M. A., 2011, ApJ, 734, 87

Richter O.-G., Sancisi R., 1994, A&A, 290, L9

Riess A. G., et al., 1998, AJ, 116, 1009

Rix H.-W., Zaritsky D., 1995, ApJ, 447, 82

Roberts I. D., Parker L. C., Brown T., Joshi G. D., Hlavacek-Larrondo J., Wadsley J., 2019, ApJ, 873, 42

Roberts I. D., van Weeren R. J., McGee S. L., Botteon A., Ignesti A., Rottgering H. J. A., 2021a, A&A, 652, A153

Roberts I. D., van Weeren R. J., McGee S. L., Botteon A., Ignesti A., Rottgering H. J. A., 2021b, A&A, 652, A153

Robotham A. S. G., et al., 2011, MNRAS, 416, 2640

Roediger E., Brüggen M., 2006, MNRAS, 369, 567

Roediger J. C., Courteau S., 2015, MNRAS, 452, 3209

Roediger J. C., et al., 2017, ApJ, 836, 120

Rubin V. C., Ford Jr. W. K., 1970, ApJ, 159, 379

Rudnick G., Rix H.-W., 1998, AJ, 116, 1163

Saitoh T. R., Daisaka H., Kokubo E., Makino J., Okamoto T., Tomisaka K., Wada K., Yoshida N., 2009, PASJ, 61, 481

Salim S., et al., 2007, ApJS, 173, 267

Sánchez S. F., et al., 2012, A&A, 538, A8

Sandage A., Tammann G. A., Yahil A., 1979, ApJ, 232, 352

Sawala T., Scannapieco C., Maio U., White S., 2010, MNRAS, 402, 1599

Sazonova E., et al., 2020, ApJ, 899, 85

Sazonova E., et al., 2021, ApJ, 919, 134

Schawinski K., et al., 2014, MNRAS, 440, 889

Schechter P., 1976, ApJ, 203, 297

Schindler S., Binggeli B., Böhringer H., 1999, A&A, 343, 420

Schmidt M., 1959, ApJ, 129, 243

Serra P., et al., 2023, A&A, 673, A146

Sérsic J. L., 1963, Boletin de la Asociacion Argentina de Astronomia La Plata Argentina, 6, 41

Sheth R. K., Mo H. J., Tormen G., 2001, MNRAS, 323, 1

Shuntov M., et al., 2022, A&A, 664, A61

Silk J., Rees M. J., 1998, A&A, 331, L1

Simionescu A., Werner N., Mantz A., Allen S. W., Urban O., 2017, MNRAS, 469, 1476

Skrutskie M. F., et al., 2006, AJ, 131, 1163

Smith R. J., et al., 2010, MNRAS, 408, 1417

Solanes J. M., Sanchis T., Salvador-Solé E., Giovanelli R., Haynes M. P., 2002, AJ, 124, 2440

Sorgho A., Hess K., Carignan C., Oosterloo T. A., 2017, MNRAS, 464, 530

Sparre M., Hayward C. C., Feldmann R., Faucher-Giguère C.-A., Muratov A. L., Kereš D., Hopkins P. F., 2017, MNRAS, 466, 88

Speagle J. S., Steinhardt C. L., Capak P. L., Silverman J. D., 2014, ApJS, 214, 15

Springel V., et al., 2005, Nature, 435, 629

Steinhauser D., Schindler S., Springel V., 2016, A&A, 591, A51

Stone C. J., Arora N., Courteau S., Cuillandre J.-C., 2021, MNRAS, 508, 1870

Strateva I., et al., 2001, AJ, 122, 1861

Strazzullo V., et al., 2019, A&A, 622, A117

Taylor E. N., et al., 2011, MNRAS, 418, 1587

Tonnesen S., Bryan G. L., 2009, ApJ, 694, 789

Tonnesen S., Bryan G. L., van Gorkom J. H., 2007, ApJ, 671, 1434

Toomre A., Toomre J., 1972, ApJ, 178, 623

Truemper J., 1993, Science, 260, 1769

Trujillo I., Chamba N., Knapen J. H., 2020, MNRAS, 493, 87

Tully R. B., 1987, ApJ, 321, 280

Vázquez-Mata J. A., et al., 2020, MNRAS, 499, 631

Villanueva V., et al., 2022, ApJ, 940, 176

Vollmer B., Huchtmeier W., 2007, A&A, 462, 93

Vollmer B., Cayatte V., Balkowski C., Duschl W. J., 2001, ApJ, 561, 708

Vollmer B., Beck R., Kenney J. D. P., van Gorkom J. H., 2004, AJ, 127, 3375

Vollmer B., Soida M., Chung A., Beck R., Urbanik M., Chyży K. T., Otmianowska-Mazur K., van Gorkom J. H., 2010, A&A, 512, A36

Vollmer B., Soida M., Beck R., Chung A., Urbanik M., Chyży K. T., Otmianowska-Mazur K., Kenney J. D. P., 2013, A&A, 553, A116

Wang J., et al., 2026, arXiv e-prints, p. arXiv:2606.26999

Watkins A. E., Laine J., Comerón S., Janz J., Salo H., 2019, A&A, 625, A36

Watson W. A., Iliev I. T., D'Aloisio A., Knebe A., Shapiro P. R., Yepes G., 2013, MNRAS, 433, 1230

Watts A. B., et al., 2023, Publ. Astron. Soc. Australia, 40, e017

Weaver J. R., et al., 2023, A&A, 677, A184

Weinmann S. M., van den Bosch F. C., Yang X., Mo H. J., 2006, MNRAS, 366, 2

Weisz D. R., et al., 2012, ApJ, 744, 44

Wetzel A. R., Tinker J. L., Conroy C., 2012, MNRAS, 424, 232

Willmer C. N. A., 2018, ApJS, 236, 47

Wright E. L., et al., 2010, AJ, 140, 1868

Xiao M., et al., 2024, Nature, 635, 311

Yang X., Mo H. J., van den Bosch F. C., 2009, ApJ, 695, 900

Yoon H., Chung A., Smith R., Jaffé Y. L., 2017, ApJ, 838, 81

York D. G., et al., 2000, AJ, 120, 1579

Yoshida M., et al., 2002, ApJ, 567, 118

Zabel N., et al., 2022, ApJ, 933, 10

Zaritsky D., Rix H.-W., 1997, ApJ, 477, 118

Zwicky F., 1933, Helvetica Physica Acta, 6, 110

de Graaff A., et al., 2025, arXiv e-prints, p. arXiv:2511.21820

de Vaucouleurs G., 1948, Annales d'Astrophysique, 11, 247

van der Burg R. F. J., et al., 2020, A&A, 638, A112

APPENDICES

Appendix A

A.1 Data table

Environment	Dist from M87 (Mpc)	Sample	N	α	$\mathcal{M}*$ ($\log(M_*/\mathrm{M}_\odot)$)	$\phi*$ (cluster^{-1}dex^{-1})
Cluster A - core	$R < 0.5$	Quiescent	239	$-1.42^{+0.03}_{-0.05}$	$11.01^{+0.78}_{-0.18}$	$2.66^{+0.85}_{-1.70}$
		Low-SFR	23	$-1.03^{+0.08}_{-0.11}$	$11.54^{+0.64}_{-0.24}$	$2.29^{+0.98}_{-1.30}$
		Star-forming	12	$-0.99^{+0.11}_{-0.19}$	$10.78^{+1.12}_{-0.25}$	$1.61^{+0.93}_{-1.20}$
Cluster A - inner ring	$0.5 < R < 1.0$	Quiescent	217	$-1.51^{+0.03}_{-0.04}$	$11.73^{+0.89}_{-0.32}$	$0.57^{+0.37}_{-0.40}$
		Low-SFR	33	$-1.17^{+0.07}_{-0.12}$	$11.02^{+0.94}_{-0.23}$	$1.89^{+0.98}_{-1.34}$
		Star-forming	27	$-1.02^{+0.08}_{-0.13}$	$10.89^{+0.62}_{-0.21}$	$3.24^{+1.26}_{-1.94}$
Cluster A - outer ring	$1.0 < R < 1.5$	Quiescent	161	$-1.44^{+0.04}_{-0.07}$	$10.70^{+1.07}_{-0.18}$	$2.14^{+0.82}_{-1.62}$
		Low-SFR	20	$-1.28^{+0.08}_{-0.16}$	$11.03^{+1.32}_{-0.30}$	$0.62^{+0.46}_{-0.53}$
		Star-forming	25	$-0.88^{+0.10}_{-0.13}$	$10.66^{+0.42}_{-0.19}$	$5.48^{+2.17}_{-2.62}$
Cluster B	$R > 1.0$	Quiescent	138	$-1.49^{+0.04}_{-0.07}$	$10.82^{+1.38}_{-0.20}$	$1.16^{+0.49}_{-1.00}$
		Low-SFR	36	$-1.11^{+0.06}_{-0.12}$	$10.88^{+0.71}_{-0.20}$	$2.84^{+0.87}_{-1.82}$
		Star-forming	29	$-0.90^{+0.13}_{-0.18}$	$9.99^{+0.40}_{-0.18}$	$7.25^{+3.06}_{-3.52}$
Clouds	...	Quiescent	92	$-1.42^{+0.05}_{-0.06}$	$11.91^{+0.73}_{-0.33}$	$0.74^{+0.49}_{-0.48}$
		Low-SFR	49	$-1.38^{+0.07}_{-0.08}$	$11.86^{+0.76}_{-0.39}$	$0.56^{+0.45}_{-0.39}$
		Star-forming	23	$-0.90^{+0.13}_{-0.21}$	$10.44^{+0.51}_{-0.19}$	$5.73^{+2.59}_{-3.45}$
Infall	$1.0 < R < 1.5$	Quiescent	247	$-1.42^{+0.04}_{-0.06}$	$10.51^{+0.52}_{-0.17}$	$4.53^{+1.74}_{-2.53}$
		Low-SFR	42	$-1.20^{+0.06}_{-0.11}$	$11.04^{+0.91}_{-0.22}$	$1.97^{+0.99}_{-1.36}$
		Star-forming	39	$-0.88^{+0.09}_{-0.10}$	$10.55^{+0.30}_{-0.16}$	$8.75^{+2.96}_{-2.98}$

Table A.1: Best fit parameters and uncertainties for the fits to the quiescent, low-SFR and SF populations across the Virgo environment

Appendix B

B.1 Masking of contaminating sources

We show in Table B.1 the default PHOTUTILS parameters used in each step of the masking run. We note that in certain cases, parameters were changed from these defaults after visual inspection and identification of over- or under-deblending.

Parameter	'Hot' mode	'Cool' mode	'Cold' mode
NSIGMA	97th percentile	2σ	2σ
NPIXELS	1 pixel	20 arcsec^2	20 pixels
CONTRAST	4×10^{-1}	10^{-4}	...
NLEVELS	32	32	...
MASK	Original	Original	Object mask

Table B.1: PHOTUTILS parameters used in object masking routine

To help visualise the masking process, we show in Fig. B.1 an example of the masking process on VCC 483, which has a close neighbour, VCC 497. The first panel shows the r-band postage stamp centred around VCC 483. In the second panel, we show regions detected in the 'hot' run in red and the 'cool' run in blue. These two runs create an object mask, with any blue regions beyond $4r_{\rm e,i}$ from the centre being masked, as well as any blue regions containing a red region (except for the central red region pertaining to the target galaxy). Using this mask, the segmentation map and mask are created in the final 'cold' run and are shown in the third and fourth panel.

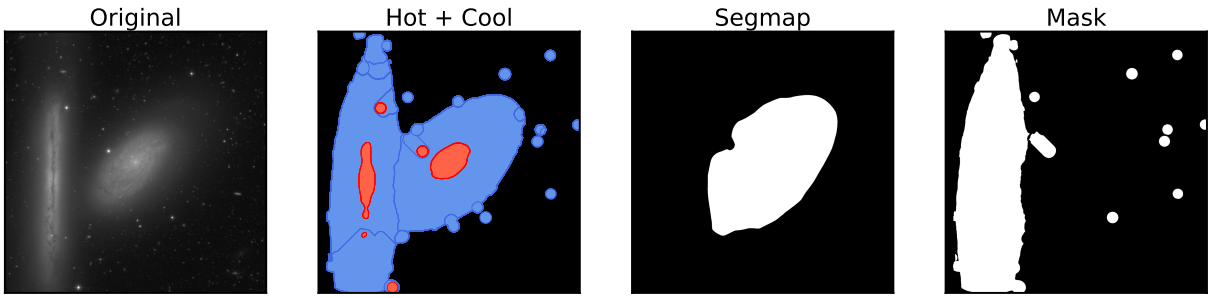


Figure B.1: Masking routine for VCC 483. From left to right: original r-band postage stamp, hot (red) and cool (blue) runs, final segmentation map and final mask. The red (hot) regions are bright peaks in the images, whereas the blue (cool) regions are extended surfaces with a low surface brightness threshold.

B.2 Correcting profiles for inclination effects

The majority of galaxies in the VESTIGE sample have moderate axis ratios between 0.5 and 0.8 - however there are a number of galaxies that are more substantially inclined. Radially averaged profiles of disc galaxies will vary depending on the inclination of the galaxy. The simplest model to correct for inclination effect is to consider the change in projected area for a galaxy with $i = 0°$ to $i > 0°$. Since the projected area of a disc galaxy with $i = 0°$ is a circle with area $A = \pi a^2$, where a is the semi-major axis then the annulus used to measure surface brightness would have area of $A = \pi\,(a_{out}^2 - a_{in}^2)$, where a_{out} and a_{in} represent the semi major axis (radius) of the outer and inner rings of the annulus, respectively. A galaxy with non-zero inclination will have a projected area of $A = \pi ab$ where b is the semi-minor axis and $b = a\sec(i)$. Thus, the annuli used to measure the surface brightness will have area $A = \pi\,(a_{out}b_{out} - a_{in}b_{in}) = \pi\,(a_{out}^2 - a_{in}^2)\sec(i)$. The line-of-sight flux measured within the annulus is constant (neglecting inclination effects on extinction), and the surface brightness is measured as $\mu = -2.5\log(F/A) + ZP = m + 2.5\log(A) + ZP$. Therefore, the difference

in surface brightness μ as a function of inclination angle is simply:

$$\begin{aligned}
\mu_{i=0^\circ} - \mu^\circ_{i=i'} &= 2.5 \log \left(\frac{A^\circ_{i=0}}{A^\circ_{i=i'}} \right) \\
&= 2.5 \log \left(\frac{\pi \left(a^2_{out} - a^2_{in}\right)}{\pi \left(a^2_{out} - a^2_{in}\right) \sec\left(i\right)} \right) \\
&= 2.5 \log \left(\frac{1}{\sec\left(i\right)} \right) \\
&= 2.5 \log \left(\frac{a}{b} \right).
\end{aligned} \tag{B.1}$$

This simple correction assumes a disc with negligible height and also assumes that internal dust extinction is not a function of inclination. For the purposes of this analysis, we expect that both of these assumptions suffice for $b/a > 0.3$. After removing these highly inclined objects from our analysis, we find negligible differences in the overall results, so we choose to leave them in our sample.

B.3 Examples of peculiar galaxies

B.3.1 Starburst galaxies with Hα filaments

Starburst galaxies with Hα filaments were not excluded from our sample. The detection of Hα-emitting filaments extending beyond the central starburst give these galaxies $R_{\rm sSFR}/R_{\rm norm}$ values close to unity; however, these galaxies do not have an intact SF disc. Fig. B.2 shows VCC 1190 as an example, in the Hα (left) and r-band (right). This galaxy is massive, extremely gas-deficient and yet has $R_{\rm sSFR}/R_{\rm norm} \sim 0.9$.

B.3.2 Galaxies with unphysical $R_{\rm sSFR}$

In a small number of cases (18), visual inspection of the sSFR profiles showed features that caused the measured $R_{\rm sSFR}$ value to be unphysical. Typically this was due to a spike in the sSFR values at large galactocentric radii. This could be due to local background variations or artefacts such as bright star halos that were not entirely masked. Additionally, local variation in the continuum subtraction could bias the Hα flux in low-SB regions to be higher than the true value. All of these galaxies were removed from our sample. We show

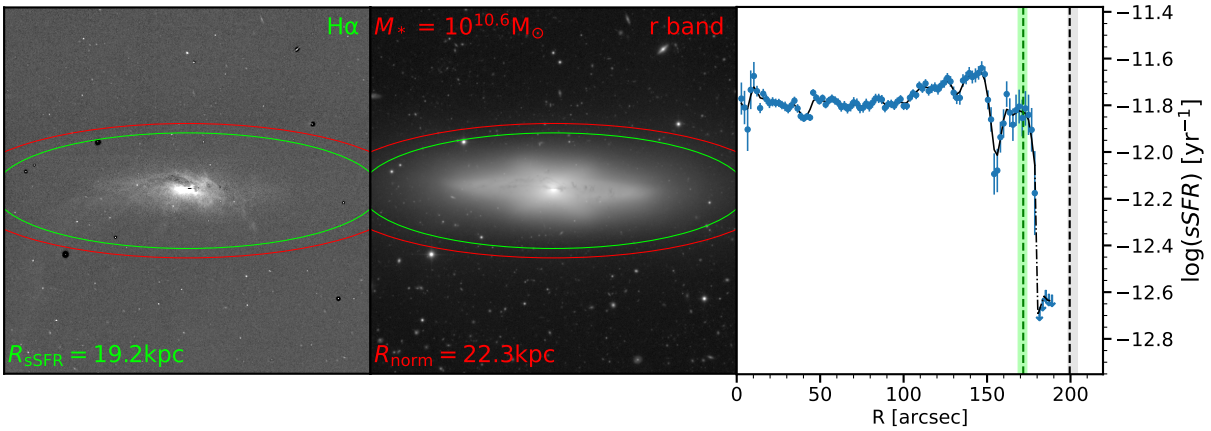


Figure B.2: Hα NB emission (*left*), r-band optical emission (*centre*), and sSFR profile (*right*) for VCC 1190. In the left and centre postage stamps, the green ellipse outlines $R_{\rm sSFR}$ while the red ellipse outlines $R_{\rm norm}$. On the sSFR plots, we show $R_{\rm sSFR}$ and its associated uncertainty range as a green vertical line and band, and $R_{\rm norm}$ and its uncertainty range as a grey vertical line and band.

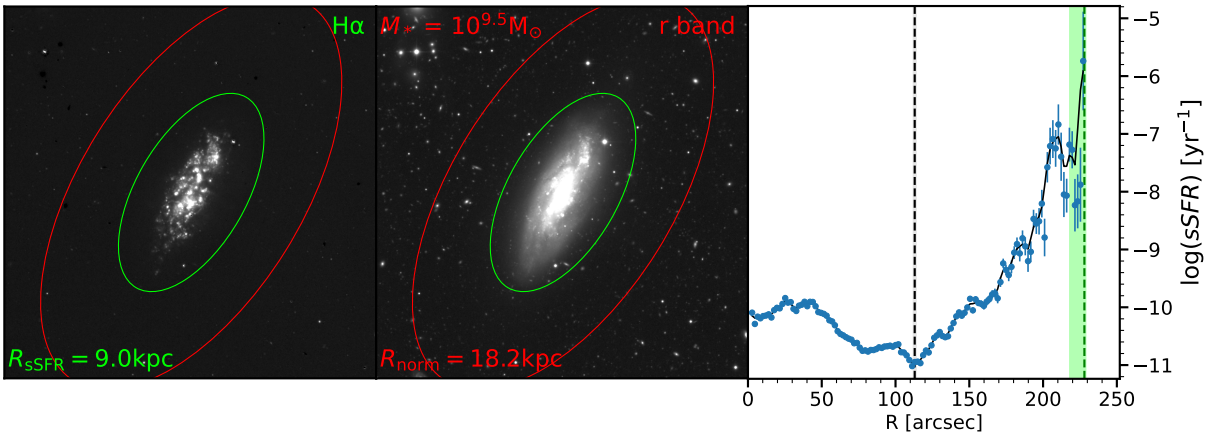


Figure B.3: Same as Fig. B.2 but for VCC 465. The value shown for $R_{\rm sSFR}$ is visually a poor representation of the last valid local maximum on the sSFR plot, and drastically overestimates the extent of the Hα emission.

an example of VCC 497 in Fig. B.3, with the Hα image on the left with an ellipse showing the unphysical $R_{\rm sSFR}$ and the sSFR profile on the right. Clearly the green ellipse outlining $R_{\rm sSFR}$ radius extends well beyond the Hα emission.

B.4 Updated VESTIGE footprint figure

We present an updated version of Figure 3.7, which shows the RA and DEC distribution of truncated disks across the Virgo cluster. In addition to highlighting substructures, we show X-ray contours taken from the ROSAT All-sky survey (Truemper, 1993; Böhringer et al., 1994). The greyscale in the background shows the quenched fraction, calculated using Gaussian KDEs, in the same manner as Figure 3.9.

B.5 Galaxy and quenching models

To define the radial profiles of the gas and SFR, we use the sub-kiloparsec Kennicutt-Schmidt law defined by Bigiel et al. (2008) along with the gas density threshold concept used throughout this work. Choosing an example galaxy to have $M_* = 10^{9.5}$ M$_\odot$, our fits to the $\Sigma_*(R_{\rm edge}) - M_*$ and $R_{\rm edge} - M_*$ relations from C22 give a threshold $\Sigma_*(R_{\rm edge}) = 0.6$ M$_\odot$ pc^{-2} and $R_{\rm edge} = 8.1$ kpc. Calculating the scale radius of the exponential profile from the critical Σ_* value and the total stellar mass, we land on a scale radius $r_s = 1.3$ kpc.

From Huang et al. (2012), we have scaling relations for HI and SFR as a function of stellar mass:

$$\log(M_{\rm HI}) = \begin{cases} 0.712\log(M_*) + 3.117, & \log(M_*) \leq 9\ {\rm M}_\odot \\ 0.276\log(M_*) + 7.042, & \log(M_*) > 9\ {\rm M}_\odot \end{cases}, \tag{B.2}$$

$$\log(sSFR) = \begin{cases} -0.149\log(M_*) - 8.207, & \log(M_*) \leq 9.5\ {\rm M}_\odot \\ -0.759\log(M_*) - 2.402, & \log(M_*) > 9.5\ {\rm M}_\odot \end{cases}. \tag{B.3}$$

For the example galaxy, $M_* = 10^{9.5}$ M$_\odot$ gives $\log(M_{\rm HI}) = 9.7$ M$_\odot$ and SFR $= 0.75$ M$_\odot$ yr^{-1}. We can then build a $\Sigma_{\rm SFR}$ profile with the same shape as the Σ_* profile if we assume a flat sSFR profile. Following Bigiel et al. (2008), $\Sigma_{\rm SFR} = 10^{-3.1}\Sigma_{\rm H_2}$ (with $\Sigma_{\rm SFR}$ in M$_\odot$ kpc^{-2} and $\Sigma_{\rm H_2}$ in M$_\odot$ pc^{-2}) and galaxies have relatively flat HI profiles with a value around 8 M$_\odot$ pc^{-2}. This allows us to determine an H_2 profile that also has an edge at 8.1 kpc, and

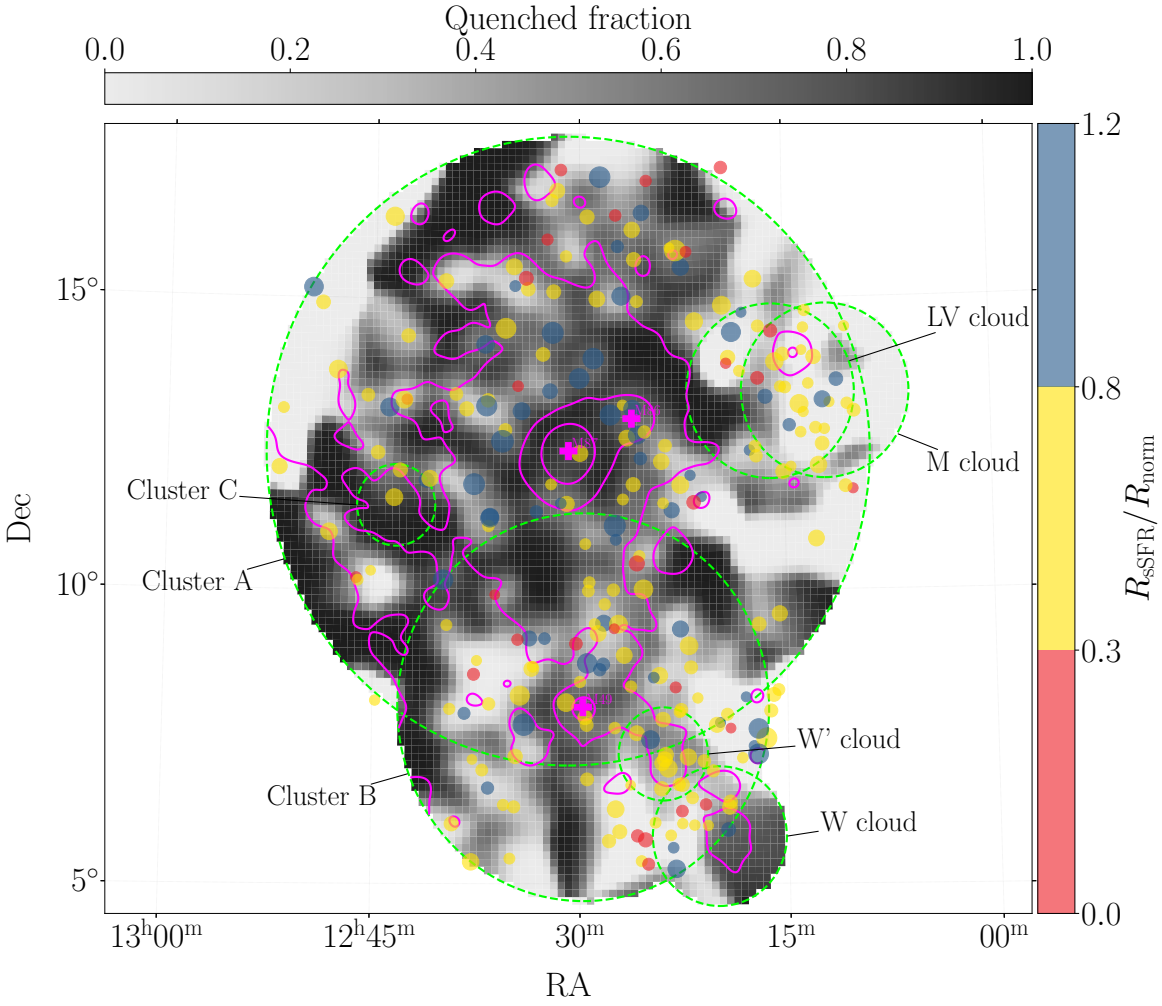


Figure B.4: Update to Figure 3.7, but including X-ray contours in magenta, and background greyscale showing quenched fraction. X-ray contours come from the ROSAT All-sky survey hard energy band (0.4 to 2.4 keV). Quenched fractions are calculated by using Gaussian KDEs to compare the distribution of Hα emitters from VESTIGE with the total number of galaxies frmo NGVS, for $M_8 > 10^8 \mathrm{M}_\odot$.

an HI profile that extends beyond the SF disc to 13.5 kpc (assuming the total HI content follows the scaling relations in Huang et al. (2012), our galaxy has $M_{\rm HI} = 10^{9.7}$ M$_\odot$). The initial gas and SFR density profiles for the galaxy are shown in Fig. B.5. Since the edge of the galaxy occurs at 8.1 kpc and beyond this point there is only HI gas, the total gas density threshold for star formation is determined by this value of HI, which is 8 M$_\odot$ pc^{-2}.

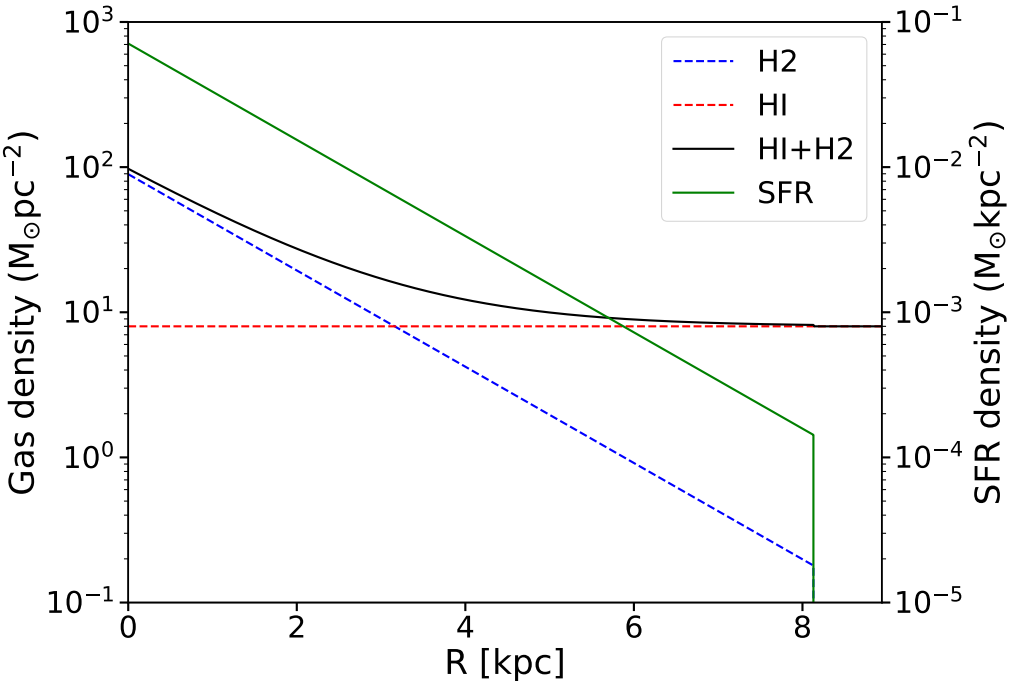


Figure B.5: Initial SFR (green), HI (red), H_2 (blue) and total gas (black) density profiles for a $10^{9.5}$M$_\odot$ galaxy.

We assume that there is no radial dependence of the HI to H_2 conversion, and that the global HI content just drops by whatever amount necessary to replenish the H_2 at each timestep. As such, the HI profile drops but remains constant at all radii. In Fig. B.6, we show the gas and SFR density profiles in the first and second rows, respectively. Each column shows a different timestep (2, 5 and 8 Gyr after infall). On the SFR density plots, we show the $R_{\rm sSFR}$ determined by where the total gas density falls below the threshold value of 8 M$_\odot$ pc^{-2}. In the bottom row, we show the evolution of the global SFR, gas deficiency and $R_{\rm sSFR}$. We see that in this model, truncations occur early as the HI begins to deplete; however it takes several gigayears for the global SFR to drop significantly; by this time, the galaxy is completely anaemic in terms of its HI gas content.

Our RPS model assumes a galaxy falling into the cluster radially and face-on, such that the direction of the ram-pressure force is orthogonal to the plane of the disc. The efficiency of RPS can vary moderately as a function of inclination angle (e.g. Roediger & Brüggen, 2006; Steinhauser et al., 2016). The restoring force holding the gas to the galactic disc is given by

$$f = \left[g_*(\mathrm{r}) + \mathrm{g_{HI}(r)} + \mathrm{g_{H_2}(r)} + \mathrm{g_{DM}(r)}\right]\ \Sigma_{\mathrm{HI}}(r), \tag{B.4}$$

where $g_*(\mathrm{r})$, $g_{\mathrm{HI}}(r)$, $g_{\mathrm{H_2}}(r)$ and $g_{\mathrm{DM}}(r)$ are the contributions to the gravitational acceleration from the different galactic components (stars, HI, H_2 and dark matter), and $\Sigma_{\mathrm{HI}}(r)$ is the surface density of HI gas. Since our stellar component is simply an exponential disc, it follows that

$$g_*(r) = 2\pi G\Sigma_*(r) = 2\pi G\Sigma_{0,*}e^{-\mathrm{r/r_s}}, \tag{B.5}$$

where $\Sigma_{0,*}$ is the central stellar mass surface density and r_s is the scale radius. Our H_2 profile is also an exponential so it will take the same form. Our HI profile is flat and as such $\Sigma_{\mathrm{HI}}(r) = \Sigma_{0,\mathrm{HI}}$. For the dark matter halo, we deviate from Roberts et al. (2019) only in that we use a Navarro-Frenk-White (NFW; Navarro et al. 1996) profile instead of a Hernquist profile (Hernquist, 1990), with

$$\Phi(r,\ z) = \frac{4\pi G\rho_0 a^3}{\sqrt{r^2+z^2}} \ln\left(1 + \frac{\sqrt{r^2+z^2}}{a}\right), \tag{B.6}$$

where we determine the halo mass, M_{h}, from the stellar-to-halo mass relation of Girelli et al. (2020), which allows the determination of R_{200}. The scale radius, $a = R_{200}/c$, where c is the concentration determined from the concentration-halo mass relation from Diemer & Kravtsov (2015). ρ_0 is the central density of the NFW profile which can be be determined from M_{h}, R_{200} and a. We calculate the gravitational acceleration of the dark matter profile by taking the maximum of the derivative along the z axis, where z is the direction perpendicular to the disc:

$$\begin{aligned} g_{\mathrm{DM}}(r) &= \max_{\mathrm{z}} \frac{\partial\Phi(r,\ z)}{\partial z} \\ &= \max_{\mathrm{z}} 4\pi G\rho_0 a^3 z \left[\frac{\ln\left(a+\sqrt{r^2+z^2}\right) - \ln(a)}{\left(r^2+z^2\right)^{3/2}}\right. \\ &\qquad \left. - \frac{1}{\left(r^2+z^2\right)\left(a+\sqrt{r^2+z^2}\right)}\right]. \end{aligned} \tag{B.7}$$

To determine the ram-pressure at a given point in phase space, we use the beta profile fit from Schindler et al. (1999), with $r_c = 12.9$ kpc and $\beta = 0.47$, and determine the central ICM density from Simionescu et al. (2017) to be $n_0 = 2.33 \times 10^{-2}$ cm^{-3}. We then can determine the ICM mass density based on this relation from Boselli et al. (2022):

$$\rho_{\rm ICM}(r) = 1.92\,\mu\,n_{\rm e}(r)\,m_{\rm p} = 1.15\,n_{\rm e}(r)\,m_{\rm p}, \tag{B.8}$$

where $\mu = 0.6$.

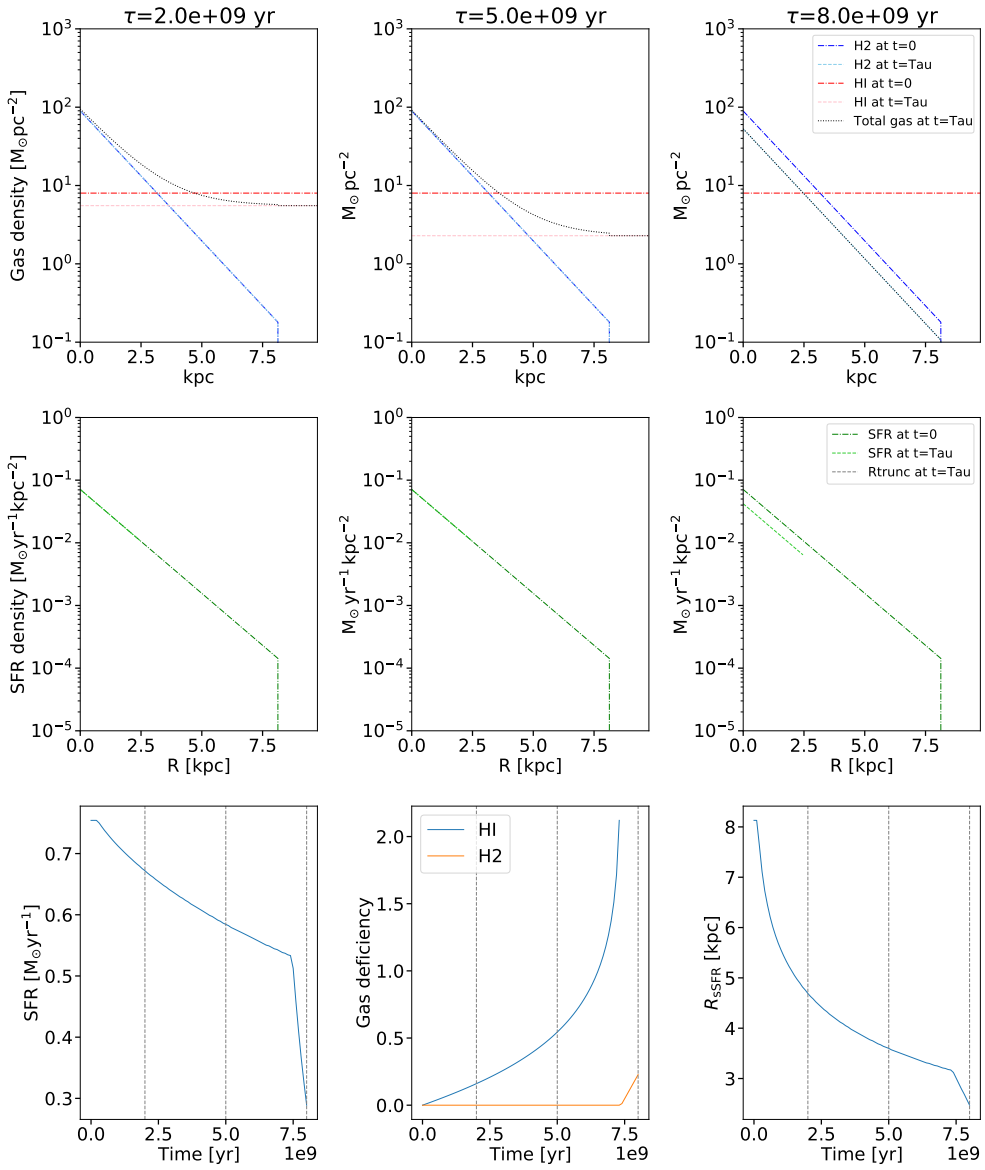


Figure B.6: *Top*: Gas density profiles at three timesteps for starvation model. Initial profiles for HI and H_2 are shown in red and blue, respectively while evolved profiles are shown in pink and light blue, respectively. Evolved total gas density profile is shown in black. *Middle*: SFR density profiles at three timesteps, where the initial profile is shown in green and the evolved profile in light green. The grey vertical line shows $R_{\rm sSFR}$. *Bottom*: Time evolution of global SFR, gas deficiency and $R_{\rm sSFR}$.

B.6 Additional radial profile plots

We show in Fig. B.7 the equivalent of Fig. 3.1 for eight galaxies spanning a range of stellar masses.

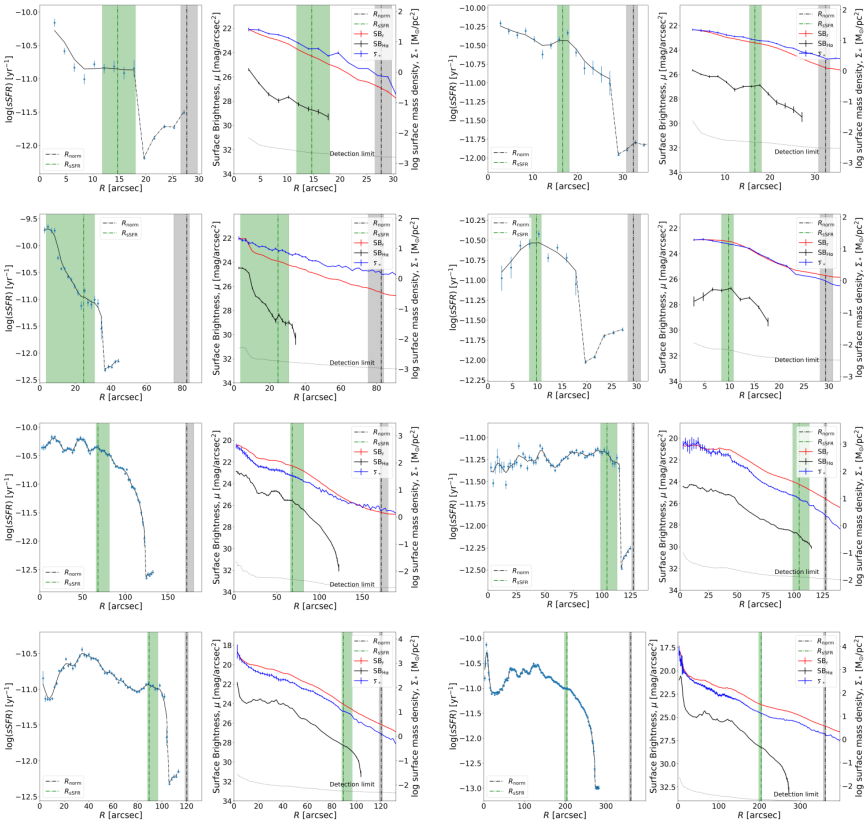


Figure B.7: Same as Fig. 3.1 but for all galaxies shown in Fig. B.8. From top to bottom and left to right: VCC 304, VCC 2037, VCC 865 (NGC 4396), VCC 157 (NGC 4208), VCC 1605, VCC 565, VCC 1868 (NGC 4607) and VCC 596 (NGC 4321).

B.7 Additional postage stamps

In Fig. B.8, we show postage stamps alongside radial sSFR profiles (same as Fig. 3.3) for eight galaxies spanning a range of stellar masses.

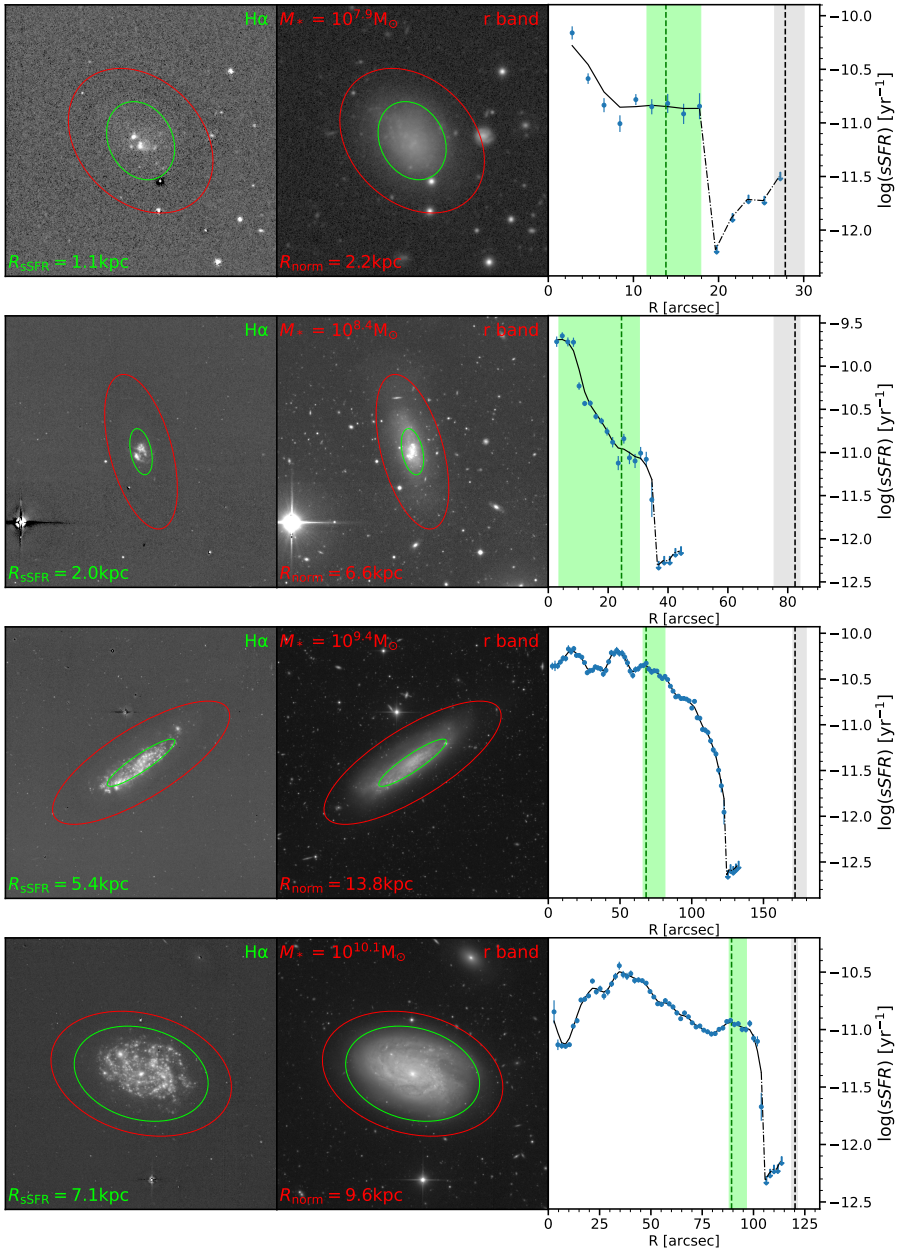


Figure B.8: Same as Fig. 3.3 for VCC 304, VCC 2037, VCC 865 (NGC 4396), and VCC 157 (NGC 4208).

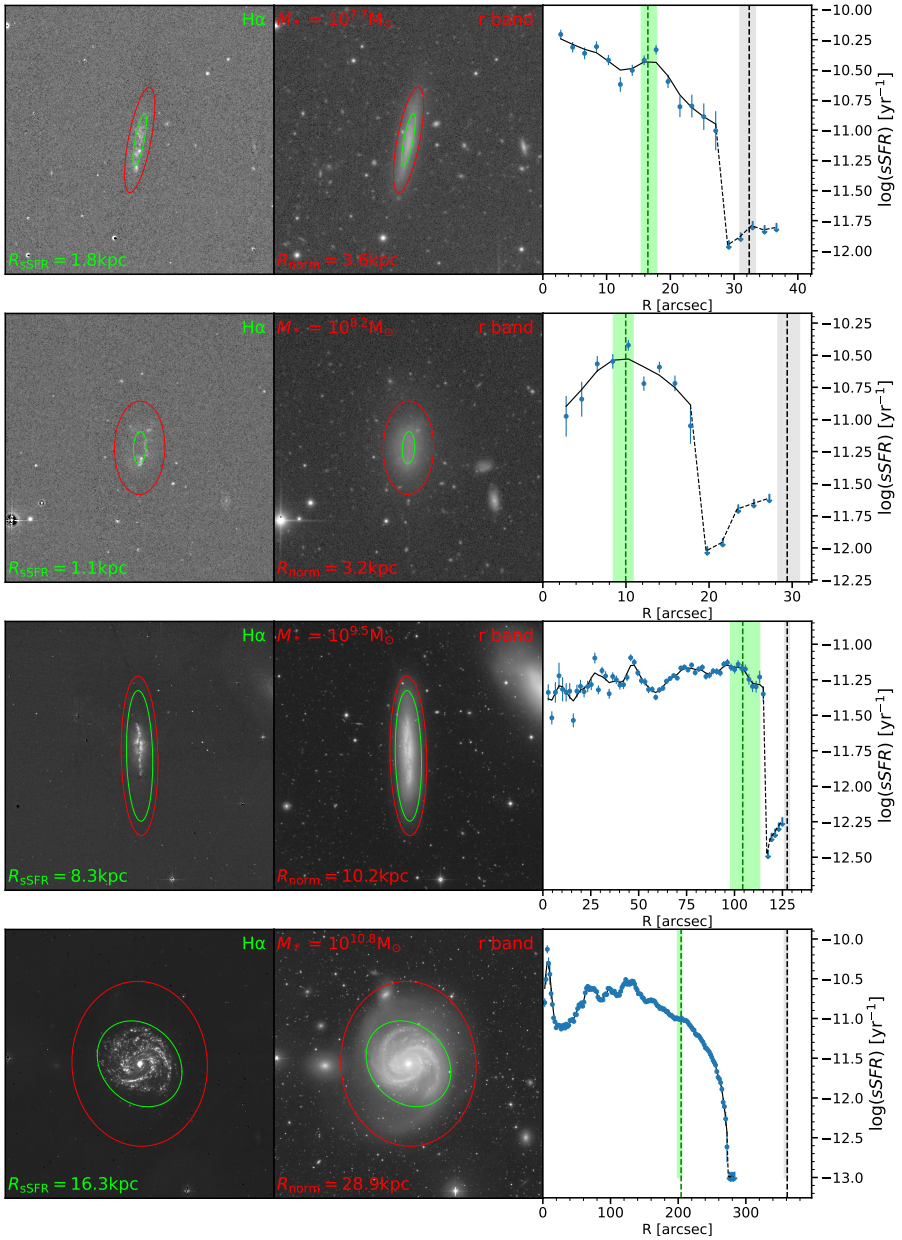


Figure B.8: (Cont.) Same as Fig. 3.3 for VCC 1605, VCC 565, VCC 1868 (NGC 4607) and VCC 596 (NGC 4321).

Appendix C

C.1 CIGALE parameters

C.2 MaNGA emission line analysis

C.3 Full data table and additional figures

Module	Parameter	Values
`sfhdelayedbq`	τ_{main} (Myr)	500, 750, 1000, 1250, 1500, 1750, 2000, 2250, 2500, 3000
	t_{main} (Myr)	4000, 5000, 6000, 7500, 10000, 13000
	t_{bq} (Myr)	10
	$r_{\mathrm{SFR},1}$	0.0, 0.05, 0.1, 0.15, 0.2, 0.25, 0.3, 0.35, 0.4, 0.45, 0.5, 0.6, 0.75, 0.9, 1.0, 1.2, 1.5
	$t_{\mathrm{bq},2}$ (Myr)	400
	$r_{\mathrm{SFR},2}$	0.0, 0.05, 0.1, 0.15, 0.2, 0.25, 0.3, 0.35, 0.4, 0.45, 0.5, 0.6, 0.75, 0.9, 1.0, 1.2, 1.5
`bc03`	IMF	Chabrier
	Metallicity (Z)	0.008, 0.02, 0.05
	Separation age (Myr)	10
`nebular`	$\log U$	-3.0
	Z_{gas}	0.02
`dustatt_modified_starburst`	$E(B-V)_{\mathrm{lines}}$	0.10, 0.15, 0.20, 0.25, 0.30, 0.35, 0.40, 0.45, 0.50, 0.55, 0.65
	$E(B-V)_{\mathrm{factor}}$	1.0
	UV bump amplitude	0.0
	R_V	4.05
`dl2014`	q_{PAH}	2.5, 3.0
	U_{min}	0.1, 0.5, 1.0, 5.0, 10.0
	α	1.0, 2.0, 3.0
	γ	0.02, 0.1, 0.2

Table C.1: CIGALE SED fitting configuration parameters.

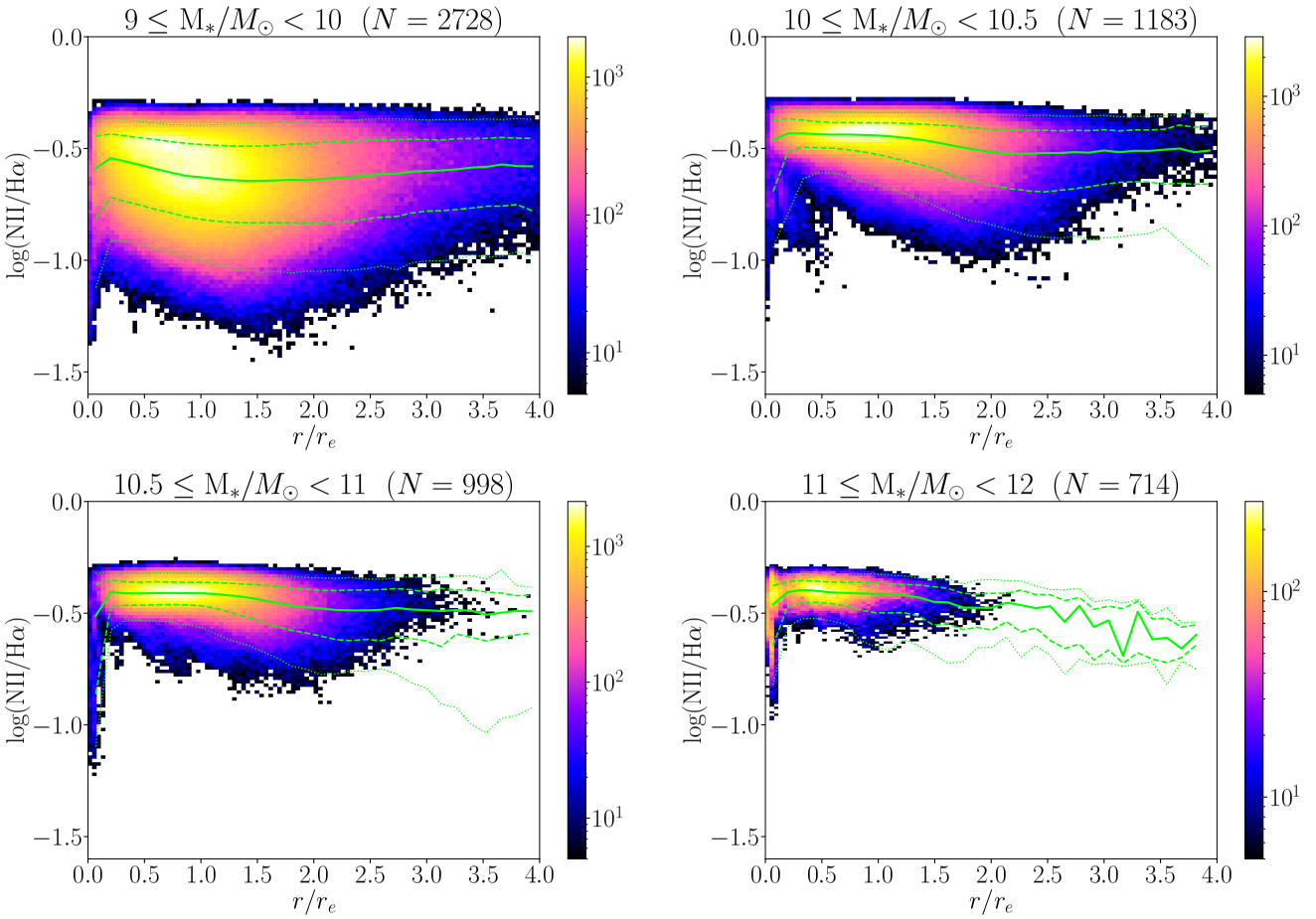


Figure C.1: NIIHα ratios for star-forming spaxels in MaNGA star-forming galaxies as a function of galactocentric radius. Each panel shows a different range of integrated galaxy stellar mass, with the colourmap showing the density of spaxels. The solid green line shows the running median, with the dashed and dotted lines showing the $16^{\text{th}}/84^{\text{th}}$ and $2.5^{\text{th}}/97.5^{\text{th}}$ percentiles, respectively.

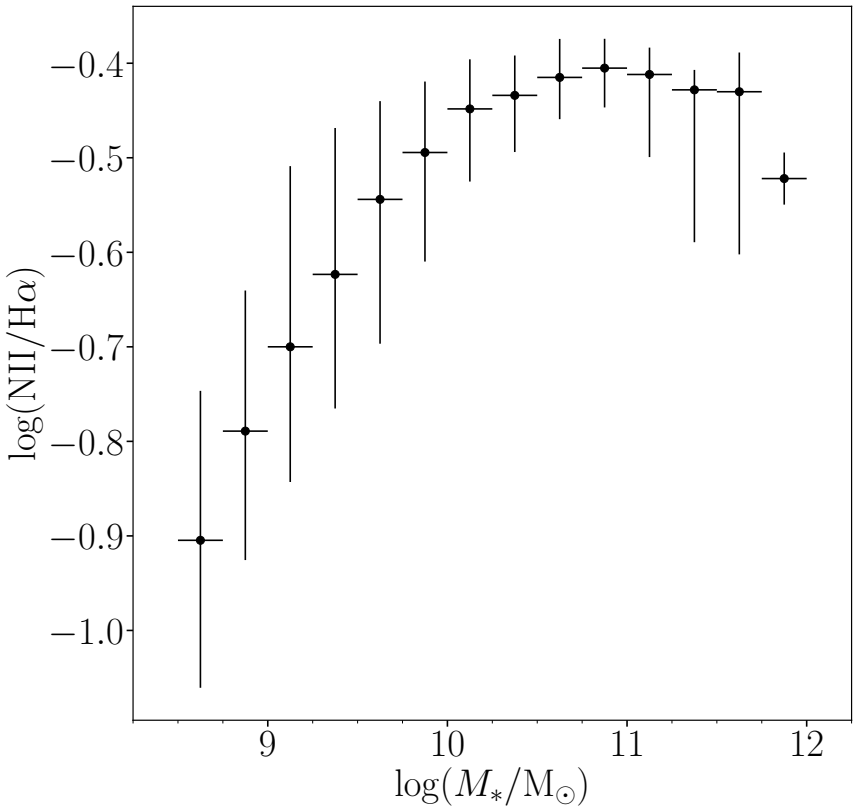
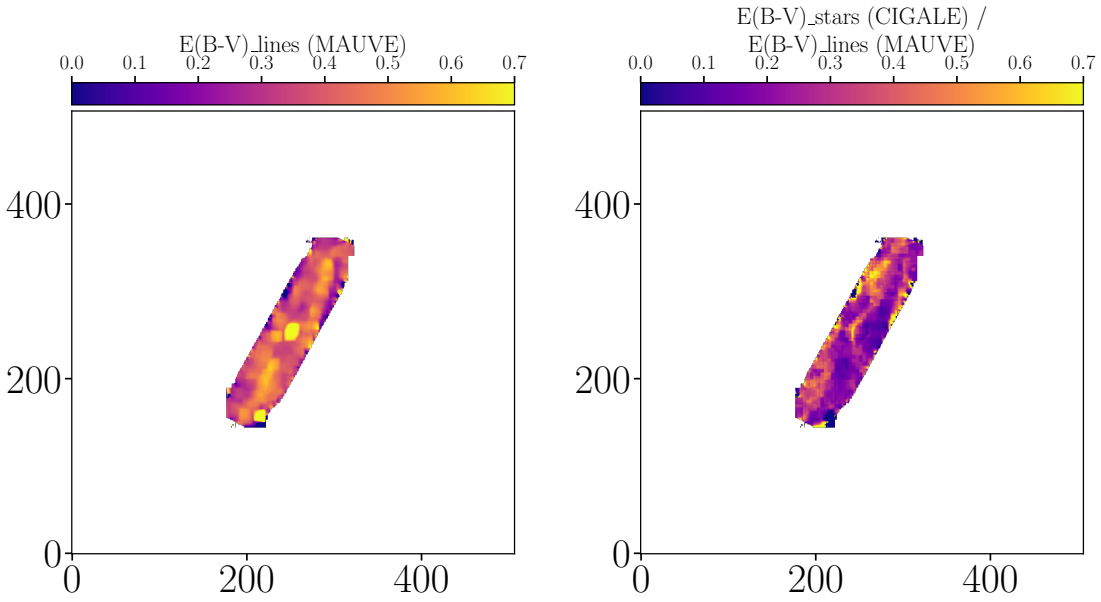
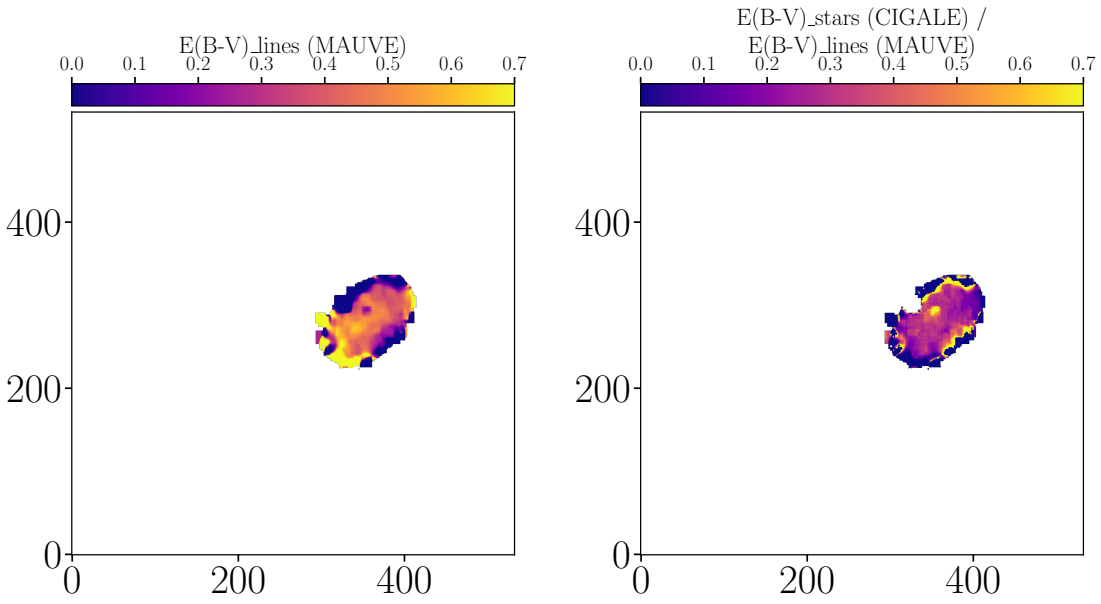


Figure C.2: NII/Hα ratio as a function of stellar mass in MaNGA star-forming galaxies.

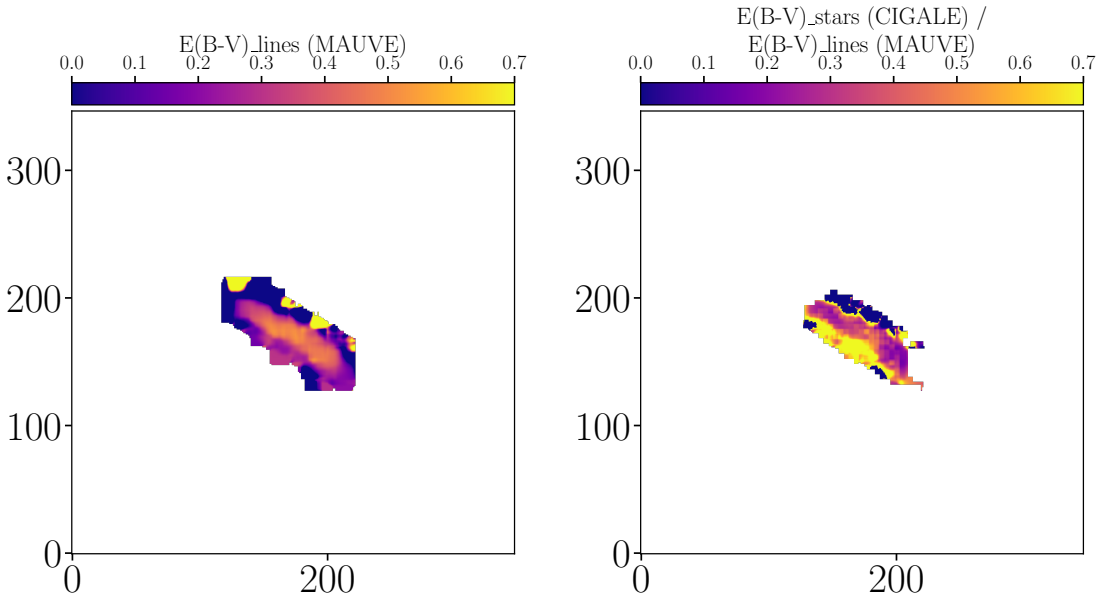


(a)

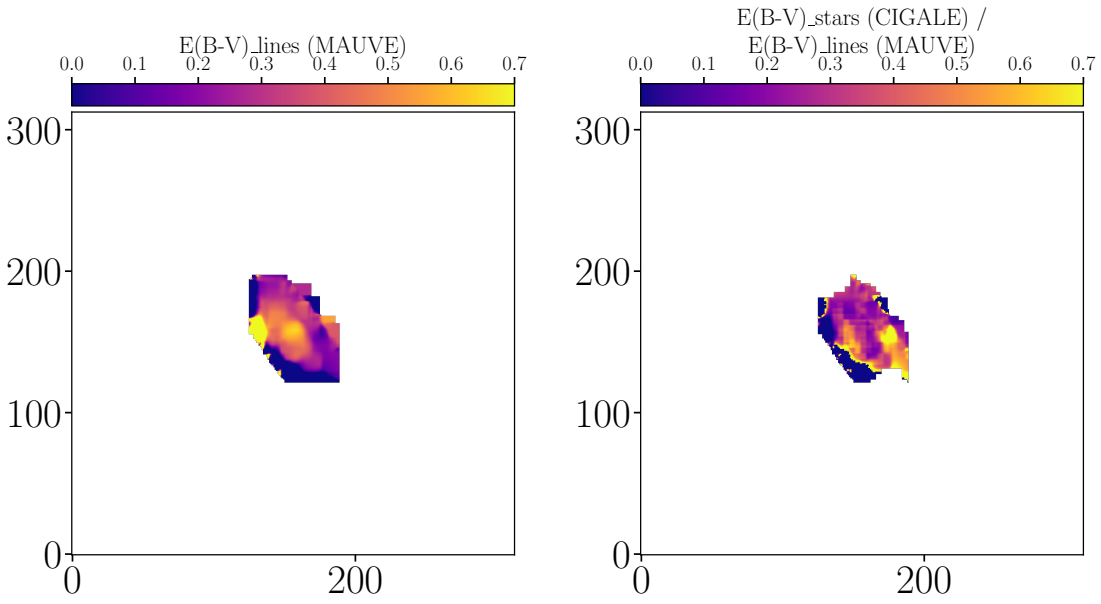


(b)

Figure C.3: Same as Figure 4.8, but for VCC 92 (a) and VCC 483 (b).



(c)



(d)

Figure C.3: (Cont.) Same as Figure 4.8, but for VCC 630 (a) and VCC 1516 (b).

VCC name	$\log\left(\frac{M_*}{M_\odot}\right)$	HI-def	σ from SFMS	Trunc ratio[a]	VIVA group	RPS cand?[b]	$A_{1,\mathrm{global}}$ (GALEX)	$\nabla(\mathrm{dex}/R_e)$ (GALEX)	$A_{1,\mathrm{global}}$ (UVIT)	$\nabla(\mathrm{dex}/R_e)$ (UVIT)
VCC1002	9.97	0.56	-0.03σ	0.47	-	N	$0.23^{+0.18}_{-0.13}$	-0.07 ± 0.13	$-99.00^{+0.00}_{-0.00}$	-99.00 ± 0.00
VCC1043	10.74	1.27	-0.53σ	0.97	-	Y	$0.17^{+0.03}_{-0.03}$	-0.04 ± 0.02	$-99.00^{+0.00}_{-0.00}$	-99.00 ± 0.00
VCC1086	9.83	1.57	-1.61σ	0.88	-	N	$0.90^{+0.08}_{-0.07}$	-0.05 ± 0.09	$-99.00^{+0.00}_{-0.00}$	-99.00 ± 0.00
VCC1118	9.77	0.90	-0.30σ	0.66	-	N	$0.35^{+0.05}_{-0.05}$	0.22 ± 0.20	$-99.00^{+0.00}_{-0.00}$	-99.00 ± 0.00
VCC1190	10.61	2.81	-3.42σ	0.85	-	Y	$0.34^{+0.31}_{-0.19}$	-0.46 ± 0.88	$-99.00^{+0.00}_{-0.00}$	-99.00 ± 0.00
VCC135	9.54	2.36	-1.97σ	0.75	-	N	$0.00^{+0.00}_{-0.00}$	0.18 ± 0.15	$-99.00^{+0.00}_{-0.00}$	-99.00 ± 0.00
VCC1401	10.92	0.55	-0.81σ	0.89	2	N	$0.52^{+0.18}_{-0.18}$	0.02 ± 0.05	$0.33^{+0.03}_{-0.03}$	0.05 ± 0.04
VCC145	9.65	0.27	-0.45σ	nan	-	N	$0.30^{+0.03}_{-0.03}$	-0.09 ± 0.02	$-99.00^{+0.00}_{-0.00}$	-99.00 ± 0.00
VCC1508	9.51	0.07	0.71σ	0.79	-	N	$0.39^{+0.01}_{-0.01}$	-0.04 ± 0.07	$-99.00^{+0.00}_{-0.00}$	-99.00 ± 0.00
VCC1516	9.55	0.93	-0.48σ	0.89	2	Y	$1.25^{+0.03}_{-0.03}$	-0.01 ± 0.05	$1.85^{+0.06}_{-0.05}$	0.02 ± 0.05
VCC1535	10.98	0.48	-3.90σ	0.86	-	N	$0.53^{+0.10}_{-0.09}$	0.92 ± 0.59	$-99.00^{+0.00}_{-0.00}$	-99.00 ± 0.00
VCC1555	10.53	0.16	-0.47σ	0.80	1	Y	$0.10^{+0.04}_{-0.04}$	-0.36 ± 0.13	$0.11^{+0.01}_{-0.01}$	-0.68 ± 0.06
VCC157	10.13	0.90	-0.00σ	0.75	-	N	$0.12^{+0.03}_{-0.03}$	0.10 ± 0.09	$-99.00^{+0.00}_{-0.00}$	-99.00 ± 0.00
VCC167	10.93	0.59	-1.70σ	nan	4	N	$0.48^{+0.04}_{-0.04}$	-0.20 ± 0.05	$-99.00^{+0.00}_{-0.00}$	-99.00 ± 0.00
VCC1673	10.07	0.28	-0.53σ	0.97	0	N	$0.15^{+0.03}_{-0.02}$	-0.10 ± 0.03	$-99.00^{+0.00}_{-0.00}$	-99.00 ± 0.00
VCC1676	10.31	0.72	0.41σ	1.18	0	N	$0.57^{+0.03}_{-0.03}$	0.08 ± 0.09	$-99.00^{+0.00}_{-0.00}$	-99.00 ± 0.00
VCC1690	10.74	1.07	-1.03σ	2.17	3	Y	$0.48^{+0.04}_{-0.04}$	0.69 ± 0.34	$-99.00^{+0.00}_{-0.00}$	-99.00 ± 0.00
VCC1727	10.90	0.97	-2.28σ	0.84	4	N	$0.14^{+0.02}_{-0.02}$	0.29 ± 0.14	$0.06^{+0.04}_{-0.03}$	0.28 ± 0.15
VCC199	10.73	0.92	-3.97σ	0.74	-	N	$0.00^{+0.00}_{-0.00}$	-0.02 ± 0.29	$-99.00^{+0.00}_{-0.00}$	-99.00 ± 0.00
VCC226	9.97	1.02	0.11σ	0.73	-	N	$0.39^{+0.04}_{-0.04}$	0.06 ± 0.10	$-99.00^{+0.00}_{-0.00}$	-99.00 ± 0.00
VCC307	10.52	0.06	0.78σ	1.24	1	N	$0.10^{+0.01}_{-0.01}$	0.03 ± 0.04	$-99.00^{+0.00}_{-0.00}$	-99.00 ± 0.00
VCC393	9.56	0.60	0.34σ	0.52	-	N	$0.10^{+0.03}_{-0.03}$	-0.14 ± 0.13	$0.10^{+0.04}_{-0.04}$	-0.13 ± 0.13

[a] From Morgan et al. (2024).
[b] Based on Boselli et al. (2022) and references therein.

Table C.2: Relevant galaxy parameters for entire sample analyzed.

VCC name	$\log\left(\frac{M_*}{M_\odot}\right)$	HI-def	σ from SFMS	Trunc ratio[a]	VIVA group	RPS cand?[b]	$A_{1,\mathrm{global}}$ (GALEX)	$\nabla(\mathrm{dex}/R_e)$ (GALEX)	$A_{1,\mathrm{global}}$ (UVIT)	$\nabla(\mathrm{dex}/R_e)$ (UVIT)
VCC47	9.82	0.92	-1.13σ	1.21	-	N	$0.12^{+0.07}_{-0.06}$	0.07 ± 0.04	$-99.00^{+0.00}_{-0.00}$	-99.00 ± 0.00
VCC483	10.09	0.63	0.05σ	0.69	2	Y	$0.31^{+0.02}_{-0.02}$	0.02 ± 0.02	$0.34^{+0.02}_{-0.02}$	-0.02 ± 0.02
VCC497	10.11	0.47	-2.12σ	nan	2	Y	$0.33^{+0.07}_{-0.06}$	0.05 ± 0.11	$0.35^{+0.02}_{-0.02}$	0.12 ± 0.11
VCC524	10.21	1.56	-1.27σ	0.78	-	N	$0.31^{+0.09}_{-0.08}$	-0.10 ± 0.09	$-99.00^{+0.00}_{-0.00}$	-99.00 ± 0.00
VCC534	9.88	1.81	-3.09σ	0.61	-	N	$0.42^{+0.18}_{-0.15}$	0.83 ± 0.37	$-99.00^{+0.00}_{-0.00}$	-99.00 ± 0.00
VCC559	9.91	1.62	-0.98σ	0.83	-	N	$0.37^{+0.10}_{-0.11}$	1.00 ± 0.57	$-99.00^{+0.00}_{-0.00}$	-99.00 ± 0.00
VCC570	10.01	1.60	-2.72σ	0.78	-	N	$0.70^{+0.07}_{-0.06}$	0.32 ± 0.16	$-99.00^{+0.00}_{-0.00}$	-99.00 ± 0.00
VCC576	9.82	0.34	0.33σ	1.03	-	N	$0.80^{+0.05}_{-0.04}$	-0.16 ± 0.06	$-99.00^{+0.00}_{-0.00}$	-99.00 ± 0.00
VCC58	9.92	0.21	-1.31σ	0.68	-	N	$0.41^{+0.15}_{-0.14}$	-0.22 ± 0.06	$-99.00^{+0.00}_{-0.00}$	-99.00 ± 0.00
VCC596	10.83	0.41	-0.37σ	0.57	0	N	$0.16^{+0.01}_{-0.01}$	0.19 ± 0.13	$0.21^{+0.01}_{-0.01}$	-0.01 ± 0.13
VCC613	10.17	0.74	-2.06σ	0.85	-	N	$0.00^{+0.00}_{-0.00}$	0.11 ± 0.10	$-99.00^{+0.00}_{-0.00}$	-99.00 ± 0.00
VCC630	9.59	1.17	-1.10σ	0.82	2	Y	$1.53^{+0.04}_{-0.05}$	-0.04 ± 0.02	$-99.00^{+0.00}_{-0.00}$	-99.00 ± 0.00
VCC656	10.16	0.75	-1.21σ	0.70	-	N	$0.25^{+0.06}_{-0.06}$	-0.33 ± 0.05	$-99.00^{+0.00}_{-0.00}$	-99.00 ± 0.00
VCC692	9.71	1.04	-1.97σ	0.62	1	N	$0.46^{+0.03}_{-0.04}$	-0.00 ± 0.13	$0.23^{+0.05}_{-0.04}$	-0.04 ± 0.13
VCC792	10.41	1.10	-1.67σ	0.75	4	N	$0.10^{+0.03}_{-0.03}$	0.08 ± 0.09	$0.17^{+0.04}_{-0.05}$	0.06 ± 0.08
VCC827	9.76	0.23	-0.14σ	nan	-	N	$0.55^{+0.07}_{-0.07}$	0.01 ± 0.02	$-99.00^{+0.00}_{-0.00}$	-99.00 ± 0.00
VCC836	10.19	0.93	0.08σ	0.93	2	Y	$0.25^{+0.03}_{-0.03}$	0.45 ± 0.09	$0.17^{+0.04}_{-0.04}$	0.36 ± 0.08
VCC849	9.58	0.55	-0.21σ	0.26	-	N	$0.42^{+0.14}_{-0.14}$	-0.40 ± 0.11	$-99.00^{+0.00}_{-0.00}$	-99.00 ± 0.00
VCC873	10.05	0.87	1.01σ	0.94	2	Y	$1.32^{+0.06}_{-0.07}$	0.50 ± 0.18	$-99.00^{+0.00}_{-0.00}$	-99.00 ± 0.00
VCC89	10.38	0.16	-0.08σ	nan	0	N	$0.16^{+0.03}_{-0.02}$	-0.02 ± 0.05	$0.15^{+0.03}_{-0.03}$	-0.13 ± 0.04
VCC912	9.76	1.24	-1.16σ	0.55	-	N	$0.17^{+0.03}_{-0.03}$	0.43 ± 0.39	$-99.00^{+0.00}_{-0.00}$	-99.00 ± 0.00
VCC92	10.67	0.20	-0.52σ	nan	4	N	$0.30^{+0.02}_{-0.02}$	-0.04 ± 0.03	$0.65^{+0.02}_{-0.03}$	-0.05 ± 0.02
VCC938	9.53	0.81	-0.82σ	nan	-	N	$0.26^{+0.02}_{-0.02}$	-0.08 ± 0.05	$-99.00^{+0.00}_{-0.00}$	-99.00 ± 0.00
VCC939	9.76	0.13	-0.92σ	0.68	-	N	$0.06^{+0.02}_{-0.02}$	0.01 ± 0.10	$-99.00^{+0.00}_{-0.00}$	-99.00 ± 0.00
VCC97	10.27	0.48	-0.51σ	0.75	-	N	$0.30^{+0.05}_{-0.05}$	-0.16 ± 0.07	$-99.00^{+0.00}_{-0.00}$	-99.00 ± 0.00

[a] From Morgan et al. (2024).
[b] Based on Boselli et al. (2022) and references therein.

Table C.2: (Cont.) Relevant galaxy parameters for entire sample analyzed.